THE UNIVERSITY OF CHICAGO

IN SITU PROBING OF TWO-DIMENSIONAL QUANTUM GASES

A DISSERTATION SUBMITTED TO

THE FACULTY OF THE DIVISION OF THE PHYSICAL SCIENCES

IN CANDIDACY FOR THE DEGREE OF

DOCTOR OF PHILOSOPHY

DEPARTMENT OF PHYSICS

BY

CHEN-LUNG HUNG

CHICAGO, ILLINOIS

AUGUST 2011

To my family

ABSTRACT

This thesis reports on *in situ* probing of two-dimensional (2D) quantum gases of ^{133}Cs atoms with tunable inter-atomic interactions. With spatially resolved *in situ* density measurements, the experimental work described in this thesis presents detailed studies on local equilibrium properties, near-equilibrium fluctuations and correlations, and non-equilibrium transport in 2D samples prepared near the critical points of continuous phase transitions. Specifically, we investigated the Berezinskii-Kosterlitz-Thouless (BKT) superfluid transition in the bulk and the superfluid-to-Mott insulator transition in an optical lattice.

The enabling experimental techniques include a new vacuum chamber design which permits a large numerical aperture for high resolution microscopy, a new approach of implementing all-optical cooling of cesium atoms to Bose-Einstein condensation (BEC), and the fabrication of a novel 2D optical trap. In particular, a fast and runaway evaporative cooling is realized using a tilted optical potential, allowing the production of a large atom number BEC in only 2~4 s. A novel two-dimensional "pancake"-like optical trap is subsequently employed to convert a BEC into a monolayer of 2D quantum gas. This trap can be smoothly transformed into a 2D square lattice potential, simulating the paradigmatic Bose-Hubbard model.

Using this 2D trapping potential, we realize the superfluid-to-Mott insulator quantum phase transition in two dimensions and report the direct observation of incompressible Mott-insulating domains in deep lattices. Investigations on dynamics across the superfluid-insulator transition are presented, in which we observed anomalously slow mass transport and statistical evolution, indicating prolonged global many-body time scales across the insulator quantum phase transition.

For weakly interacting 2D Bose gases without the 2D lattice potential, we report on the observation of universal scaling behaviors in samples prepared at different temperatures and various interaction strengths. We confirm the scale invariance due to the intrinsic scaling symmetry of 2D gases and the universality near the BKT superfluid transition. A growing density-density corre-

lation in the BKT critical region was observed and analyzed, and the static structure factors were extracted.

The experimental schemes and analysis methods we developed in this thesis to determine the universal scaling behaviors, fluctuations, correlations, and transport properties can be applied to other strongly correlated many-body atomic systems near a continuous phase transition. They form an important set of tools for our future objectives to study both the static and dynamic properties of quantum critical gases in optical lattices.

ACKNOWLEDGMENTS

I would like to express my gratitude to Prof. Cheng Chin for his guidance over these years. Cheng is an incredibly resourceful, thoughtful, and open-minded advisor that I am privileged to work with. He creates an open environment for brainstorming discussions from which I benefited enormously. His strong sense of physics as well as his optimism over research provide me with the courage and the valuable guidance to develop my own research interest.

I would like to thank Prof. Nate Gemelke, whose creativity and insight in physics had greatly inspired me during his stay as a postdoctoral fellow. The cesium experiment has benefited greatly from his numerous original ideas. I enjoyed all the discussions with him, for science and for his humor.

I would like to thank my lab partner Xibo Zhang, whose patience and persistence ensure that different elements of the lab are in order and in place. His full commitment of pursuing quality works forms the important foundation that drives our system to go this far. I am glad to share with him all the hard works, discussions, and the cheerful moments in my Ph.D. career.

I would like to thank Dr. Kathy-Anne Soderberg, who worked in the cesium-lithium experiment, for many of her helps. She is the warmest person in the group. I would like to thank Dr. Shih-Kuang Tung and Li-Chung Ha for bringing new perspectives to the cesium experiment. I believe the group will continue to thrive with their input.

Besides the few people that I have mentioned, there are many more that contributed enormously to this experiment. I would like to thank Jeffrey Gebhardt for his valuable work on designing and building the vacuum system. It is the most beautiful and unique creation that I have ever seen. I was also lucky to work with Prof. Selim Jochim during the summer of 2006 before he took his position at Heidelberg University. I would like to thank Kuo-Tung Lin for his countless help on building electronics and machining and for his warm friendship outside the lab over these years. I would also like to thank Robert Berry for his incredibly precise machining that helps our lasers

CONTENTS

LIST OF FIGURES

LIST OF TABLES

CHAPTER 1

INTRODUCTION

1.1   Toward universal quantum simulation

Cold alkali atoms, with their internal structures and collisional properties known to high accuracy, offer a clean and highly controllable platform boosting tremendous advances in areas of metrology, quantum information science, and precision measurements [1]. The realization of Bose-Einstein condensation (BEC) [2, 3, 4] further opened up a new era of ultracold atomic physics, offering unprecedented opportunities in studying novel quantum many-body phenomena, many of which were traditionally studied in the context of condensed matter physics, nuclear physics, or were proposed without real wold analogy.

The appealing features in an ultracold atomic system are that the atoms are well isolated from the environment, yet can be coherently manipulated by means of electromagnetic fields; the diluteness of the sample permits a simple and universal description in the two-body interacting potential [5], while the strength of the interaction parameter can acquire great tunability via, e.g., the magnetic Feshbach resonances [6]. The size of the system can vary from just a few particles to a large number (typically 10^5 atoms) approaching the thermodynamic limit; the constituent particles can be chosen to be bosons, fermions or even heterogeneous mixtures. At ultracold temperatures, both quantum and thermal fluctuations manifest at low enough energy scales that near-equilibrium dynamics can potentially be monitored with enhanced spatial and temporal resolutions. Building on these features, one can assemble complex many-body or few-body Hamiltonians from bottom (single particle level) to top (many-body level) with great tunability and even adjustable dimensionality. The behavior of quantum gases can be studied with great detail in well controlled experimental conditions and be directly compared to results derived from analytical theories or first principle (*ab initio*) calculations, providing benchmarks or even challenges to our understanding of complex

quantum many-body or few-body systems.

For many years, condensed matter systems were the sole laboratory test ground of modern field theories. Now with the realization of bosonic and fermionic matter wave fields, ultracold atomic systems are among the strongest candidates toward the realization of a *universal quantum simulator*, envisioned by Richard Feynman almost 30 years ago [7]: *"It's been noted time and time again that the phenomena of field theory (if the world is made in a discrete lattice) are well imitated by many phenomena in solid state theory (which is simply the analysis of a latticework of crystal atoms, and in the case of the kind of solid state I mean each atom is just a point which has numbers associated with it, with quantum-mechanical rules). For example, the spin waves in a spin lattice imitating Bose-particles in the field theory. I therefore believe it's true that with a suitable class of quantum machines you could imitate any quantum system, including the physical world."*

The past decade has presented astonishing advancements toward this goal. Interacting Bose condensates were loaded into a periodic lattice potential formed by crossing and interfering laser beams [8] to simulate the paradigmatic Bose-Hubbard model [9, 10]; clean signatures of superfluid-to-Mott insulator quantum phase transitions in one-, two-, and three-dimensional lattice geometries have been observed through drastic changes of coherence properties in thr time-of-flight momentum distributions [8, 11, 12, 13]. The use of optical lattice potentials has since triggered many research activities [14], particularly on low-dimensional systems, which often exhibit intriguing quantum many-body phenomena. A one dimensional lattice potential is used to form a series of quasi-two dimensional traps, which slice a condensate into multiple copies of two-dimensional quantum gases [15]. The Berezinskii-Kosterlitz-Thouless transition [16, 17] of ultracold Bose gases was studied using matter wave interference [18], vortex counting [19], and interferometric measurements [20]. On the other hand, a two-dimensional lattice potential can fragment the condensate into multiple independent one-dimensional clouds, each realizing a system of 1D bosons. Fermionization of bosons in the Tonks-Girardeau limit [21, 22], has been observed in the strong

interaction regime through measurements of momentum distributions [23], thermalization properties [24], and photo-association rates [25]; the quantum phase transition from a Luttinger liquid to a Mott insulator in one dimension has recently been observed through measurements of transport properties and excitation spectra of 1D Bose gases [26].

1.2   Current technical limitations

Despite demonstrations of various paradigmatic condensed matter models, current experiments mostly concentrate on bulk measurements after time-of-flight (TOF) expansions. Although excellent in revealing phase coherence and momentum distribution in quantum gases, time-of-flight measurements present bulk properties of atomic samples and suffer from the inhomogeneity of external trapping potentials. Interpretations of these results often require close comparison with theoretical calculations. From TOF images, extracting information about the homogeneous model systems is a challenging task in current ultracold atomic experiments, especially for systems prepared in strongly-correlated regimes, where thorough theoretical understandings remain elusive.

Probing atomic samples *in situ* presents an ideal way to offer complementary information to TOF measurements, as the in-trap atomic density distribution is preserved during the time of detection. This is implemented by shining a short laser pulse, and imaging the shadow or fluorescence photons emitted by trapped atoms [27].

There are, however, difficulties for imaging bulk gases *in situ*. The first strong limitation is that one can only obtain column density distributions when imaging a three-dimensional object. A column density measurement again suffers from the trap inhomogeneity, as it presents an integrated property along one of the trap axes. The second difficulty is that degenerate quantum gases are optically dense. Therefore, standard absorption imaging yields a very limited dynamic range in the atomic density detection. Only light atomic species, such as lithium atoms, which become quantum degenerate at lower densities permit *in situ* measurements in the bulk. Phase contrast

imaging is often the only solution to image heavier and optically dense samples [27].

Many innovative methods attempted to overcome the above limitations, notably microwave tomographic imaging [28] and density reconstruction using inverse Abel transformation [29, 30, 31]. Since many useful local information is lost in an *averaged* measurement, investigating near equilibrium fluctuations and non-equilibrium dynamics using these methods also remains non-trivial.

1.3   Our approach –*in situ* imaging of two-dimensional quantum gases

We aim at resolving the aforementioned difficulties by *in situ* imaging in a new configuration. Our approach, accomplished in this thesis, is to realize a tunable many-body system in a monolayer of two-dimensional (2D) quantum gas, in which the atomic motional degree of freedom along the imaging axis is frozen to its quantum zero-point motion. Interesting thermodynamics and quantum physics therefore only manifest themselves in the 2D plane. Images of such 2D samples do not suffer from the axial inhomogeneity. The optical density is reasonably close to the order of unity, permitting large dynamic range for density detection. It would allow a single *snapshot*, revealing a precise in-trap density distribution (see Fig .1.1). We perform *in situ* absorption imaging with a high resolution microscope objective[1] to obtain images of atomic samples with a micron-sized resolution, retaining the resolving power of many-body correlations.

In the 2D configuration, a spatially resolved *in situ* density measurement offers tremendous advantages in studying both equilibrium and non-equilibrium dynamics of many-body systems. In equilibrium, assuming the local density approximation, a weakly trapped atomic sample can be divided into many locally homogeneous subsystems. We can assign a local chemical potential to each subsystem according to its trap potential energy and turn the remaining 2D trap inhomo-

---

1. Experiment groups in Harvard [32] and MPQ [33] explored single-site resolved 2D quantum gas microscopy based on fluorescence imaging inside a 2D lattice formed by optical molasses. This technique yields binary detection due to radiative loss.
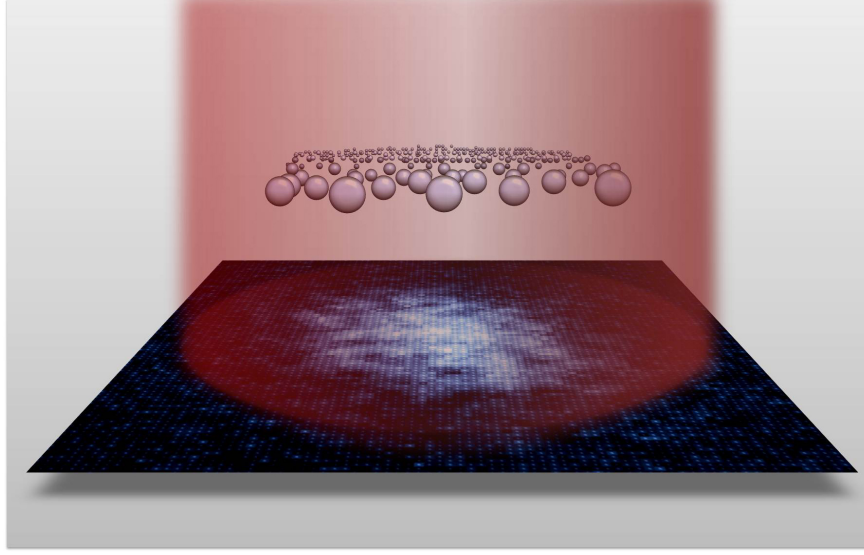
Figure 1.1: Illustration of *in situ* imaging of a 2D quantum gas. Due to the 2D geometry, the atomic distribution can be fully captured in a single *snapshot* image.

geneity into a great advantage: performing spatially resolved local density measurements reveal a wealth of information on the many-body phase diagram with many values of local chemical potentials. Moreover, a spatially resolved *in situ* probe also allows sensitive detection of near-equilibrium density fluctuations and their spatial or even non-equal time correlations,[2] which is crucial in revealing collective and statistical behaviors of a many-body system [34, 35, 36, 37]. We also gain the opportunity to monitor non-equilibrium dynamics by applying controlled local-perturbations to the sample to extract local transport properties of underlying many-body phases [38], which is a rarely explored territory in ultracold gases.

We use cesium-133 bosonic atoms to form highly tunable 2D quantum gases. Cesium has very rich collisional properties [39] and is ideal for studies that requires tunable atomic interactions. We use the lowest energy hyperfine spin state to produce a highly stable quantum fluid [40]. Its atomic interaction strength can be smoothly adjusted from strongly attractive to strongly repulsive, over three orders of magnitude, using a broad Feshbach resonance at low magnetic fields [39].

---

2. This would require an implementation of phase contrast imaging.

Moreover, there are narrow Feshbach channels convenient for efficient creation of molecules [41, 42, 43]. There exist universal three- [44] and four-body [45, 46] bound states near an Efimov resonance [44], forming a nice testbed for universal few-body physics.

1.4 Physical phenomena of interest

Our aim is to study many-body physics in strongly correlated systems which could not be resolved in the time-of-flight bulk measurements. Some of these systems can be found near critical regions of continuous quantum or classical phase transitions where competing orders lose their dominance over the many-body state and the system develops strong fluctuations and correlations. A quantum phase transition, driven by quantum fluctuations, happens at zero temperature, whereas a classical phase transition happens at a finite temperature and is driven by thermal fluctuations. We are particularly interested in finite temperature quantum and classical critical fluctuation regimes, where both static and dynamic behaviors of thermodynamic observables near their critical values can develop universal dependence on the thermal energy or the thermal de Broglie wavelength with proper scalings [47, 48, 49, 50]. The universal behavior, classical or quantum, is expected to be described by the Ginzburg-Landau type of effective field theories which capture physics of an emerging order parameter as well as its critical fluctuations and spatial correlations. While both classical and quantum criticality might be studied in a unified view, a quantum field model often carries intriguing time evolution dynamics in addition to the spatial correlations in its classical counterpart [51, 49, 52]. Studying these critical behaviors has been a challenging topic and is currently heavily investigated in various systems such as heavy fermion metals [53, 54] or high-Tc superconductors [55, 56].
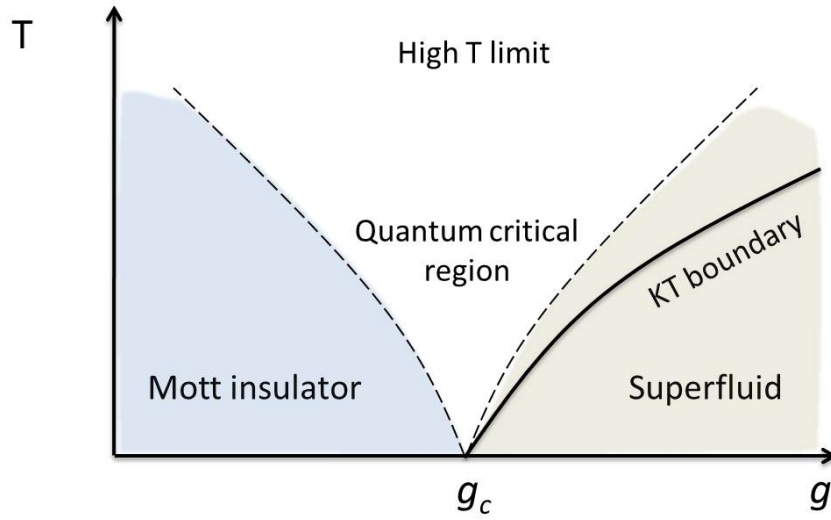
Figure 1.2: Illustration of the phase diagram of the superfluid-to-Mott insulator quantum phase transition in two dimensions, shown as a function of the temperature T and a tuning parameter g. The tuning parameter can either be chosen as chemical potential μ or the ratio between the tunneling energy t and the on-site interaction U. At zero temperature, the transition happens at $g = g_c$. At finite temperatures, the system shows quantum critical behavior in the V-shape region bounded by the two dashed lines. The BKT phase boundary is shown as a solid line, separating the superfluid phase and the normal gas (thermal disorder) phase. Classical criticality exists within a finite region near the BKT transition boundary.

1.4.1 The Berezinskii-Kosterlitz-Thouless superfluid transition and the Mott insulator-to-superfluid transition in a 2D quantum gas

A tunable 2D quantum gas should provide us great opportunities to realize both classical and quantum phase transitions as well as to investigate their critical behaviors. The classical phase transition in the proposed 2D system is the Berezinskii-Kosterlitz-Thouless superfluid transition (BKT-transition) [16, 17], where a superfluid with quasi-long range order emerges from thermal disorder. The quantum phase transition is the superfluid-to-Mott insulator transition predicted by the Bose-Hubbard model [9], where a superfluid (SF) with long range order competes with a Mott insulator (MI) of localized commensurate boson density. A SF-MI transition can be realized by loading a 2D quantum gas into a 2D square optical lattice. Inside the lattice, both the classical and the quantum criticality can coexist. The homogeneous phase diagram of SF-MI transition is illustrated in Fig. 1.2, where a BKT transition boundary also departs from a zero temperature SF-MI quantum critical point and extends to the high temperature region. Developing a thorough understanding on criticality of the BKT transition and the SF-MI transition in two dimensions is one of the major scientific goals of our experiment.

1.5 Overview of the thesis

The work of this thesis started with building a new cesium apparatus toward a partial realization of its scientific goal. We realized the SF-MI transition in a 2D quantum gas and observed the emergence of an incompressible MI domain. We then developed experimental tools to study dynamics of mass transport and statistical evolution across the SF-MI phase boundary. We further diverged our research focuses separately into studying classical as well as quantum criticality. I studied the BKT transition and its classical critical phenomena, where we confirmed the universal description of a classical Ginzburg-Landau field theory and observed growing correlations in the critical fluctuation region. I then developed analysis tools to study density-density correlations and the static

structure factors of 2D quantum gases. Investigation on quantum criticality near the SF-MI transition as well as quantum critical dynamics are ongoing projects and some of the discussions will appear as an outlook of this thesis. Below, we briefly summarize topics covered in each chapter.

- Chapter 2 will be a review of the cesium apparatus. Descriptions on laser cooling to high phase space density will be given.

- Chapter 3 describes the realization of a tilted-evaporation scheme, with which we achieve fast and runaway evaporative cooling to BEC. In this research, we overcome the speed limitation in conventional dipole trap cooling techniques, and reach BEC in as few as 2 seconds by using only a large volume crossed dipole trap.

- Chapter 4 describes the experimental scheme of making and probing 2D quantum gases, with an introduction on properties of 2D Bose gases. Our method of producing a monolayer of 2D gas, implementation of a 2D square optical lattice, as well as techniques of *in situ* absorption imaging of 2D gases will be introduced.

- The first in-situ observation of an incompressible Mott insulating domain will be presented in Chapter 5. We observed the SF-MI transition by identifying a "wedding cake" density structure in a 2D gas after turning on a deep optical lattice. We extract local properties such as compressibility and density fluctuations in both the SF and MI regimes. We also found qualitative validation on the fluctuation-dissipation theorem.

- Investigations on dynamics across the SF-MI transition is described in Chapter 6. Through ramping on the lattice potential fast enough to violate global adiabaticity, we studied mass transport and statistical evolution of an atomic gas crossing the SF-MI transition. We identified very long global equilibration time scales as compared to local tunneling and interaction time scales.

- Chapter 7 presents the observation of scale invariance and universality in 2D Bose gases, where we confirmed that the equation of states and the density fluctuations measured at different temperature, chemical potential, and interaction strength can be rescaled and mapped to four universal behaviors. Through these measurements, we also detect the growing density-density correlations in the fluctuation region and the superfluid region across the BKT phase boundary, which is deeply related to the fundamental fluctuation-dissipation theorem, forming the topic of the next chapter.

- In Chapter 8, we present an analysis on density-density correlations and static structure factors of 2D quantum gases. At long length scales, our measurements agree with the fluctuation-dissipation theorem; at shorter length scales, our measurements reveal the correlation lengths of interacting 2D quantum gases and possibly their collective excitation spectrum. The presented work and the analysis tool should make *in situ* imaging technique a desirable tool to study the finite temperature density response of interacting quantum gases.

- I will finally discuss in Chapter 9 the outlook of this experiment. With an apparatus capable of studying quantum gas with high spacial resolution, there are many possibilities opened up for future investigations, notably quantum critical scaling and quantum critical dynamics.

CHAPTER 2

EXPERIMENTAL SETUP

In this chapter, we describe details of the cesium apparatus. We will give a brief overview on properties of cesium atoms, followed by technical descriptions of the vacuum system, the diode laser system, the computer control, the imaging system, and the magnetic field control. Based on these apparatuses, we perform conventional laser cooling and trapping, as well as degenerate Raman sideband cooling, magnetic levitation, and dipole trapping of ultracold cesium gases, discussed in the second half of this chapter following the actual experimental order.

2.1 Cesium-133 atom

Cesium-133 is the only stable bosonic isotope of the cesium atomic species. It has a nuclear spin $I = 7/2$ and an unpaired electron at the outermost shell. The electronic ground state $6^2 S_{1/2}$ of the unpaired electron has two hyperfine levels $F = 3$ and $F = 4$ with an energy splitting corresponding to an exact frequency of 9.192631770 GHz (the clock transition). The first excited states in the $6P$-orbital are the fine structure doublets $6^2 P_{3/2}$ and $6^2 P_{1/2}$, separated by a frequency splitting of 16.6 THz. Hyperfine splittings in the excited states are smaller at 150~250 MHz between the $6^2 P_{3/2}$ hyperfine states (denoted by $F' = 2, 3, 4, 5$) and 1 GHz between the $6^2 P_{1/2}$ hyperfine states ($F' = 3, 4$). The optical transitions from the ground state to the $6P$ fine structure doublets, $6^2 S_{1/2} \rightarrow 6^2 P_{3/2}$ and $6^2 S_{1/2} \rightarrow 6^2 P_{1/2}$, are abbreviated as the D_2 and D_1 line transitions, respectively. The D_2 line has the strongest cycling transition, and is the leading option for optical cooling of cesium atoms. The D_1 line will only be discussed in optical trapping using far off resonant lasers. Figure 2.1 shows the detailed D_2 line hyperfine structure as well as the central frequencies of the diode lasers, which we built for laser cooling experiments.
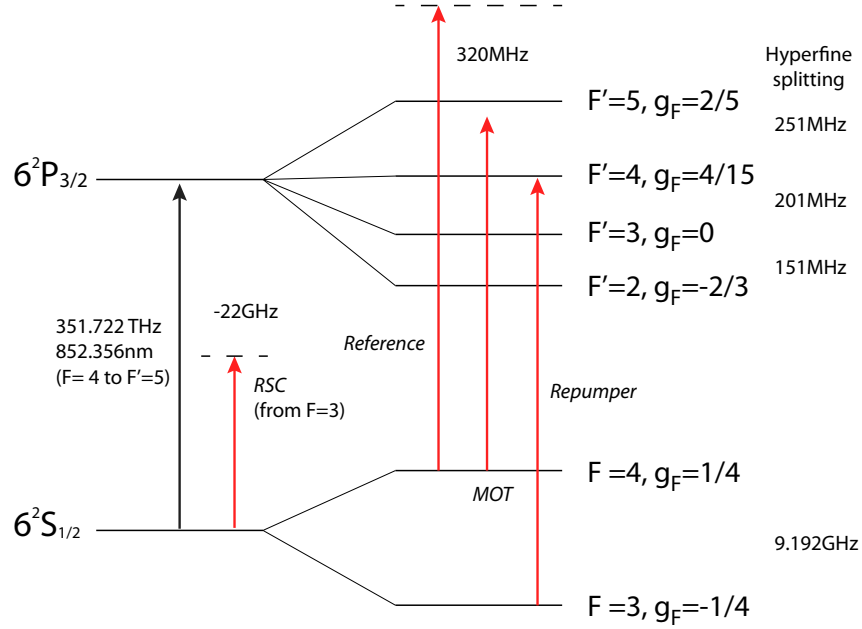
Figure 2.1: Cesium-133 ground state and D_2 line hyperfine structure. F and F' denote the total spin quantum number of the $6^2S_{1/2}$ and $6^2P_{3/2}$ states, respectively. g_F is the Landé g-factor. The black arrow marks the main optical transition for laser cooling and imaging; red arrows mark the central frequencies of the diode lasers (discussed in Section 2.3).

2.1.1 Cesium collisional properties

Throughout the thesis work, we produce cesium quantum gases using the absolute lowest energy ground state, $|F = 3, m_F = 3\rangle$ (abbreviated as $|3, 3\rangle$), of which the inelastic two-body processes are fully suppressed at low temperatures [57, 39]. Atomic two-body elastic collisions can be fully described by the s-wave scattering length a [5], which is known to vary smoothly at low magnetic fields [39] due to a wide Feshbach resonance located at $B \approx -12$ G [39, 6].

A Feshbach resonance occurs when the energy of two colliding free atoms is tuned very close to a molecular bound state. The scattering length of free atoms can therefore be modified through resonant coupling to the bound state [6]. A Feshbach resonance can be induced through adjusting the background magnetic field, since the molecular states typically have different magnetic moments from that of the free atoms and the energy difference can be adjusted by the magnetic

Zeeman shift.

Cesium has a very rich bound state structure near the scattering continuum, and its scattering length is highly adjustable even at very low magnetic fields [39]. The weakly bound molecular structure near the scattering continuum has been pinned down using high resolution Feshbach spectroscopy [57, 39], or directly measured using magnetic moment [42], microwave frequency [42], and radio frequency spectroscopy [58]. These measurements enabled precise calculations of cesium collisional properties [59, 60, 39, 58]. Figure 2.2 shows $|3,3\rangle + |3,3\rangle$ scattering length and bound state energies at low fields [39]. For $B = 0 \sim 150$ G, the smooth variation of scattering length a can be well fit using a formula [39, 44]

$$\frac{a}{a_0} = (1722 + 1.52\, B/G) \left(1 - \frac{28.72}{B/G + 11.74}\right) \qquad (2.1)$$

where $a_0 = 0.53$ Åis the Bohr radius. In particular, Eq. (2.1) characterizes well the scattering length near the zero crossing at 17.1 G [39, 61], and is used in our experiment to calculate a for $B = 0 \sim 50$ G. Note that Eq. (2.1) does not include features from other low field narrow Feshbach resonances, notably a g-wave resonance around 19.84 G and a d-wave resonance around 47.8 G. Near these narrow resonances, the scattering length can be described by a generalized form

$$\frac{a}{a_{bg}} = 1 - \frac{\Delta}{B - B_0}, \qquad (2.2)$$

where a_{bg} is the background scattering length at the location of resonance, Δ is the effective resonance width, and B_0 is the resonance position. For example, an analysis of experiment data [58] determined that the d-wave resonance at $B_0 = 47.78(1)$ G has an effective width of $\Delta = 0.16(1)$ G.
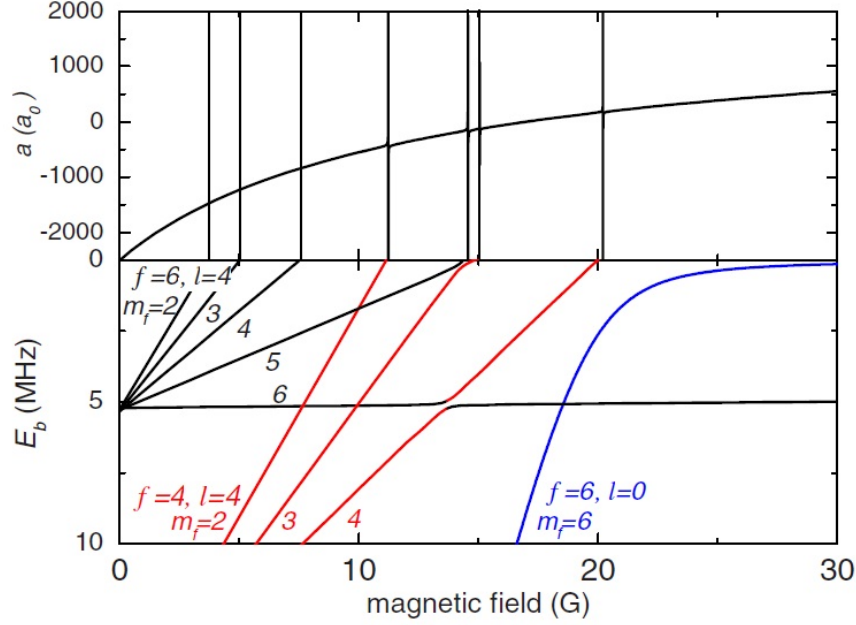
Figure 2.2: Scattering length and bound state energies for $|3,3\rangle + |3,3\rangle$ atoms as functions of the background magnetic field. Reprinted figure with permission from Ref. [6]. Copyright 2010 by the American Physical Society.

2.1.2 Inelastic collision loss

For experiments at high densities, inelastic collisions can create a loss of atoms and release energy into the sample. Since all two-body inelastic processes are forbidden in collisions between atoms polarized in the $|3,3\rangle$ state, the dominant collisional loss process is three-body recombination.

Ultracold three-body recombination loss is itself an interesting property of cesium atoms. When three-body recombination occurs, two out of the three colliding atoms form a molecule, releasing its binding energy, which causes the third atom and the molecule to be lost from the trap. The rate of three body recombination is characterized by the loss equation $\frac{\dot{n}}{n} = L_3 n^2$, where L_3 is the loss coefficient and n is the atomic density. In the low temperature limit, the recombination molecules are weakly bound near the continuum, and their binding energy follows the universal form $E_b = \hbar^2/ma^2$. Here, $\hbar$ is the Plank constant divide by 2π and m is the cesium atomic mass.
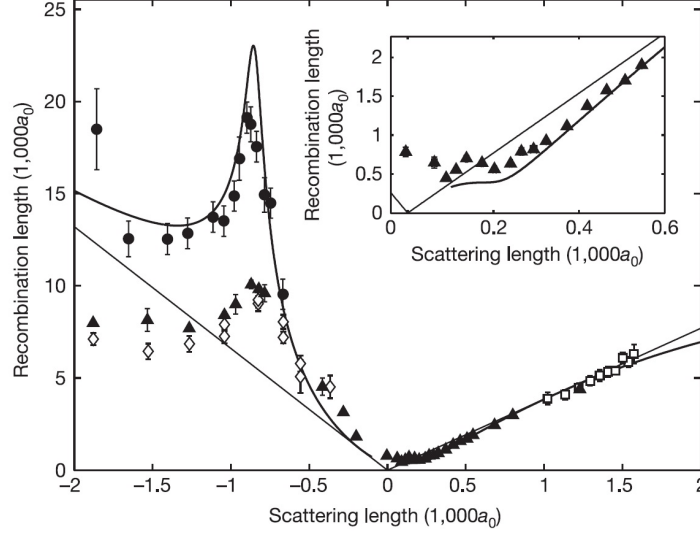
Figure 2.3: Three-body recombination length $\rho_3 = (\frac{2m}{\sqrt{3}\hbar}L_3)^{1/4} = 1.36C^{1/4}a_s$ of the $|3,3\rangle$ state. Reprinted by permission from Macmillan Publishers Ltd: *Nature* Ref. [44], copyright 2006.

It can be shown that the loss coefficient L_3 follows the universal a^4-scaling relation [62, 63, 64] with $L_3 = 3C\hbar a^4/m$, where $C(a)$ is a coefficient showing additional oscillatory dependence on a. The coefficient C has an upper bound C^+ for $a > 0$ and a lower bound C^- for $a < 0$. At negative a, C is larger than for positive a [64, 44]. For positive scattering lengths, $C^+ \approx 70$ is theoretically predicted [63, 64, 65] and experimentally measured [66, 44].

The oscillatory behavior of $C(a)$ originates from quantum interference with a set of universal three body bound states. These bound states were first predicted by Vitaly Efimov [67, 68] in the context of nuclear physics. The value of C is expected to oscillate at multiples of scattering lengths $a_- < 0$ and $a_+ > 0$. Here, a_- denotes the scattering length at which the first Efimov trimer resonantly couples to the free atomic state, while a_+ denotes the smallest positive scattering length at which Efimov trimers destructively interfere in the atom-dimer decay channels [63, 64, 65]. Universal Efimov bound states appear whenever $a/a_\pm = 22.7^l$, $\forall l \in \mathbb{N}$, and there will be a strong enhancement or suppression in the three-body recombination rate.

The universal a^4 scaling behavior in L_3, as well as the Efimov resonant maximum and interfer-

ence minimum in $C(a)$ have been observed in cesium ultracold gases polarized in the $|3,3\rangle$ state [66, 44]. The measured loss rates are plotted in Fig. 2.3, where we see that L_3 can be adjusted remarkably by over six orders of magnitude. The three-body loss minimum at $a = 210\ a_0$ renders a loss coefficient similar to other alkali species, and has been identified as an ideal place for evaporative cooling to Bose-Einstein condensation [40]. Moreover, in later chapters we shall see that fast three-body losses due to an Efimov resonance can be converted into experimental probes inside optical lattices. Note also that, in Fig. 2.3, the data are taken from thermal gas experiments. For condensate atoms, we expect the loss coefficient to be $\frac{1}{3!}$ times smaller than the values shown here.

2.2   Vacuum system

For BEC experiments, it is necessary to operate under an ultra high vacuum (UHV) environment. Nevertheless, we also need a bright atomic source, which inevitably requires a high background vapor pressure, to reach a sufficient number of trapped atoms within an experimentally accessible time. In order to maintain the pressure difference between the two regions, it is standard to design a UHV cell (the science chamber) connected to a differential pumping region, and then to the atomic source (the oven). In our setup, a Zeeman slower tube connects the oven and the science chamber, which not only serves as a differential pump but also provides a region for laser slowing of the axial velocity of the atomic flux, which increases the loading efficiency of the magneto-optical trap (MOT) in the science chamber. It then becomes fairly easy to maintain UHV pressure in the science chamber using an ion pump and a titanium sublamation pump. Our vacuum system is illustrated in Fig. 2.4.
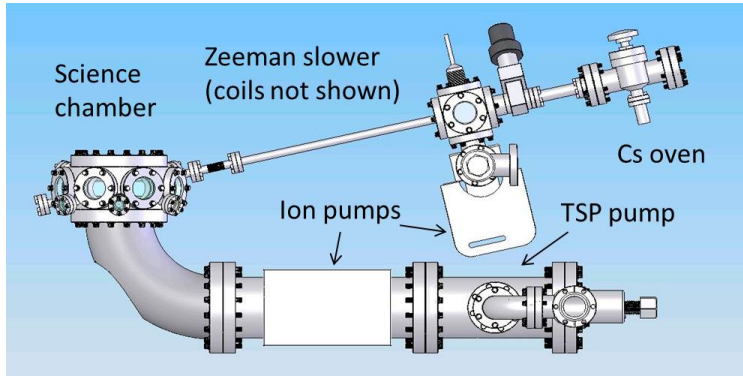
Figure 2.4: Schematic of the vacuum system.

2.2.1 Cesium oven

Our cesium oven design employs the combination of a hot vapor cell and a cold trap that offers high cesium atomic flux while maintaining a low partial vapor pressure. Our cesium vapor cell contains five grams of cesium metal stored in a glass tube (Pyrex). The cesium metal is heated to 60°C, producing a vapor pressure of 3×10^{-5} torr. The temperature throughout other parts of the vapor cell is kept slightly higher than that of the glass tube to prevent unnecessary transfer of cesium metal inside the cell. Hot cesium atoms are only allowed to leave the cell through two apertures (1 mm radius, heated to $> 80^\circ$C) attached to both ends of a 3" long nipple tube, resulting in a collimated atomic beam ejecting from the oven and traveling along the Zeeman slower tube toward the center region of the science chamber. The nipple tube is thermal-electrically cooled to 0°C, forming a cold trap which absorbs background cesium vapors and reduces the vapor pressure to below 10^{-7} torr. The oven is connected to an intermediate chamber (2.75 cubic inch) through a gate valve that can seal the vacuum for future maintenance in the cesium oven. A motor-driven wobble stick, fed through a flexible bellow, can be used to block the atomic beam during the experiment. The pressure inside the intermediate chamber is $< 10^{-9}$ torr, maintained by an ion pump (Gamma Vacuum: 40S-CV-2D-SC-N-N) at a pumping rate of 40 L/s.

17

2.2.2 Zeeman slower

Following the intermediate chamber is the Zeeman slower. The Zeeman slower is a long, thin tube surrounded by tapered magnetic coils, connecting the science chamber and the cesium oven. The Zeeman slower tube offers differential pumping to UHV in the science chamber; the tapered coils generate a spatially varying magnetic field for laser cooling, discussed in Section 2.7.1. The tube is 7 mm in diameter and is 40 cm long, supporting a low vacuum conductance of 0.06 L/s. The gas throughput, from the cesium oven to the science chamber, is less than 6×10^{-11} torr-L/s. The slower tube connects to the science chamber through a 1-1/3" conflat flange (CF) bellow.

2.2.3 Science chamber

The schematic of the science chamber is shown in Fig. 2.5. The main chamber is a stainless steel spherical octagon (Kimball Physics MCF600-SO200800). Eight 2.75" CF side ports are mounted with six broadband coated viewports (MDC: fused silica, 1.5" clear aperture) and two ZnSe viewports mounted at opposite sides of the chamber for dipole trapping using a CO_2 laser. The top and bottom ports are mounted with recessed viewports (Special Techniques Group: 4 mm thick Spectrosil 2000 fused quartz) with a 30 mm clear aperture; both inner surfaces of the top and bottom viewports are 0.5" from the center of the chamber. Eight additional 1-1/3" CF ports are custom milled between the 2.75" CF ports for additional optical access, with $\pm 13°$ tilt angles. Seven ports are mounted with 0.75" clear aperture viewports (MDC: fused silica) and one is counted to the Zeeman slower tube through a flexible bellow.

All 17 viewports are reserved for optical access. The connection to an additional UHV pump region is through an elbow-tube-viewport assembly; see Fig. 2.5. The bottom viewport is welded onto a vacuum tube, which is inserted into a 90 degree elbow and is shaped and welded onto a hole at the outer radius of the elbow (see Fig. 2.5 for detail). One end of the elbow is mounted to the bottom port of the science chamber and the other end is mounted to a 100 L/s ion pump (Gamma

18

1-1/3" CF
fused silica
viewports (x7)

Connected to
bellow+ Zeeman
slower

ZnSe viewports (x2)
(the other side not
shown)

2-3/4" CF
fused silica
viewports (x6)

Optical access

Top and bottom
viewports

Vacuum conducting
cylindrical region
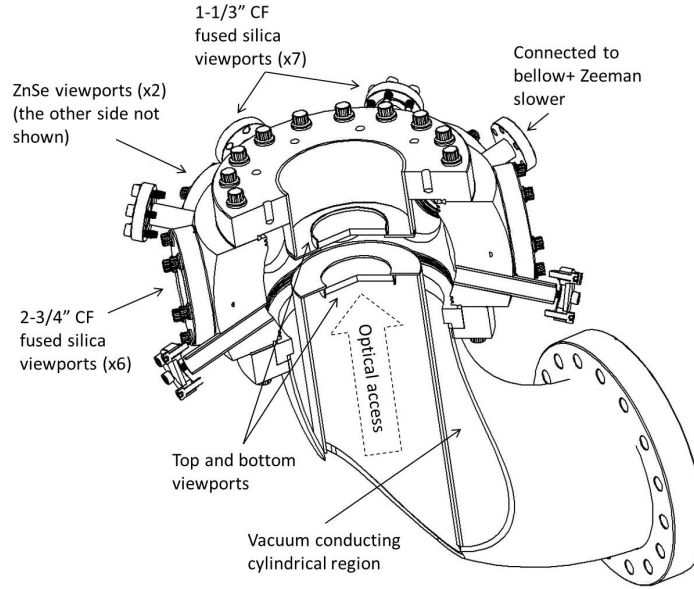
Figure 2.5: Cross section of the science chamber and the vacuum conducting elbow.

Vacuum: 100L-DI-6D-SC-US110-N). This assembly still permits a large cylindrical region conducting vacuum between the chamber and the ion pump. The bottom viewport is accessible from inside the tube, whose open end is conveniently located at 4.5" above the optical table. An additional advantage of this design is that the elbow, together with two other supporting pillars, lifts the chamber above the UHV pump region, permitting a full $360°$ optical access around the chamber.

2.2.4   UHV pump region

A titanium sublimation pump (TSP) is attached to the end of the 100 L/s ion pump, offering further UHV pumping capability. A large 6" CF tube is mounted to the ion pump, providing large pumping surface area. Three titanium filaments (Gamma Vacuum) are inserted for sublimation coating of the tube. A separate ionization gauge (Varian Vacuum Technology: UHV-24P Extended Range, dual thoria-iridium filaments) is used to measure the pressure.

19

2.2.5 Preparation of vacuum system

All stainless steel components of the science chamber are ultrasonically cleaned, assembled, and then baked at a high temperature (350°C) for two weeks to remove deeply trapped molecules under the surface of the stainless steel (with gases pumped out using a turbo pump). Before high temperature baking, the CF ports are sealed with blank flanges and the permanent magnets in the ion pumps are removed. After the baking, we remove the blank flanges and put on the fused silica viewports. The Zeeman slower assembly (which was pre-baked at a lower temperature $180\ ^\circ$C), the science chamber, and all optical viewports are separately prepared and are put together after the high temperature baking. The whole system is leak-checked using a helium leak detector (Adixen ASM 142) to ensure all components are sealed for UHV. We then bake the entire system under 180°C for another two weeks. During the baking, the roughing port is shut off and the ion pumps are activated. The filaments of the TSP are then activated several times during the baking to help pump the vacuum. After the system is cooled down, the pressure of the ionization gauge reads $< 3 \times 10^{-12}$ torr. Considering the finite vacuum conductance of the elbow, we expect the background pressure in the science chamber is $\sim 10^{-11}$ torr. The UHV has lasted for five years without significant degradation.

2.3 Diode laser system

In this section, we describe the diode laser systems for driving cooling and imaging transitions. The relevant experiment stages are Zeeman slowing, MOT/molasses cooling, degenerate Raman sideband cooling (dRSC), and absorption imaging. In each stage, we need one main beam driving the cooling or imaging transition, and one repump beam to empty the atomic population accumulating in the unwanted hyperfine ground state. During the stage of dRSC, an additional laser beam is needed to form a near-detuned optical lattice. In Table 2.1, we summarize all atomic transitions driven in each individual stage.

Table 2.1: D_2 line cooling and imaging transitions

Experiment stage	Main	Repump	Detuning
Zeeman slowing	$F = 4 \rightarrow F' = 5$	$F = 3 \rightarrow F' = 4$	-100 MHz
MOT and molasses	$F = 4 \rightarrow F' = 5$	$F = 3 \rightarrow F' = 4$	-15∼-80 MHz
dRSC	$F = 3 \rightarrow F' = 2$	$F = 4 \rightarrow F' = 4$	<1 MHz
dRSC (optical lattice)	$F = 3 \rightarrow F' = 4$		-22 GHz
Imaging	$F = 4 \rightarrow F' = 5$	$F = 3 \rightarrow F' = 4$	0

Five diode lasers are built to drive the optical transitions listed in Table 2.1. Four external cavity-feedback diode lasers (ECDLs) deliver laser beams at stable frequencies with narrow linewidths. One free running diode laser offers high power at 150 mW, and is injection-locked by one ECDL laser to narrower linewidth.

The ECDLs are set up according to the Littrow configuration. The part number of the laser diodes is JDS Uniphase SDL-5411-G1. The diode temperature and injection current are feedback-locked to provide a stable lasing frequency. The temperature is fixed at around $18°$C, two degrees below the room temperature. At the output of each ECDL, beam ellipticity and astigmatism is corrected by an anamorphic prism pair (Thorlabs) to an $1/e^2$ beam diameter of ∼1 mm. A dual stage optical isolator (Isowave: I-80-U4) is placed closely after the prism pairs to block possibly retro-reflected beams back to the diode. The nominal output power of the ECDLs are set to 20∼40 mW and the free running wavelengths are tuned to desired values near 852.335 nm (*Repumper*), 852.356 nm (*MOT* and *Reference*), and 852.390 nm (*dRSC master*). *Reference*, *MOT* and *Repumper* frequencies are feedback-stabilized to within MHz linewidth using different schemes.

The free running diode laser (*dRSC slave*) is built using a JDS Uniphase SDL-5420-G1 diode, capable of generating 150 mW maximum output power. Except for the grating feedback, the setup follows those implemented in an ECDL. A tunable dual stage optical isolator (Isowave: I-80-T4-H) with escape ports is used, with which we couple a few microwatt of the *dRSC master* beam into the *dRSC slave* diode and create a forced oscillation inside the laser cavity (injection-lock). The injection-locked *dRSC slave* is used to form the optical lattice in the dRSC stage.

The frequency of *Reference* is stabilized at $+320$ MHz detuned from the $F = 4 \rightarrow F' = 5$ (abbreviated as $4 \rightarrow 5'$) transition using a room-temperature vapor cell and polarization spectroscopy [69]. This is done by first splitting a weak beam from the *Reference*, and then shifting its frequency by -320 MHz using second-order double pass through an 80 MHz acousto-optic modulator (AOM) before directing the beam for spectroscopy. The spectrum of the polarization spectroscopy is asymmetric and the amplitude strongest at the $4 \rightarrow 5'$ transition. It is used as an error signal for the injection current and the piezo voltage feedback control. Setup of the polarization spectroscopy follows that implemented in Ref. [70]. The $+320$ MHz frequency shift in *Reference* is manifested in the locking scheme of *MOT*, discussed later.

MOT and *Repumper* are frequency stabilized to drive D_2 line transitions from the $F = 4$ and $F = 3$ hyperfine ground states, respectively. We stabilize and control the *MOT* frequency by interfering the *MOT* and *Reference* beams on a fast photodiode (Hamamatsu G4176-03), and locking their beat note frequency f_b. We obtain the feedback error signal by feeding a beat note $f_b \div 1020 \div 4$ (frequency divider: RF BAY, FPS-1020-4; ripple counter: 74HC393) to a phase locked loop (PLL) chip (LM565), and measure the VCO voltage of the PLL chip. The VCO free-running frequency in the PLL chip is tuned to 140 kHz with a hold-in range of $\pm 60\%$. This corresponds to a tunable range of $f_b \approx -230 \sim -920$ MHz (with the frequency of *MOT* smaller than the frequency of *Reference*), which is sufficient to cover all transition frequencies to the D_2-line hyperfine manifold. The *Repumper* frequency is similarly locked and controlled, except that the beat note is at microwave frequencies 8.4 ± 0.6 GHz and is first subtracted by 9.1 GHz, using a mixer and a local oscillator (Jersey Microwave: PLDRO-9100-1210) referenced to a 10 MHz rubidium frequency standard (SRS: FS725), before sending it through the frequency divider and PLL lock circuit.

We split the *MOT* and *Repumper* beams into multiple paths for use in different cooling and imaging stages, as shown schematically in Fig. 2.6. Each beam is frequency shifted and intensity modulated by an AOM, and is directed to the science chamber via a single mode, polarization-

22
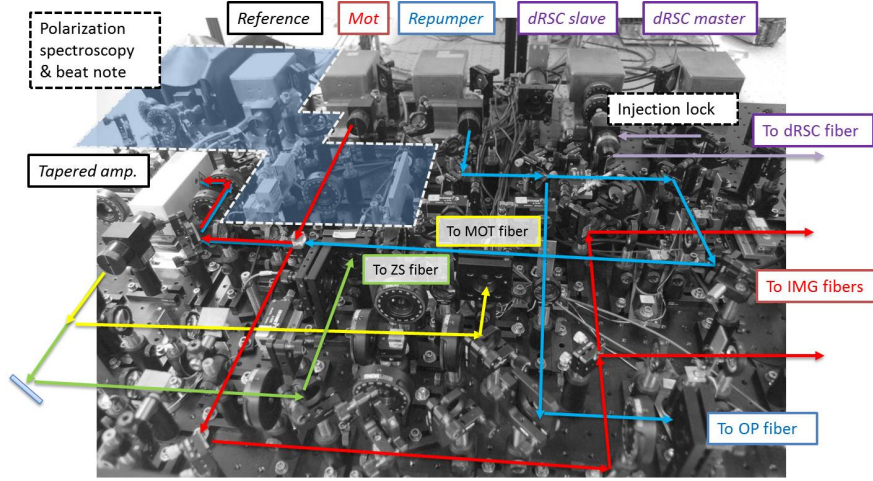
Figure 2.6: Actual layout of the diode laser system. All beams are coupled to optical fibers for the following purposes: Magneto-optical trap (MOT), Zeeman slowing (ZS), dRSC optical pumping (OP), dRSC optical lattice (dRSC), imaging (IMG).

maintaining optical fiber. To reach a high extinction ratio, a mechanical shutter is used to completely block the beam. The typical power attenuation through these components is $1 \sim 2$ dB. To gain sufficient power to drive $4 \rightarrow 5'$ transitions with the MOT cooling and Zeeman slowing beams, we use a tapered amplifier (Sacher Laser: TEC400), seeded by a 20 mW *MOT* beam, to increase the laser power to 300 mW (Max:500 mW). We also mix the seed beam with a 1 mW *Repumper* beam such that the amplified output contains a weak $3 \rightarrow 4'$ repump frequency component. The tapered amplifier is protected by an optical isolator, after which the amplified output is further separated into two parts: one beam is frequency shifted by $+80$ MHz, serving as the MOT cooling beam; the other is used as the Zeeman slowing beam. Quite unexpectedly, the tapered amplifier output has a TEM$_{01}$-like double-peak structure, which is bad for fiber coupling. This forces us to reshape the beams using prism pairs and to redistribute the power within the double-peak structure, through adjusting the seed beam angle, to maximize their coupling efficiency into the optical fibers. The coupling efficiency is no better than 45%.

2.4   Computer control

Computer control offers precise manipulation of experimental parameters such as laser frequencies, laser intensities, and magnetic field strengths in a synchronized order. A schematic diagram of the computer control is illustrated in Fig. 2.7. A computer (*Dimer*) is equipped with four National Instrument PCI-boards, listed below, to generate analog output and digital (TTL) voltages.

- One 32-channel, 20 MHz digital I/O board (PCI-6534). Outputs 5V TTL signals.

- Two 8-channel (1 MS/s per channel), 12-Bit analog I/O boards (PCI-6713). Resolution is $20\,\text{V}/2^{12} = 4.883$ mV. Both are triggered by channel 1 of the DIO board.

- One 32-channel (45 kS/s per channel), 13-Bit analog output board (PCI-6723). Resolution is $20\,V/2^{13} = 2.441$ mV. Triggered by channel 2 of the DIO board.

Dimer runs a program (written in LabVIEW) which takes a list of experimental control sequences, converts them into digitized update tables, and uploads the tables into the on-board FIFO memories of the output boards as well as various other instruments. The digital board clocks the experiment, generating TTL signals in pre-programed waveforms. Two channels are reserved to trigger three analog boards; the rest of the channels are used to trigger other instruments. Upon receiving a trigger signal from the digital board, an analog board updates voltages in every channel according to the update table stored in the on-board FIFO memory. Due to the slow PCI data transfer rate, we limit the size of update tables to the size of on-board FIFO memories to prevent interruption during an experiment cycle. Currently, we do not suffer from this limitation since our experiment does not involve many ramps that require an excessive number of updates. New models using PCI express or PXI bus have sufficient data transfer rates, and remove such a limitation. Field-programmable gate array (FPGA) boards have now also become a popular choice for fast, realtime programmable outputs.

Figure 2.7: Schematic diagram of computer control, data processing, and data storage.

Another computer (*Quatromer*) is used to collect all experimental out data, such as CCD images, and perform simple on-the-fly analyses using a lab-developed analysis program. At the end of an experiment cycle, *Dimer* sends the table of experiment sequences through Ethernet to *Quatromer* and the analysis program saves the image, experiment sequences, and pre-analyzed data into the database in binary format.

2.5   Imaging system

The major detection method in our experiment is absorption imaging. Details on absorption imaging will be covered in Chapter 4 and we only discuss here the experimental technical setups.

We use two imaging systems to probe the atomic density distribution: one vertical setup is for high resolution *in situ* imaging through the top viewport; one horizontal setup, imaging through a side viewport, is for regular time-of-flight absorption imaging.

2.5.1   Horizontal imaging

In the horizontal imaging path, two lenses (GRADIUM plano-convex, focal lengths: 125 mm for front lens and 150 mm for back lens) forming telescope pairs are used to image the atoms

onto a CCD camera (Andor DU-434-BV). The camera and the lenses are mounted separately on the optical table. The position of camera is adjusted using a translational stage. The image magnification is 1.2, calibrated using atomic free fall under gravity. Image resolution is limited by the CCD pixel size to $13\ \mu\text{m}/1.2 = 10.8\ \mu\text{m}$.

The horizontal imaging beam shares an optical path with the MOT beam in the y-direction as well as the y-dipole trapping beam. See Fig. 2.15 for a schematic of the optics and discussion in Section 2.7.2 for more details.

2.5.2 *Vertical imaging optics*

In the vertical imaging path, we gain a much larger numerical aperture since the top viewport is only 0.5" away from the center of the chamber. We use a commercial long working distance (34 mm), M Plan APO microscope objective (Tech-specialties, OKHNL10) with a coating for near-infrared (NIR) wavelengths. Transmission is 91% for 852 nm wavelength. The numerical aperture is N.A. $= 0.28$ and the resolution is 1.8 μm for 852 nm. Image magnification is $10\times$ when combining the objective with a 200 mm standard tube lens optics. We use the InfiniTube standard with an additional $2\times$ amplifier to form the back tube lens system. Both optics are coated for NIR (99 % total transmission). The total image magnification is $20\times$.

Image resolution and magnification were bench-tested using a 1951 USAF test target as well as using absorption images of thermal atoms. Results from the latter method differ from the test target result for reasons discussed in Chapter 8, where we extract the image point spread function and modulation transfer function from 2D thermal gases. In Chapter 4, we discuss the determination of the image magnification using the recoil velocity of atoms diffracted off from a lattice potential.

The vertical imaging beam (σ^+ polarization) shares an optical path with the vertical MOT σ^- beam; see Fig. 2.14. We insert two thin polarization optics, a wire grid polarizer (Meadowlark, VersaLight) and a $\lambda/4$-waveplate (CVI zero-order quartz) between the objective and the top view-

port. The principal axis of the optics are aligned such that the MOT beam can be reflected while the imaging beam is transmitted. The transmission is around 70 % for 0° angle of incidence (AOI) and drops to about 50 % at 15° AOI, which slightly influences the modulation transfer function of the imaging optics (see Chapter 8). Replacing the quartz waveplate with a polymer waveplate can maintain constant transmission up to an AOI as large as 30°. For orientation of the polarization optics, see Fig. 2.14.

The objective and the back tube lens are mounted onto the CCD camera (Andor DU-434-BRDD), which is supported by a 3D translational stage for focusing as well as aligning atoms to the center of field-of-view. The whole assembly is then mounted directly onto the science chamber for mechanical stability.

2.5.3   CCD cameras

We use back-illuminated CCD cameras for improved high quantum efficiency. An Andor CCD camera DU-434-BRDD has 90 % quantum efficiency at 850 nm and is used on the vertical imaging path. An Andor camera DU-434-BV with 70 % quantum efficiency is installed on the horizontal path. The CCD chips in both cameras have the same physical size (1024×1024 pixels, 13 μm^2 per pixel), clock rate, and readout noise. Yet, the BRDD model is *deep depletion* processed to enhance sensitivity on NIR photons. However, it suffers more from dark current noise and needs to operate at temperatures much below 0°C.

In both cameras, we utilize the factory *fast kinetics* mode to record two images, with and without the atomic absorption, separated only by a short time ($\sim$ 20 ms). The typical readout time of a CCD chip is about a second, limited by the speed of the A/D converter (set to 1 MHz). *Fast kinetics* mode allows the use of a smaller number of rows on the CCD chip to take multiple images separated only by a few milliseconds of vertical shift time, and followed by a final single readout. This is useful for imaging fast processes or improving fringe cancellations. In our experiment, we

apply a metallic mask to block image light from two-thirds of the CCD chip and configure the camera to run the *fast kinetics* mode for taking two images with 341×1024 pixels each. To take the first image, we trigger the camera to start recording photo-electrons (meaning stop the cleaning cycle) for 100 μs and simultaneously pulse on the imaging beam (pulse width $15 \sim 40$ μs). After 100 μs, the camera shifts the photo-electron charge distribution by 341 rows down to the masked region and then waits for the second trigger. The shift time is about 4.4 ms, which equals the number of rows times the vertical shift speed of 13 μs/row. After a certain wait time (typically around $20 \sim 30$ ms to ensure all atoms are gone), we repeat the trigger and imaging pulse to take the second image. After this, both images are shifted down to fill the entire mask-protected area, followed by the final slow readout.

In general, one can apply a mask to cover $n/(n+1)$ part of the CCD chip and operate the *fast kinetics* mode to record n consecutive images. This can be useful for future non-destructive measurements using phase contrast imaging.

Interline CCD cameras can also operate similarly to *fast kinetics* mode with two images of full CCD size. In our earlier experiment, we used a PixelFly QE interline CCD camera from PCO imaging, configured to run the factory *double shutter* mode. The advantage of an interline CCD is that every row of pixels has a nearby row of *storage* pixels under a built-in mask. With only a microsecond of shift time, the CCD can be ready for a second exposure. Another advantage of an interline CCD is the short cleaning cycle ~1 ms compared to 22 ms of the back-illuminated chips in Andor cameras. Despite these advantages, the quantum efficiency is only ~ 15 % at 850 nm, which is unfavorable for *in situ* imaging with large image magnification; see Chapter 4.

2.6   Magnetic field control

In an ultracold cesium experiment, controlling the magnetic field is primarily required for manipulating atomic collision properties. The field needs to be stable to within a few milligauss to access

certain narrow Feshbach resonances and has to switch fast enough to offer a sufficient time window for monitoring fast collision processes. Since magnetic field trapping is not required in a cesium experiment and several magnetic Feshbach resonances are accessible within a magnetic field of $0 \sim 50$ G, we adopted a fairly simple design of magnetic coils and built a stable and agile current servo.

2.6.1   Magnetic coils

We use a pair of air-cooled magnetic coils, running currents in a superposition of Helmholtz and anti-Helmholtz configurations, to generate a magnetic field offset as well as a field gradient along the vertical (z-)direction. The coils have 35 windings each, wound using 2 mm square magnet wire and filled with strong holding epoxy (Stycast 2850FT, catalyst 23LV) in each layer. The inner and outer radii are 23.7 mm and 35.8 mm, respectively (cross section: 12.1×12.2 mm^2). The coil inductance is $L_c =$ 27 μH. The coils are individually attached to a polycarbonate mount. One is mounted onto the top port of the science chamber; the other one is supported by stable cage rods beneath the bottom port. The coils are located 17 mm (measured from the bottom of the coils) above and below the center of the science chamber without direct point contact with its parts. Together the coils produce a field gradient of

$$B' = 1.6 \Delta I \text{ G/cm} \cdot \text{A}, \tag{2.3}$$

for $\Delta I = I_1 - I_2$ being the difference of currents running in top (I_1) and bottom (I_2) coils, and a field offset of

$$B_o = 6.7 \bar{I} \text{ G/A}, \tag{2.4}$$

for $\bar{I} = (I_1 + I_2)/2$ being the average current in the two coils. During most of the experiments, the average coil temperature is around 30 °C. When continuously running currents at 13.5 A and

29

generating an offset field $B_o = 100$ G, the coils temperature rises to 55 °C. Air-cooling is considered sufficient since most of our experiments run at much lower currents and at a much lower duty cycle.

In addition to the top and bottom quadrupole coils, three pairs of bias coils run static currents to null the background magnetic field at the center of the chamber, as well as providing fine bias field controls in the $x-$, $y-$, and $z-$directions during experiments; the x, y, z coils have 50, 70, and 50 turns, respectively, and are configured to run currents in the same orientation, offering 2.1, 1.8, and 5.9 G/A in each pairs. These coils are driven by Howland current sources formed by power op-amps (Apex PA12) and are feedback stabilized. The current switching time is about 1 ms.

2.6.2 *Magnetic field stabilization*

We built a bipolar current servo providing currents flowing in both orientations for the top and bottom quadrupole coils. Each coil-servo loop consists of two power MOSFET (IXYS, IXFN80N50P) current mirrors connected with the magnetic coil as shown in Fig. 2.8. The current flowing through the MOSFETs is provided by an Agilent 6657A running at supply voltage $V_s = \pm 8$ V. Each power MOSFET runs a 10 A bias current and drives the magnetic coil symmetrically above and below the bias point. Under this configuration, the current slew rate could be limited by the supply voltage to $dI/dt = V_s/L_c = 0.3$ A/μs in both upward and downward slews. To mitigate this limitation, two transformers are installed into the current loop to effectively cancel the coil inductance during the current slew. This way, the slew rate is boosted by the breakdown voltage $V_{ds}^{br} \gg V_s$ of either side of the two MOSFETs and $dI/dt = V_{ds}^{br}/L_c \approx 4$ A/μs. The mirror FETs (IXTP) are chosen to match the threshold voltage of the power MOSFETs with a large channel-width ratio, offering high current gain and good linearity. To achieve good current stability, feedback is provided by a current sensor through measuring the potential drop (instrumentation amplifier INA103) across a 10 mΩ shunt resistor (Canadian Shunt), connected in series with the magnetic coil. The closed-
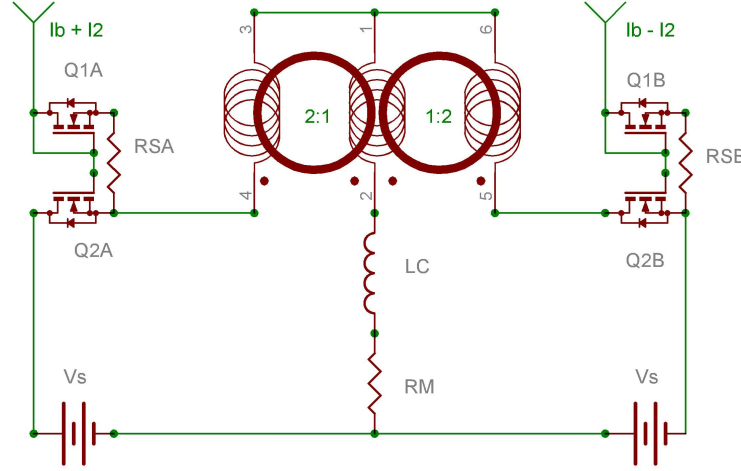
Figure 2.8: Schematic diagram of the current servo loop (for one coil). Q1A(B): mirror FETs, Q2A(B): power MOSFETs, LC: magnetic coil, RM: shunt resistor. Transformers are connected in series to the coil, as illustrated.

loop bandwidth is 30 kHz. An independent current sensor monitors the long term current stability to be < 20ppm. The Fast current feedforward is achieved by running the mirror with a cascode FET (IRF9610). The cascode is powered by a Howland current source formed by power op-amps (Apex PA12), supplying as large as 3 A of feedforward currents.

We stabilize the currents in the quadrupole coils, I_1 and I_2, and therefore the field offset B_o and gradient B' according to values of $\bar{I} = (I_1 + I_2)/2$ and $\Delta I = I_1 - I_2$ set by the voltages of computer analog output (AO) channels. Either $\bar{I}$ or ΔI is determined by the sum of two AO channel voltages V_{coarse} and V_{fine}, with the latter electronically rescaled by a factor of 0.01. The conversion from the control to the actual field B_o and gradient B' is initially calculated through the electronic gain in the circuit board and the coil geometry. The control voltage resolution for V_{fine} is 2.4 mV, corresponding to a fine increments of 1.6 mG in the offset field and 0.8 mG/cm in the field gradient. To achieve higher precision, we calibrated the value of the computer controlled offset magnetic field using microwave spectroscopy and found a precise conversion formula to within 0.7 mG; see later discussion in magnetic field calibration.

31

A variation of background magnetic field is present in the lab due to nearby elevators, which adds a 7 mG uncertainty to the magnetic field offset in the vertical direction. To detect the background field variation in the vertical direction, a magnetic flux sensor is placed at an angle of $\sim 35°$ relative to the coil axis, which is tested to be blind to the vertical component of the dipole pattern generated by the coils. A feedback controlled current flowing through a 5'×5' wire loop is used to remove the field variation caused by the elevators.

2.6.3 Magnetic field calibration

The magnetic field can be very well calibrated using microwave spectroscopy on the $|3, 3\rangle$ to $|4, 4\rangle$ transition, which has the largest difference in the magnetic Zeeman splitting and, therefore, is most sensitive to the offset magnetic field. The energy of a ground state $|F = \frac{7}{2} \pm \frac{1}{2}, m_F\rangle$ is calculated using the Breit-Rabi formula [71]

$$E_{F,m_F} = \frac{\Delta E_{hfs}}{2} + g_I \mu_B m_F B \pm \frac{\Delta E_{hfs}}{2} \left(1 + \frac{m_F \alpha}{2} B + \alpha^2 B^2\right)^{1/2}, \qquad (2.5)$$

where $\Delta E_{hfs} = h \times 9192.63177$ MHz is the ground state hyperfine splitting, $g_I = -0.000398854$ is the nuclear g-factor, $\mu_B = h \times 1.39962481$ MHz/G is the Bohr magneton, $\alpha = \frac{(g_J - g_I)\mu_B}{\Delta E_{hfs}}$, and $g_J = 2.00254032$ is the ground state fine structure Landé g-factor. To the leading order expansion, the above formula gives a linear Zeeman shift $\Delta E_z = g_F m_F \mu_B B$, where $g_F = g_I \pm (g_J - g_I)/8 \approx \pm\frac{1}{4}$ is the hyperfine Landé g-factor for $F = 4$ and $F = 3$ ground states.

A. Microwave spectroscopy

To calibrate the magnetic field, we perform microwave spectroscopy on polarized $|3, 3\rangle$ atoms held inside the dipole trap with an offset field B_o and zero gradient B' (set by computer control). We apply microwaves for > 50 μs and then perform absorption imaging to detect population in the

$|4, 4\rangle$ state. Once we determine the resonant frequency, it can be used to infer the actual offset field B_o using Eq. (2.5).

The microwave is created using a 9.1 GHz carrier band mixed with an adjustable radio frequency signal. The carrier is created by a PLDRO (Jersey Microwave) referenced to a 10 MHz rubidium frequency standard. The radio frequency component is generated by a function generator (Agilent 33250A), whose output is frequency-doubled and low-pass filtered. The mixed microwave is amplified using a solid state amplifier (MITEQ: AMF-6B-06001800-70-40P-PS) and is emitted through a microwave horn placed near a viewport of the science chamber. The microwave amplitude is adjusted through a PIN diode switch which controls the amplitude of the radio frequency signal to the mixer.

The conversion from the computer control voltage V_{coarse} and V_{fine} to the actual field B_o is determined to within 0.7 mG in the range of $0 \leq B_o \leq 80$ G,

$$B_o(V_{\text{coarse}}, V_{\text{fine}}) = B_{bg} - 67.046 \text{G/Volt} \times (1.0001 V_{\text{coarse}} + 0.00977 V_{\text{fine}}), \qquad (2.6)$$

where B_{bg} is an offset (~ 170 mG) weakly depending on B' and background field (variation ~ 5 mG). The value of B_{bg} is calibrated on a daily basis.

B. Feshbach spectroscopy

An alternative field calibration method is through performing high resolution Feshbach spectroscopy. One convenient loss channel is located at $B_o = 19.840(4)$ G with a narrow width of 40 mG [72]. We repeated the measurement and found good agreement on the location of this resonance compared to our microwave calibration. The Feshbach resonance location is frequently used to recheck our field calibration to within 4 mG. Figure 2.9 shows a sample scan. The atomic sample is first prepared inside a tight 2D optical trap and a background magnetic field of 17.7 G. The field is then switched to a designated value near 19.8 G to induce three-body recombination
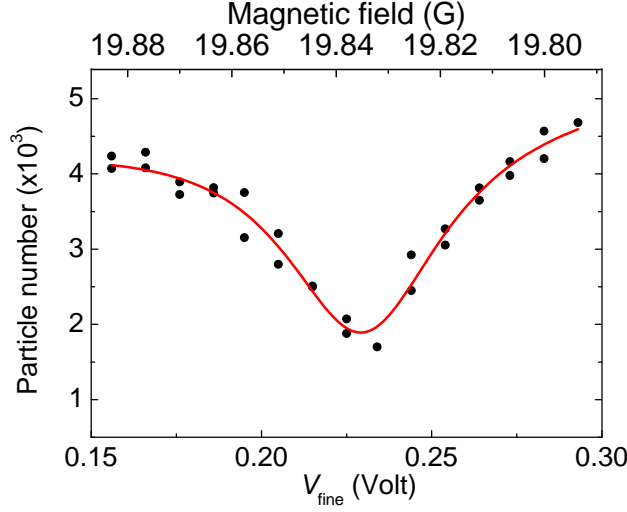
Figure 2.9: Feshbach spectroscopy of a g-wave resonance around 19.84 G.

loss. After 1.4 ms of hold time, the field is switched back to 17.7 G and the remaining atomic population is detected using resonant absorption imaging. The Feshbach resonance location is determined by fitting the center of the valley in the loss spectrum. The loss feature in Fig. 2.9 is slightly asymmetric because the field is scanned from below the resonance location.

2.6.4   *Fast magnetic field switching by pre-emphasis control*

Despite a fast current slew in the coil-current servo loop, the actual magnetic field switching time can be limited by the decay time scale of the eddy currents. This can put strong limitations on experiments intended to measure fast collision dynamics. To mitigate this problem, we electronically limit the slew rate of the offset magnetic field control to 0.3 G/μs, [1] generating a fixed ramp rate for offset field switching, and use a *pre-emphasis* circuit to calculate the necessary current overshoots to compensate the field contribution from eddy currents.

Accompanying every magnetic field switch, eddy currents are induced in the metallic parts of

---

1. Only the slew rate of the offset field control is electronically limited.

or near the science chamber. They generate a magnetic field that slowly decays in millisecond time scales. The pre-emphasis creates a controlled overshoot on top of a current slew to compensate the field contributions from the eddy currents, bringing the magnetic field switch profile closer to the ideal one. To correct the magnetic field pulse profile to leading order, the overshoot consists of several signals I_p, each of which is a high-pass filtered version of the ideal switch profile I_s. The time constant τ of each high-pass filter matches the decay time constant of a certain eddy current. I_p satisfies $\dot{I}_p + \frac{I_p}{\tau} = G\dot{I}_s$, where G is the gain in the high-pass circuit. On the other hand, an eddy current I_ϵ induced by the field switch is determined by $\dot{I}_\epsilon + \frac{R}{L}I_\epsilon = -\frac{M}{L}\dot{I}_s$, where R is the resistance of the object generating the eddy current, L is its self-inductance, and M is the mutual inductance. Compensating the field requires $\tau = L/R$ and $G = M\Omega/(L + M\Omega)$, where Ω is a geometric factor determining the ratio of magnetic field per unit current between the object and the coil.

We match the time scales and the amplitudes of the controlled overshoots using magnetic field pulse profile measurements. We determine the time scales of the eddy currents by generating a current pulse and measuring the corresponding magnetic field pulse profile using a Hall sensor near the bottom viewport. Figure 2.10 shows a measurement of a magnetic field pulse from 19 G to -18 G. The measured field pulse profile can be well fit by two exponential decays with time constants 0.2 ms and 1.1 ms. The slow ramps in the magnetic field are the contributions from the eddy currents, whose time constants are to be matched by the *pre-emphasis* circuit. After setting the time constants, the amplitude of the overshoot current can be determined by directly minimizing the magnetic field pulse error using microwave spectroscopy on atoms polarized in the $|3, 3\rangle$ state. We have adjusted the *pre-emphasis* circuit such that the field can be stabilized to less than 2% within 400 μs. Figure 2.11 shows a sample magnetic field pulse profile with a designated 0.3 G to 17.5 G field jump. Clearly the slow eddy current contribution is removed and the remaining time constant of 100 μs is close to the time scale associated with the slew-rate limited pulse slope.
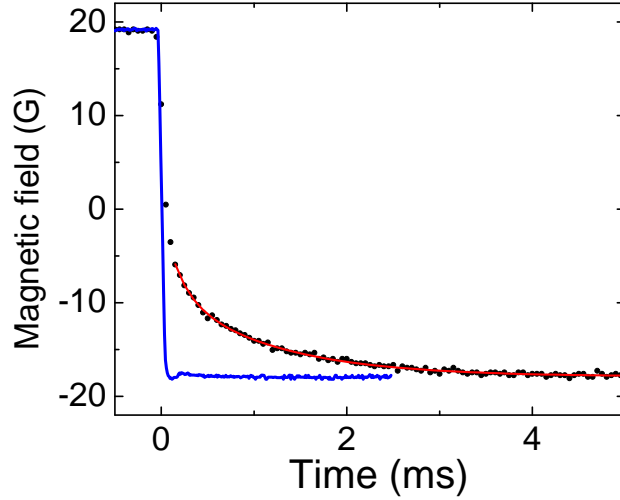
Figure 2.10: Magnetic field pulse profile (circles) generated without the *pre-emphasis* control. The ideal pulse profile (blue solid line), calculated according to the measured current pulse in the quadrupole coils, is plotted for comparison. The magnetic field is measured by a Hall sensor placed beneath the bottom viewport. The current pulse is measured through an independent Hall current sensor in the current servo. After the current slew has ceased, a fit with two exponential decays (red solid line) reveals magnetic field contributions from eddy currents with time constants 0.2 and 1.1 ms.

2.7 Laser cooling

In this section, we briefly summarize several laser cooling schemes carried out in our experiment. We describe experiment setups of the Zeeman slower, the magneto-optical trap and optical molasses, and finally the degenerate Raman sideband cooling.

2.7.1 Zeeman slowing

In the Zeeman slower, the atomic beam is slowed down by a counter-propagating laser beam, whose frequency is kept resonant to the atomic transition by a spatially varying magnetic Zeeman shift compensating the Doppler shift. Inside the slower, an atom saturated by the resonant laser beam feels a constant deceleration $a_z = \eta_s \hbar \Gamma / 2\lambda m$, where $\hbar$ is the Plank constant h divided by
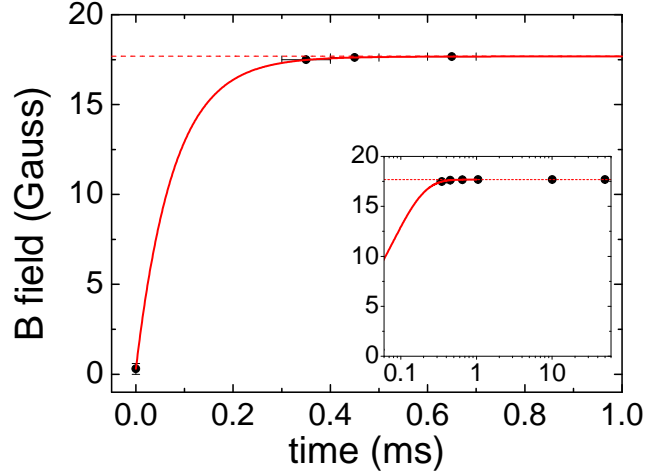
Figure 2.11: Magnetic field pulse profile from 0.3 G to 17.5 G (indicated by the dashed line) with pulse error minimized by the *pre-emphasis* circuit. The magnetic field is determined through microwave spectroscopy on the $|3,3\rangle$ state. The microwave pulse length in the spectroscopy is 100 μs, as shown in the horizontal error bar. The solid line is a single exponential fit with a time constant of 96 μs. The inset shows the field with a larger time window. The field ceased to evolve at times $t > 0.5$ ms after the pulse initiates.

2π, $\Gamma = 2\pi \times 5$ MHz is the transition linewidth, $\lambda = 852$ nm is the laser wavelength, and m is the cesium atomic mass; η_s is a safety factor, a constant less than unity, which parametrizes the ratio between the actual photon scattering rate and its ideal value $\Gamma/2$, and can be incorporated into the design in the Zeeman slower. A parabolic-shaped magnetic field is required to match the Doppler shift seen by atoms moving under constant deceleration,

$$B(z) = \frac{h}{\Delta\mu}\left(\Delta + \frac{1}{\lambda}\sqrt{v_i^2 - 2a_z z}\right), \tag{2.7}$$

where z is the axial position in the Zeeman slower, $\Delta\mu = \pm\mu_B$ depends on the polarization of photons driving $4 \rightarrow 5'$ cycling transition, Δ is the laser detuning at zero-field, and v_i is the maximum axial velocity of atoms that can be Zeeman-slowed. Ignoring transverse heating and other imperfections, atoms with initial axial velocity $v \leq v_i$ entering the slower leave this region

37

with a final velocity $v \approx v_f = \sqrt{v_i^2 - 2a_z L}$, where L is the length of the slower.

We design our Zeeman slower, with a safety factor $\eta_s = 0.5$, capable of slowing atoms with axial velocities $v \leq v_i = 152$ m/s to $v_f = 42$ m/s, within the capture velocity of the MOT. A cesium atomic beam with a mean axial velocity of $v = 230$ m/s therefore ends up with more than 15 % of its population trappable by the MOT, in sharp contrast with an estimated $< 1\%$ without the Zeeman slowing. The parameters used for designing the slower are summarized in Table 2.2. A detuning $\Delta = -100$ MHz is employed to prevent the Zeeman slower laser from interfering with the MOT operating simultaneously in the science chamber.

Table 2.2: Zeeman slower parameters

Parameter	Designed value	Optimized value
Slower tube length L	40 cm	
Cesium oven temperature	80 °C	
Safety factor η_s	0.5	0.82
Laser detuning Δ	-100 MHz	-93 MHz
Velocity range for slowing ($v_f \sim v_i$)	42~154 m/s	50~205 m/s
Atomic flux in MOT capture range	$< 9 \times 10^8$ s^{-1}	8×10^8 s^{-1}
(ignoring transverse heating)		

We designed tapered magnetic coils, running 1 A currents, to generate the desired parabolic field profile, computer program-optimized to within a half linewidth everywhere inside the Zeeman slower. The Zeeman slower field and the tapered coil design are shown in Fig. 2.12. Since the field profile has a zero crossing within the slower, the two coils are facing from the tapered end. Before the slower tube is assembled onto the chamber, we wind the coils directly onto the tube using square magnet wire (width 2 mm) filled with epoxy in each layer. A bias coil (4mm by 40cm), designed to offer a uniform bias field at 13.2 G/A, is first wound onto the slower tube. The tapered coils are then wound on top of the bias coil. Two additional thin coils, designed to run 3 A currents, are wound to both ends of the Zeeman slower to enforce a sharp rise of local magnetic field. We measured the Zeeman slower field running under designated currents and found very
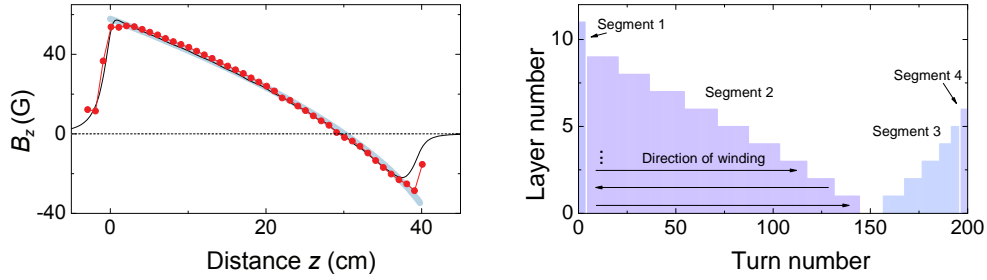
Figure 2.12: Zeeman slower magnetic field: design (solid line), measurement (red circle), and the tapered-coil design (color bars). Shaded curve indicates the magnetic field calculated using the designed parameters listed in Table 2.2; the width corresponds to the FWHM of the transition line width. Applied currents are 3, 1, -1, and -3 A from segment 1 to 4.

good agreement to within a half linewidth; see Fig. 2.12.

The actual Zeeman slower parameters are optimized by maximizing the measured slow atomic flux with the MOT quadrupole field turned on. The Zeeman-slowed atomic flux is measured in the science chamber with a weak probe beam crossing the atomic beam at a small angle. We scanned the probe beam frequency to measure the absorption spectrum, thus detecting the velocity distribution and obtaining the total atomic flux. We found rather different parameters from those of the original design. We run the bias coil with a rather high current at 3.4A, generating a bias field at 45 G; the tapered magnetic coils run currents of 1.2 A (segment 2) and -1 A (segment 3), respectively; the last thin coil (segment 4) runs a current of -0.91 A while the first one (segment 1) runs 0 A (it does not influence the flux). The slower laser detuning is optimized to around -93 MHz while the flux mildly saturates at a laser power around 25 mW. We detected an absorption peak centered around $v \approx 50$ m/s with its peak area corresponding to a flux rate of 8×10^8 atom/s. With the MOT lasers also turned on, we found a better MOT loading rate (10 % larger) when arranging the Zeeman slower field in the direction opposite to the quadrupole field at the entrance of the MOT region. Figure 2.13 illustrates the actual magnetic field configuration.

We can explain these changes after plotting the axial magnetic field generated by the new

39
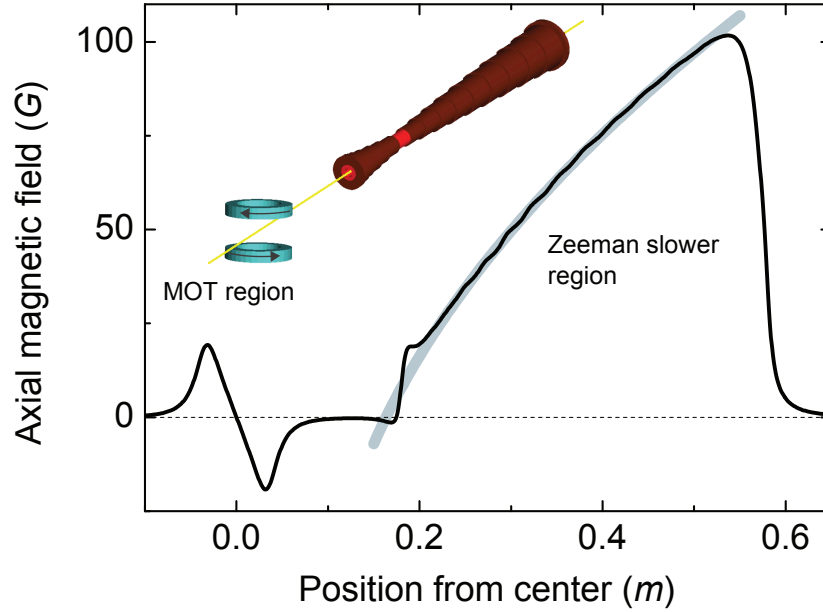
Figure 2.13: Optimized Zeeman slower magnetic field and the MOT quadrupole field. Plotted field (solid line) is the axial component along the yellow line in the three-dimensional drawing. The shaded curve indicates the magnetic field calculated using the optimized parameters listed in Table 2.2; the width corresponds to the FWHM of the transition line width. Currents in coil segments 1 to 4: 0, 1.2, -1.0, and -0.91 A. The current in the bias coil is 3.4 A.

currents; see Fig. 2.13. We observe that, with the added bias field and the increased field slope, the field matches very well with a profile that cools a velocity group ranging between 50 m/s and 205 m/s with a larger safety factor $\eta_s = 0.82$. Our tapered coil design is compatible with a variable safety factor, and gives us room for improving the flux rate in the real experiment, enhancing the total population available for MOT cooling and trapping (by almost a factor of 2 when compared to that of the original configuration). Last, we suspect that the MOT loading is better under this field configuration because the entrance MOT field acts as a negative Zeeman slower field to continue slowing down the atomic flux.

2.7.2 Magneto-optical trap and optical molasses

Entering the science chamber, Zeeman-slowed cesium atoms are cooled and captured inside the magneto-optical trap (MOT). A MOT consists of a magnetic quadrupole field with three pairs of counter-propagating laser beams, red-detuned to the $4 \rightarrow 5'$ transition, and crossing at the field center. The polarization of each beam, before crossing at the center of the quadrupole field, is arranged to be σ^- relative to the local magnetic field. Under this configuration, atoms feel both a damping force due to the Doppler cooling effect and a restoring force due to preferentially scattering local σ^- photons inside the quadrupole field [73].

Once a sufficient number of atoms are trapped inside the MOT, the quadrupole field can be removed and the detuning and intensity of the laser beams can be further adjusted to form an optical molasses where polarization gradient cooling takes place [74, 75]. In the molasses, sub-Doppler effects can further cool the atom temperature down to a few microkelvin.

The setup of the MOT optics is illustrated in Fig. 2.14 and Fig. 2.15, and is described as follows. The MOT laser beams are derived from a single fiber which couples light from the output of the tapered amplifier. The beam has a total power of 60 mW, containing both $4 \rightarrow 5'$ main transition and $3 \rightarrow 4'$ repumping frequencies. It is split into three beams with 1" diameters entering the science chamber in the $x-, y-$, and $z-$directions, and the beams are retro-reflected to create six beams for MOT. The size of each beam is adjusted by a telescope formed from a pair of plano-convex lenses and is made slightly converging to compensate for the intensity drop after passing through the atomic cloud. The $z- (y-)$ MOT beam shares the same beam path with the vertical (horizontal) imaging beam; they are combined and split by polarization beam splitters at both sides of the chamber. In the $z-$direction, in particular, a 1.1 mm thick wire grid polarizer (Meadowlark, VersaLight) is used to retro-reflect the MOT beam and transmit the vertical imaging beam. Four $45°$ dichroic coated mirrors (reflects 1064 nm, and transmits 852 nm) are placed near the view ports in the $x-$ and $y-$directions such that the MOT beams can share the same optical access with

41

the dipole trapping beams (wavelength: 1064 nm). At each side of the chamber in the $x-$ and $y-$beam paths, we place a half-waveplate, in addition to a quarter-waveplate, to compensate for the ellipticity in the MOT beam polarization, introduced from passing through the dichroic mirror.

We tweak optical alignment and experiment parameters both to improve the MOT loading rate and the atomic density after the molasses cooling. The MOT beam detuning is set to -14 MHz. The quadrupole field is produced by the top and bottom coils running at $B' = 15$ G/cm. When the oven temperature is set to 80 °C, producing a high flux rate at 10^9 atom/s, the MOT atom number can saturate at 10^9 atoms after 5 seconds of loading time. We nevertheless optimize according to the number density, leading to 2×10^8 saturated atom number. For typical experiments, we set the oven temperature lower at 60 °C, producing a reduced flux rate at 2×10^8 atom/s, and load for two seconds to obtain $\sim 4 \times 10^7$ atoms. The MOT-captured cloud has a temperature around 40 μK. After the MOT loading stage, we turn off the Zeeman slower laser and the currents in the Zeeman slower coils, and compress the atomic cloud for 30 ms using an increased field gradient $B' = 27$ G/cm and MOT laser detuning -27 MHz. After this, we perform molasses cooling for 2 ms by shutting off the magnetic field gradient and increasing the MOT laser detuning further to -110 MHz. The molasses-cooled cloud has a much lower temperature of 10 μK with a peak density around 10^{11} cm^{-3}. The root-mean-square radius of the atomic cloud is around 0.5 mm, ideal for loading into the Raman sideband cooling 3D optical lattice, whose $1/e^2$ beam radius is around 1 mm.

2.7.3   *Degenerate Raman sideband cooling (dRSC)*

We apply three dimensional (3D) dRSC after the MOT and molasses stages to further cool down the atoms and spin polarize them to the $|3, 3\rangle$ state. The basic ingredient of dRSC is detailed in Ref. [76, 77] and is described here. Thermal atoms are first optically pumped into the $F = 3$ hyperfine ground state, and then are loaded into a tight 3D optical lattice potential. A background
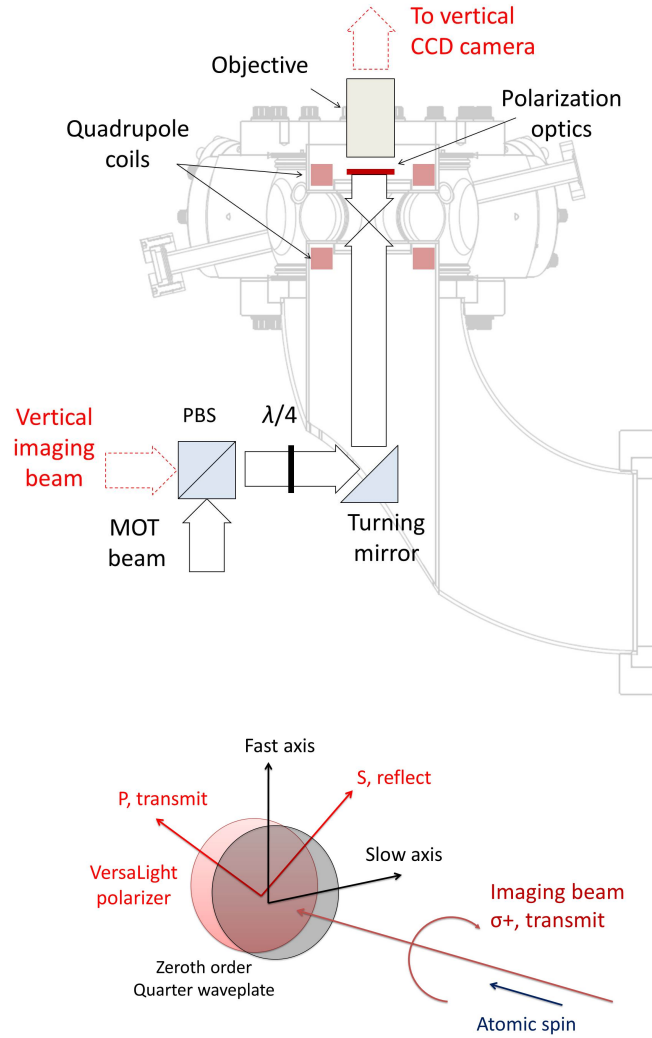
Figure 2.14: Top: schematic setup of the vertical imaging beam and the MOT beam optics. The imaging beam transmits through the polarization optics while the MOT beam is reflected back to the chamber. Bottom: schematic setup of the polarization optics in the vertical imaging beam path. Atomic spin is pointing upward in the vertical direction.
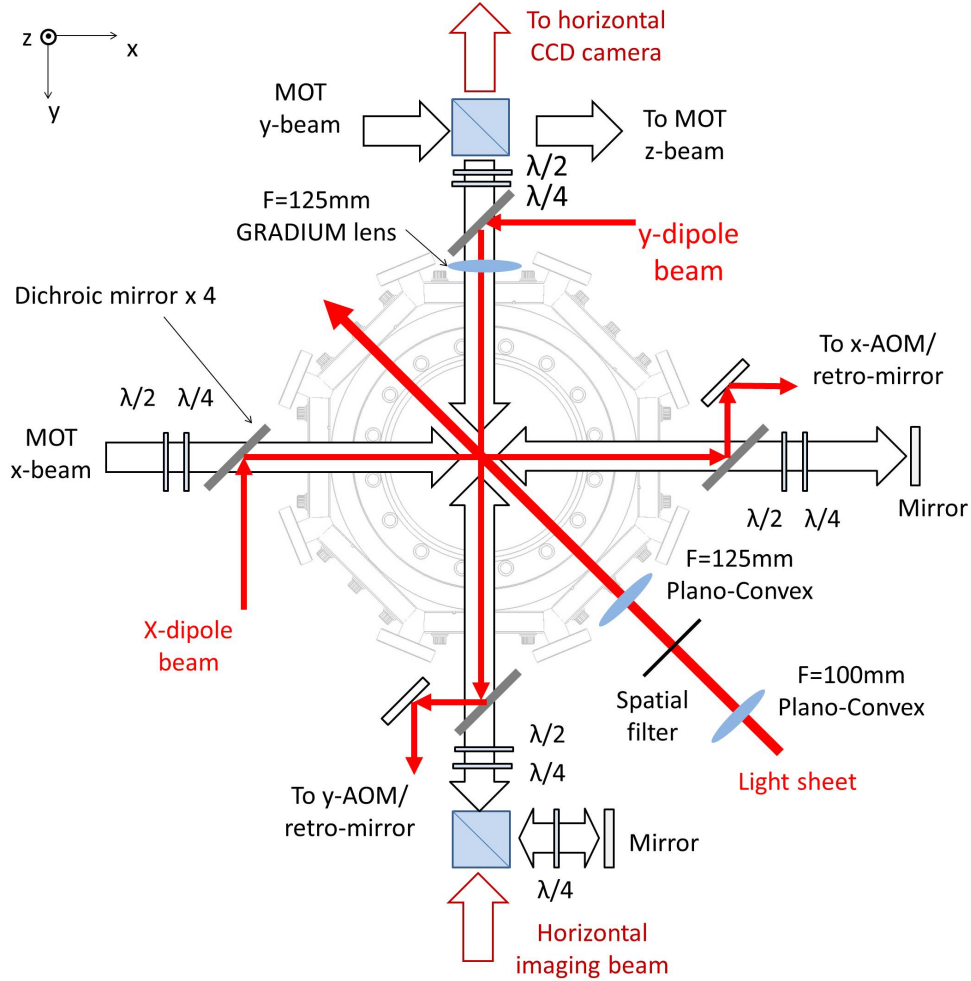
Figure 2.15: Schematic setup of the horizontal MOT beam, imaging beam, and optical dipole trapping beam optics. The x- and y- MOT beams enter the chamber from the $-x$ and $-y$ sides, respectively, and are retro-reflected back to the chamber. The horizontal imaging beam enters the chamber from the $+y$ side and shares the optics with the MOT beams in the $y-$path. Polarization optics are placed to adjust the MOT and imaging beam polarizations to the correct configuration. Four $45°$-dichroic mirrors, transmitting 852 nm and reflecting 1064 nm, are placed on four sides of the chamber in the horizontal MOT beam paths. The x- and y- optical dipole beams, entering from the $-x$ and $-y$ sides, are reflected off from the dichroic mirrors and share the same entrance viewports with the horizontal MOT beams. The light sheet enters the chamber at a $45°$ angle to the $x-y$ dipole beams. In the laser cooling stage, all beams except for the imaging beam are kept on at their nominal power.

44

magnetic field is applied such that the magnetic Zeeman splitting $\Delta E_z = 1/4\mu_B B$ matches the vibrational energy splitting $\hbar\omega$, where ω is the lattice vibrational frequency. A Raman transition couples atoms between the degenerate quantum levels $|m_F, \nu\rangle$ and $|m_F \pm 1, \nu \pm 1\rangle$, where ν is the sum of vibrational quantum number in three dimensions. Now, an optical pumping beam with σ_+ polarization is applied to drive the $|F = 3, m_F, \nu\rangle$ to $|F' = 2, m_F + 1, \nu\rangle$ transition, followed by spontaneous emission back to the $|F = 3, \nu\rangle$ hyperfine ground state manifold. The vibrational quantum number remains unchanged if the optical transition happens in the Lamb-Dicke regime. In this regime, the optical pumping preferentially pumps all atoms into the $|m_F = 2, \nu = 0\rangle$ and $|m_F = 3, \nu = 0, 1\rangle$ low energy states. If there is an additional weak π-component in the optical pumping beam, it can further remove population in the $|F = 3, m_F = 2, \nu = 0\rangle$ state, leaving the absolute lowest energy state $|F = 3, m_F = 3, \nu = 0\rangle$ as the only dark state. Thus, the atoms can be cooled down to the vibrational ground state and are simultaneously polarized into the $|3, 3\rangle$ state. After a sufficient cooling time, the optical pumping beam can be shut off, and the 3D optical lattice can be adiabatically removed, releasing local ground state atoms into free space or an external trap.

The setup of our dRSC closely follows the configuration reported in Ref. [76]. The schematic is shown in Fig. 2.17. The 3D optical lattice potential is formed by two counter-propagating laser beams ($\pm z'$) normal to the $x' - y'$ plane defined by x'-beam and y'-beam, which form a $\sim 90°$ cross. The optical lattice beams are derived from a 2 mm diameter, 70 mW fiber coupled laser beam originating from the *dRSC slave* laser. The linear polarizations of x' and y' beams lie in the $x' - y'$ plane while the $\pm z'$-beams are polarized $\pm 10°$ degree to the line bisecting the x' and y' beams. The Raman coupling is provided by the same lattice beams through a non-vanishing vector light shift due to their crossed polarizations [77]. The effective magnetic field of the vector light shift is along the direction of the $\pm z'$-beams. The weak dRSC optical pumping beam is derived from a fiber-coupled *Repumper* beam. The orientation is shown in Fig. 2.17. The optical pumping beam is polarized using a true zero-order quarter-waveplate and is retro-reflected by a gold mirror.

We apply dRSC immediately after the molasses cooling. The repumper component in the MOT
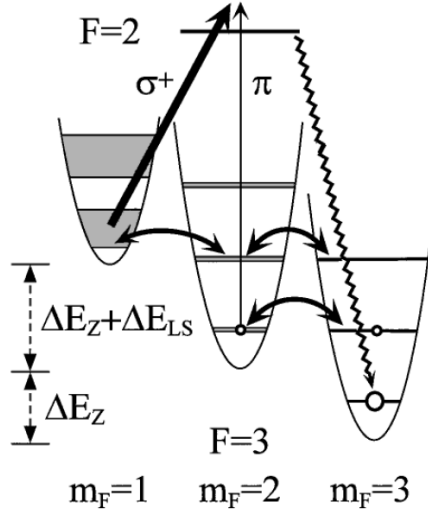
Figure 2.16: Diagram of the optical pumping scheme in degenerate Raman sideband cooling. Raman coupling (double-sided arrows) and σ^+ optical pumping quickly remove the atomic vibrational energy. A weak π-transition pumps the atoms into the dark state. Here, ΔE_z is the Zeeman shift and ΔE_{LS} is the light shift created by optical pumping. Reprinted figure with permission from Ref. [76]. Copyright 2000 by the American Physical Society.

beams is first extinguished for 1 ms to pump all atoms into the $F = 3$ hyperfine ground state. The dRSC optical lattice is then pulsed on to isolate atoms into individual lattice sites. Simultaneously, the optical pumping beam is applied to the atoms with its frequency adjusted to drive the $3 \to 2'$ transition. Meanwhile, the MOT beam intensity is greatly reduced and the frequency is switched to drive the $4 \to 3'$ transition, removing accidental population in the unwanted $F = 4$ state. The bias coils run currents to generate a background magnetic field aligned close to the orientation of the optical pumping beam. The field strength is optimized to create a degenerate Zeeman splitting. After 10 ms of cooling time, the optical pumping beam is first extinguished, followed by turning off the MOT beams. The dRSC is then ramped off in 100 μs, adiabatically releasing atoms into free space or into the optical dipole tap.

We optimize the experiment parameters by maximizing the number of dRSC-cooled atoms
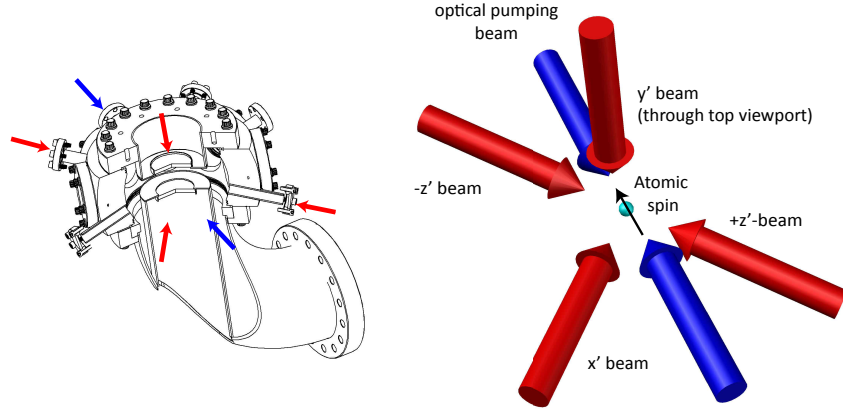
Figure 2.17: Orientation of the dRSC lattice beams (red arrows) and the optical bumping beams (blue arrows) used in this experiment. The science chamber is plotted with the same view angle to indicate the entrance viewport of each beam. Except for the y' beam, all other beams enter the chamber via 1-1/3" small viewports. The black arrow indicates the orientation of the atomic spin, which is slightly misaligned to the optical pumping beam.

and minimizing the cloud temperature in free space. We observe a very good cooling efficiency: 80% out of 10^8 molasses-cooled atoms are spin polarized into the $|3,3\rangle$ state with a free space temperature of 400 nK. We note that, due to space limitation, our optical pumping beam and therefore the orientation of the atomic spin is less perpendicular to the effective magnetic field created by the vector light shift. Despite a smaller Raman coupling strength, we do not observe a significant deterioration in the cooling efficiency compared to those reported in the literature.

The dRSC is efficient at removing local kinetic energy while freezing the spatial distribution of the atomic cloud. When an external trapping potential is present, atoms heat up by regaining trap potential energy after being released from the dRSC optical lattice. Applying multiple dRSC stages can re-cool atoms rolling down the trap and increase the peak phase space density. The number of cooling stages is nevertheless limited. When more than one atom is loaded into a single site of the optical lattice, radiative loss occurs during the optical pumping and the total particle number would begin to decrease [78]. This occurs when the peak density $n = N\bar{\omega}^3(m\lambda_{dB}/h)^3$ is larger than

$d^{-3} = 1.3 \times 10^{13} \text{cm}^{-3}$, where $d = 426$ nm is the lattice spacing, N is the total particle number, $\bar{\omega}$ is the mean trap frequency, and $\lambda_{dB} = h/\sqrt{2\pi m k_B T}$ is the thermal de Broglie wavelength. Later we shall see that our typical dipole trap has a mean trap frequency $\bar{\omega} = 2\pi \times 34$ Hz and a total particle number $N = 10^7$ atoms; the final temperature is limited to 2 μK and the peak phase space density is limited to $n\lambda_{dB}^3 = 0.02$. Similar density-limited dRSC performance was observed in various dipole trapping potentials, prepared during the past few years, where the measured temperature increases with an increasing trap frequency.

We will later discuss using multi-stage dRSC to transfer cold atoms into the optical dipole trap. All details on dRSC-assisted and magnetic field levitated dipole trap loading will be discussed in the end of Section 2.9.

2.7.4   Improving dRSC at high atomic densities

Here, I further comment on a possible improvement to dRSC. Can dRSC help achieve an even higher phase space density much closer to degeneracy? From the argument in the above paragraph, we find that the temperature after the density-limited cooling is

$$T_{\text{trap}} = \frac{m\bar{\omega}^2 d^2}{2\pi k_B} N^{2/3}. \tag{2.8}$$

We expect the above equation holds as long as the temperature is higher than the free space value, which is limited by the lattice recoil energy. From literature [76], the lowest temperature achieved is 200 nK in an 852 nm near-detuned 2D isotropic lattice, roughly corresponding to twice the recoil energy. We then assume the recoil-limited temperature depends on the lattice spacing as

$$T_{\text{rec}} = \frac{lh^2}{8mk_B d^2}, \tag{2.9}$$

where $l \approx 2$ is the ratio of thermal energy $k_B T_{\text{rec}}$ to the recoil energy. To reach this low temperature while maintaining a high in-trap density, we could use multi-stage cooling inside a trap to achieve the largest peak density $n = d^{-3}$ with other parameters chosen such that the temperature T_{trap} reaches the recoil limit T_{rec}. The largest phase space density achievable is then a universal value

$$n\lambda_{dB} = \left(\frac{4}{\pi l}\right)^{3/2} \approx 0.5, \tag{2.10}$$

which is only a factor of 2 away from degeneracy. The improvement can be realized without sacrificing much of the total particle number and trap confinement. For example, using a 532 nm laser to form the dRSC optical lattice and reducing the dipole trap frequency to $\bar{\omega} = 2\pi \times 20$ Hz, one can in principle reach the lowest temperature in density-limited cooling. It will be interesting to test this prediction in future experiments.

2.8 Magnetic levitation and (anti-)trapping

Although magnetic trapping is not emphasized in the cesium BEC experiment, it is however important to apply a magnetic force during the dipole trapping and evaporative cooling stage to support atoms against gravity. Moreover, we use a weak optical trapping potential for most of our experiments, where non-zero magnetic curvature could modify the expected trap frequencies. Below we consider magnetic levitation of cesium atoms and the (anti-)trapping potential caused by magnetic field variation.

When the magnetic coils run non-equal currents $\Delta I \neq 0$, they generate an offset magnetic field $\mathbf{B} = B_o\hat{z}$ at the center of the chamber as well as a vertical field gradient $\frac{\partial |\mathbf{B}|}{\partial z} = B'$. The field gradient creates a magnetic force $F = -\mu B'$ on the atoms, where $\mu = m_F g_F \mu_B$ is the atomic magnetic dipole moment, m_F is the magnetic quantum number, and g_F is the hyperfine Landé g-factor. For $|3, 3\rangle$ state, $g_F = -\frac{1}{4}$ and the magnetic force is $F = \frac{3}{4}\mu_B B'$; a magnetic field gradient of 31.09 G/cm generates a levitating force that balances the gravity.

In general cases with arbitrary B_o and B', the spatial dependence of the magnetic field can be calculated to leading order, using the Maxwell's equations $\nabla \cdot \mathbf{B} = 0$ and $\nabla^2 \mathbf{B} = 0$, as

$$\mathbf{B} = -\left(\frac{B'}{2} + \epsilon B_o z\right) x\hat{x} - \left(\frac{B'}{2} + \epsilon B_o z\right) y\hat{y} + \left[B_o + B'z + \epsilon B_o(z^2 - \frac{x^2 + y^2}{2})\hat{z}\right], \quad (2.11)$$

where $\epsilon = 0.087$ cm^{-2} is calculated from the actual coil geometry (coil radius $r = 3$ cm and distance $d = 4.6$ cm); non-zero ϵ is due to the departure of our coil geometry from the Helmholtz configuration ($r = d$).

We calculate the magnetic trap/anti-trap through looking at the curvature of the magnetic dipole potential. Since the atomic motion in the dipole trap is much slower than the Larmor precession, the atomic spin follows the direction of the local magnetic field, leading to a dipole potential $\mu \cdot \mathbf{B} = \mu|B|$. Therefore, we only care about the curvature of the field strength $|\mathbf{B}|$. A negative (positive) curvature in $|\mathbf{B}|$ leads to trapping (anti-trapping) for atomic states with negative magnetic moment $\mu < 0$, as is the case of the $|3,3\rangle$ state. After expanding $|\mathbf{B}|$ to quadratic order in vertical (z) and radial ($\rho = \sqrt{x^2 + y^2}$) coordinates, we find the corresponding trap frequencies near the trap center,

$$\omega_z^2 = \frac{2\mu\epsilon B_o}{m} \tag{2.12}$$

$$\omega_\rho^2 = \frac{\mu}{4mB_o}\left(B'^2 - 4\epsilon B_o^2\right). \tag{2.13}$$

The radial field curvature vanishes at $B'/B_o = \pm 0.59$ cm^{-1} and changes sign when B'/B_o crosses this critical ratio.

We use the trap frequency dependence Eq. (2.13) to improve dipole trap loading efficiency. When applying the full levitating field $B' = 31.1$ G/cm to balance the gravity, a strong magnetic field offset $|B_o| > 52.7$ G changes the anti-trap into trapping horizontally. This helps increase our optical dipole trap horizontal trap volume (see later discussion). However, when atoms become

colder, we need to set the offset field to $B_o = 21$ G near a Efimov three-body loss minimum [40]. If B' remains the same, we have an anti-trap in all directions, with anti-trap frequencies $2\pi \times 1.7$ Hz vertically, and $2\pi \times 2.8$ Hz horizontally. The expelling force due to the anti-trap can be aggravated if the dipole trap is not aligned to the magnetic trap center. In the real experiment, we overlap the center of the optical dipole trap well with the magnetic trap center, and completely turn off the field gradient at the end of evaporation, minimizing the magnetic trap/anti-trap contribution to around 1 Hz as well as improving the field homogeneity for precision Feshbach spectroscopy.

Moreover, applying a horizontal bias field B_x or B_y using the bias coils can shift the horizontal trap/anti-trap center. This is often used to induce dipole oscillations of trapped atomic clouds and to measure the trap frequencies.

2.9 Optical dipole trapping

The absolute lowest energy ground state $|3, 3\rangle$ atoms are not magnetically trappable. Trapping cesium atoms by optical means thus becomes a necessary tool for evaporative cooling to Bose-Einstein condensation, and later we will see that trapping by laser interference patterns provides the lattice potential in the optical lattice experiments.

An optical trapping potential can be best provided by linearly polarized, far-detuned laser beams. The simplest way to understand dipole trapping is by looking at the ground state light shift of a simple two-level system perturbed by far-detuned photons. Atoms in the ground state are dressed with the excited state and form weak electric-dipoles oscillating out-of (in) phase with the incident electromagnetic wave due to a negative (positive) detuning. In the rotating wave approximation, neglecting the counter-rotating term, the time-averaged dipole energy $V(\mathbf{r}) = \frac{3\pi c^2}{2\omega_0^3} \frac{\Gamma}{\Delta} I(\mathbf{r})$ forms the ground state energy shift. Here $I(\mathbf{r})$ is the laser beam intensity at position $\mathbf{r}$, c is the speed of light, ω_0 is the transition frequency, Γ is the linewidth, and $\Delta = \omega - \omega_0$ is the laser frequency detuning. The light shift induced by a red-detuned laser beam therefore forms a po-

tential that attracts atoms near its intensity maximum. On the other hand, the photon scattering rate $\Gamma_{sc}(\mathbf{r}) = \frac{3\pi c^2}{2\hbar\omega_0^3}(\frac{\Gamma}{\Delta})^2 I(\mathbf{r}) = \frac{\Gamma}{\Delta}\frac{V(\mathbf{r})}{\hbar}$ is suppressed at a sufficiently large detuning $\Delta \gg \Gamma$. We estimate that a potential depth of $U_0 = k_B \times 10\ \mu$K is sufficient for trapping dRSC-cooled atoms, and the photon scattering rate is $\Gamma_{sc} \sim 2\pi\ \text{MHz}^2/\Delta$. A commercial micron-wavelength laser could easily meet the requirement with a small photon scattering rate $< 2\pi \times 0.02$ Hz, corresponding to a heating rate <1.3 nK/s. Optical dipole traps are in fact widely used in many cold atom experiments.

For cesium atoms, one need to consider the fine-structure doublets in the $6P$ excited state when calculating the ground state light shift. In particular, our trapping laser is at 1064 nm wavelength, whose frequency resolves the fine-structure splitting in the $6P$ state. The ground state light shift at this wavelength is therefore calculated as the summed contribution of the D_1 and D_2 lines, weighted by their relative line strengths $\frac{1}{3}$ and $\frac{2}{3}$, respectively,

$$V(\mathbf{r}) = \frac{3\pi c^2}{2}\left(\frac{1}{3}\frac{\Gamma_1}{\omega_1^3\Delta_1} + \frac{2}{3}\frac{\Gamma_2}{\omega_2^3\Delta_2}\right) I(\mathbf{r}) = \alpha I(\mathbf{r}). \tag{2.14}$$

Here $\Gamma_1 = 2\pi \times 4.56$ MHz and $\Gamma_2 = 2\pi \times 5.22$ MHz are the natural line widths of the D_1 and D_2 lines, respectively, $\omega_1 = 2\pi \times 335.1$ THz and $\omega_2 = 2\pi \times 351.7$ THz are their transition frequencies, $\Delta_1 = -2\pi \times 53.34$ THz and $\Delta_2 = -2\pi \times 69.94$THz are the corresponding laser frequency detunings, and $\alpha = -k_B \times 2.35$ nK $\cdot$ cm^2/W.

In experiment, we use Gaussian beams (spatial TEM$_{00}$ mode) to form the trapping potential. The intensity profile of a Gaussian beam propagating along the y-direction is described by

$$I(\mathbf{r}) = I(x, y, z) = \frac{2P}{\pi w_x w_z}e^{-(2x^2/w_x^2 + 2z^2/w_z^2)}, \tag{2.15}$$

where P is the total beam power, and w_x (w_z) is the $1/e^2$ beam radius along the $x-$ ($z-$) direction. Due to diffraction, $w_i = w_{i0}\sqrt{1 + (\frac{y}{y_{ri}})^2}$ expands as the distance y increases. Here,

i indicates either $x-$ or $z-$axis, w_{i0} is the beam waist along the $i-$axis, and $y_{ri} = \pi w_{i0}^2/\lambda$ is the Rayleigh length. Near the intensity maximum, $V(x, y, z) = \alpha I(x, y, z)$ can be approximated by a harmonic trap with trap frequencies $\omega_{x,y,z} = \sqrt{\frac{4\alpha P}{\pi m w_{x0} w_{z0}}}(w_{x0}^{-1}, y_r^{-1}, w_{z0}^{-1})$, where $y_r^{-1} = \sqrt{(y_{rx}^{-2} + y_{rz}^{-2})/2} \ll w_{x0}^{-1}, w_{z0}^{-1}$.

2.9.1 Design of the dipole trap potential

For dipole trapping and evaporative cooling, as well as optical lattice experiments, we use two laser beams, orthogonally crossed at the center of the chamber and propagating along the $x-$ and $y-$axes, to provide trapping in the horizontal plane. Each beam has a variable power, normally fixed at around 2 W, and a round beam waist of $w_{x,y} = w_z = 300\ \mu$m. Together they offer a large trapping volume to capture dRSC-cooled atoms and provide weak confinement to achieve moderate trapped atomic densities. The crossed dipole beams provide a trap depth of $V_0 = k_B \times 10\ \mu$K and a horizontal trap frequency of $2\pi \times 14$ Hz. The beams can be retro-reflected to create interference patterns and form a two-dimensional optical lattice potential, to be discussed later.

Trapping in the vertical ($z-$) direction is strongly influenced by gravity. To enhance the trap confinement in the $z-$direction, we add an additional elliptical beam (aspect ratio 6:1) in the horizontal plane intersecting the crossed dipole beams with a $45°$ angle. The vertical beam waist is $45\ \mu$m and the beam power is around 400 mW, forming a light sheet capable of supporting atoms against gravity without significantly modifying the horizontal trap volume.

Without changing the beam intensity, the trap strength depends on the magnetic field gradient that offers an additional levitating force against gravity, as discussed in the previous section. With the magnetic force canceling out gravity, the dipole trap created by the three intersecting dipole beams is at its full strength. The trap depth is $k_B \times 18\mu$K, and the horizontal and vertical trap frequencies are $2\pi \times 20$ Hz and $2\pi \times 110$ Hz, respectively; under the gravitational pull, however, the dipole trap is tilted along the direction of gravity with an effective trap depth as shallow as a

few tens of nanokelvin. The vertical trap frequency remains moderately strong at around $2\pi \times$ 60 Hz even with such a great reduction in trap depth. Utilizing this fact, we further developed an evaporation scheme by gradually removing the magnetic force to tilt open the trap while cooling trapped cesium atoms to reach nearly pure BEC, similar to the scheme discussed in the next chapter.
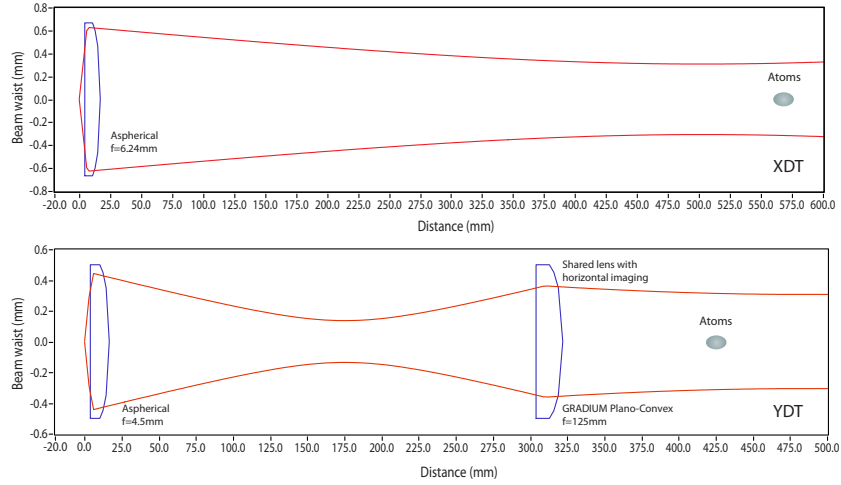
Figure 2.18: Schematic setup of the Gaussian beam optics for x- and y-dipole beams.

2.9.2   Technical setup

At the time of writing this thesis, all three 1064 nm wavelength dipole beams are derived from a commercial single mode, single frequency laser (InnoLight, Mephisto MOPA) with an 18 W total output power. The laser beam is first split into three parts: two for the horizontal dipole beams and one for the light sheet. The frequency of each beam is then offset via individual AOMs (Crystal Technology, part number: 97-02848-01) to avoid creating stationary interference patterns in the crossed dipole trap. The frequency offsets are -80 MHz for the $x-$beam, $+80$ MHz for the $y-$beam, and $+180$ MHz for the light sheet (double pass). Each beam is then transported via an
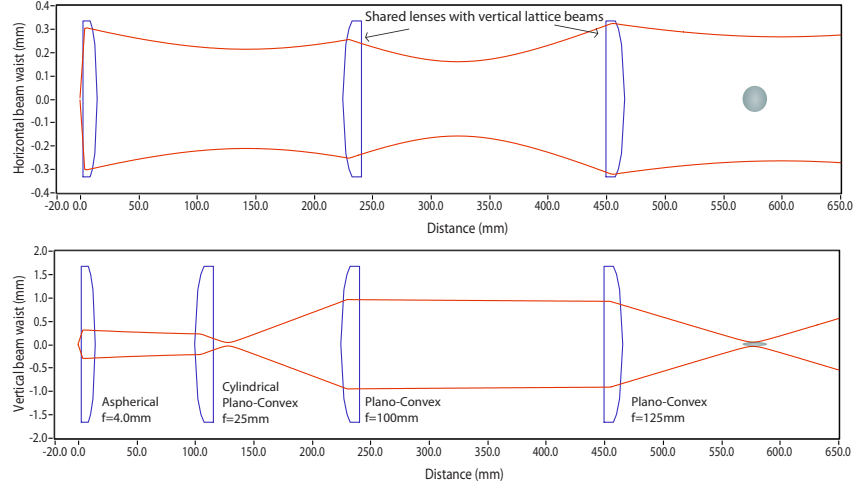
Figure 2.19: Schematic setup of the Gaussian beam optics for the light sheet.

optical fiber (OFR: FCPP-1064-2-FC/APC2) to the science chamber to remove pointing instability due to thermal contractions in the AOM crystal. The polarization of each fiber output is cleaned up using a high extinction ratio (1000:1) polarizing cube. The beam power is then feedback-stabilized via controlling the RF amplitude to the AOM circuit. To avoid stimulated Brillouin scattering (SBS), we couple only a few watts of power into each fiber since the core size is small (Mode Field Diameter $< 10 \ \mu$m) and has high intensity within. We chose a short fiber length of 2 to 3 meters to attain larger SBS threshold power, and tested the fibers to ensure continuous delivery of a maximum output power of 4 W without degradation in the coupling efficiency.

All the fiber-coupled beams are reshaped by lenses to achieve the desired $1/e^2$ beam radius at the position of the atoms. Figures 2.18 and 2.19 show the schematics of the optical setup in each beam path. At each fiber outlet, an aspherical lens is mounted with the fiber facet to collimate the output beam. Subsequent lenses then collimate each beam near the center of the chamber. To ensure we obtain the desired beam profile at designated high power without suffering from a possible change in the beam divergence, we tweak the position of all lenses when the laser is running at full power, and use a pick up beam to measure its profile.

Ideally, to avoid mechanical pointing instability, one would prefer to use lens pairs to also image the fiber facet onto the position of atoms. Nevertheless, we have chosen to avoid this type of configuration after finding multiple fringes fragmenting the Bose-condensed atoms. The fringes are likely caused by scattered light between the back surface of the aspherical lens and the fiber facet or the fiber facet imperfections, which co-propagates with the dipole beam and is imaged onto the atoms. Alternatively, using configurations plotted in Fig. 2.18, we still observe only $\sim 1\ \mu$m shot-to-shot cloud center fluctuation. We believe that the mechanical stability of the fiber mount suffices to provide good pointing stability.

2.10   DRSC-assisted dipole trap loading

We now describe in detail the dRSC-assisted, magnetic field-levitated dipole trap loading procedure. The $x - y$ beams and the light sheet are turned on throughout all laser cooling stages to minimize transient thermal effects in transmissive optics. Since the resonant radiation pressure is much stronger than the far-detuned dipole force, the performance of the MOT and molasses cooling is not influenced much by the dipole beams. After the molasses, dRSC is applied for a few ms to remove atomic kinetic energy. Once atoms are cold, all resonant laser beams are extinguished, followed by ramping off the dRSC optical lattice. A magnetic field gradient is simultaneously switched on to levitate the atoms and restore the full strength of the optical dipole trap, allowing cold atoms to slosh down to the trap center. The levitating field gradient $B' = 31.1$ G/cm, with an offset field $B_o = 13$ G pointing in the vertical direction, is generated by a current pulse in the quadrupole coils. During the field switch, the background magnetic field remains finite and the atomic spin follows the field orientation. After 4.8 ms of atomic sloshing time, the currents in the quadrupole coils are removed, returning the magnetic field back to the initial condition. Simultaneously, atoms are loaded back into the dRSC optical lattice and the next cooling cycle begins. The same procedure is repeated three times, allowing more atoms to be captured when falling through

the oblate-shaped dipole potential, formed by the $x - y$ dipole beams and the light sheet. After the last dRSC cycle, the levitating field is turned on and the offset field is increased to 58 G, enhancing the horizontal trap strength to preserve more atoms populating the extended arms of the crossed dipole beams.

2.10.1   Experiment condition before evaporative cooling

The current experiment begins with 4×10^7 molasses-cooled atoms, and uses three-stage dRSC to transfer 10^7 atoms into the dipole trap. The transfer efficiency is around 25 % and the temperature of the cloud is $\sim 2\mu$K, which is much smaller than the molasses temperature of 10 μK; the cooling performance reaches the dRSC lattice density limit (see previous discussions). Comparing to loading without the dRSC, there is an enormous boost in the transfer efficiency: less than 5% of molasses-cooled atoms ($1/e^2$ cloud radius 0.5 mm, peak density 10^{11} cm^{-3}) are initially located inside the trap volume $\sim \frac{4}{3}\pi 0.3 \times 0.3 \times 0.045$ mm^3 determined by the $1/e^2$ beam radii. We calculate the peak phase space density to be around 0.02, only two orders of magnitude away from Bose condensation.

CHAPTER 3

RUNAWAY EVAPORATIVE COOLING TO BOSE-EINSTEIN CONDENSATION IN OPTICAL TRAPS

In this chapter, we discuss our simple scheme to achieve fast, accelerating (runaway) evaporative cooling of optically trapped atoms by tilting the optical potential with a magnetic field gradient. Runaway evaporation is possible in this method due to the weak dependence of vibration frequencies on trap depth, which preserves atomic density during the evaporation process. Using this scheme, we show that Bose-Einstein condensation with $\sim 10^5$ cesium atoms can be realized in $2 \sim 4$ s of forced evaporation. The performance is in sharp contrast to > 20 s of evaporation time if we adopt conventional cooling method by reducing the dipole beam intensity. The evaporation speed and energetics of this new scheme are consistent with the three-dimensional evaporation picture, despite the fact that atoms can only leave the trap in the direction of tilt.

This chapter is adapted from a published work by C.-L. Hung, X. Zhang, N. Gemelke, and C. Chin in *Phys. Rev. A* **78**, 011604(R) (2008). Copyright 2008 by the American Physical Society.

3.1   Introduction

Evaporative cooling proceeds by lowering the depth of a confining potential, which allows atoms with high kinetic energy to escape and the remaining particles to acquire a lower temperature and higher phase space density through rethermalization. Starting from a sample of precooled atoms in a dipole trap, one can perform forced evaporative cooling on optically trapped atoms by constantly reducing the trap depth until quantum degeneracy is reached. This method has been successful in creating rubidium BEC in a dipole trap [79], and has become a critical component in recent experiments on quantum gases of Cs [40], Li [80], K [81] and Yb [82]. In all these experiments, forced evaporative cooling in the dipole trap is realized by reducing the intensity of the trapping

58

beam, and consequently also the restoring forces. In later discussion, we will refer to this approach as the trap-weakening scheme.

Evaporative cooling in optical traps remains one of the most time-consuming and technically challenging steps in condensate production. Fundamentally, this is due to the fact that cooling by weakening the trapping potential inevitably reduces the collision rate. Here runaway (accelerating) evaporation is essentially impossible even with perfect evaporation efficiency and purely elastic collisions [1]. Within experimentally accessible times, the trap-weakening method puts a severe limit on the maximum gain in phase space density one can reach. Several auxiliary schemes have been successfully implemented in order to increase the evaporation speed, including the dimple trap [40] and a zoom lens system [84]. These methods often increase the complexity of the apparatus or require delicate optical alignment or manipulation.

3.2   A simple way of evaporative cooling: tilting the trap

To overcome the limit trap-weakening scheme, we developed a new and simple evaporative cooling scheme which can be immediately implemented in many existing experiments. Instead of reducing the intensity of the trapping beam, we reduce the trap depth by applying an external force on the optically trapped atoms. This trap-tilting method entails only a weak reduction in confinement strength over a large range of potential depth and can significantly speed up the cooling process. Using this method, we demonstrate runaway evaporative cooling in a large volume dipole trap and reach Bose-Einstein condensation of cesium significantly faster than previous results [85]. Finally, we comment on the conditions for runaway evaporation in a tilted trap and investigate the dimensionality of atomic energy selection in the evaporation.

---

1. The only possible runaway evaporation in a weakening trap is on resonant Fermi gas, see Ref. [83]
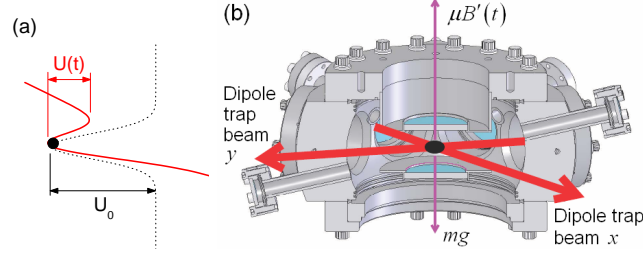
Figure 3.1: Trap-tilt based evaporation and experimental apparatus. (a) Trap depth U decreases when an external potential gradient is applied to the optically trapped atoms. (b) Apparatus for evaporation of cesium atoms (black dot) in a crossed-beam dipole trap. A strong, slowly-varying magnetic field gradient $B'(t)$ over-levitates the atoms with magnetic moment μ against gravitational pull mg and evaporates them upward.

3.3 Key advantage in the trap-tilting scheme: preserving the trap confinement

To understand the advantage of the trap-tilting scheme, we analyze how the trap frequency is modified in a model Gaussian potential during the evaporative cooling process. We combine the magnetic gradient potential and the gravitational potential as $-\gamma m g z$, where $\gamma = B'/B'_c - 1$. The total potential $V(x, y, z)$ can be modeled as

$$V = -\frac{U_o}{2}[e^{-2(x^2+z^2)/w^2} + e^{-2(y^2+z^2)/w^2}] - \gamma m g z, \tag{3.1}$$

where the first two terms come from the two horizontal trapping beams, and the last term is the tilt potential. Here, we assume the two beams have the same beam waist w and peak light shift $U_0/2$ for convenience.

We introduce the tilt parameter $\zeta = \sqrt{e}\gamma m g w / 2 U_0$ to parameterize the trap depth U and trap frequencies $\omega_{x,y,z}$. The trap depth $U = V(0, 0, z_a) - V(0, 0, z_b)$ is the difference between the local trap maximum at $z = z_a$ and the local trap minimum at $z = z_b$, as shown in Fig. 3.1 (a). Near the

60
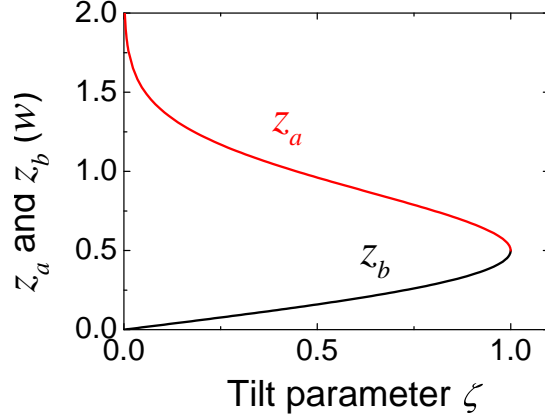
Figure 3.2: Location of the local trap maximum at $z = z_a$ and minimum at $z = z_b$.

trap center in the $x - y$ coordinate, the extrema can be found at $z = \text{sgn}(\zeta)w|\sqrt{W(-\zeta^2/e)}|/2$, where $\text{sgn}(x)$ denotes the sign of x and $W(x)$ is the two-valued Lambert W-function satisfying $W(x)e^{W(x)} = x$ for $-1/e \leq x \leq 0$. Figure 3.2 (a) shows z_a and z_b as functions of the tilt parameter ζ. The trap depth $U(\zeta)$ is then evaluated through the analytic form of $z_{a,b}(\zeta)$ and the result is plotted in Fig. 3.3 (a), normalized to the untilted trap depth $U_0 = U(0)$. Note that when $\zeta \geq 1$, no extremum exists and the trap opens.

Expanding Eq. (3.1) near the local trap minimum, we calculate both the horizontal and vertical harmonic trap frequencies

$$
\begin{aligned}
\omega_x &= \omega_y = \omega_x^0 e^{-z_b(\zeta)^2/w^2} \\
\omega_z &= \omega_z^0 \sqrt{1 - \frac{4z_b(\zeta)^2}{w^2}e^{-z_b(\zeta)^2/w^2}},
\end{aligned}
\tag{3.2}
$$

where $\omega_{x,z}^0$ are the trap frequencies of an untilted potential, and $\omega_z^0 = \sqrt{2}\omega_x^0 = \sqrt{4U_0/mw^2}$. Figure 3.3 (a) shows ω_x and ω_z as functions of ζ, whose fractional change remains moderate compared to that of the trap depth U as the tilt increases. The geometric mean of the trap frequencies

61
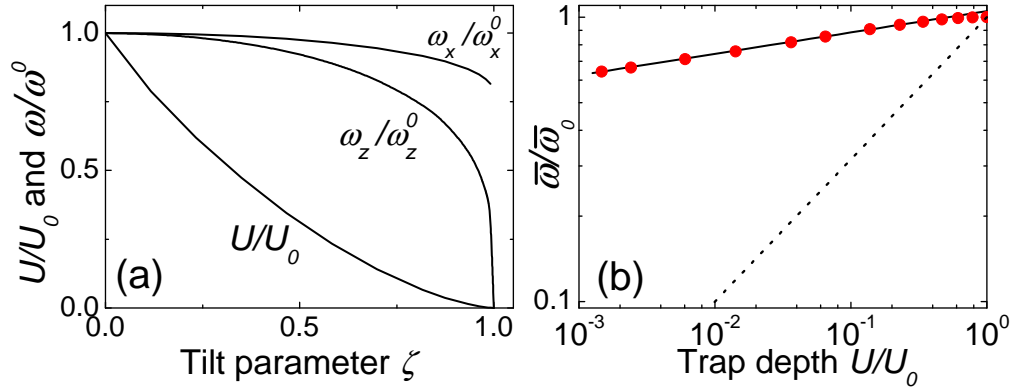
Figure 3.3: Depth and oscillation frequency of a tilted trap. (a) shows the calculated normalized trap depth and frequencies ω_z and $\omega_x = \omega_y$ as a function of the tilt ζ, based on Eq. (1). In (b), mean trap frequencies are plotted against the trap depth for a tilted trap (solid dots) and for a weakened trap (dotted line). The solid line shows a power-law fit to the mean frequency, see Eq. (2).

$\bar{\omega} = (\omega_x \omega_y \omega_z)^{1/3}$ can be written as

$$\bar{\omega}(\zeta) = \bar{\omega}_0 \left[1 - \frac{4 z_b(\zeta)^2}{w^2} \right]^{\frac{1}{6}} e^{-z_b(\zeta)^2/w^2}, \tag{3.3}$$

where $\bar{\omega}_0$ is the mean frequency of an untilted trap. Within the range of $10^{-3} < U/U_0 < 1$, we found $\bar{\omega}_0$ varies approximately as

$$\frac{\bar{\omega}}{\bar{\omega}_0} \approx 1.05 \left(\frac{U}{U_0} \right)^{0.075(1)}, \tag{3.4}$$

showing a weak power law dependence on U, see Fig. 3.3 (a).

The key advantage of a tilted trap lies in the gentle, almost negligible weakening of the trap confinement when the trap depth decreases. As the trap depth reduces by a factor of 100, the trap frequency only decreases by 45% in the $z-$direction and 14% in the other two directions, in contrast to the trap-weakening method, which reduces trap frequencies by a factor of 10 under the same condition. In general, a weakening trap with $\bar{\omega} \propto U^\nu$ and $\nu = 0.5$ shows a much stronger dependence on the trap depth than the tilting trap with $\nu = 0.075$.

Preserving the trap confinement can maintain or even increase collision rates during evaporation, therefore reaching the condition for runaway evaporative cooling. In a harmonic trap, collision rates $\Gamma \propto n\langle v \rangle$, where $n \propto N\bar{\omega}^3 T^{-3/2}$ is the peak atomic density, N is the total particle number, and $\langle v \rangle \propto T^{1/2}$ is the mean relative velocity. Assuming the truncation parameter $\eta = U/k_B T$ is kept constant during the cooling process, we have

$$
\begin{aligned}
\Gamma &\propto N\bar{\omega}^3 T^{-1} \\
&\propto U^{1/\alpha} U^{3\nu} U^{-1} \equiv U^\beta,
\end{aligned}
\tag{3.5}
$$

where $\beta = 1/\alpha + 3\nu - 1$, and $\alpha > 0$ parameterizes the cooling efficiency by removing atoms [86], discussed in later paragraphs. The condition for runaway evaporation is then given by $\beta < 0$. For the trap weakening scheme with $\nu = 1/2$, β is positive for all η. Runaway evaporation is thus impossible. For the tilting scheme with $\nu = 0.075$, the exponent β is negative when $\alpha > 1.08$ ($\eta > 5.4$, shown in later discussion), suggesting runaway evaporation with increasing collision rate is possible.

3.4 Experiment

For this study, cesium atoms are first slowed by a Zeeman slower, collected in a magneto-optical trap (MOT) for 2 s, molasses precooled, and finally cooled and spin polarized by degenerate Raman-sideband cooling (dRSC) [87] to the lowest hyperfine ground state $|3, 3\rangle$. A crossed dipole trap and magnetic field gradient are employed to levitate and collect the cooled atoms. The dipole trap is formed by intersecting two laser beams on the horizontal $(x - y)$ plane; both beams are extracted from a single-mode, single frequency Yb fiber laser operating at the wavelength of 1064 nm, frequency offset by 80 MHz, focused to a $1/e^2$ beam diameter of 540 μm (620 μm) and power of 1.9 W (1.6 W) in the $y-(x-)$ direction. In the absence of trap tilt, the trapping frequencies near
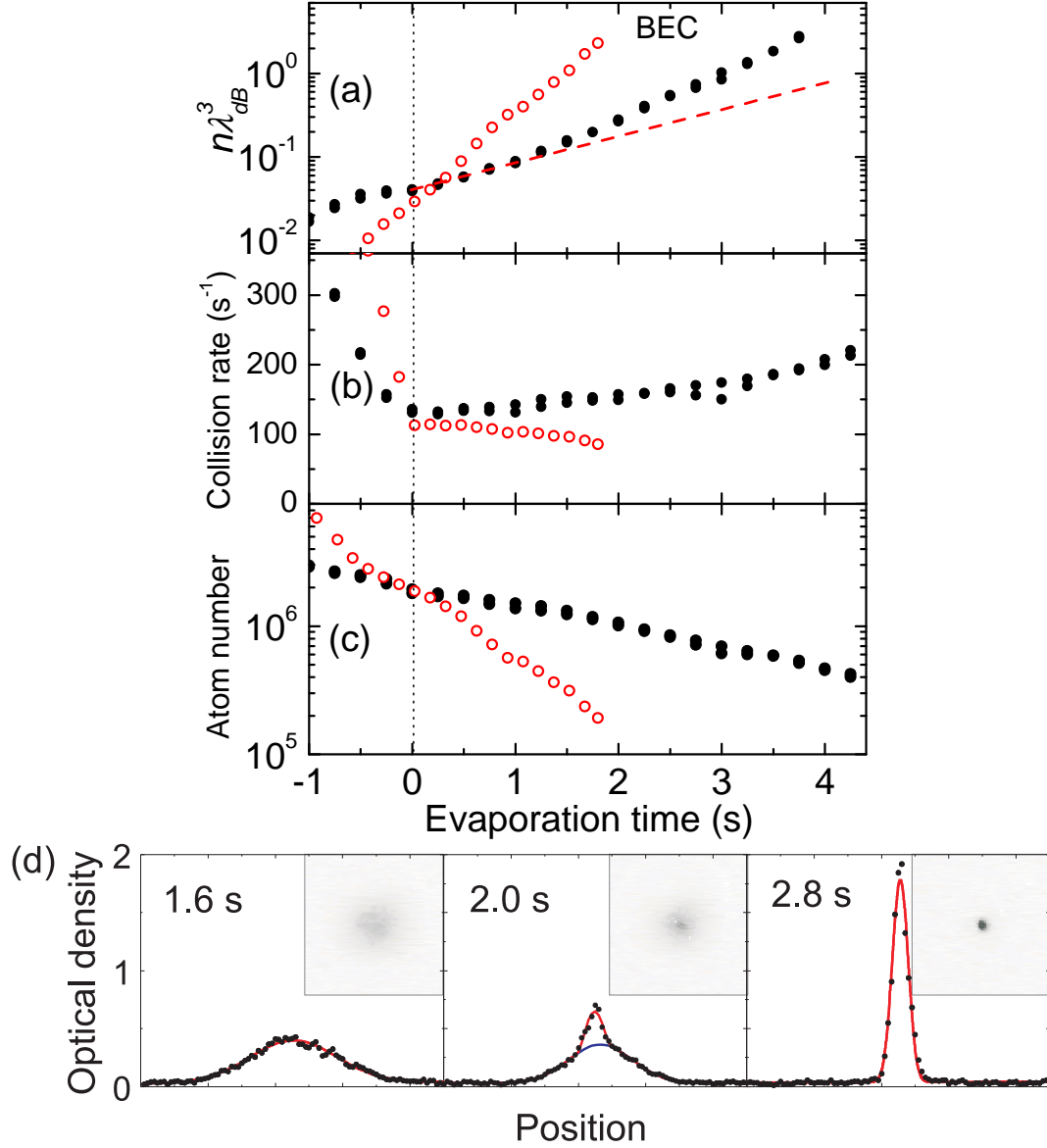
Figure 3.4: Performance of trap-tilting based forced evaporation: (a) phase space density, (b) collision rate, (c) particle number and (d) density profile. Two evaporation paths: 4 s (solid dots) and 1.8 s (open circles) are shown. The dashed line in (a) shows simple exponential increase. In (d), time-of-flight absorbtion images and single-line optical density profiles are taken from the 1.8 s evaporation path. The expansion time is 70 ms, and the field of view is 1.2 mm × 1.2 mm.

the bottom of the potential well are $(\omega_x^0, \omega_y^0, \omega_z^0) = 2\pi \times (17, 34, 38)$ Hz. During the dipole trap loading process, we switch on a uniform magnetic field of 58 G in the (vertical) z-direction to improve the atom number following the loading process (see discussion on magnetic trapping in previous chapter) and apply a levitating magnetic field gradient of $B_c' = mg/\mu$=31.3 G/cm, where mg is the gravitational force, $\mu = 0.75\,\mu_B$ is the magnetic moment of the atoms in $|3, 3\rangle$, and μ_B is the Bohr magneton. After 1 s of thermalization and self-evaporation in the dipole trap, we ramp the magnetic field to 20.8 G, where three-body loss is minimized [88], and the field gradient to 37.8 G/cm in 1.85 s and begin our study on forced evaporation. At this point, which we define as time $t = 0$, there are $N_0 = 1.9 \times 10^6$ atoms in the trap with a temperature of $T_0 = 470$ nK, peak atomic density of $n = 3.8 \times 10^{12}$ cm^{-3}, and peak collision rate of $\Gamma_0 =$133 /s. The background collision rate is below 1/60 s.

We perform forced evaporative cooling by linearly increasing the magnetic field gradient B' from 37.8 to 41.4 G/cm in 2.2 s and then to 43.5 G/cm in another 3 s, which reduces the calculated trap depth from 3.0 μK to 1.0 μK and then to 170 nK. The magnetic field and dipole trap intensity are kept constant throughout the process. To evaluate the cooling performance, we interrupt the evaporation at various times to measure the particle number N, temperature T and trap frequencies $\omega_{x,y,z}$. Particle number and temperature are extracted from absorption images taken at low magnetic fields, following a 70 ms time-of-flight expansion at $B = 17$ G to minimize the collisions and $B' = B_c'$ to levitate the atoms. Trap frequencies are measured from small amplitude oscillations of the atomic momentum by abruptly displacing the trap center. Peak phase space density is calculated from $\phi = n\lambda_{dB}^3$, where $n = N\omega_x\omega_y\omega_z(m\lambda_{dB}/h)^3$, $\lambda_{dB} = h(2\pi m k_B T)^{-1/2}$ is the thermal de Broglie wavelength, k_B is the Boltzmann constant and h is the Planck constant. Collision rates are calculated as $\Gamma = n\langle\sigma v\rangle$, where the elastic collision cross section is $\sigma = 8\pi a^2$, scattering length at 20.8 G is $a = 200\,a_0$ [89], and $\langle v\rangle = (16k_B T/\pi m)^{1/2}$.

After 4 s forced evaporative cooling, we observe Bose-Einstein condensation from the appearance of bimodality and anisotropic expansion in time-of-flight images. At this point, the

temperature is 64 nK and total particle number is 5×10^5. An almost pure condensate with 10^5 atoms was obtained after another 2.5 s. In this evaporation process, the mean truncation parameter is calculated to be $\bar{\eta} = \langle U/k_B T \rangle = 6.5(3)$, and the evaporation efficiency is $\bar{\gamma}_{ev} = -\log(\phi/\phi_0)/\log(N/N_0) = 3.4$. We observe an increasing collision rate and accelerating evaporation, indicating achievement of runaway evaporation; see Fig. 3.4.

An alternative evaporation path is developed to minimize the time to reach BEC. After a shorter magnetic field ramping process of 1 s, we ramp the field gradient from 38.9 G/cm at $t = 0$ to 41.3 G/cm in 0.5 s and then to 43.5 G/cm in another 1.5 s. Here we reach BEC in as short a period as 1.8 s of forced evaporation. Another 1 s evaporation allows us to obtain 4×10^4 atoms in an almost pure condensate, see Fig. 3.4(d). Despite the rapid increase of phase space density, the collision rate actually decreases by 25% at the end of evaporation. The truncation parameter and evaporation efficiency are $\bar{\eta} = 4.6$ and $\bar{\gamma}_{ev} = 1.9$, respectively.

Throughout both evaporation processes, the peak density is moderate, $n < 1.5 \times 10^{13} \text{cm}^{-3}$. The collision loss rate, dominated by three-body recombination process [88], is below $1/40$ s at 20.8 G. Trap loss from collisions is negligible in the following discussion.

3.5 Performance of evaporation in the tilted-trap scheme

To study the performance of evaporation under the tilted scheme, we analyze the phase space density gain during evaporation, using the kinetic theory derived in Ref. [90, 86] and scaling arguments discussed in Ref [91].

We first evaluate the total energy loss rate $\dot{E} = 3\dot{N}k_B T + 3N k_B \dot{T}$ during the evaporation. Assuming no background collisional loss and three-body recombination loss, the atom number

loss rate $\dot{N}$ and the energy loss rate $\dot{E}_{ev}$ due to evaporating hot atoms are

$$\dot{N} = -\lambda N\Gamma \tag{3.6}$$

$$\dot{E}_{ev} = \dot{N}(U + \kappa k_B T), \tag{3.7}$$

where λ is the fraction of collisions producing an evaporated atom, and $\kappa k_B T$ is the excess thermal energy carried by atoms leaving the trap. Both λ and κ depend on the truncation parameter η and the dimensionality of evaporation, and can be calculated using a truncated Boltzmann distribution and the kinetic theory [90]. In the case of atoms allowed to leave a harmonic trap in all directions (3D evaporation),

$$\lambda_{3D} = \frac{1}{\sqrt{2}}\left[\eta\gamma(3,\eta) - 4\gamma(4,\eta)\right]e^{-\eta} \tag{3.8}$$

$$\kappa_{3D} = 1 - \frac{\gamma(5,\eta)}{\eta\gamma(3,\eta) - 4\gamma(4,\eta)}, \tag{3.9}$$

where $\gamma(\alpha,\eta) = \int_0^\eta x^{\alpha-1}e^{-x}dx/\Gamma(\alpha)$ is the lower incomplete gamma function normalized by the gamma function $\Gamma(\alpha)$. For $\eta \gg 1$, $\gamma(\alpha,\eta) \approx 1$, and the above expressions can be simplified to $\lambda_{3D} \approx (\eta-4)e^{-\eta}/\sqrt{2}$ and $\kappa_{3D} \approx (\eta-5)/(\eta-4)$ [91].

There is additional energy change $\dot{E}_{ad}$ due to adiabatic weakening of the trap confinement. Since the potential energy is $E/2 \propto \bar{\omega}^2 \propto U^{2\nu}$, we find $\dot{E}_{ad} = \dot{E}/2 = \nu E\dot{U}/U = \nu E\dot{T}/T$. The total energy loss rate is then

$$\dot{E} = \dot{E}_{ev} + \dot{E}_{ad} = (\eta + \kappa)\dot{N}k_B T + \nu E\frac{\dot{T}}{T}. \tag{3.10}$$

Comparing the above equation to $\dot{E}/E = \dot{N}/N + \dot{T}/T$, we arrive at the rate equation $\dot{T}/T =$

$\alpha \dot{N}/N$, where α is the cooling efficiency

$$\alpha = \frac{d \log T}{d \log N} = \frac{\eta + \kappa - 3}{3 - 3\nu}. \tag{3.11}$$

As previously discussed, the cooling efficiency α forms the condition for runway evaporation $\beta = 1/\alpha + 3\nu - 1 < 0$, which requires α to be larger than 1.08. From Eqs. (3.9) and (3.11), we find $\eta > 5.4$ satisfying the runaway condition.

Time evolution of the phase space density $\phi(t)$ can now be derived based on the scaling $\phi \propto \bar{\omega}^3 N / T^3 \propto N T^{3\nu - 3}$ together with Eqs. (3.5), (3.6), and (3.11). We find

$$\phi(t) = \phi(0)(1 + \lambda \alpha \beta \Gamma_0 t)^{2/\beta - 1}, \tag{3.12}$$

where Γ_0 is the initial collision rate. Here, we see that a negative $\beta < 0$ leads to a faster-than-exponential growth of the phase space density, which eventually diverges at time $t = (-\lambda \alpha \beta \Gamma_0)^{-1}$. We compare the models and our experiment result in Fig. 3.5. To reach the same final phase space density, the trap-tilting scheme would require a much shorter evaporation time than the weakening scheme. For comparison, a potential with fixed trap frequency ($\nu = 0$), e.g., radio-frequency based evaporation in magnetic traps, permits an even stronger runaway effect, see Fig. 3.5.

3.6   Dimensionality of tilted evaporation

Remarkably, the performance of our evaporation is consistent with the 3D evaporation model. The consistency of our evaporation speed with the 3D model is somewhat surprising. In a strongly tilted trap where hot atoms can only escape the trap in the tilted direction (see Fig. 3.6), it is generally expected that the evaporation will exhibit performance consistent with one dimensional evaporation. In momentum space, atoms allowed to evaporate along the direction of tilt, with $p_z^2 \sim 2mU$, spans a small transverse area $2\pi m k_B T$, due to thermal motion in the transverse

68
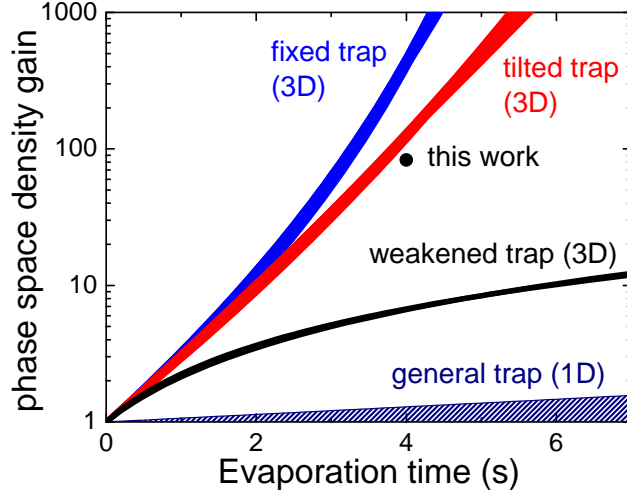
Figure 3.5: Evaporation speed: experiment (4 s path, solid dot) and models. We assume an initial collision rate of Γ_0=133 /s, $\eta = \bar{\eta} = 6.2 \sim 6.8$ and no collision loss. Shaded area covers the 1D evaporation region with $0 \leq \nu \leq 1$ and all possible η.

direction. Compared this area to that of a full evaporating sphere $8\pi mU$, one estimates a reduction in the evaporation rate by a factor of 4η [92, 86] and thus $\lambda_{1D} \approx \lambda_{3D}/4\eta$. Performance of 1D evaporation for all possible η is shown in the shaded area in Fig. 3.5. Our experiment result exhibits evaporation speeds much faster than the any 1D prediction.

We suspect 3D-like evaporation in a tilted trap results from the inseparability of the potential and the existence of a saddle point located at the rim of the potential barrier, which can lead to stochastic single particle motion [92]. When atoms with sufficiently high energy are created by collisions, stochastic motion can allow them to efficiently find escape trajectories. If the energetic atoms have a high probability to escape, regardless of their initial direction of motion, evaporation is effectively three dimensional [92]. In realistic models, stochastization may also be induced by the intensity irregularities of the trapping laser beams.

To further investigate the "dimension of evaporation" in a tilted trap, we come back to $\eta + \kappa$,
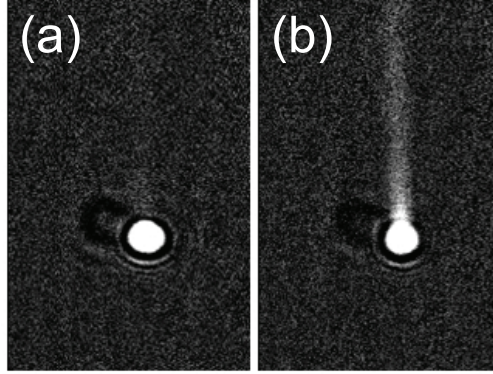
Figure 3.6: Snapshot of in situ atomic distribution during (a) slow and (b) fast evaporation processes. Hot atoms leave the trap in the upward direction due to a strong vertical magnetic force.

which parameterizes the energy removed by evaporating a single atom, or

$$\eta + \kappa = -(k_B T)^{-1} dE/dN. \tag{3.13}$$

For 3D evaporation, we expect $\kappa_{3D} \approx (\eta - 5)/(\eta - 4)$, which is $\kappa_{3D} = 0.6(1)$ for our parameter $\bar{\eta} = 6.5(3)$; for 1D evaporation, energy selectivity applies to the axial, but not the transverse motion, which has a mean energy of $2\,k_B T$ per particle (shown to be $7/4\,k_B T$ with careful calculation in Ref. [93]). Hence, we expect a higher energy removed per particle with $\kappa_{1D} = \kappa_{3D} + 2 = 2.6(1)$ for our parameter [93]. Experimentally, we can test these predictions by evaluating the cooling efficiency α, which has a simple dependence on κ as shown in Eq. 3.11. We show in Fig. 3.7 that our 4 s evaporation data is excellently fit to the power-law function with $\bar{\alpha} = 1.46(2)$. Using Eq. 3.11, we derive $\kappa = 0.6(3)$, which is consistent with the 3D value and confirms the 3D nature of the trap-tilt based evaporation.
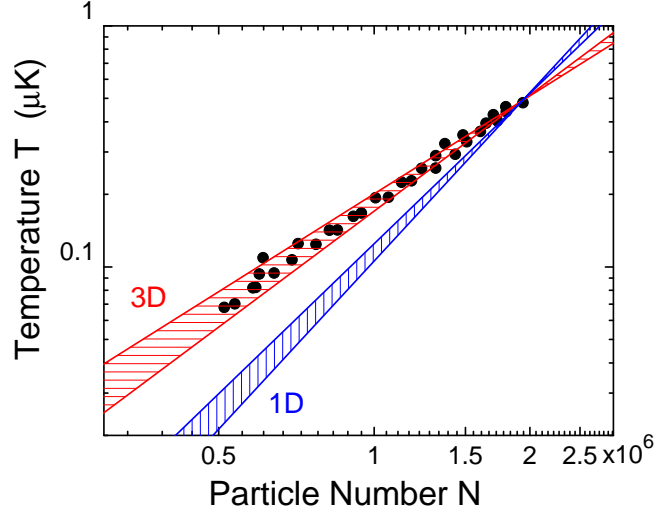
Figure 3.7: Temperature and particle number dependence. Based on the 4 s evaporation data (solid circles), the temperature shows a power-law dependence on particle number $T \propto N^{\alpha}$, with $\alpha = 1.46(2)$. For comparison, predictions from 3D and 1D evaporation models are shown using our experiment initial condition and $\eta = 6.5 \pm 0.3$.

3.7 Fast evaporation to BEC for 2D gas experiments

The current experiment begins with 10^7 atoms loaded into the light sheet plus the $x - y$ crossed dipole traps under a full magnetic levitation balancing gravity (see Section 2.10.1). We implement a fast evaporation procedure since a 2D gas experiment does not need a large atom number BEC. The magnetic field gradient B' is reduced in 1.5 s from 31.1 G/cm to 0.66 G/cm, and to 0 G/cm in another 1.5 s. During the ramp of B', the magnetic field offset B_o is ramped from 48.1 G to 24.6 G in 600 ms to reduce the scattering length to a moderate value of $a = 370\ a_0$ (the collision rate > 150 Hz). The field offset is fixed for 2.4 s, followed by a 200 ms ramp to 20.6 G near an Efimov three-body loss minimum ($a = 198\ a_0$). After the fast evaporation, we have a nearly pure BEC supported by the light sheet against gravity with an atom number of 3×10^4.

CHAPTER 4

MAKING AND PROBING TWO-DIMENSIONAL QUANTUM GASES

After producing a pure 3D condensate, we are now in a position to advance to the 2D world. In this chapter, I will first introduce the background of 2D physics, followed by a general discussion on the experimental scheme. I will then discuss more technical details on the setup of the 2D optical trap and the loading procedures. Finally, a detailed discussion of *in situ* absorption imaging will be given.

4.1   Theory: properties of 2D Bose gases

4.1.1   Properties of 2D thermal gases

The properties of 2D thermal gases are well understood and, therefore, form the *standard candle* of our experiment. They can be used to calibrate experimental parameters or perform thermometry when they are in full thermal equilibrium with other regions inside the gas. The first well known property is the equation of state of an ideal 2D thermal gas. It can be easily derived from the Bose distribution function [5]

$$
\begin{aligned}
n_{th}(\mu, T) &= \int \frac{d^2 p}{(2\pi\hbar)^2} \frac{1}{\exp[\beta(p^2/2m - \mu)] - 1} \\
&= -\lambda_{dB}^{-2} \ln(1 - e^{\beta\mu}).
\end{aligned}
\tag{4.1}
$$

where $\lambda_{dB} = h/\sqrt{2\pi m k_B T}$ is the thermal de Broglie wavelength and $\mu < 0$ is the chemical potential. When a weak external trapping potential $V_{\text{ex}}(\mathbf{r})$ is present, according to the local density approximation, one might replace μ with a local chemical potential $\mu(\mathbf{r}) = \mu_0 - V_{\text{ex}}(\mathbf{r})$, where μ_0 is the global chemical potential of the sample. For interacting 2D thermal gases, a mean field

potential can be added into Eq. (4.1), forming a self-consistent mean field equation

$$n_{mf}(\mu, T) = -\lambda_{dB}^{-2} \ln\left[1 - e^{\beta(\mu - 2gn_{mf})}\right],$$ (4.2)

where g is the effective 2D interaction strength, to be discussed later. Equations (4.1-4.2) provide a method for thermometry to determine the global chemical potential μ_0 and temperature T from the thermal tail density distribution in a trapped 2D gas.

Other well known behaviors of thermal gases are their coherence properties, derived in Ref. [94] for 3D thermal gases and extended here for the 2D case. The first-order correlation function between two points $\mathbf{r}$ and $\mathbf{r}'$, defined as $G^{(1)}(\mathbf{r}, \mathbf{r}') = \langle \hat{\Psi}^\dagger(\mathbf{r})\hat{\Psi}(\mathbf{r}') \rangle$ with $\hat{\Psi}$ the Bose field operator and $\langle . \rangle$ the ensemble average, can be calculated using the Fourier transform of the Wigner function $W(p, q) = \frac{1}{(2\pi\hbar)^2} \frac{1}{\exp^{\beta[p^2/2m - \mu(q)]} - 1}$ under the local density approximation as

$$
\begin{aligned}
G^{(1)}(\mathbf{r}, \mathbf{r}') &= \int d^2p\, e^{-i\mathbf{p}\cdot(\mathbf{r}-\mathbf{r}')/\hbar} W(\mathbf{p}, \frac{\mathbf{r}+\mathbf{r}'}{2}) \\
&= \lambda_{dB}^{-2} g_1(e^{\beta\mu}, e^{-\pi(\mathbf{r}-\mathbf{r}')^2/\lambda_{dB}^2}),
\end{aligned}
$$ (4.3)

where $g_\gamma(x, y) = \sum_{k=1}^{\infty} x^k y^{1/k}/k^\gamma$ is the generalized Bose function and μ is the local chemical potential. The first-order correlation function reveals the phase coherence across a thermal gas, which decays exponentially at the thermal length scale of λ_{dB}. When $\mathbf{r} = \mathbf{r}'$, Eq. (4.3) gives the mean density $\bar{n} = G^{(1)}(\mathbf{r}, \mathbf{r}) = \lambda_{dB}^{-2} g_1(e^{\beta\mu}, 1) = -\lambda_{dB}^{-2} \ln(1 - e^{\beta\mu})$.

The second-order correlation function, defined as $G^{(2)}(\mathbf{r}, \mathbf{r}') = \langle \hat{\Psi}^\dagger(\mathbf{r})\hat{\Psi}^\dagger(\mathbf{r}')\hat{\Psi}(\mathbf{r})\hat{\Psi}(\mathbf{r}') \rangle$, is related to the behavior of density fluctuations and density-density correlations (see Chapter 8 and Eq. (8.1)). It can be evaluated based on $G^{(1)}(\mathbf{r}, \mathbf{r}')$ [94],

$$
\begin{aligned}
G^{(2)}(\mathbf{r}, \mathbf{r}') &= G^{(1)}(\mathbf{r}, \mathbf{r})G^{(1)}(\mathbf{r}', \mathbf{r}') + |G^{(1)}(\mathbf{r}, \mathbf{r}')|^2 \\
&= \bar{n}^2 + \lambda_{dB}^{-4}|g_1(e^{\beta\mu}, e^{-\pi(\mathbf{r}-\mathbf{r}')^2/\lambda_{dB}^2})|^2.
\end{aligned}
$$ (4.4)

From the second-order correlation function, we obtain the density-density correlation of a 2D thermal gas

$$\langle \delta n(\mathbf{r})\delta n(\mathbf{r}')\rangle \;=\; \bar{n}\delta(\mathbf{r}-\mathbf{r}') + \lambda_{dB}^{-4}|g_1(e^{\beta\mu}, e^{-\pi(\mathbf{r}-\mathbf{r}')^2/\lambda_{dB}^2})|^2, \tag{4.5}$$

where $\delta n(\mathbf{r}) = n(\mathbf{r}) - \bar{n}$ is the local density fluctuation around the mean value $\bar{n}$ and $\delta(\mathbf{r})$ is the delta function in two dimensions. Clearly, the first term in Eq. (4.5) is the auto-correlation of atoms, while the second term reveals the behavior of bosonic bunching. When $\mathbf{r} = \mathbf{r}'$, the bunching term is equal to $\bar{n}^2$, as expected [95]. Equation (4.5) is important to understand density fluctuations and their correlations in a 2D thermal gas as well as to calibrate *in situ* absorption imaging; see later discussions.

4.1.2 *Effective two-body interaction strength*

For dilute, ultracold gases in three dimensions, the two-body s-wave scattering potential can be approximated by a contact potential

$$V_{sc} = g_0\delta^3(\mathbf{r}), \tag{4.6}$$

where $\delta^3(\mathbf{r})$ is the delta function in three dimensions. The coupling constant g_0 depends on the scattering length a as

$$g_0 = \frac{4\pi\hbar^2 a}{m}, \tag{4.7}$$

which is obtained by solving the *scattering amplitude* $f(k) \to a$ in the limit of zero scattering momentum $k \to 0$ [5]. This approximation is generally satisfied for $ka \ll 1$.

For a 2D quantum gas, which is vertically confined to the ground state of a harmonic oscillator $\phi_z(z) = \frac{1}{\sqrt[4]{\pi l_z^2}}e^{-z^2/2l_z^2}$ with a harmonic oscillator length l_z satisfying $l_z \gg a$, one would expect the two-body scattering physics to still follow that of a 3D case. The 2D interacting potential should remain contact-like with an effective 2D coupling strength g calculated by simply integrating out

74

the wave function in the vertical direction

$$g = g_0 \int dz |\phi_z(z)|^4 = \frac{\sqrt{8\pi}\hbar^2 a}{ml_z}. \tag{4.8}$$

Equation (4.8) and the assumption of 3D scattering characteristics, however, is an approximation which needs closer inspection. In fact, by carefully matching the scattering boundary conditions [96, 97], the scattering amplitude is found to depend on the momentum q in the 2D plane as

$$f(q) = \frac{a/l_z}{\sqrt{2\pi} + a/l_z[\ln(C/\pi q^2 l_z^2) + i\pi]}, \tag{4.9}$$

where $C \approx 0.915$ is a constant [97]. Therefore, omitting the complex term, the 2D coupling strength g is modified as

$$g(\epsilon) = \frac{4\pi\hbar^2 f(\epsilon)}{m} = \frac{\sqrt{8\pi}\hbar^2 a}{ml_z} \frac{1}{1 + a/\sqrt{2\pi}l_z \ln(2mC\epsilon/\pi\hbar^2 l_z^2)}, \tag{4.10}$$

where $\epsilon = \hbar^2 q^2/2m$ may be replaced by the chemical potential μ in the superfluid phase [96], or the thermal energy $k_B T$ in the normal gas regime. The logarithmic term in the denominator of Eq. (4.10) can only cause a significant modification in g when ϵ becomes extremely small. Nevertheless, for typical experiment parameters of $l_z = 200$ nm and $a < 200\,a_0 = 10$ nm, the correction is $< 2\%$ even at a very small energy scale of $k_B \times 5$ nK. Thus, Eq. (4.8) is a very good approximation for weakly interacting gases and it will be used to derive the coupling constant g in the following studies. We will, however, be cautious when advancing toward the study of strongly interacting gases and use Eq. (4.10) to evaluate their effective coupling strength.

4.1.3 Berezinskii-Kosterlitz-Thouless (BKT) superfluid transition in two dimensions

Two-dimensional Bose gases are among the textbook examples exhibiting intriguing thermodynamic properties different from 3D Bose gases. For example, an ideal 2D gas cannot form a BEC. This can be observed from Eq. (4.1), as when μ approaches zero, n_{th} diverges logarithmically, implying that there will be no accumulation of ground state atoms. The exceptions are trapped ideal 2D gases where the modified density of states can remove such a divergence in the excited state population [98]. For example, the number of excited state atoms inside a harmonic trapping potential saturates at a critical temperature $T_{BEC} = \sqrt{6N}\hbar\bar{\omega}/\pi$, allowing a macroscopic ground state population at temperature $T < T_{BEC}$. Here, N is the total particle number and $\bar{\omega}$ is the mean trap frequency.

For interacting, homogeneous 2D gases, it was rigorously proved by Hohenberg [99] that a symmetry breaking phase $\langle \phi \rangle \neq 0$ is prohibited at low dimensions (meaning $D < 3$). Thermal fluctuations at finite temperature can destroy true long range order. The formation of a BEC is two dimensions is then forbidden. For trapped interacting samples, we expect that finite repulsive interactions at the mean-field level can smear out the trap effect and a true condensate is similarly prohibited [100].

Despite the absence of true long range order, an interacting 2D gas can nevertheless acquire superfluidity. It was pointed by Kosterlitz and Thouless in Ref.[17] that a continuous phase transition (BKT-transition) from normal gas to superfluid with quasi-long-range order can occur at a low critical temperature T_{BKT}. Unlike the BEC transition, the BKT-transition does not involve symmetry breaking. The onset of superfluidity is entirely due to thermodynamic suppression of topological defects, which are the lowest energy excitations that destabilize any form of long range order. Low energy topological defects in 2D Bose gases are vortices, whose energies are $E = \frac{\hbar^2 \pi n_s}{m} \ln(R/\xi)$. Here, n_s is the superfluid density, R is the size of the system, and ξ is the healing length.

To develop a heuristic picture of why the BKT transtion occurs, let us consider minimizing the free energy inside a 2D superfluid. The entropy of a vortex is $S = k_B \ln(R^2/\xi^2)$. Therefore, the free energy associated with a single vortex is

$$F = E - TS = \left(\frac{\pi \hbar^2 n_s}{m} - 2k_B T \right) \ln(R/\xi), \tag{4.11}$$

which can change sign if the ratio between n_s/T crosses a critical value. In view of minimizing the free energy, Eq. (4.11) suggests a critical temperature

$$T_{BKT} = \frac{\hbar^2 \pi n_s}{2k_B m}. \tag{4.12}$$

For temperature $T > T_{BKT}$, the vortex free energy is negative, $F < 0$, suggesting that vortex defects are thermodynamically favorable and an unbounded number of vortices eventually renders zero superfluid density; for low temperature $T < T_{BKT}$, $F > 0$ and a larger superfluid density becomes more stable against free vortices. The simple free energy argument [17] predicts a superfluid jump $n_s \lambda_{dB}^2 = 4$ at the critical temperature, in agreement with the calculation in Ref. [101]. Below the critical temperature T_{BKT}, vortices and anti-vortices (with opposite circulation) form metastable bound pairs [17], supporting a superfluid with a quasi-long range order. The first-order correlation is of a form with slow algebraic decay $g^{(1)}(r) \propto (\xi/r)^\eta$. Here, the exponent $\eta = 1/n_s \lambda_{dB}^2$ is the inverse of superfluid density.

4.1.4 *Critical point and critical behavior near the BKT transition*

In the above paragraphs, we have discussed the origin of the BKT transition, and the relation between the critical temperature and the critical superfluid density. A quantitative calculation of the total critical density, or the phase boundary, and the critical behavior of a BKT transition requires additional theoretical treatment.

Arguments given in Ref. [102, 103] estimated the critical density to follow the form

$$n_c \lambda_{dB}^{-2} = \ln \frac{\xi \epsilon_T}{\epsilon_*} = \ln \frac{\xi \hbar^2}{mg}, \tag{4.13}$$

where ξ is a universal constant. Equation (4.13) is obtained through reevaluating the Bose distribution function in Eq. (4.1), and assuming that at the critical point the dominant excited state populations are within the energy range $\epsilon_T \gtrsim \epsilon \gtrsim \epsilon_*$. Here, $\epsilon_T \sim k_B T$ is the energy of thermal atoms and $\epsilon_* \sim \frac{m k_B T g}{\hbar^2}$ is roughly the energy when excited states become strongly coupled [103]. Similar argument would render the critical chemical potential

$$\frac{\mu_c}{k_B T} = \frac{g}{\pi} \ln \frac{\xi_\mu \hbar^2}{mg}, \tag{4.14}$$

where ξ_μ is a universal constant. There is currently no analytic theory that can determine the exact values of ξ and ξ_μ. A Monte Carlo calculation, assuming a classical field describing the universal (long wave) behavior near the BKT transition, determines the constants to be $\xi = 380 \pm 3$ and $\xi_\mu = 13.2 \pm 0.4$ [103].

4.1.5   Classical $|\psi|^4$-field model and universality in weakly interacting Bose gases

For weakly interacting Bose gases, an effective classical $|\psi|^4$-field theory is used to calculate thermodynamics near the phase transition [104, 105, 103, 106]. The Hamiltonian of the classical field is

$$\mathcal{H} = \int d^D x \frac{\hbar^2}{2m} |\nabla \psi_0|^2 - \mu' |\psi_0|^2 + \frac{U_0}{2} |\psi_0|^4, \tag{4.15}$$

where D is the dimensionality, ψ_0 is a two-component $O(2)$ classical field, μ' is a renormalized chemical potential after removing a model-dependent ultraviolet cutoff [103, 106], and U_0 is a

coupling constant; $U_0 = g$ in two dimensions. The classical field theory is similar to the Ginzburg-Landau free energy formalism which captures physics of an emerging order parameter as well as its critical fluctuations and spatial correlations. The field theory has been studied in both three and two dimensions to evaluate BEC and BKT critical points of weakly interacting Bose gases [104, 105, 103, 106].

Due to its marginal dimensionality, a weakly interacting 2D Bose gas is predicted to exhibit extended critical fluctuation region [107]. The classical field model Eq. (4.15) was also used to calculate the universal relations of density observables in the critical region [103, 107, 106]. The universal functions, tabulated by the classical field Monte Carlo calculations [107], were recently verified using *ab initio* quantum Monte Carlo calculations [108, 109]. Before this thesis work, there has been no direct experimental demonstration (using cold atoms) of the universal behaviors, as well as the phase boundary of the BKT transition at various coupling constants g. In Chapter 7, we will show the first experimental verification of the critical universality of the BKT transition and a close comparison with the classical field description as well as the quantum Monte Carlo calculations.

4.2 Theory: 2D Bose gas in 2D optical lattice

4.2.1 Single particle Bloch wavefunctions and band structure

Without the external potential, the eigenfunction of a free particle is simply a plane wave $\phi_{free}(x) = e^{ipx/\hbar}$, where p is the free space momentum. Inside a periodic potential $V(x) = V(x + d)$, the simple plane wave solution will be modified according to Bloch's theorem [110]. The new eigenfunction has the form $\phi_q(x) = e^{iqx}u_q(x)$, where $u_q(x + d) = u_q(x)$ has the same periodicity of the external potential. q is called the quasi-momentum analogous to the free space momentum, but is now limited to a finite interval due to the presence of the external potential which makes the translational invariant symmetry discrete. $q \in [-\pi/d, \pi/d]$ in the 1D case, and the function

79

$u_q^{(n)}(x)$ acquires series of solutions at different energy bands labeled by the quantum number n. Inserting this ansatz wavefunction into the Schrödinger equation, we find

$$\frac{(\hat{p} + \hbar q)^2}{2m} u_q^{(n)}(x) + V(x) u_q^{(n)}(x) = E_q^{(n)} u_q^{(n)}(x) \tag{4.16}$$

is the differential equation for the wavefunction at the n-th energy band with quasi-momentum q. For lattice structures in higher dimensions, more discrete symmetries can be found, leading to rich band structure with the quasi-momentum confined to multiple regions, called the Brilloiun zones. For the 2D square lattice explored in this thesis, we only discuss physics in the first Brilloiun zone.

For a 1D optical lattice potential $V(x) = V_0 \sin^2 kx$, the Schrödinger equation

$$-\frac{\hbar^2}{2m} \nabla^2 \phi_q^{(n)}(x) + V_0 \sin^2 kx \phi_q^{(n)}(x) = E_q^{(n)} \phi_q^{(n)}(x) \tag{4.17}$$

can be written in the form of Mathieu's differential equation, $d^2 y / dx^2 + (a - 2s \cos 2x) y = 0$, as

$$\frac{\partial^2 y}{\partial x^2} + \left(\frac{E_q^{(n)}}{E_R} - \frac{V_0}{2E_R} + \frac{V_0}{2E_R} \cos 2x \right) y = 0, \tag{4.18}$$

where $E_R = \hbar^2 k^2 / 2m$ is the recoil energy. At a given lattice depth $s = -\frac{V_0}{4E_R}$, periodic solutions of $y(x)$ can be found only at certain characteristic values of $a = \frac{E_q^{(n)}}{E_R} - \frac{V_0}{2E_R}$, giving the band structure $E_q^{(n)} / E_R = a - 2s$. The periodic solutions to Mathieu's equation have been tabulated as the Mathieu sine $Se(a, s, x)$ and Mathieu cosine $Ce(a, s, x)$ functions according to their odd and even parities.[1] The Bloch wavefuction $\phi_q^{(n)}(x)$ is the linear combination of the Mathieu sine and cosine functions. According to Bloch's theorem (mathematically being Floquet's theorem),

---

1. We are adopting here the definition from Ref. [111]
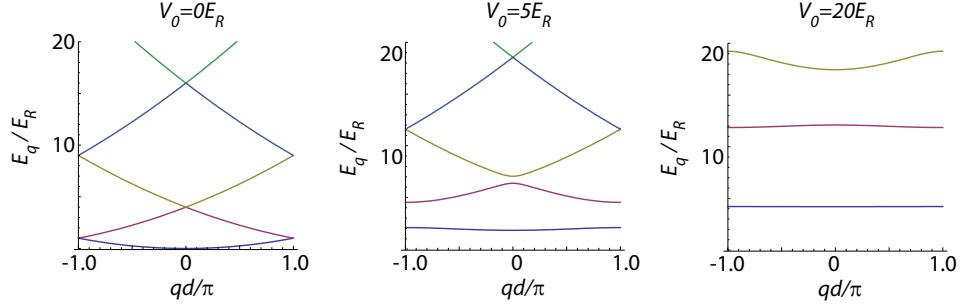
Figure 4.1: Band structure $E_q^{(n)}$ in 1D lattice potentials with various lattice depths V_0.

$\phi_q^{(n)}(x)$ is written in the Floquet form

$$\phi_q^{(n)}(x) = e^{i\nu kx}u_\nu(kx) = Ce(a,s,kx) \pm iSe(a,s,kx), \tag{4.19}$$

where the characteristic exponent $\nu = q \pm (-1)^n \pi [n + (n \bmod 2)]$ is related to the quasi-momentum q and band quantum number n, and the plus-minus sign follows the sign of q. Given the exponent $\nu(q,n)$ and the lattice depth $V_0/E_R = -4s$, the characteristic parameter $a(\nu,s)$, the band structure $E_q^{(n)}/E_R = a - 2s$ (see Fig. 4.1), and the Bloch wave functions (see Fig. 4.2) can be fully evaluated using Eq. (4.19) and the tabulated Mathieu's functions as well as characteristic parameters in *Mathematica*; see Appendix C.

4.2.2   The Wannier state basis

Just like the particle-wave dual description in free space, atomic states inside a periodic lattice potential can also be expanded by a set of localized wavefunctions. A Wannier state is the Fourier transform of the Bloch waves, which is analogous to the point-like Dirac delta function in free space but has finite spread and an oscillatory tail within a few sites. Assuming no relevant energy

81
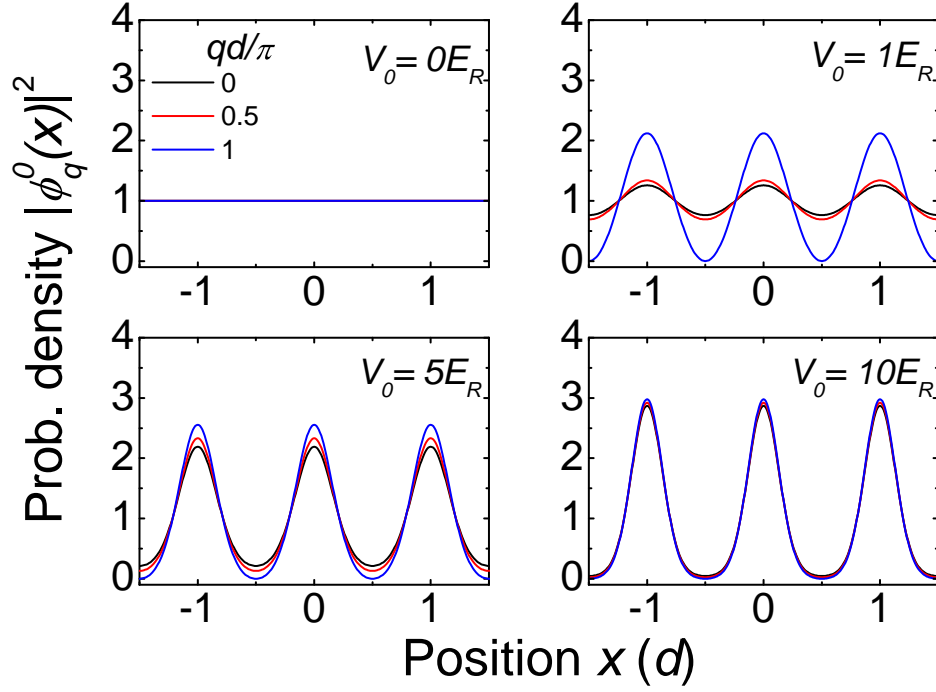
Figure 4.2: Probability density of the ground band Bloch waves at various lattice depths V_0.

scales exceed the lattice band gap, the atomic motion is restricted to the ground band and the Wannier state is written as[2]

$$
\begin{aligned}
w(x - x_i) &= \frac{1}{L} \sum_q e^{-iqx_i} \phi_q^{(0)}(x) = \frac{1}{L} \sum_q e^{iq(x - x_i)} u_q^{(0)}(x) \\
&= \frac{1}{L} \int_{-\pi/d}^{\pi/d} dq \left[\cos(qx_i) Ce(q, kx) + \sin(qx_i) Se(q, kx) \right] \quad (4.20)
\end{aligned}
$$

where x_i is the central position of the i-th lattice site, L is a normalizing constant, and the summation goes over the first Brillouin zone. It can also be seen from Eq. (4.20) that the Wannier states at different sites are orthogonal and form a convenient basis to expand localized wave functions. Fig. 4.3 shows sample Wannier functions. Here we see that for sufficiently deep lattices, the Wannier wave function already behaves like a Gaussian wave function in the limit of a single

---

2. From here forward, we omit the band quantum number $n = 0$ in the superscript.
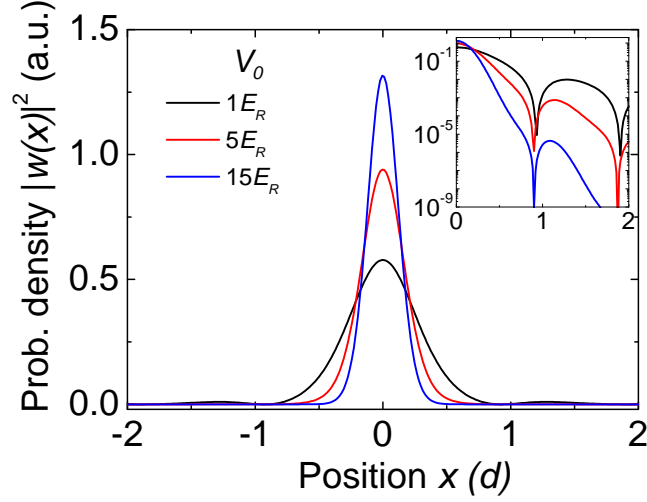
Figure 4.3: Probability density of the ground band Wannier states at various lattice depths V_0. Inset shows oscillatory tails in the logarithmic scale.

harmonic potential. Nevertheless, quantum tunneling to neighboring sites is still allowed, which is manifested in the tail distribution of the Wannier state, a feature strongly suppressed in a Gaussian distribution.

4.2.3 Tight-binding model

In deep lattices, we can expand the single particle wave function using the Wannier basis $\psi(x) = \sum_i c_i w(x - x_i)$. This would change the Shrödinger equation to a discretized form [112] $-i\hbar\dot{c}_i = -\sum_l t_l(c_{i-l} + c_{i+l}) + \epsilon_0 c_i$, where t_l is the off-diagonal tunnel coupling to the l-th nearest neighboring sites

$$t_l = \int dx w(x + ld)\hat{H}_0 w(x), \tag{4.21}$$

and $\epsilon_0 = \int dx w(x)\hat{H}_0 w(x)$ is the diagonal on-site energy shift. Here, $\hat{H}_0 = \frac{\hbar^2 \hat{p}^2}{2m} + V(x)$ is the single-particle Hamiltonian. It can be shown [112], by expanding Eq. (4.21) and assuming a periodic boundary condition, that $E_q = -2\sum_l t_l \cos lqd$. Keeping only the nearest neighbor
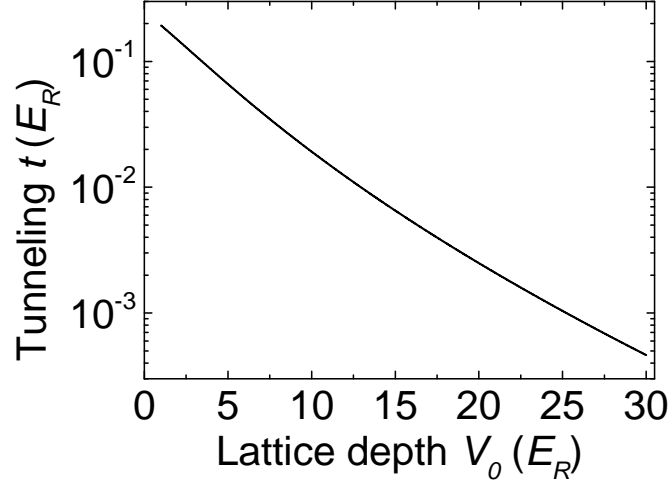
Figure 4.4: Tunneling t as a function of lattice depth V_0 calculated using Eq. (4.23) in the tight-binding regime.

tunnel coupling $t = t_1$, we have

$$E_q = -2t \cos qd, \tag{4.22}$$

since $t \gg t_l \ \forall l > 1$ in a deep lattice. Conversely, the tunneling t can be determined using

$$t = (E_{q=\pi/d} - E_{q=0})/4, \tag{4.23}$$

where the ground bandwidth can be directly calculated from the Mathieu characteristic parameter a. In Fig. 4.4, we plot the tunneling t evaluated using Eq. (4.23).

4.2.4 *Interacting atoms inside a 2D optical lattice and mapping to a 2D Bose-Hubbard Hamiltonian*

In the previous sections, we discussed non-interacting atoms in a 1D homogeneous lattice potential. Generalization to higher dimensions is straightforward since the lattice potential is separable and we only consider the first Brillouin zone. Furthermore, adding the two-body interaction maps the system into the Bose-Hubbard model. Below we consider the full Hamiltonian including the two-body interaction and an external trapping potential in the framework of the grand canonical ensemble.

The full Hamiltonian of a trapped, interacting 2D quantum gas inside a 2D lattice potential is [10]

$$\hat{H} = \int d^2x \hat{\Phi}^\dagger(\mathbf{x}) \left[\hat{H}_0 + V_{\text{ex}}(\mathbf{x}) - \mu \right] \hat{\Phi}(\mathbf{x}) + \frac{g}{2} \int d^2x \hat{\Phi}^\dagger(\mathbf{x}) \hat{\Phi}^\dagger(\mathbf{x}) \hat{\Phi}(\mathbf{x}) \hat{\Phi}(\mathbf{x}), \qquad (4.24)$$

where $\hat{\Phi}(\mathbf{x})$ is the Bose field operator, $\hat{H}_0 = -\frac{\hbar^2 \nabla^2}{2m} + V_0(\sin^2 kx + \sin^2 ky)$ is the single particle Hamiltonian, $V_{\text{ex}}(\mathbf{x})$ is the external trapping potential, μ is the chemical potential, and $g = \sqrt{8\pi}\hbar^2 a/ml_z$ is the 2D coupling strength.[3]

In the tight-binding regime, we can similarly use the 2D Wannier states to expand the Bose field $\hat{\Phi}(\mathbf{x}) = \sum_i \hat{a}_i w(x - x_i)w(y - y_i)$, where $\hat{a}_i$ is the particle annihilation operator at the i-th site with position (x_i, y_i). Expanding Eq. (4.24), we obtain the 2D Bose-Hubbard Hamiltonian [9]

$$\hat{H} = -t \sum_{\langle i,j \rangle} \hat{a}_i^\dagger \hat{a}_j + \frac{U}{2} \sum_i \hat{n}_i(\hat{n}_i - 1) - \sum_i \mu_i \hat{n}_i, \qquad (4.25)$$

where $\langle i, j \rangle$ denotes summation over the nearest neighboring sites (coordination number $z = 4$), $n_i = \hat{a}_i^\dagger \hat{a}_i$ is the on-site number operator, and $\mu_i = \mu - V_{\text{ex}}(\mathbf{x}_i)$ is the local chemical potential.

---

3. Here, we have assumed that the scattering length a is much smaller than the harmonic oscillator strength in all three directions such that Eq. (4.8) still applies.
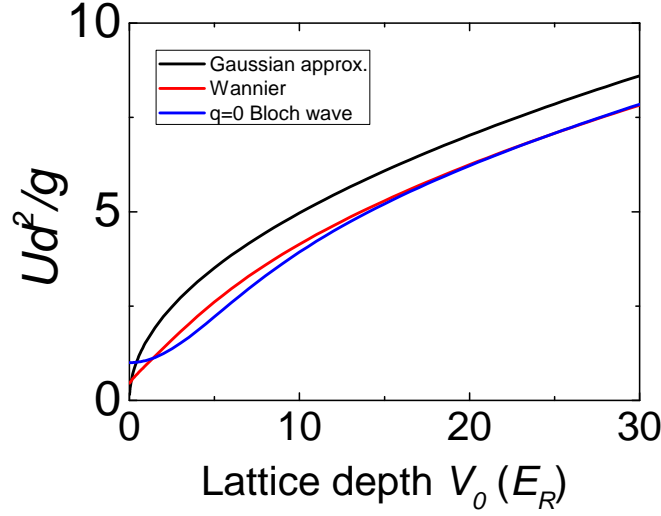
Figure 4.5: On-site interaction U evaluated using the Wannier wavefunction (red line), the ground state of a harmonic oscillator (black line), and the zero quasi-momentum Bloch wave (blue line).

Here, the local density approximation applies in a weak trapping potential $|\nabla V_{\text{ex}}| \ll U/d, t/d$. The tunneling t is similarly given by the band dispersion relation in Eq. (4.22). The on-site interaction U is calculated as

$$U = g \int dx dy |w(x)|^4 |w(y)|^4 = g \left[\int dx |w(x)|^4 \right]^2 . \tag{4.26}$$

Figure 4.5 shows the on-site interaction evaluated at various lattice depths V_0. An increased $U > g/d^2$ is due to the increased on-site density.[4]

Obtaining Eq. (4.25), we see that the many-body Hamiltonian of a weakly trapped interacting superfluid loaded into a 2D optical lattice can be mapped onto a 2D Bose-Hubbard model with various local chemical potentials. The ratio between tunneling t and interaction energy U can be

---

4. Comparing U evaluated using Eq. (4.26) to those calculated by replacing $w(x)$ with the ground state of a harmonic oscillator assuming $V_{\text{ex}} = V_0 k^2 (x^2 + y^2)$, we find that even in deep lattices, the approximation yields a value $\sim 0.8 g/d^2$ larger than the Wannier calculations even in very deep lattice depths. We also calculate U by replacing $w(x)$ with the zero quasi-momentum Bloch wave, and carry out the integration within a unit cell. The Bloch wave calculation shows the correct limit of $Ud^2/g \to 1$ at shallow lattice depths.

widely adjusted by varying the lattice depth V_0 (see Fig. 4.4 and 4.5) or the 2D coupling strength g, ideal for exploring the Bose-Hubbard many-body phase diagram.

4.2.5 *The superfluid-to-Mott insulator quantum phase transition in the Bose-Hubbard model*

At zero temperature, a homogeneous 2D Bose-Hubbard Hamiltonian predicts two types of many-body ground states in regimes dominated by the tunneling t and on-site interaction energy U, respectively. In the kinetic energy dominated regime $t \gg U$, when hopping between sites is energetically favorable, atoms form a delocalized superfluid (SF) state exhibiting long range phase coherence. In the interaction energy dominated regime $U \gg t$, when hopping is suppressed due to increased on-site interaction, atoms form a localized Mott-insulator (MI) state with an integer site occupancy.

While it is possible to adjust the ratio of t/U to drive the SF-MI quantum phase transition, Mott insulator states can only form at commensurate bosonic densities. Departing from these densities, a small number of excess particles or holes gain the freedom to tunnel between sites, recovering a phase coherent superfluid state. Therefore, at sufficiently small t/U, a SF-MI transition can alternatively be driven by the competition between on-site interaction U and the coupling μ to the particle reservoir, i.e. the chemical potential.

The complete SF-MI phase boundary of the Bose-Hubbard model is formed by critical values of $(t/U)_c$ and $(\mu/U)_c$ in the $\frac{t}{U} - \frac{\mu}{U}$ parameter space, as illustrated in Figure 4.6. Adjusting the couplings t/U or μ/U across the phase boundary, quantum fluctuations at zero temperature drive the quantum phase transition from the superfluid to the Mott insulator phase, or vise versa. The location of the phase boundaries can be estimated using a mean-field calculation [9], and more accurate values can be calculated using strong coupling expansions [113, 114], as well as quantum Monte Carlo methods [115].
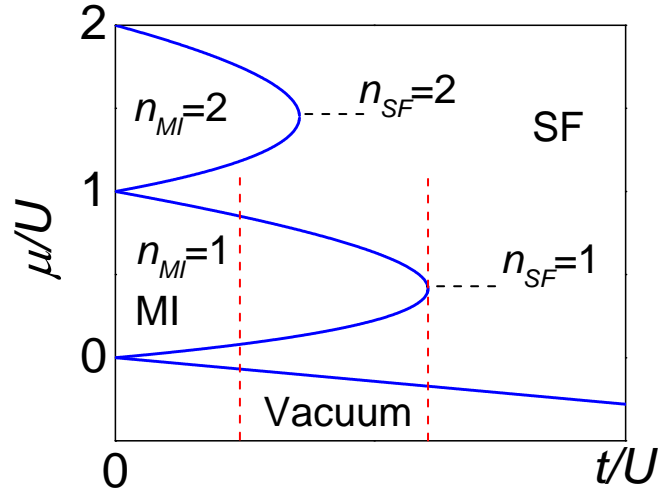
Figure 4.6: Illustrations of the zero-temperature 2D Bose-Hubbard model phase diagram in the μ/U-t/U plane. Here, MI denotes the Mott insulator state, SF denotes the superfluid state, and vacuum denotes the state with no atoms occupying lattice sites. The horizontal dashed lines indicate the commensurate fillings in the superfluid region $n_{SF} = 1, 2$. Local phases in a trapped gas map out the phase diagram vertically (with fixed t/U), as illustrated by the vertical dashed lines. One of the dashed line crosses the tip of a boundary lobe, where a multi-critical point of SF-MI transition resides. The phase boundary is generated using a mean field calculation $\mu/U = n_{MI} - 1/2 - Dt/U \pm \sqrt{(Dt/U)^2 + (2n_{MI} + 1)Dt/U + 1/4}$ [9, 113], where n_{MI} is the site occupancy and $D = 2$ is the dimensionality.

4.2.6 Critical universality class and critical behavior of the SF-MI quantum phase transition

One interesting aspect of the SF-MI transition is its critical behavior. The lobe-like structure of the Bose-Hubbard phase boundary reflects the fact that there are two types of critical behaviors that can occur in this model. One is the generic SF-MI transition driven by adjusting the chemical potential μ at a constant value of t/U, crossing the upper or lower side of the boundary lobe. This type of transition belongs to the dilute Bose gas universality class, which can be described by the classical $O(2)$ XY model in two dimensions [9]. To understand this mapping, consider the behavior of particle (hole) excitations near the upper (lower) side of the lobe. When the chemical potential is adjusted to approach the critical point, the many-body gap $\Delta \propto (\mu - \mu_c)^{z\nu}$ to create particle (hole) excitations vanishes and the excitations can Bose-condense, forming a superfluid. Here, z is the dynamic critical exponent, and ν is the correlation length exponent. The critical scaling behavior therefore follows that of a dilute Bose gas, with $z = 2$ and $\nu = 1/2$ [9]. In fact, the effective field theory describing the critical behavior of particle (hole) excitations in this generic phase transition is identical to that of a superfluid BKT transition in 2D [49, 9]. It may be compared with measurements of a 2D gas without the lattice potential, with an additional renormalization on the dynamics (non-zero Matsubara frequency modes) [116, 106] that has been dropped in deriving the classical field Eq. (4.15) for weakly interacting Bose gases [104].

The second type of transition occurs at the tip of the lobe, where the upper and the lower phase boundaries meet. The transition happens at a commensurate density. It is a multi-critical point where the particle and hole excitations become energetically degenerate [9]. The particle-hole degeneracy creates a space-time symmetry in the effective field theory describing the critical behavior [49, 9], mapping the transition to the universality class of the $O(2)$ quantum rotor model in two dimensions [49] or the $O(2)$ classical XY model in 2+1 dimensions [49, 9]. The critical point can be traversed via tuning the coupling t/U or can be tangentially cut through by adjusting

the chemical potential μ. The theoretical expectation for the dynamic critical exponent is $z = 1$, while the correlation length exponent depends on the tuning parameter: $\nu = 1$ for approaching the critical point by scanning the chemical potential μ, and $\nu \approx 0.67$ for adjusting t/U to drive the SF-MI transition [115]. The latter intriguing value can be compared with a recent experimental value of $\nu = 0.67 \pm 0.13$, which is determined through the scaling of correlation length $\xi \propto |T - T_c|^{-\nu}$ near the BEC critical temperature T_c of a 3D bulk gas [117]. The BEC transition assumes an $O(2)$ XY universality class in three dimensions [118].

Measuring quantum critical behavior near the SF-MI critical points presents a challenging experimental task, and is currently pursued as another thesis project in this experiment. We will leave the details to Ref. [38] and some discussions in the last chapter.

4.2.7 *In situ signature of the superfluid and the Mott insulator states*

One of the static features distinguishing the superfluid and the Mott insulator states is their isothermal compressibility, defined as $\kappa = \frac{\partial n}{\partial \mu}$. Here n is the mean site occupancy. While a superfluid is a gapless, compressible fluid with $\kappa_{SF} \sim \frac{1}{ng}$, a Mott-insulator state is protected by a many-body gap Δ, with $0 < \Delta \leq U$, preventing particles with energy smaller than Δ from being added to or removed from the system. This leads to a zero compressibility $\kappa_{MI} = 0$. The incompressibility of an insulator is also revealed in the phase diagram. For constant t/U, a Mott insulator regime with site occupancy n_{MI} can persist for a finite adjustment of the chemical potential before the superfluid phase prevails.

For a trapped atomic sample, the locally varying chemical potential presents a vertical cut across the phase diagram, as illustrated in Fig. 4.6. This suggests coexisting domains of Mott insulator and superfluid phases can be observed inside one single sample. They are distinguishable via the mean site occupancy or the compressibility profiles. Inside the superfluid domain, the mean site occupancy increases as the local chemical potential increases; within the Mott insulator domain,

the incompressibility leads to a density plateau or shoulder. In a harmonic trapping potential, these domains manifest in the density profile as a wedding cake-like density distribution, which is considered an important *in situ* signature of the SF-MI quantum phase transition. *Ab initio* quantum Monte Carlo calculations have confirmed the existence of wedding cake structures, for example see Ref. [119]. In Chapter 5, we image the cake structure *in situ*. Similar experimental observations were also reported in Refs. [28, 120, 121, 33, 122] using various experimental techniques.

4.2.8   Finite temperature Mott insulator

In experiment, we prepare samples at finite temperatures. Thermal fluctuations enter as a competing energy scale which complicates the Bose-Hubbard physics. Without resorting to quantum Monte Carlo calculations, analytic calculations of finite temperature Mott insulators in the small tunneling limit $t \ll k_B T, U$ can be found in Ref. [123, 124]. In the following discussions we consider a thermal insulator in the zero tunneling limit.

When tunneling is negligible $t \ll U, k_B T$, the system enters the thermal insulator regime where particle and hole excitations are only generated by thermal fluctuations. The local site occupancy of a thermal insulator can be modeled analytically [123, 124]. Here, the mean occupation number can be written as

$$\bar{n} = \frac{\sum n P_n}{\sum P_n} = \frac{\sum n e^{-\beta[Un(n-1)/2 - \mu n]}}{\sum e^{-\beta[Un(n-1)/2 - \mu n]}}, \tag{4.27}$$

where $P_n = \exp(-\beta H_n)$ is the probability for n particles to occupy one lattice site, H_n is the associated free energy (assuming $t = 0$), $\beta = 1/k_B T$, and μ is the local chemical potential. Assuming $\mu(r_i) = \mu_c - V_{\text{ex}}(r_i)$ for a fully thermal-equilibrated sample held inside a weak trap with potential energy $V_{\text{ex}}(r)$, Eq. (4.27) can be turned into a density profile function $\bar{n}(r; T, \mu_c)$ with temperature T and chemical potential at the trap center μ_c as two free parameters. An illustration of density profiles calculated using Eq. (4.27) is shown in Fig. 4.7(a) based on parameters close to our experiment. The calculation shows that the plateau feature is clear only at temperatures equal

91
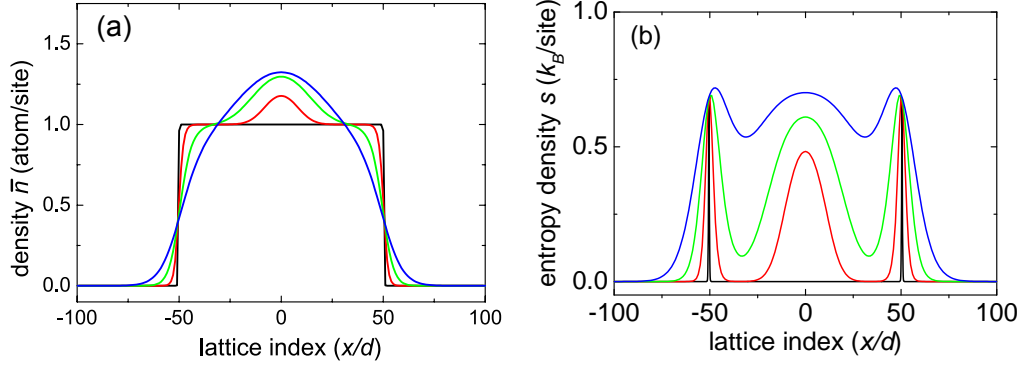
Figure 4.7: (a) Density and (b) entropy density profiles in the deep Mott insulator regime. The profiles are calculated based on Eq. (4.27), Eq. (4.29), and parameters relevant to our experiment: $U = k_B \times 24\,\text{nK}$, total particle number $N = 8,000$ and $V_{\text{ex}}(r) = k_B \times 9.0\,\text{pK}(r/d)^2$. Temperatures are 0.1 nK (black), 1 nK (red), 2.5 nK (green) and 5 nK (blue).

or below 2.5 nK and quickly disappear approaching 5 nK or higher. This observation is consistent with Ref. [123] that an insulator plateau melts at temperatures $T^* > 0.2U/k_B$.

More thermodynamic functions can be extracted from the simple thermal insulator model. Equation (4.27) is derived from the grand potential

$$\Omega(T,\mu) = \beta^{-1} \ln \left[\sum_n e^{-\beta H_n} \right], \tag{4.28}$$

which can also be used to calculate the entropy per site

$$s(T,\mu) = \frac{\partial \Omega}{\partial T}\Big|_\mu = k_B \left\{ \ln \left[\sum_n e^{-\beta H_n} \right] + \beta \frac{\sum_n [\frac{U}{2}n(n-1) - \mu n]e^{-\beta H_n}}{\sum_n e^{-\beta H_n}} \right\}. \tag{4.29}$$

Figure 4.7(b) shows entropy density profiles calculated using Eq. (4.29) and parameters used in plotting Fig. 4.7(a). Here we see that the entropy is mostly concentrated near the boundary of the insulator domains where thermal excitations are populated, while inside the density plateau the entropy density is small. These regions might be isolated to form low entropy quantum simulators, similarly discussed in Ref. [125] for fermions inside optical lattices.

92

The wedding-cake density structure of a thermal insulator and its ripple-like entropy distribution could raise concern regarding the non-trivial mass and heat transport during experimental preparation of loading a bulk superfluid gas to form an insulator sample. In Chapter 6, we shall discuss global equilibration dynamics across the SF-MI transition, using the thermal insulator model for local thermometry.

4.2.9 Thermometry

Fitting the temperature of an atomic cloud loaded into an optical lattice proceeds in several ways depending on the phase of the sample. Inside deep lattices, assuming sufficient global thermalization, one can compare the global density profile to the thermal insulator model Eq. (4.27) and obtain the temperature and peak chemical potential. For intermediate lattice depths, we use a formula derived from the Bose distribution function to fit the low density thermal gas region

$$
\begin{aligned}
\bar{n} &= \int_{BZ} \frac{dk^2}{(2\pi)^2} \frac{1}{e^{\beta(E_k-\mu)} - 1} \\
&= \int_{BZ} \frac{dk^2}{(2\pi)^2} \sum_{l=1}^{\infty} z^l e^{-l\beta E_l} \\
&= d^{-2} \sum_{l=1}^{\infty} z^l I_0(2t\beta l)^2,
\end{aligned}
\tag{4.30}
$$

where the integration goes over the first Brillouin zone, $E_k = -2t(\cos k_x d + \cos k_y d)$ is the energy of the ground band, and $I_0(x)$ is the modified zeroth order Bessel function of the first kind. Here, we expand the Bose distribution function using the fugacity $z = e^{\beta\mu}$. To include interaction, we add a mean-field potential into the local chemical potential $\mu_{mf} = \mu - 2g\bar{n}$ and solve the mean field equation self-consistently. The fit formula has been tested on the quantum Monte Carlo data and the result agrees to within 3%.

4.3 Experimental preparation of a 2D quantum gas

We describe the experimental preparation of 2D quantum gases at the time of thesis writing. Figure 4.8 illustrates the optical setup of our 2D gas experiment. A 2D gas is formed by freezing the atomic motion along the vertical axis into the quantum mechanical ground state. This is realized in our experiment through loading a thin condensate into a single site of a one dimensional lattice potential, formed by a laser standing wave. The lattice trap vibrational energy is made to be large compared to the interaction and thermal energy scales in the quantum gas to ensure all excitations are strictly two-dimensional. The lattice depth and periodicity are chosen to be large enough such that during the course of experiment, atoms do not tunnel to adjacent lattice sites. Once converting the condensate into a 2D gas, the temperature can either be lowered by further evaporating inside the lattice or be raised by applying magnetic field pulses (therefore pulsing the scattering length) to excite the atoms. After the 2D sample is sufficiently thermalized, we apply subsequent manipulations and perform *in situ* measurement.

For experiments on simulating the Bose-Hubbard Hamiltonian, a horizontal 2D lattice potential is further applied to the sample. The 2D lattice is formed by introducing the retro-reflections of x- and y- dipole beams. Unlike the vertical lattice, the horizontal lattice has a much shorter periodicity and permits fast inter-site tunneling. The lattice depth can be adjusted with a wide dynamic range, forming a highly tunable 2D Bose-Hubbard potential. Typical experiments begin with slowly ramping up the retro-beams, allowing the atomic sample to evolve inside the lattice potential. After subsequent experimental procedures, the horizontal beams are shut off, allowing the on-site atomic wave function to relax and fill the space within a lattice site. After $100\,\mu$s of short expansion, absorption imaging is applied to record the *in situ* density distribution. The imaging setup also permits a longer ~ 10 ms time-of-flight time for probing the momentum distribution or coherence property of the gas.

To probe the *in situ* density distribution, we perform resonant absorption imaging by shining a
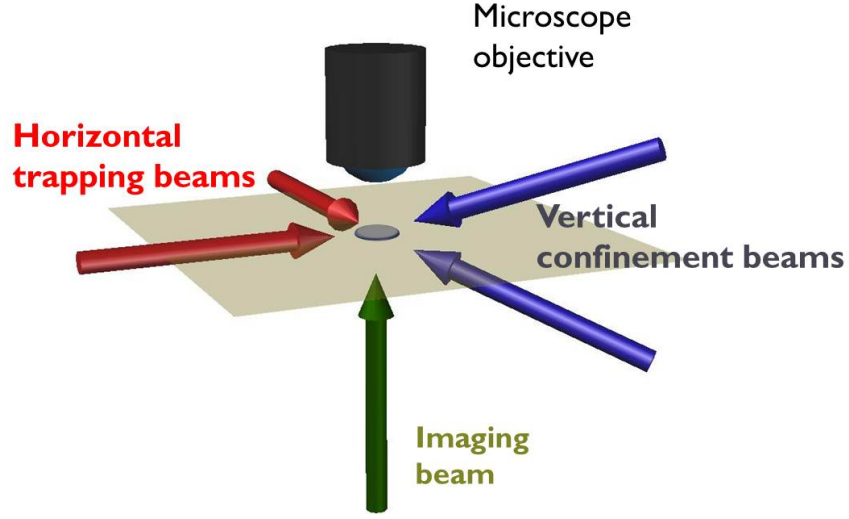
Figure 4.8: Optical setup of the 2D gas experiment. A condensate is loaded into a single site of a 1D optical lattice formed by the vertical confinement beams. The crossed dipole beams provide the horizontal confinement. Atomic density is probed via resonant absorption imaging, with a long working distance microscope objective.

probe beam from beneath the quantum gas and use a long working distance microscope objective with a standard tube lens to image the density shadow onto the CCD camera. The imaging pulse length is chosen to be short to ensure that atoms are imaged near the focal plane. The imaging is always performed at a magnetic field of 17.7 G, where the atomic scattering length is small, to fix the imaging condition and to reduce any possible light-assisted collisions during the imaging pulse [126].

4.3.1 Forming a lattice potential

Optical lattices are dipole potentials formed by laser interference patterns. Consider the simplest case of two coherent laser beams interfering with parallel linear polarizations. The beams propagate with wave vectors, $\vec{k}_1$ and $\vec{k}_2$, crossing at an angle $\theta > 0°$. The fringe pattern forms along the

95

direction (assumed to be the z-axis) parallel to $\vec{k}_1 - \vec{k}_2$, and the intensity varies as

$$I(z) = \left[(\sqrt{I_1} + \sqrt{I_2})^2 - 4\sqrt{I_1 I_2} \sin^2(\Delta k z + \frac{\phi}{2}) \right], \qquad (4.31)$$

where I_1 and I_2 are laser beam intensities, ϕ is the phase difference, $\Delta k = |\vec{k}_1 - \vec{k}_2|/2 = k \sin \frac{\theta}{2}$, and k is the wavenumber of the beams. According to Eq. (2.14), the fringe pattern creates a one-dimensional lattice potential

$$V_{1D} = -4\alpha \sqrt{I_1 I_2} \sin^2 \Delta k z, \qquad (4.32)$$

where $\alpha = -k_B \times 2.34$ nK $\cdot$ cm^2/W is the polarizability derived in the previous section. The lattice laser beams typically have Gaussian profiles and the intensities I_1 and I_2 vary spatially as Eq. (2.15). Since the lattice periodicity $\pi/\Delta k$ is typically much smaller than the laser beam waist, intensity variation in the beam profile results in a weak external trapping potential $V_{\text{ex}} = \alpha(\sqrt{I_1} + \sqrt{I_2})^2$.

4.3.2   Tight, vertical confinement by an optical lattice

The vertical lattice provides tight confinement in the z-direction, and is formed by two beams crossing the horizontal plane at $+8°$ and $-8°$. The horizontal plane is defined by the propagation direction of the horizontal dipole beams, in which the condensate is formed, and the vertical lattice beams are carefully aligned to cross at the position of the BEC. The fringe pattern is described by Eq. (4.31), with $\Delta k = k \sin 8°$, resulting in a lattice periodicity of 3.8 μm and a vertical harmonic confinement frequency of 2 KHz.

To ensure a stable interference pattern on the atoms, the vertical lattice beams share common optics along their paths. The two beams are derived from a fiber-coupled 1064 nm laser beam (from InnoLight, Mephisto) with a maximum output power of 900 mW. The main beam is split into two parts by a YVO$_4$ Wollaston polarizer (DayOptics, PWS8010). Three lenses (including one
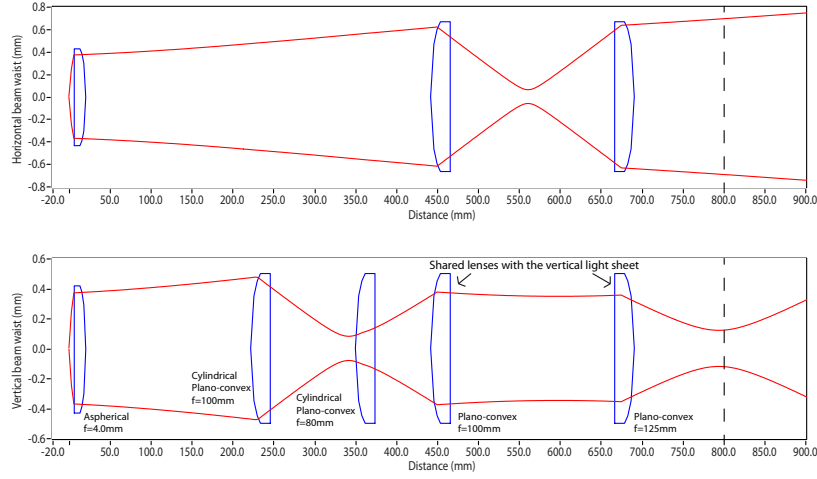
Figure 4.9: Schematic setup of the Gaussian beam optics for the vertical lattice beam. Vertical line indicates the position of the atoms.

cylindrical lens), as shown in Fig. 4.9, are placed in order to image the splitting point inside the polarizer onto the position of the atoms as well as to shape the beam profiles. The phase noise due to mechanical instability is commonly rejected in this optical setup. The only exception is a half wave plate placed in one of the beam paths, which rotates the beam polarization and maximizes the fringe contrast. Note that the light sheet, which defines the vertical position of the condensate, also passes through the same optics. As a result, the lattice pattern is very stable at the position of the condensate. The power of the lattice beams is feedback stabilized to remove intensity noise.

To reduce horizontal confinement exerted by the vertical lattice beam, we chose to shape the lattice beam profiles to be elliptical at the position of the atoms with their long axes lying on the horizontal plane. The beam waists are 700 μm horizontally and 120 μm vertically. At the maximum lattice depth, the horizontal trap frequencies are kept reasonably small at around 10 Hz, which preserves low surface densities in the 2D sample.

97
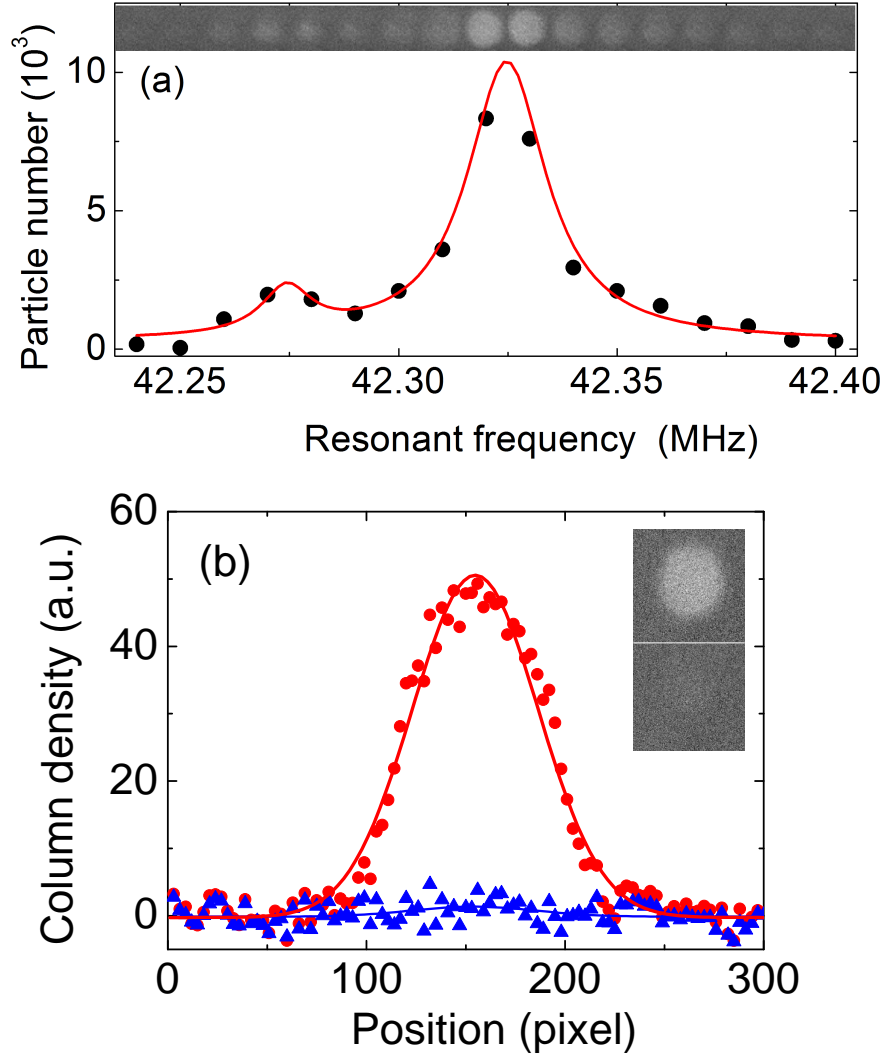
Figure 4.10: Microwave tomographic imaging of the atomic population inside the vertical lattice. (a) shows the microwave-transferred atomic population at various resonant frequencies. The solid line is a two-Lorentzian fit. The alignment of the anti-node is tuned to load a small population into one of the neighboring sites (the minor site). (b) shows density profiles measured when the microwave frequency is resonant to the center position of the major (red circles) and the minor (blue triangles) sites. The anti-node is well aligned to the condensate. In each profile, we have subtracted out a small off-resonantly pumped contribution from the other site, estimated from the line shape measured in (a). From (b) we deduce that there are fewer than 2% of the atoms in the minor site. Insets show the raw images.

4.3.3 Loading a monolayer of 2D gas - technical details

To convert the condensate into a 2D gas, we adiabatically turn on the vertical confinement beams in 100 ms to an intermediate intensity, compressing almost all condensate atoms into a single site of the vertical lattice. The high loading efficiency can be achieved by carefully aligning one anti-node of the lattice potential to the position of the condensate. The alignment is conveniently realized by adjusting the intensity of the light sheet at the end of the tilted evaporation.[5] After ramping on the vertical lattice potential, the intensity of the light sheet is then ramped to zero. The vertical lattice depth is chosen to be shallow enough such that the thermal atoms excited during the compression can further evaporate out of the lattice site. After 400 ms of evaporative cooling, the vertical lattice potential is ramped in 100 ms to its full strength, converting the condensate into a 2D quantum gas.

We test the loading efficiency by applying microwave tomographic imaging to detect the population in individual vertical lattice sites. We first apply a strong vertical magnetic field gradient ~ 50 G/cm to create a position-dependent Zeeman energy shift in the magnetic sub-levels. We than apply a microwave pulse driving the $|3, 3\rangle$ to $|4, 4\rangle$ transition, which is resonant at different vertical positions. The number of atoms transfered into the $|4, 4\rangle$ states are then directly imaged vertically through *in situ* absorption imaging. Figure 4.10(a) shows a sample tomographic scan. Here the on-site atomic population is proportional to the resonant peak value. Multiple peaks at different frequency shifts indicate that atoms are populating multiple lattice sites. Condensate atoms are typically loaded into less than two sites, as shown in Fig. 4.10(a), due to the small vertical size (~ 2 micron) of a pure condensate compared to the 3.8 micron periodicity of the vertical lattice. When one anti-node is aligned well to the position of the condensate, we detect less than 4% of the atomic population in the neighboring sites, as shown in Fig. 4.10(b). We frequently check the single site loading efficiency and the position of the majorly populated site. We found that the alignment can last for hours or for more than a day.

---

5. See previous chapter on the dependence of the trap minimum on the tilt parameter.

4.3.4   The 2D Bose-Hubbard lattice potential

In the Bose-Hubbard lattice experiment, we create a 2D square lattice by introducing the retro-reflections of the horizontal $(x - y)$ dipole beams. By increasing the intensity I_{ret} of the retro-reflected beam, the 2D optical trap is transformed into a 2D square lattice potential. Assuming the x- and y-beams have the same peak intensity I_0 and the same retro-efficiency $\epsilon = I_{ret}/I_0$, we derive the 2D intensity pattern I (at $z = 0$) from Eqs. (2.15) and (4.31),

$$
\begin{aligned}
I(x, y, 0) & = I_0(1 + \sqrt{\epsilon})^2(e^{-2y^2/w^2} + e^{-2x^2/w^2}) \\
& \quad - 4I_0\sqrt{\epsilon}\left[e^{-2y^2/w^2}\sin^2(kx + \frac{\phi_x}{2}) + e^{-2x^2/w^2}\sin^2(ky + \frac{\phi_y}{2})\right], \quad (4.33)
\end{aligned}
$$

where all beams are assumed to have the same beam waist w, and $\phi_{x,y}$ are the phase differences in the x- and y-beams. Near the center of the crossed-dipole beams, we have a 2D square lattice potential with an envelope harmonic trap

$$
V(x, y) = \frac{1}{2}m\omega_{\mathrm{ex}}^2(x^2 + y^2) + V_0[\sin^2(kx + \frac{\phi_x}{2}) + \sin^2(ky + \frac{\phi_y}{2})], \quad (4.34)
$$

where $V_0 = -4\alpha I_0\sqrt{\epsilon}$ is the lattice depth, and $\omega_{\mathrm{ex}}^2 = -\frac{4\alpha I_0(1+\sqrt{\epsilon})}{mw^2}$ is the envelope trap frequency. Because the lattice potential is heterodyne-amplified, a small $\epsilon \sim 0.1$ already creates sufficiently deep lattice for Bose-Hubbard physics. The envelope frequency can be kept nearly constant during the lattice loading, or can be easily adjusted (reduced) by changing the incident beam intensity I_0.

Our lattice setup requires a large dynamic range in controlling the retro-reflected intensity. It also needs a high extinction ratio to ensure a corrugation-free dipole potential during forced evaporation to BEC. This is achieved by sending each dipole beam, after it passes through the atomic cloud once, through two AOMs controlled by a single radio-frequency (rf) source, then off a retro-reflection mirror. The AOMs induce an overall zero frequency shift, but permit a dynamic control of the retro-reflection intensity over six orders of magnitude. The retro-beam intensity is
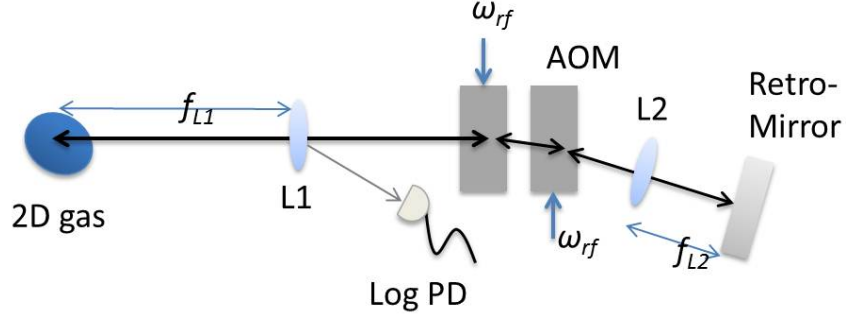
Figure 4.11: Schematic setup of the AMO controlled retro-reflection. L1, L2: beam-shaping lenses. Log PD: logarithmic photodetector, which measures a pickup beam reflected off from L1. ω_{rf} is the frequency of the rf source. In this setup, all higher order Bragg diffractions are blocked (not shown).

measured using a logarithmic photodetector, and is feedback stabilized via controlling the rf level into the AOMs. For the setup, see Fig. 4.11. Two additional lenses are placed to image the retro-mirror onto the atoms to ensure a good retro-alignment as well as to reshape the retro-reflected beam to a similar waist as that of the incident beam.

4.3.5   Lattice depth calibration

The lattice depth is calibrated by measuring the lattice vibrational frequency. We first adiabatically load non-interacting condensate atoms (prepared at $B_o = 17.1$ G) into the lattice potential and then induce a small on-site center-of-mass (c.o.m.) oscillation by suddenly shifting the position of the lattice well. The shift is conveniently created by changing the rf frequency ω_{rf} to the retro AOMs, which modifies the beam deflection angle and therefore the light path. The small change in the light path adds additional phase difference $\Delta\phi$ between the incident and the retro beams and can shift the lattice well (Eq. (4.11)). After a variable oscillation time, we shut off the lattice potential and image the atomic interference pattern after time-of-flight expansion. The on-site c.o.m. oscillation frequency can be measured via observing the amplitude modulation of the $\pm 2\hbar k$

101
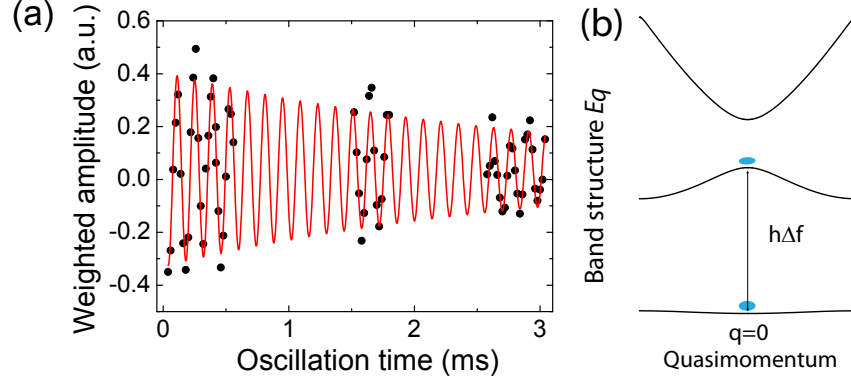
Figure 4.12: Lattice depth calibration. (a) Recoil peak amplitude (weighted) oscillation. Solid line shows a fit of damped oscillation. Fitted frequency is $\Delta f = 7.146(8)$ kHz, corresponding to a lattice depth of $V_0 = 8.91(3)\ E_R$. (b) Illustration of the excited state population in the lattice band structure.

recoil peaks. Figure 4.12 shows the oscillation of the weighted sum $A_{2\hbar k} - A_{-2\hbar k}$ of recoil peak amplitudes.

The amplitude modulation of recoil peaks can be understood in the language of Bloch waves similarly found in Ref. [127]. Our condensate (non-interacting) is initially prepared at the ground band $|\phi_{q=0}^{(0)}\rangle$ Bloch wave and is suddenly perturbed by a position shift operator $\hat{X}$. After the shift, the condensate evolves as

$$|\Psi(\tau)\rangle = \sum_{n=0}^{\infty} a^n e^{iE_0^{(n)}\tau/\hbar}|\phi_0^{(n)}\rangle, \tag{4.35}$$

where τ is the evolution time, and $a^n = \langle\phi_0^{(n)}|\hat{X}|\phi_0^{(0)}\rangle$ is the projection coefficient. Shutting off the lattice potential projects the condensate into the plane wave states $|p = 2l\hbar k\rangle$,

$$|\Psi(\tau)\rangle = \sum_{n=0}^{\infty} \sum_{l} a^n b_l^n e^{iE_0^{(n)}\tau/\hbar}|2l\hbar k\rangle, \tag{4.36}$$

where b_l^n is the projection coefficient of the Bloch wave $|\phi_0^{(n)}\rangle = \sum_{-l}^{l} b_l^n |p = 2l\hbar k\rangle$. Measuring the amplitude modulation of $A_{2\hbar k} - A_{-2\hbar k}$ shows the time-dependence of $|\sum_{n=0}^{\infty} a^n b_1^n e^{iE_0^{(n)}\tau/\hbar}|^2 -$

$|\sum_{n=0}^{\infty} a^n b_{-1}^n e^{iE_0^{(n)}\tau/\hbar}|^2$. For a very small shift, the excitation is mostly populated in the first excited band $n = 1$, ($a^1 \gg a^3, a^5 \ldots$). The oscillation frequency is therefore equal to $\Delta f = (E_0^{(1)} - E_0^{(0)})/h$, which can be used to calibrate the lattice depth.

4.4 *In situ* imaging

4.4.1 *Absorption imaging of a three-dimensional sample*

Absorption imaging is performed by shining a resonant laser pulse through the sample and measuring the intensity attenuation, from which we determine the atomic column density. For an imaging beam with intensity I propagating along the z-direction, the intensity attenuation is described by

$$\frac{dI}{dz} = -n_{3D}(x, y, z)\sigma I, \tag{4.37}$$

$$\sigma(I) = \frac{\sigma_0}{1 + I/I_{sat}}, \tag{4.38}$$

where $n_{3D}(x, y, z)$ is the 3D atomic density, $\sigma(I)$ is the scattering cross section with a maximum value $\sigma_0 = 3\lambda^2/2\pi$ for imaging using the cycling transition, and $I_{sat} = \hbar\omega_0^3\Gamma/12\pi c^2$ is the saturation intensity. Conventional absorption imaging assumes $I \ll I_{sat}$, leading to an intensity-independent scattering cross section, and the transmission through a dilute sample follows Beer's law

$$\frac{I_t(x, y)}{I_0(x, y)} = e^{-\sigma_0 \int n_{3D}(x,y,z)dz}, \tag{4.39}$$

where $I_0(x, y)$ is the incident beam intensity profile and $I_t(x, y)$ is the transmitted intensity profile. The atomic column density $n(x, y) = \int n_{3D}(x, y, z)dz$ is then given by

$$n(x, y) = -\frac{1}{\sigma_0} \ln \frac{I_t(x, y)}{I_0(x, y)}. \tag{4.40}$$

The intensity profiles $I_t(x, y)$ and $I_0(x, y)$ are measured using a CCD camera, obtaining the photo-electron counts, $P_{t,\text{CCD}}(x_i, y_i)$ and $P_{0,\text{CCD}}(x_i, y_i)$, with and without the atomic absorption (method described in Section 2.5). Here, (x_i, y_i) labels the position of the i-th CCD pixel. Each CCD image contains a signal from the imaging beam photons, as well as a background signal $\Delta_{bg}(x_i, y_i)$ from the leakage light, the dark current, and the readout noise. The background signal $\Delta_{bg}(x_i, y_i)$ can be separately measured by repeating the imaging procedure without pulsing on the imaging beam. Subtracting off $\Delta_{bg}(x_i, y_i)$ from $P_{\text{CCD}}(x_i, y_i)$, we obtain the number distribution of imaging photo-electrons,

$$P(x_i, y_i) = P_{\text{CCD}}(x_i, y_i) - \Delta_{bg}(x_i, y_i). \tag{4.41}$$

We expect that $P(x_i, y_i) = QAI(x_i, y_i)\tau/\hbar\omega_0$. Here, the quantum efficiency Q of the imaging system, the pixel size A, the imaging time τ, and the energy quanta $\hbar\omega_0$ per imaging photon are common factors of $P_t(x_i, y_i)$ and $P_0(x_i, y_i)$. Equation (4.40) can therefore be written as

$$n(x_i, y_i) = -\frac{1}{\sigma_0} \ln \frac{P_{t,\text{CCD}}(x_i, y_i) - \Delta_{t,bg}(x_i, y_i)}{P_{0,\text{CCD}}(x, y) - \Delta_{0,bg}(x_i, y_i)} = -\frac{1}{\sigma_0} \ln \frac{P_t(x_i, y_i)}{P_0(x_i, y_i)}, \tag{4.42}$$

which forms the density conversion formula of weak absorption imaging.

In the horizontal path, atoms are released from the trap for a finite time-of-flight time to form a dilute absorptive sample. We measure $P_i(x, y)$ and $P_t(x, y)$ using the CCD camera in the horizontal path, independently calibrate the maximum scattering cross section σ_0, and obtain the column density of the atomic sample.

In situ absorption imaging along the vertical imaging path is significantly different from the weak absorption case. First, a degenerate quantum gas is optically dense, $n\sigma_0 \gg 1$, leading to strong absorption. To increase the transmitted signal $P_t(x_i, y_i)$, one either adopts a longer imaging pulse length τ or uses a strong incident beam intensity to saturate the atomic absorption.

Improvement using the former method is quite limited since we set the criterion that atoms should travel less than the depth of focus during the pulse (to be discussed in the next section). The latter method, nevertheless, requires a carefully calibrated saturation intensity I_{sat}^* (rather than the ideal value I_{sat}) since the scattering cross section Eq. (4.38) becomes intensity-dependent and Eq. (4.42) has to be modified. Moreover, the value of I_{sat}^* deviates from I_{sat} due to imperfectness of the imaging beam polarization, a transient optical pumping effect, and a broadened transition line width caused by laser jitter or atomic collisions. A similar modification applies to the maximum cross section σ_0^* (rather than σ_0) [128]. For a strong incident beam intensity I_0, we find the column density now relates to absorption in a modified Beer-Lambert law as [128]

$$n(x,y)\sigma_0^* = -\ln\frac{I_t(x,y)}{I_0(x,y)} + \frac{I_i(x,y) - I_t(x,y)}{I_{sat}^*}, \qquad (4.43)$$

where I_{sat}^* and σ_0^* are to be independently calibrated.

There is another advantage to use a stronger probe beam for *in situ* imaging. In deriving all of the above equations, we assume photon scattering is a single atom process. Nevertheless, since the atomic separation is comparable to the laser beam wavelength, there might be coherent effects on the scattered field causing density-dependent atomic absorption [109]. Since the atom-photon scattering rate should ultimately be limited by the transition linewidth, using a strong incident field to saturate the atoms can suppress a possible collective effect [109, 129] which might complicate the conversion of the column density.

4.4.2   *Absorption imaging of a two-dimensional sample*

Applying Eq. (4.43) to *in situ* imaging of a thin 2D sample, one pauses when noticing that the intensity loss caused by crossing a 2D cloud only happens within the axial extent of the atomic wave packet. All atoms should see a similar imaging beam intensity and Eq. (4.37) might be inapplicable since it is a semi-classical equation describing the continuous intensity drop inside an

atomic ensemble where atoms are sparsely spread over the axial direction. To deduce 2D density from absorption images, we should instead use a probability description starting from the atom-photon scattering rate

$$R = \frac{\Gamma}{2} \frac{I/I^*_{sat}}{1 + I/I^*_{sat}}, \tag{4.44}$$

and find the number of photons that are scattered off by individual atoms within the pulse interval.

Here, we show that 2D absorption can still be approximated by the semi-classical formula Eq. (4.43) in the limit of saturated absorption imaging. We adopt an argument established in Ref. [129]. Inside a small area A, where the photon wavefunction is uniform, the number of photons scattered by N atoms is predicted to be $NR\tau$, where $\tau \gg 1/\Gamma$ is the imaging pulse time. The number of transmitted photons out of N_0 incident photons is then given by $N_t = N_0 - NR\tau$, which can be converted into intensity in the classical formula as

$$I_t = I_0 - n\sigma^* I. \tag{4.45}$$

Here $\sigma^* = \sigma^*_0/(1 + I/I^*_{sat})$ is the modified scattering cross section, and I is an effective intensity determining the scattering rate of the illuminated sample. The probability of transmitting an incident photon is[6] $(1 - \frac{\sigma^*(I)}{A})^N \approx e^{-n\sigma^*(I)}$. Accumulating N_t transmitted photons, we have

$$\frac{N_t}{N_0} = \frac{I_t}{I_0} \approx e^{-n\sigma^*(I)}. \tag{4.46}$$

Solving Eq. (4.45) and Eq. (4.46), we obtain

$$n\sigma^*_0 \approx -\ln\frac{I_t}{I_0} + \frac{I_0 - I_t}{I^*_{sat}}, \tag{4.47}$$

---

6. Within a small time interval $d\tau$, there will be $R(I)d\tau$ photons per atom scattered out from $I_0 A d\tau/\hbar\omega$ incident photons. The probability of transmission through a single atom is $p = 1 - \frac{R(I)\hbar\omega_0}{I_0 A} = 1 - \frac{\sigma^*}{A}$. For N atoms seeing the same photon, transmission propability is p^N.

which is identical to Eq. (4.43). We see that the approximation holds for $n\sigma^* \sim\lesssim 1$. This is usually satisfied in our experiment with an incident beam intensity $I_0 \approx 6I^*_{sat}$ and $\sigma^*_0 = 0.12\ \mu\text{m}^2$ (calibrated value).

4.4.3   Experimental calibration of 2D absorption imaging

In this section, we first describe our procedure for testing the validity of Eq. (4.47), followed by the calibration of I^*_{sat}, similarly discussed in [128]. We then describe two independent ways of determining σ^*_0. Last, we describe calibrating the image magnification using recoil momentum.

Calibration of the saturation intensity

To verify Eq. (4.47) and to calibrate I^*_{sat}, a straightforward method is to fix the atomic density, perform imaging at different intensities, and measure how the absorption changes. As discussed in the previous section, we expect that the absorption is described by the modified Beer-Lambert law Eq. (4.47) and, for a fixed density n, our measurements of $\text{OD} = \ln\frac{P_0}{P_t}$ and $\Delta P = P_0 - P_t$ should reveal the following linear relation

$$\text{OD} + \frac{\Delta P}{P^*_{sat}} = n\sigma^*_0 = \text{const.}, \tag{4.48}$$

where $1/P^*_{sat} = \hbar\omega/QAI^*_{sat}\tau$ is the slope of the linear curve.

Experimentally, we test the linearity using 2D thermal gases prepared at identical experimental conditions. In each image, we pick the center 10×10 pixels, where n is identical, to evaluate the averaged OD and $\Delta P/\tau$. Figure 4.13 shows sample OD versus $\Delta P/\tau$ curves measured at two different densities. Here we indeed find a good linear dependence over a wide range of imaging beam intensity $I_0 = 1 \sim 8\ I_{sat}$, where $I_{sat} = 1.1\ \text{mW/cm}^2$ is the saturation intensity of $4 \rightarrow 5'$ cycling transition. We also tested the linearity over a density range $0 \lesssim n\sigma^* \lesssim 2$,
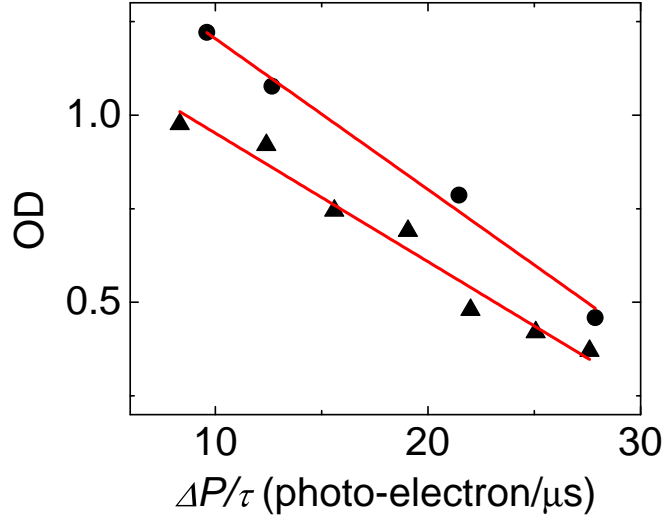
Figure 4.13: Sample curves of OD versus ΔP at different atomic densities. Solid lines are the linear fits.

and found that the fitted slope is nearly density independent, giving $P^*_{sat}/\tau = 26(4)\ \mu s^{-1}$ and $I^*_{sat} = P^*_{sat}\hbar\omega_0/\tau QA \approx 2.3(3)\ \text{mW/cm}^2 \approx 2I_{sat}$. Here we have used $Q \approx 0.6$, the product of the overall transmission of imaging optics and the quantum efficiency of the camera, and $A = (666\ \text{nm})^2$, the calibrated CCD pixel size in the object plane (to be discussed later). In our experiment, P^*_{sat} suffices to calculate the atomic density since only its ratios to P_0 and P_t matter.

Calibration of the scattering cross section

We continue to calibrate the scattering cross section σ^*_0 from $n\sigma^*_0$ evaluated using Eq. (4.47). In the first calibration method, we use a strong imaging beam to probe a vertically thin ($\Delta z \approx 2.5\ \mu m$) and nearly pure 3D condensate, with a known peak column density, as a density ruler to extract σ^*_0. The peak column density $n_0 = \frac{m^2\omega_x^3 R_x^3}{6\pi\hbar^2 a\omega_z} = \frac{m^2\omega_y^3 R_y^3}{6\pi\hbar^2 a\omega_z}$ can be determined from the Thomas-Fermi radii $R_{x,y}$ in the x and y directions, as long as the atomic scattering length a and the harmonic trap frequencies $\omega_{x,y,z}$ are known. The trap frequencies can be independently determined by
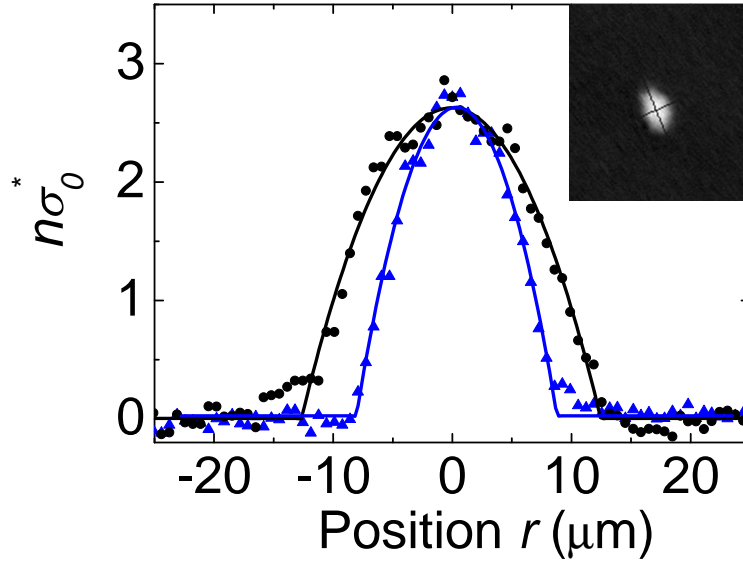
Figure 4.14: Line-cut profiles along the principal axes of a 3D condensate. Solid lines are the fitted curves using the Thomas-Fermi profile Eq. (4.49). Inset: 2D image of the condensate, where the solid lines indicate the directions of line-cuts.

measuring the frequency of atomic dipole oscillations in the x-, y-, and z-directions or from the *in situ* root-mean-square radii of a 2D thermal cloud (for determining $\omega_{x,y}$), whose temperature can be measured from time-of-flight expansions. The atomic scattering length can be well-determined from the background magnetic field using Eq. (2.1). We fit the condensate column density using the Thomas-Fermi form

$$n(x,y)\sigma_0^* = n_0\sigma_0^*[1 - (x/R_x)^2 - (y/R_y)^2]^{3/2}, \tag{4.49}$$

with $n_0\sigma_0^*$, and the Thomas-Fermi radii $R_{x,y}$ as fit parameters. We then deduce n_0 from R_x or R_y and obtain the calibrated value of the scattering cross section σ_0^*.

Figure 4.14 shows line-cut density profiles of a nearly pure condensate held in an oblate dipole trap with trap frequencies $\omega_{x,y,z} = 2\pi \times (16, 11, 58)$ Hz. The atomic scattering length is adjusted to $a = 370\ a_0$, reducing the condensate peak density to a moderate value comparable to a typical

109

2D gas peak surface density. We find that each line cut can be well fit by the Thomas-Fermi form Eq. (4.49), giving the Thomas-Fermi radii $R_x = 8.5$ μm and $R_y = 13$ μm. The expected peak column density is $n_0 = 2.2(3) \times 10^9$ cm^{-2}. Comparing to the measured peak value of $n_0 \sigma_0^* = 2.6$, we obtain $\sigma_0^* = 1.2(2) \times 10^{-9}$ cm$^2 = 0.34 \sigma_0$, where $\sigma_0 = 3\lambda^2/2\pi$ is the resonant cross section of the cycling transition.

Finally, we justify using a thin condensate to calibrate the atom-photon cross section of a 2D gas. Indeed the vertical size of the condensate is around 2.5 μm, which is larger than the 2D gas vertical harmonic oscillator length of 200 nm. Nevertheless, the surface density conversion Eq. (4.47) in 2D is formally identical to the column density formula Eq. (4.43) in 3D, and we expect the scattering process is single atom-like using a strong probe beam, giving σ_0^* and I_{sat}^* independent of the atomic distribution. Calibration using a thin condensate should be an approximately valid method.

We also cross-check our calibrated value independently using atomic shot-noise in a 2D thermal gas to further strengthen our assertion. The shot-noise behavior of a 2D thermal gas measured inside an area V is expected to be

$$\langle \delta N^2 \rangle = \alpha \langle N \rangle, \tag{4.50}$$

where N is the number of particles inside the area V, $\delta N = N - \langle N \rangle$, and $\langle . \rangle$ denotes an ensemble average. Here, α is a number slightly larger than 1 due to bosonic bunching. For an ideal thermal gas with a density n and a thermal de Broglie wavelength λ_{dB} , α can be evaluated based on Eq. (4.5) as[7]

$$\alpha \approx 1 + \frac{1}{g_1(z,1)\lambda_{dB}^2} \int_V |g_1(z, e^{-\pi r^2/\lambda_{dB}^2})|^2 d\mathbf{r} \tag{4.51}$$

$$\approx \frac{g_0(z,1)}{g_1(z,1)} = \frac{-z}{(1-z)\ln(1-z)}, \text{ for } V \gg \lambda_{dB}, \tag{4.52}$$

---

7. See Chapter 8 for discussions on arbitrary area V, λ_{dB}, as well as the finite resolution effect on density fluctuation measurements.

where the integration goes over the area V, $g_\gamma(x, y) = \sum_{k=1}^{\infty} x^k y^{1/k}/k^\gamma$ is the generalized Bose function, and z is a constant (fugacity) such that the 2D density $n = \lambda_{dB}^{-2} g_1(z, 1) = -\lambda_{dB}^{-2} \ln(1 - z)$. When the area V is much larger than the thermal de Broglie wavelength, the integration can be evaluated as $\lambda_{dB}^2 [g_0(z, 1) - g_1(z, 1)]$, leading to Eq. (4.52). In this limit, one can also obtain Eq. (4.52) by directly applying the fluctuation-dissipation theorem[95] $\langle \delta N^2 \rangle = k_B T \partial N/\partial \mu = V g_0(z, 1)/\lambda_{dB}^2$, where we have used $\partial g_1(z, 1)/\partial z = g_0(z, 1)$. For a weakly interacting thermal cloud far from the critical fluctuation regime, one can use the mean field approximation to modify the fugacity $z' = z e^{-2\beta g n}$, where g is the interaction strength of the 2D gas. Under this approximation, Eq. (4.52) generalizes to

$$\alpha(g) = \frac{-z e^{-2\beta g n}}{[1 - (1 - \frac{mg}{\pi \hbar^2}) z e^{-2\beta g n}] \ln(1 - z e^{-2\beta g n})}, \tag{4.53}$$

which describes the bosonic bunching factor of a weakly interacting cloud in the normal gas region. Comparing measured noise with the expectation value using Eq. (4.50) and (4.52-4.53) can also calibrate the atom-photon cross section.

Before proceeding to the analysis, one needs to consider the additional complication that in the real experiment we measure $n\sigma_0^*$ with a finite image resolution. Denoting the experimental measurement of $n\sigma_0^*$ with $n_{exp}\sigma_0^*$ and evaluating its noise $\langle \delta n_{exp}^2 \sigma_0^{*2} \rangle$, we expect

$$\langle \delta n_{exp}^2 \sigma_0^{*2} \rangle V = \frac{\sigma_0^{*2}}{V} \Theta \langle \delta N^2 \rangle = \alpha(g) \sigma_0^* \Theta \langle n_{exp} \sigma_0^* \rangle, \tag{4.54}$$

where Θ is a reduction coefficient due to the finite image resolution. Θ depends on the ratio between $\sqrt{V}$ and the resolution limited length r. When $\sqrt{V}$ is comparable to or smaller than r, the atomic signal is blurred into an area larger than the detection area, reducing the detected shot-noise with $\Theta < 1$; when $\sqrt{V} \gg r$, all atomic signals are well contained within the area V and $\Theta \approx 1$. Studying $\langle \delta n_{exp}^2 \sigma_0^{*2} \rangle V$ versus $\alpha \langle n_{exp} \sigma_0^* \rangle$ in the large V limit is then necessary to remove the finite
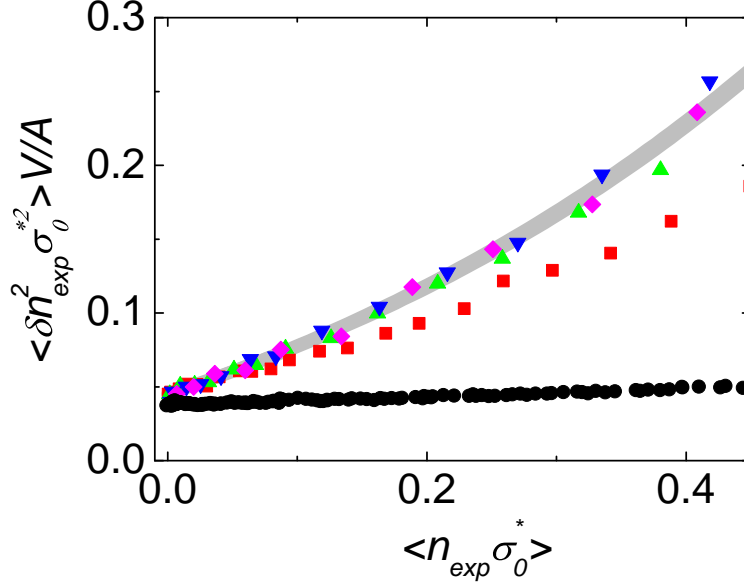
Figure 4.15: Noise of an ideal thermal gas evaluated using different pixel binning $V = L^2 A$: $L^2 = 1$(circle), 36 (square), 81 (up triangle), 100 (down triangle), and 144 (diamond). The shaded curve indicates the fit to the noise curve of $L^2 = 144$, using Eq. (4.53-4.54) and setting σ_0^* as a free parameter. The width indicates a $\pm 10\%$ uncertainty.

resolution effect.

Experimentally, we bin the CCD pixels to evaluate the atomic density noise in the large V limit. We first obtain the absorption images of 2D thermal gases prepared at a temperature $T = 90$ nK and $g \approx 0$. We then evaluate $\langle \delta n_{exp}^2 \sigma_0^{*2} \rangle V$ using different binned areas $V = L^2 A$. Here L is the linear bin size. In Fig. 4.15, we plot $\langle \delta n_{exp}^2 \sigma_0^{*2} \rangle V$ as a function of $\langle n_{exp} \sigma_0^* \rangle$, evaluated using multiple bin sizes. We observe that by increasing the bin size V, the fluctuation curve saturates to a single curve independent of the area V, indicating that the finite resolution effect is removed ($\Theta \approx 1$). We also see that the entire fluctuation curve is nonlinear with respect to the atomic density, which is expected due to the nonlinearity in α. Finally, all curves have a non-zero noise floor due to the image photon shot-noise and the background noise. The noise floor is almost independent of the bin size.

At $L = 11 \sim 12$, the fluctuation curve can be well fitted using Eq. (4.53-4.54) with only σ_0^*

as a free parameter; see Fig. 4.15. We find $\sigma_0^* = 1.25(15) \times 10^9$ cm^2 agrees very well with the calibrated value $\sigma_0^* = 1.2(2) \times 10^9$ cm^2 using a 3D condensate Thomas-Fermi radius-to-peak density conversion.

4.4.4   Optimization of the signal-to-noise ratio

For *in situ* imaging, using a strong probe beam or a longer imaging pulse can increase the number of transmitted photons and improve the range of density detection. Nevertheless, applying excess probe beam intensity could impose much larger photon shot-noise compared to the real atomic signal, while a longer pulse width can deteriorate image resolution. We therefore need to find out the optimal intensity as well as imaging pulse width to achieve the best signal-to-noise ratio.

From the modified Beer-Lambert law Eq. (4.43), it is not difficult to find out that the noise in two images P_t and P_0 contributes to the measured density noise δn_{img}^2 as

$$\delta n_{img}^2 \sigma_0^{*2} = \frac{\delta P_t^2}{P_t^2}\left(1 + \frac{P_t}{P_{sat}^*}\right)^2 + \frac{\delta P_0^2}{P_0^2}\left(1 + \frac{P_0}{P_{sat}^*}\right)^2,\tag{4.55}$$

where $P_{sat}^* = Q I_{sat}^* A\tau/\hbar\omega_0$ is the corresponding photo-electron number of one saturation intensity I_{sat}^*. Each image's noise, $\delta P_0^2 = P_0 + \Delta_0$ and $\delta P_t^2 = P_t + \Delta_t$, contains the photo-electron shot-noise $\delta P_{0,t}^2 = P_{0,t}$ as well as the background noise[8] $\delta\Delta_{0,t}^2 = \Delta_{0,t}$. Equation (4.55) can now be further written as

$$\delta n_{img}^2 \sigma_0^{*2} = P_{sat}^{*-1}\left[(\gamma + \Delta_0')(1 + \gamma^{-1})^2 + (\gamma e^{-n\sigma^*} + \Delta_t')(1 + \gamma^{-1}e^{n\sigma^*})^2\right],\tag{4.56}$$

where $\gamma = P_0/P_{sat}^*$ and $\Delta_{0,t}' = \Delta_{0,t}/P_{sat}^*$. To emphasize the weak density dependence in the image noise, we have used Eq. (4.46) to replace P_t/P_0 with $e^{-n\sigma^*}$.

---

8. For simplicity, we assume the background noise is shot-noise limited. In reality, the noise can acquire a different behavior and can be directly measured experimentally.
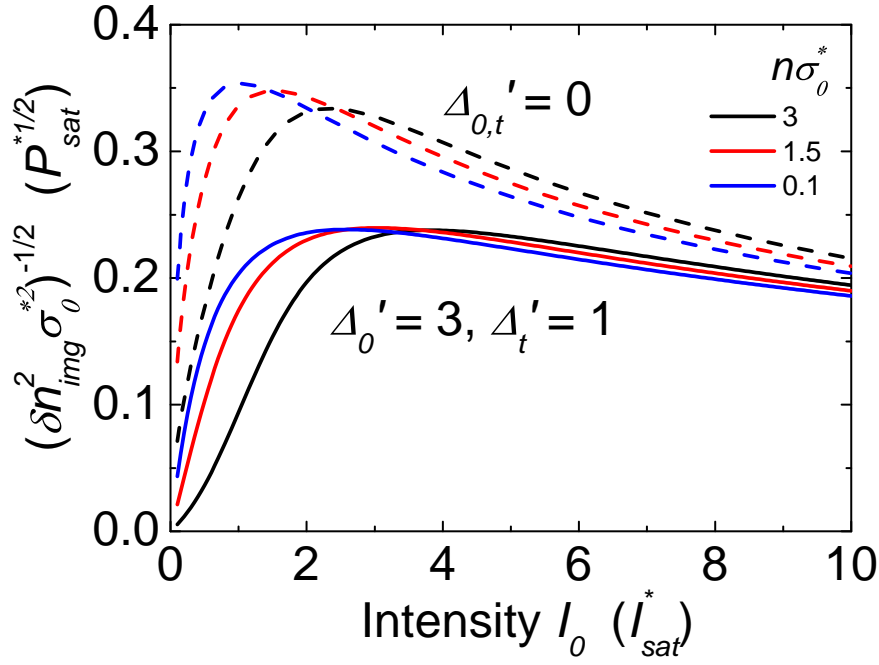
Figure 4.16: Inverse square-root of the image noise $1/\sqrt{\delta n_{img}^2 \sigma_0^{*2}}$ as a function of imaging beam intensity I_0 at various densities $n\sigma_0^* = 3$ (black), 1.5(red), and 0.1(blue) with background image noise $\Delta_0' = 3\Delta_t' = 3$ (solid lines, experiment condition) and $\Delta_{0,t}' = 0$ (dashed lines).

From Eq. (4.56), it is clear that the overall signal-to-noise level can be elevated by increasing the value of P_{sat}^*. The terms in the bracket can also be optimized. They depend on the ratio of intensity $\gamma = I_0/I_{sat}^*$ which is independent of the imaging time τ and the optimal value can be easily determined.

Although the actual value of $P_{sat}^* = QI_{sat}^* A\tau/\hbar\omega$ can be increased to improve the overall signal-to-noise ratio, it is nevertheless quite limited if one desires to preserve the image resolution. The adjustable factors in P_{sat}^* are the quantum efficiency Q, the pixel area A, and the imaging time τ. While we have improved the overall quantum efficiency to $Q \approx 0.6$ (limited by the transmissive optics in the imaging beam path; see Section 2.5.2), imaging atoms with high resolution sets strong limits on the values of A and τ. The pixel size $\sqrt{A} = 666$ nm is chosen to be smaller than the resolution limited spot size; the imaging time is limited to $15\ \mu$s such that, under coherent light

pressure, the atoms travel less than 6 μm near the focal plane, which is comparable to the depth of focus. These limitations constrain $P_{sat}^* \approx 400$.

To qualitatively estimate the general constraint on P_{sat}^* for an arbitrary image resolution, consider that the depth of focus d.o.f. $\sim \lambda/\text{N.A.}^2$ is related to the diffraction limited spot size $r = 0.61\lambda/\text{N.A.}$ as d.o.f. $= 2.7r^2/\lambda$, where N.A. is the numerical aperture of the objective. Both the pixel size $\sqrt{A}$ and the vertical traveling distance of an atom $l = \frac{\hbar\omega_0(P_0-P_t)\tau}{2nAmcQ}$ will be limited by the resolution r. Choosing $\sqrt{A} = r/3$ and constraining $l \leq$ d.o.f. $\approx 3r^2/\lambda$, we find

$$P_{sat}^* \lesssim \sqrt{\frac{mI_{sat}^*r^6}{27\pi\hbar^2\omega_0\sigma_0^*}(1+\gamma^{-1})Q^2} \approx \zeta Q \left(\frac{r}{1\ \mu\text{m}}\right)^3, \tag{4.57}$$

where $\zeta \approx 140$ is a constant determined by the calibrated values of $I_{sat}^* = 2.3$ mW/cm^2 and $\sigma_0^* = 1.2 \times 10^{-9}$ cm^2. Our experimental parameter is bounded by this criterion.

We also determine the optimal imaging beam intensity $I_i = \gamma I_{sat}^*$. Figure 4.16 shows the intensity dependence of $1/\sqrt{\delta n_{img}^2\sigma_0^{*2}}$ in a density range of experimental interest. For our background noise of $\Delta_0' \approx 3$ and $\Delta_t' \approx 1$, the optimal imaging beam intensity is at $I_0/I_{sat}^* = 2 \sim 4$. There we have $1/\sqrt{\delta n_{img}^2\sigma_0^{*2}} = 0.24\sqrt{P_{sat}^*}$. For $P_{sat}^* = 400$, signal-to-noise is around 2 for a density corresponding to one atom per lattice site $(532\text{ nm})^2$. We currently use $\gamma = 6$, which is not far from the optimum.

We determine the background noise $\Delta_0' \approx 3$ and $\Delta_t' \approx 1$ by counting the image noise recorded on the CCD without pulsing on the imaging beam. In our experiment, background noise mainly comes from the noise of integrated dark current during the readout time ~ 1 sec. The unequal amount of background noise $\Delta_0 > \Delta_t$ is due to the readout order of $P_{t,\text{CCD}}$ and $P_{0,\text{CCD}}$. The dark current causes $0\sim1600$ e^- counts per pixel across the CCD chip. It can be further reduced by a factor of 100 through cooling the CCD from 0°C down to -40°C.

4.4.5 Calibration of image magnification

For vertical imaging, the standard ruler for calibrating the image magnification is the recoil velocity of atoms diffracting off from the horizontal 2D square lattice. To measure the recoil velocity, we first adiabatically load a BEC into the lattice. The lattice beams are then shut off, allowing atoms to expand inside the vertical confinement potential without leaving the focal plane. We expect diffraction peaks appearing at positions $\Delta x = \Delta y = \pm v_r \tau$ away from the zero-th diffraction order, where $v_r = 2\hbar k/m = 5.644$ mm/s is the known recoil velocity and τ is the time-of-flight time. Figure 4.17 shows the diffraction pattern measured at $\tau = 10$ ms and Fig. 4.17 shows the averaged line-cut profile after correcting for the $11.5°$ rotation angle relative to the x-axes defined by the $x-$lattice beam. By comparing measured Δx and Δy to the expectation value, we determine the image magnification to be 19.5 ± 0.1. The linear size of the CCD pixel corresponds to a length of 666 ± 4 nm in the focal plane.
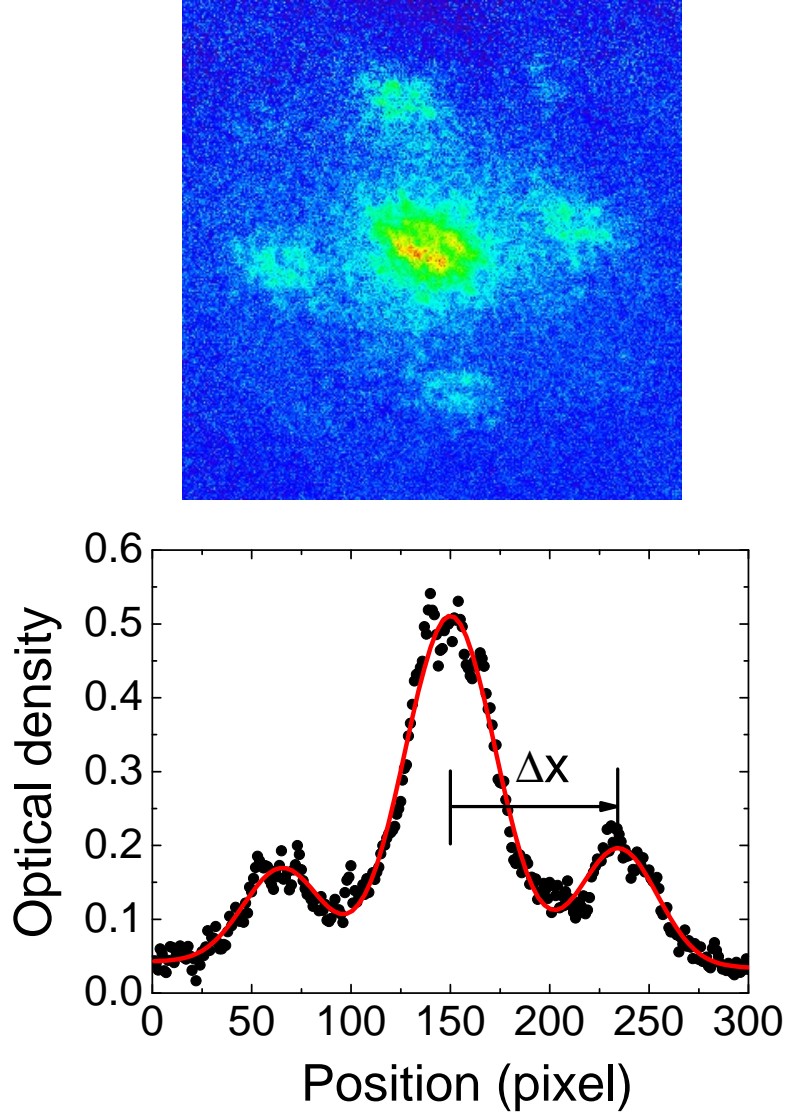
Figure 4.17: Calibration of the image magnification in the vertical imaging path. (a) Diffraction pattern of BEC atoms recorded via the vertical imaging path after they are released from a 2D square optical lattice for a time-of-flight time of 10 ms. Image size is 300×300 pixels. Camera is rotated by $11.5°$ relative to the x-axes. (b) Averaged line-cut profile (circles) along the x-axes defined by the x-lattice beam. Solid line is a three-Gaussian fit to the data, assuming the ± 1 recoil peaks are both at a distance Δx away from the central peak.

CHAPTER 5

IN SITU OBSERVATION OF INCOMPRESSIBLE MOTT-INSULATING DOMAINS IN ULTRACOLD ATOMIC GASES

The observation of the Superfluid (SF) to Mott-insulator (MI) phase transition of ultracold atoms in optical lattices [8] was an enabling discovery in experimental many-body physics, providing the first tangible example of a quantum phase transition (one that occurs even at zero temperature) in an ultracold atomic gas. For a trapped gas, the spatially varying local chemical potential introduces multiple quantum phases into a single sample, complicating the interpretation of bulk measurements [8, 130, 12, 131, 132]. Here, we report spatially resolved, in situ imaging of a two-dimensional ultracold atomic gas as it crosses the SF to MI transition, providing unprecedented and direct access to individual characteristics of the insulating, superfluid and normal phases. We present results for the local compressibility in all phases, showing a strong suppression in the insulator domain, and observe suppressed density fluctuations for the MI in accordance with the fluctuation-dissipation theorem. Furthermore, we obtain a direct measure of the finite temperature of the system. Taken together, these methods make possible a highly complete characterization of multiple phases in a strongly correlated Bose gas, and of the interplay between quantum and thermal fluctuations in the quantum critical regime.

This is a published work by N. Gemelke, X. Zhang, C.-L. Hung, and C. Chin in *Nature* **460**, 995 (2009).

5.1   Introduction

Since its theoretical inception [133, 9, 10], two of the most celebrated properties of the bosonic Mott insulator have been its incompressibility and suppression of local density fluctuations [134], induced by the enhanced importance of inter-particle repulsion for particles subject to a strong lat-

tice potential. The result for a trapped atom gas is the remarkable "wedding-cake" density profile, where successive MI domains are manifest as plateaus of constant density. Related phenomena have been studied through the coherence [8, 130], transport [8, 12], noise correlations [131], and number variance [8, 132], but direct observation of the incompressibility has proven difficult due to the inhomogeneous nature of all experiments to date, and to the technical difficulty of making spatially resolved measurements. Innovative experimental efforts incorporating tomographic imaging and other advanced techniques have yielded evidence [28, 120] that shell structure exists in the Mott insulator regime, though none has directly observed the incompressibility of the insulating density plateaus by imaging a complete and single physical system in situ.

We report studies based on direct in-situ imaging of an atomic MI. By loading a degenerate Bose gas of cesium-133 atoms into a thin layer of a two-dimensional optical lattice potential, and adiabatically increasing the optical lattice depth, we observe the emergence of an extremely flat density near the center of the cloud, which corresponds to a MI phase with accurately one atom-per-site. From density profiles, we extract important thermodynamic and statistical information, confirming the incompressibility and reduction of density fluctuations in the MI as described by the fluctuation-dissipation theorem.

5.2 Experiment

The single layer, two-dimensional (2D) optical lattice is formed by two pairs of counter-propagating laser beams derived from a Yb fiber laser at wavelength $\lambda = 1064$ nm. The pairs are oriented orthogonally on the horizontal $(x - y)$ plane, forming a square lattice with site spacing $d = \lambda/2 = 0.532$ μm. A weak harmonic potential of $V_H = m(\omega_x^2 x^2 + \omega_y^2 y^2)/2$ localizes the sample, where m is the cesium mass, and the geometric mean of the trap frequencies is $\omega_r = \sqrt{\omega_x \omega_y} = 2\pi \times 9.5$Hz (a weak dependence on lattice depth is described in Section 5.5). Vertical confinement is provided by an additional vertical optical lattice with a site spacing 4 μm,

formed by two beams intersecting at an angle of $15°$, confining atoms in a gaussian wavepacket of width (oscillator length) $a_z = 0.30$ μm. The sample is loaded into a single site of the vertical lattice, kept deep to prevent vertical tunneling. Tunneling in the horizontal 2D lattice is controlled by varying the lattice depth V [8]. Details on preparation of the atomic sample can be found in Chapter 4 and Ref. [135].

We obtain a top view of the sample using absorption imaging, directly revealing the atomic surface density $n(x, y)$ on the horizontal plane. The imaging resolution is $3 \sim 4\mu$m, and magnification such that one imaging pixel corresponds to an area of $(2\mu\text{m})^2$ on the object plane. Unit filling in a 2D optical lattice has a conveniently measurable optical absorption on resonance.

The superflulid-to-Mott insulator (SF-MI) transition of ultracold atoms in an optical lattice is described by the Bose-Hubbard model, characterized by on-site interaction U and the tunneling t [10]. In 2D optical lattices, superfluid is converted into a MI when U/t exceeds 16 [130, 13] near the density of one atom per site. Here, the SF-MI phase transition can be induced by either increasing the lattice potential depth V (typically measured in units of recoil energy $E_R = h\,1.3$kHz, where h is Planck's constant) [8, 130, 120] or the atomic interaction strength (characterized by scattering length a) via a magnetically-tuned Feshbach resonance [6], together providing complete, independent control of U and t.

Atomic density profiles in the lattice are shown in Fig. 5.1. For weak lattice depths (superfluid regime), the density profiles are bell-shape, with negative curvature at the center (Fig. 5.1a), indicating a finite, positive compressibility dictated by the interaction coupling constant (discussed below.) In sufficiently deep lattices, we observe a flattened density at the center of the sample (Fig. 5.1b,c), indicating development of a Mott insulating phase with one particle per lattice site. This density plateau, an important feature of the MI phase, arises from incompressibility.

A primary check on the MI is to compare the measured density in the plateau to that corresponding to one atom-per-site, given by MI physics as a "standard candle" of atomic density. Using the known scattering cross-section, correcting for saturation effects (see Section 5.5), we determine the
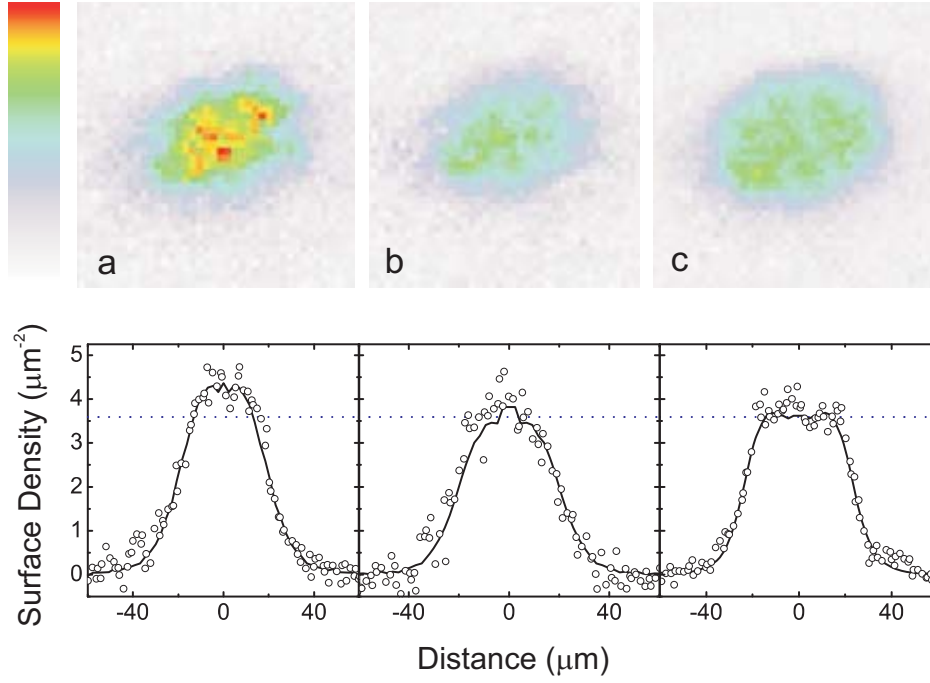
Figure 5.1: False color absorption images and line cuts along major axis of density profiles for $N = 7500$ ultracold cesium atoms at scattering length $a = 310\ a_B$ in a 2D optical lattice. (a) Superfluid regime (shallow lattice $V = 2.4E_R$), (b) Phase transition regime (medium lattice depth $V = 9.4E_R$), and (c) Mott insulator regime (deep lattice $V = 22E_R$). Images are averaged over three experiment repetitions. Colorbar shows linear variation with density from zero to peak value of $5.4\mu m^{-2}$. Line cuts are taken along the major axis, and compared to radial average of density (solid line) over the entire image as described in text. The blue horizontal line indicates the density of one atom per site.

plateau density to be $n = 3.5(3)/\mu\text{m}^2$, in agreement with the expected value $1/d^2 = 3.53/\mu\text{m}^2$.

To distinguish a MI from superfluid or normal gas, we histogram the occurrence of pixels $h(n)$ in the images corresponding to a density n with a bin size of $\Delta n \ll n$. The MI plateau, containing a large number of pixels with similar atomic density, appears as a peak at $n = 1/d^2$ (Fig. 5.2a). In general, the occurrence of a particular density n can be regarded as the rate at which local chemical potential changes with density, multiplied by the number of pixels $w(\mu)\Delta\mu$ corresponding to a chemical potential between μ and $\mu + \Delta\mu$. The occurrence at density n is then

$$h(n) = \Delta n \, w(\mu)\Delta\mu/\Delta n \approx \Delta n \, w(\mu)\kappa^{-1}, \tag{5.1}$$

where $\kappa = \partial n/\partial \mu$ is the local compressibility [136]. In a harmonic trap, $w(\mu) = 2\pi/md^2\omega_r^2$ is constant, and the histogram is a particularly useful tool to distinguish different phases. For a pure BEC in the Thomas-Fermi limit, the compressibility is constant to the maximally-allowed density n_{pk}, and results in a constant $h(n)$ for $n \leq n_{pk}$ (see Fig. 5.2b for $0.5/d^2 < n < 1.5/d^2$). For the MI, the density is insensitive to chemical potential in a narrow range near $n = 1/d^2$, indicating a vanishing compressibility, and thus a sharp histogram peak at $n = 1/d^2$. The peak's presence in Fig. 5.2a is thus directly related to the incompressibility in the Mott phase. Finally, the compressibility of a normal (ideal) gas is proportional to its density, thus $h(n) \propto 1/n$, leading to the strong upturn at low densities in Fig. 5.2a,b for both regimes.

Much more information can be obtained from the density profiles, as recently suggested in Ref. [29]. For example, the compressibility in a two-dimensional cylindrically symmetric trap can be written

$$\kappa = \partial n/\partial \mu = -n'(r)/(rm\omega_r^2), \tag{5.2}$$

where we have assumed the local density approximation, and that the chemical potential depends on the trapping potential $\mu = \mu_0 - V_H(r)$. For a BEC in the Thomas-Fermi regime, the compress-
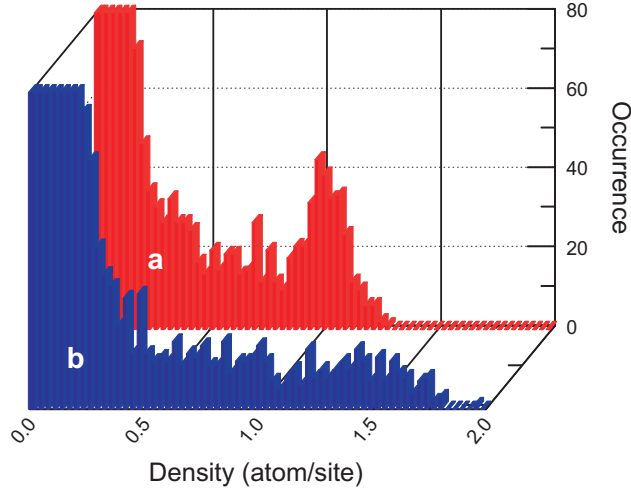
Figure 5.2: Histograms of density profiles in the MI regime (a, $V = 38E_R$, $a = 460a_B$) and the superfluid regime (b, $V = 0.5E_R$, $a = 460a_B$.) The histograms are based on an average of three density images. The bin size is $\Delta n = 0.03$.

ibility is positive and constant, $\kappa_{BEC} = 1/g$, where $g = \sqrt{8\pi}a\hbar^2/ma_z$ is the (2D) interaction parameter[96]. We can thereby relate the measured compressibility to that of a BEC as

$$\frac{\kappa}{\kappa_{BEC}} = -(\frac{2}{\pi})^{7/2}\frac{n'(r)}{rd^{-4}}\frac{a}{a_z}(\frac{E_R}{\hbar\omega_r})^2. \tag{5.3}$$

We evaluate κ from azimuthally averaged density profiles (Fig. 5.3a). Eccentricity of the trap is corrected by rescaling the principal axes as determined from the density profile, and verified to be consistent with direct measurement of trap frequencies. Due to the singular nature of $n'(r)/r$ near the center, we evaluate κ there by fitting $n(r)$ to a quadratic, $n(r) = n(0) - \alpha r^2$. The curvature then gives the compressibility as $\kappa(0) = 2\alpha/m\omega_r^2$, for which we obtain $\kappa/\kappa_{BEC} = 0.34(10)$ in a weak lattice and $\kappa/\kappa_{BEC} = 0.013(6)$ in a strong lattice (See Fig. 5.3). In the weak lattice (SF regime), the finite and constant compressibility at the center agrees with expectation for the superfluid phase, though lower than expected, which we attribute to finite temperature and calibration of trap parameters. The finite temperature is also clear in the exponential tail of the density profile and the compressibility [123], from which we derive the temperature $10(2)$ nK in
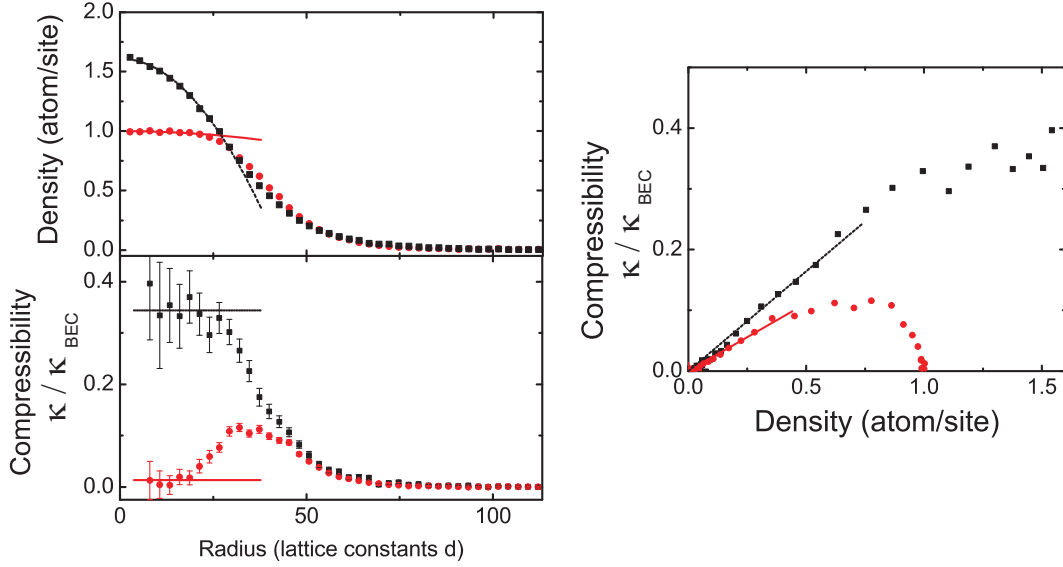
Figure 5.3: Extraction of compressibility from density profiles. (a) Radially averaged profiles (3 images) in the superfluid (black squares: $V = 0.3E_R$, $N = 7200$) and MI (red circles: $V = 22E_R$, $N = 6700$), with $a = 310a_B$. A quadratic fit to the sample's center extracts the curvature near $r = 0$. (b) Normalized compressibilities derived from (a) using Eq. (1) in the superfluid (black squares) and MI (red circles) regimes. The horizontal lines indicate compressibility near $r = 0$, estimated from the quadratic fits in (a). Rising compressibility at $r = 30d$ marks the MI boundary. (c) The dependence of compressibility on atomic density. Linear dependence at low densities (normal gas) is best fit by solid lines. Error bars indicate standard error in the mean.

the superfluid regime ($V = 0.3E_r$) and $15(3)$ nK in the MI regime ($V = 22E_r$).

In a deep lattice (MI regime), we observe a strong reduction of the compressibility in the trap center, below that in the superfluid phase for the weak lattice, strongly supporting the emergence of a MI phase at the center of the sample. Away from center, κ suddenly increases at $r = 20d$, then decreases for $r > 40d$. The exponential decay is again consistent with a normal gas. Between MI and normal gas ($20d < r < 40d$), a more detailed measurement and model of compressibility would be necessary to identify the local phase.

5.3 Qualitative comparison to the fluctuation-dissipation theorem

Within the local density approximation, one may consider any small area of the sample as a thermodynamic subsystem in a grand-canonical ensemble, assumed to be in equilibrium with the remainder of the gas. One can then invoke the fluctuation-dissipation theorem (FDT) (see e.g. Refs. [136, 95]) to ascertain that incompressibility necessarily implies a low local particle number fluctuation; this relationship takes the form

$$\delta n^2 \approx \kappa \, k_B T \tag{5.4}$$

Resolved in-situ imaging provides an enticing opportunity to measure fluctuations of the local density [137, 134], and thus check the validity of the FDT. We measured fluctuations by recording multiple absorption images, calculating the variance of density measured in each pixel (each collects signals from a patch of $(2\mu m/d)^2 \approx 14$ lattice sites). Fig. 5.4 shows the recorded fluctuations, where pixels are binned according to their mean atomic density. Fluctuations consist of detection (photo-electron shot) noise and thermal and quantum atomic density fluctuations. Detection shot noise can be well-calibrated and modeled by analyzing portions of the images with low density; extension to higher optical depth (density) shows the weak dependence illustrated in Fig. 5.4.

Above the detection noise, density fluctuations (see Fig. 5.4) show a strong qualitative agreement with the compressibility presented in Fig. 5.3 as expected from the FDT. For example, the Mott-phase shows a strong suppression of fluctuations at the density of one atom-per-site. The superfluid regime lacks this feature, instead showing a pronounced flattening as the sample transitions from normal gas to superfluid, as expected from the constant compressibility in the superfluid phase (Figure 3c). Finally, at low density, the normal gas shows a temperature-independent fluctuation of $\delta n = \gamma \sqrt{n}$, which can be anticipated from Figure 3c, and agrees with the FDT. The coefficient γ is roughly consistent with the FDT, and measured imaging resolution (see Section 5.5).
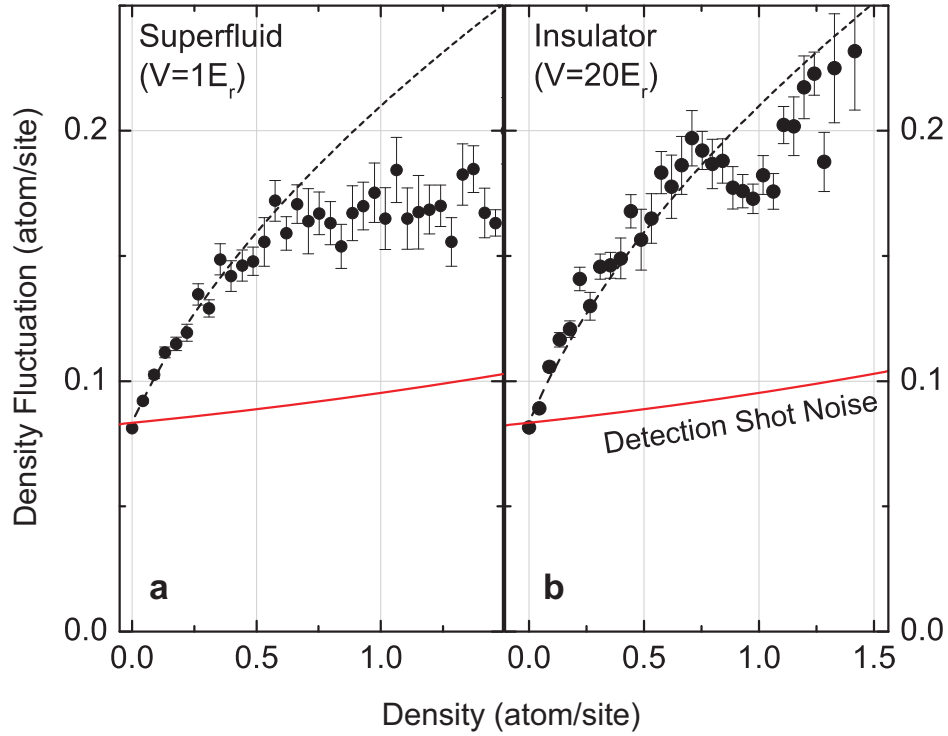
Figure 5.4: The fluctuation of local density extracted from a set of twelve absorption images in the weak (a) and deep (b) lattice regimes. The insulator and superfluid show a pronounced difference at one atom-per-site, where the insulator's fluctuation is suppressed by incompressibility. In the superfluid, constant compressibility initiates a flattening. At low densities, in both regimes, the fluctuation shows a characteristic $\sqrt{n}$ dependence, where the gas is presumed to be normal; the dashed line shows best fit $\sqrt{n}$ dependence. The total number of atoms was $N = 8300$ (SF) and $N = 9600$ (MI) with $a = 310a_B$ for both sets. Error bars indicate standard error in the mean.

5.4   Conclusion

Clearly, in situ imaging of the Mott insulator is a powerful new tool to investigate new quantum phases of cold atoms in optical lattices. From the density profiles, not only can one observe the density plateau, incompressibility and reduction of fluctuations in the Mott insulating phase, but also demonstrate a qualitative validation of the fluctuation-dissipation theorem. Relatively modest extension of this work holds new promise for studying the role of quantum fluctuations, correlation and thermodynamics near a quantum phase transition.

5.5   Methods Summary

Cesium Bose condensates are produced by forced evaporative cooling in a crossed beam dipole trap. The condensate is compressed vertically by loading into a single layer of an optical lattice with the scattering length tuned near zero. After this, the lattice is adiabatically instated by controlled retroreflection of dipole trapping beams, and the scattering length brought to its final value. Imaging is performed absorptively along the vertical, calibrated for saturation effects by varying the intensity of the imaging light. Fluctuations of density are calculated for each pixel in a series of images taken at identical experimental parameters, and plotted against the mean density at that pixel. The parameter γ is estimated from a model of the expected averaging of thermal fluctuations over an imaging resolution limited spot.

5.5.1   Preparation of BEC in a thin 2D optical lattice

The ^{133}Cs BEC is formed in a crossed-beam dipole trap by an efficient evaporative cooling method [135]. The dipole trap consists of three beams on the horizontal plane: two orthogonal beams at the wavelength of 1064 nm (Yb fiber laser, YLR-20-1064-LP-SF, IPG), focused to $1/e^2$ radii of 350 μm, and one CO_2 laser beam at the wavelength of 10.6 μm (Gem-Select 100, Coherent),

focused to a vertical $1/e^2$ radius of 70 μm and horizontal of 2 mm . The CO_2 beam intersects the Yb laser beams at an angle of $45°$ and provides an enhanced vertical confinement to support the atoms against gravity. With $N = 10^4$ atoms in a pure condensate, the Thomas-Fermi radii of the condensate are $(r_x, r_y, r_z) = (23, 14, 3.6)\mu$m.

After a pure BEC is obtained, the sample is compressed vertically by introducing a vertical lattice, formed by two laser beams (Mephisto, Innolight) inclined at $+7.5°$ and $-7.5°$ relative to the horizontal plane. The vertical lattice has a spacing of 4 μm and, together with the crossed dipole trap, forms an array of 2D oblate "pancake" potentials, with harmonic confinement frequencies of 850Hz at its maximum depth.

In order to load the condensate into a single pancake trap, we first ramp the magnetic field to 17.2 G in 400 ms, reducing the s-wave scattering length to $a < 10\ a_B$, and then turn on the vertical lattice in 100 ms. Atomic population in other lattice sites, if any, can be identified by observing an interference pattern in time-of-flight images taken from the side. For this work, we observe a sufficiently weak interference pattern contrast to conclude $> 98\%$ of the atoms are in a single pancake trap. After the vertical lattice is fully turned on, the CO_2 laser intensity is ramped to zero in 100 ms while the scattering length is ramped to its final value by tuning the external magnetic field.

The 2D lattice potential in the horizontal (x- and y-) directions is formed by introducing retro-reflections of the 1064 nm dipole trap beams. A continuous evolution from a pure dipole trap (with zero retro-reflection) to a 2D optical lattice (with significant retro-reflection) is achieved by passing each dipole trap beam (after it passes through the atomic cloud once) through two acousto-optic modulators (AOMs) controlled by the same radio-frequency (rf) source, then off a retroreflection mirror. The AOMs induce an overall zero frequency shift, but permit a dynamic control of the retroreflection intensity over six orders of magnitude. To load the lattice to a depth of $38E_r$, the retro-reflection intensities are slowly ramped over 200ms with an exponential wave-form of 36ms time constant. For smaller final lattice depths, the ramp waveform is fixed but

duration shortened. Onsite interaction energy U and tunneling rate t are evaluated from the measurements of the lattice vibration frequencies and band structure calculation. Envelope trapping frequencies were separately measured by exciting center of mass oscillations, and found to be consistent with orientation and ellipticity of in-situ images of atomic density. A weak variation of the mean envelope frequency with lattice depth was measured and accounted for by the expression $\omega_r = \sqrt{\omega_x \omega_y} = 2\pi \times 9.5(1 + V/82 E_R)$Hz.

5.5.2 Calibration of atomic surface density

By varying the intensity of the imaging beam, we measure the optical depth on resonance in the density plateau using $OD = \ln(M_0/M)$, where M is the number of photons collected by a CCD pixel in the presence of the atoms and M_0 is that without the atoms. The optical depth in the plateau is extracted from a fit to the peak in the histogram. We then fit the variation of peak optical depth assuming $OD = n\sigma/(1 + M_0/M_{sat})$ to determine the depth in the zero intensity limit $M_0 \to 0$, and thus the surface density of the sample. Here, σ=0.347 μm^2 is the known cesium atom-photon cross-section while the fit parameter M_{sat} represents the photon number on a CCD pixel at the atomic saturation intensity.

5.5.3 Fluctuation of atomic density

The fluctuations in the absorption images are estimated by taking the average of 11 images under the same experimental procedure, and calculating the mean and variance of optical depth measured at each CCD pixel. Fluctuations are presumed to arise from optical shot noise, thermal atomic fluctuation, and long lengthscale variations arising from total atom number fluctuation. The optical shot noise is calibrated by examining regions with negligible atomic density, and extended to higher optical depth using $\delta OD_{os} \propto \sqrt{1 + e^{OD}}$. For the thermal cloud, with density $n < 0.3$ atoms/site, the fluctuation-dissipation theorem predicts $\delta N_a = \sqrt{N_a}$, with N_a the number of atoms measured

in a given region. This result should be valid for a region significantly larger than the correlation length, which we expect for the normal gas to be on order of the deBroglie thermal wavelength, expected to be $< 1.5\mu$m for our sample. Though each imaging pixel corresponds to an area in the object plane consisting of $\sim$14 sites, imperfect imaging resolution is expected to effectively average away a certain fraction of the total fluctuation. This effect can be calculated, assuming statistical independence for each site, by summing the weight $w_{i,j}$ of a resolution-limited spot falling within a given pixel j for each lattice site i, giving a variance reduced by $\sum_i w_{i,j}^2$. The result for our parameters is a reduction to $\delta n = \gamma\sqrt{n}$, with $\gamma \sim 0.11(1)$. This should be compared with the fraction of the total fluctuation shown in Fig. 5.4 corresponding to thermal fluctuations in the superfluid regime. To make this comparison, we reject global fluctuations associated with variation of the total atom number by subtracting the variance we calculate after first applying a resolution-spoiling gaussian blur to the images from the variance without modification. We find, for the remaining high spatial-frequency fluctuations, a best fit to γ of 0.15(2), using a gaussian blur $1/e^2$ radius of $r_b = 14\mu$m to remove global variations (the result varies within stated error for blur radii 7μm$< r_b < 28\mu$m). The remaining discrepancy is likely due to calibration of imaging resolution, and possibly the effect of a nonnegligible correlation length.

CHAPTER 6

SLOW MASS TRANSPORT AND STATISTICAL EVOLUTION OF AN ATOMIC GAS ACROSS THE SUPERFLUID-MOTT INSULATOR TRANSITION

In this chapter, we study transport dynamics of ultracold cesium atoms in a two-dimensional optical lattice across the superfluid-Mott insulator transition based on *in situ* imaging. Inducing the phase transition with a lattice ramping routine expected to be locally adiabatic, we observe a global mass redistribution which requires a very long time to equilibrate, more than 100 times longer than the microscopic time scales for on-site interaction and tunneling. When the sample enters the Mott insulator regime, mass transport significantly slows down. By employing fast recombination loss pulses to analyze the occupancy distribution, we observe similarly slow-evolving dynamics, and a lower effective temperature at the center of the sample.

This is a published work by C.-L. Hung, X. Zhang, N. Gemelke, and C. Chin. in *Phys. Rev. Lett.* **104**, 160403 (2010). Copyright 2010 by the American Physical Society.

6.1 Introduction

The thorough understanding of atomic interactions in optical lattices provides a testing ground to investigate hypothetical models widely discussed in condensed matter and many-body physics [14, 138]. Because of the simplicity and tunability of the underlying Hamiltonian, research on optical lattices generates new fronts to perform precise, quantitative comparison between theoretical calculations and measurements. This new class of "precision many-body physics" has generated tremendous interest in recent years to locate the superfluid (SF) to Mott insulator (MI) phase boundaries [8, 130, 139], described by the Bose-Hubbard model [9, 10], and to characterize Mott and band insulators in Fermi gases [140, 141], described by the Fermi-Hubbard model [142]. Many

new, exotic quantum phases in optical lattices have also been proposed [138], even in the absence of counterparts in condensed matter physics.

As promising as the precise characterization of quantum phases is, fundamental assumptions such as the thermal dynamic equilibrium of the sample should be investigated. Since the preparation of quantum gases generally involves ramping up the lattice potential, dynamics are an inseparable part of all optical lattice experiments. Very slow equilibration processes have been reported in one-dimensional optical lattices [143] and have been suggested by the observation of long-lived repulsively bound pairs [144] and doublons [145] in three-dimensional lattices. Prospects of non-equilibrium dynamics in optical lattices have also attracted much interest recently. Mass and entropy transport in the optical lattices can provide a wealth of information to characterize the underlying quantum phases [146, 147]. Dynamic passage across a phase transition can lead to the proliferation of topological defects in the optical lattices [148].

In the following sections, we study global dynamics of ultracold atomic gases in a monolayer of two-dimensional (2D) optical lattice. After ramping up the lattice potential, we observe both mass transport and statistical distribution of atomic occupancy in the lattice. Mass transport is directly seen from *in situ* density profiles, while occupancy statistics is probed by inducing loss in sites of three or more atoms using a fast three-body recombination loss pulse (see Fig. 6.1). Both processes show intriguing behavior at times much longer than microscopic time scales for atomic interaction and tunneling.

6.2   Experiment

We begin the experiment with a ^{133}Cs quantum gas in a 2D optical trap. Details on the preparation of the quantum gas and optical lattice loading procedure can be found in Ref. [135] and Ref. [149], respectively. In brief, a nearly pure Bose condensate is loaded into a 2D optical dipole trap, formed by two orthogonally crossed beams on the $x - y$ plane and a one-dimensional vertical optical
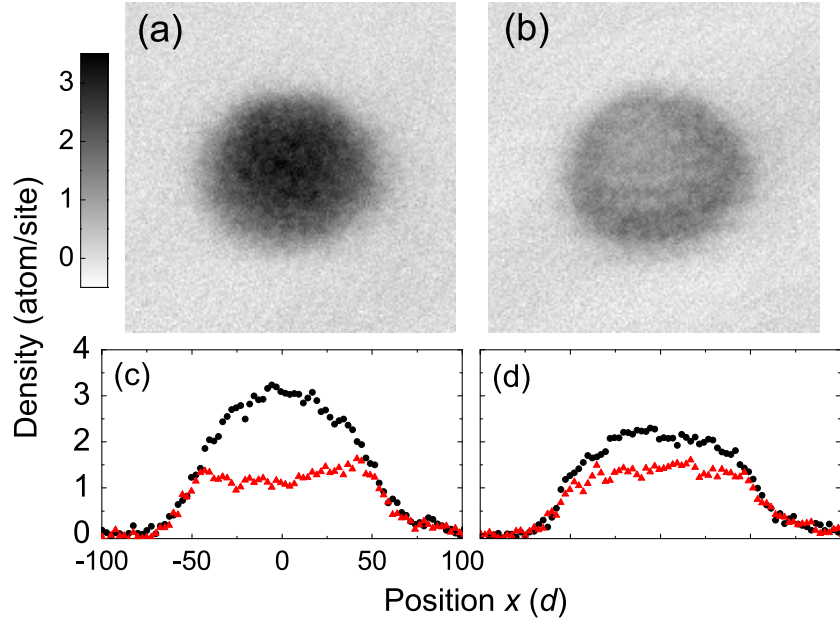
Figure 6.1: Averaged absorption images and density cross sections of $N = 2 \times 10^4$ cesium atoms in a monolayer of 2D optical lattice. After ramping the lattice in 150 ms to a lattice depth $V_f = 13\ E_R$, (a) shows the sample immediately after the ramp. In (b), an additional fast recombination pulse removes atoms in sites of occupancy three or more. (c) shows the average density cross sections of (a) (circles) and (b) (triangles). (d) shows the average density cross sections of the samples with additional 800 ms hold time after the ramp, without (circles) and with the recombination loss pulse (triangles). Image size is $(106\ \mu\mathrm{m})^2 = (200\ \mathrm{sites})^2$ and seven images are used in each averaged result.

133

lattice of 4 μm spacing which confines the whole sample in a single "pancake"-like lattice site [149]. Using microwave tomography, we find $\sim 95\%$ of the atoms are loaded into a single pancake trap. The remaining $\sim 5\%$ in the neighboring sites do not contribute to the main results reported in this letter. The trap vibration frequencies are $(\omega_x, \omega_y, \omega_z) = 2\pi \times (11, 13, 1970)$ Hz, and the cloud temperature is $T = 11$ nK. The ratios $\hbar\omega_i/k_B T = (0.05, 0.06, 9)$ indicate the sample is two-dimensional. After 2D trap loading, we adjust the atomic scattering length a by ramping the magnetic field to a designated value, typically, $B = 20.7$ G where $a = 200\ a_B$ and a_B is the Bohr radius. At this field, the three-body recombination loss rate is at the Efimov minimum [44].

We introduce a 2D optical lattice by slowly turning on retro-reflections of the crossed dipole beams which add a square lattice potential with lattice spacing $d = 532$ nm and a weak contribution to the envelope confinement characterized by a mean radial frequency $\sqrt{\omega_x \omega_y} = 2\pi(1 + V/82E_R) \times 12$ Hz, where $E_R = k_B \times 64$ nK is the recoil energy and V is the lattice depth. Care is taken to equalize lattice depths in the x and y directions by balancing the lattice vibration frequencies to within 5%. Based on the vibration frequency measurements, we calculate tunneling t and on-site interaction U numerically from the band structure in a homogeneous 2D lattice.

We ramp on the lattice depth following $V(\tau) = V_f(1+\gamma)/[1+\gamma e^{4(\tau-\tau_c)^2/\tau_c^2}]$ [150], preceded by a 30 ms linear ramp from 0 to 0.4 E_R to ensure a smooth turning on of the lattice potential at low depth. The final depth V_f is reached at time $\tau = \tau_c$ and γ is chosen such that $V(0) = 0.4\ E_R$. After the ramp, the sample is held in the lattice for a hold time τ_{hold}. The adiabaticity parameter of the ramp is given by

$$\alpha = \hbar|\dot{t}|/t^2; \tag{6.1}$$

slow ramps with $\alpha < 1$ suggest that local equilibrium of the system is preserved [151, 150].

We obtain the *in situ* density profile of the sample by absorption imaging normal to the $x - y$ plane. After a hold time τ_{hold}, we first switch the magnetic field to $B = 17.7$ G ($a = 40a_B$) and then turn off the 2D lattice 100 μs before the imaging, reducing the on-site peak density by a factor
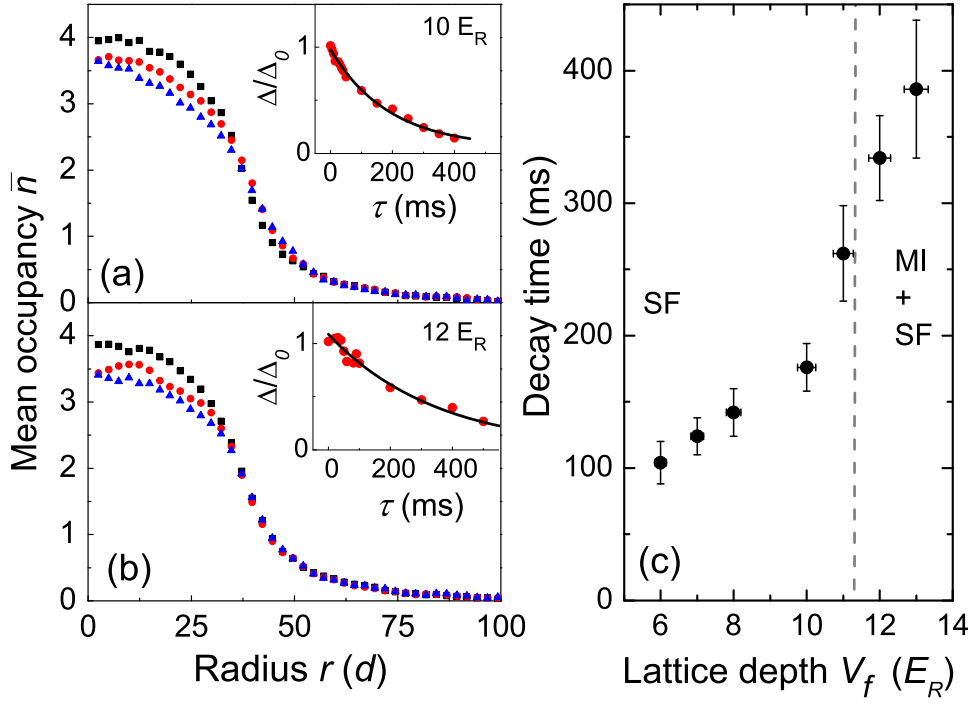
Figure 6.2: Evolution of the density profile after a short lattice ramp. Following a $\tau_c = 20$ ms ramp to $V_f = 10\ E_R$ ($U/t = 11$, $\alpha < 0.6$), (a) shows the radial density profiles measured after hold times of 0 ms (squares), 200 ms (circles) and 500 ms (triangles). Inset shows the time evolution of Δ, normalized to the initial value $\Delta_0 = \Delta(0)$ (circles) and the single exponential fit. (b) shows the profiles measured at $V_f = 12\ E_R$ ($U/t = 20$, $\alpha < 1$). The fitted decay times at different depths of V_f are shown in (c), where the dashed line marks the critical lattice depth, see text.

of 30, in order to mitigate any density dependent loss during the imaging process.[1] The atomic density is measured with a spatial resolution of 1.3 μm using a long working distance (34 mm) commercial microscope objective. The strength and duration of the imaging pulse are chosen to keep the travel distance of the atoms due to the radiation pressure from the imaging beam small compared to the depth of focus, while maintaining a good signal-to-noise ratio.

---

1. This procedure suppresses systematic distortions of the density measurement. In previous works [149], our imaging was performed at low magnetic fields, where recombination and radiative losses preferentially reduce the density at the center and can enhance the plateau feature in deep lattices.

6.3   Dynamics of mass transport

Our first step to study the global dynamics is to watch how the density profile equilibrates after a lattice ramp. Here we employ a ramp which is locally adiabatic, but is fast enough to induce detectable mass flow. An example is shown in Fig. 6.2 (a), where after a $\tau_c = 20$ ms ramp to $V_f = 10\ E_R$ ($U/t = 11$, $\alpha < 0.6$) the sample of $N = 2 \times 10^4$ atoms at scattering length $a = 200\ a_B$ gently expands and the peak density slowly decreases. This deformation is consistent with the increase of repulsive atomic interaction in stronger lattice confinement.

To quantify the rate of mass redistribution, we define the root-mean-square deviation of a density profile at hold time τ from equilibrium as

$$\Delta(\tau) = \left\{ \sum_i [\bar{n}_i(\tau) - \bar{n}_{eq,i}]^2 \right\}^{1/2}, \tag{6.2}$$

where the sum goes over lattice sites enclosing the sample. $\bar{n}_i(\tau)$ is the mean occupancy of site i at hold time τ, obtained by averaging over an annular area centered on the cloud, containing site i, and with width 1.3 μm [149]. $\bar{n}_{eq,i}$ is the mean occupancy of site i at equilibrium, which we obtain from samples that cease to evolve after long hold time of $\tau_{hold} = 500 \sim 800$ ms.

At lattice depths $V_f < 10\ E_R$, the sample shows a weak breathing mode oscillation in the first 50 ms of hold time. After 50 ms, $\Delta(\tau)$ can be fit by single exponential decays with time constants > 100 ms. When the lattice depth reaches 11 E_R or higher, the mass flow slows down significantly, see Fig. 6.2 (b) and (c), suggesting that the mass transport is suppressed in this regime. The crossover behavior near $V_f = 11\ E_R$, where $U/t \approx 15$, is consistent with a recent observation of the suppression of superfluidity at $U/t = 16$ in a 2D optical lattice [130], and quantum Monte Carlo calculations, predicting that the SF-MI transition at the tip of the $n = 1$ Mott lobe occurs at $U/t \approx 16.74$ in 2D [115]. For $V_f > 13\ E_R$, even slower dynamics require much longer hold time and the slow loss from three-body recombination limits our ability to determine the mass

redistribution time scale.[2]

The slow dynamics throughout the SF-MI regime indicate that the global thermalization is much slower than the microscopic time scales. Indeed, in the range of $V_f = 6 \sim 13\ E_R$, tunneling to neighboring sites occurs in $\tau_t = \hbar/zt = 0.6 \sim 3$ ms, where $z = 4$ is the coordination number of the 2D square lattice.

6.4   Dynamics of occupancy statistics

In the second experiment, we investigate the evolution of occupancy statistics. For this, we develop a scheme to determine the fraction of sites with three or more atoms by inducing a fast three-body recombination loss, and comparing the density profiles with and without the loss. For cesium atoms, extremely fast three-body loss can be induced by jumping the magnetic field near an Efimov resonance [44], where the loss happens much faster than atoms tunnel.

We induce the recombination loss at $V_f = 13\ E_R$ by jumping the magnetic field to $B = 2$ G for a duration of 1 ms before imaging at 17.7 G. The $1/e$ time of the field switching is below $100\ \mu$s. During the switching, the magnetic field from the eddy currents is measured by microwave spectroscopy and compensated by a controlled overshoot of currents in the magnetic coils. At 2 G, the three-body loss rate is as high as $(20\ \mu\text{s})^{-1}$ for 3 atoms in one site, much faster than the tunneling rate $1/\tau_t = (3\text{ ms})^{-1}$, and the 1 ms pulse is sufficient to remove all the atoms that could participate in the loss process.

We analyze the dynamics of on-site statistics by first ramping the lattice in τ_c =300 ms to V_f =13 E_R ($U/t = 41$, $\alpha < 0.1$) at scattering length a =310 a_B and then holding the sample for up to 800 ms. Here, the lattice ramp is slow enough to ensure negligible subsequent mass flow. Density profiles at different hold times, with and without the loss pulse, are shown in Fig. 6.3 (a-c). A larger fractional loss occurs at the central part of the sample where the density is higher, as

---

2. At $V_f = 13\ E_R$ and scattering length $a = 200\ a_0$, three body loss rate for 3 atoms per site is $\sim 0.4\ s^{-1}$

expected; there is no apparent loss in the wing. We observe a smaller fractional loss after a longer hold time, which suggests that fewer sites are found with three or more atoms.

The evolution of the statistics is best shown in Fig. 6.3 (d), where the atom loss, $\Delta\bar{n}$, is induced by the recombination pulse after different hold times. A dramatic difference is seen near the center with mean occupancy near $\bar{n} = 2$. Here the loss fraction reaches $\Delta\bar{n}/\bar{n} = 50\%$ immediately after the ramp, and it slowly declines to merely 15% after a hold time of $\tau_{hold} = 800$ ms.

To quantitatively model the loss, we assume, starting with n atoms in one site, (n modulo 3) atoms remain after the pulse. To test this model, we prepare an ideal 2D gas by tuning the magnetic field to $B = 17.1$ G, where $a \approx 0\ a_B$. We then quickly ramp on the lattice to $30\ E_R$ in 10 ms to freeze the on-site occupancy and perform the loss measurement. For non-interacting particles, we expect the occupancy obeys a Poisson distribution. The calculated atom loss, see black solid lines in Fig. 6.3 (d) and the inset, is in good agreement with our measurement.

Recombination losses measured with interacting samples and slow lattice ramps, on the other hand, deviate from the Poisson model toward lower values for all mean occupancies (see Fig. 6.3 (d)). This is a general characteristic of the strongly interacting gas.

To gain further insight into the occupancy statistics in an insulator, we compare our measurement with thermal insulator model discussed in Section 4.2.8. In deep lattices with $t \ll U, k_B T$, the probability for occupancy n can be written as $P_n = Q^{-1} e^{-\beta(H_n - \mu n)}$, where $H_n \approx (U/2)n(n-1)$, $\beta = 1/k_B T$, μ is the local chemical potential and $Q = \sum_n e^{-\beta(H_n - \mu n)}$ is the grand partition function. The mean occupancy is then $\bar{n} = \sum n P_n$ and the loss is modeled as

$$\Delta\bar{n} = \bar{n} - \sum P_n (n \bmod 3). \tag{6.3}$$

Calculations for $k_B T/U = 1, 0.5, 0.3, 0.2$ and 0 are plotted in Fig. 6.3(d). For $\bar{n} < 2.5$, all curves show smaller loss than does the Poisson model. An insulator at lower temperature experiences fewer losses because thermal fluctuation is reduced. At zero temperature, loss only occurs at
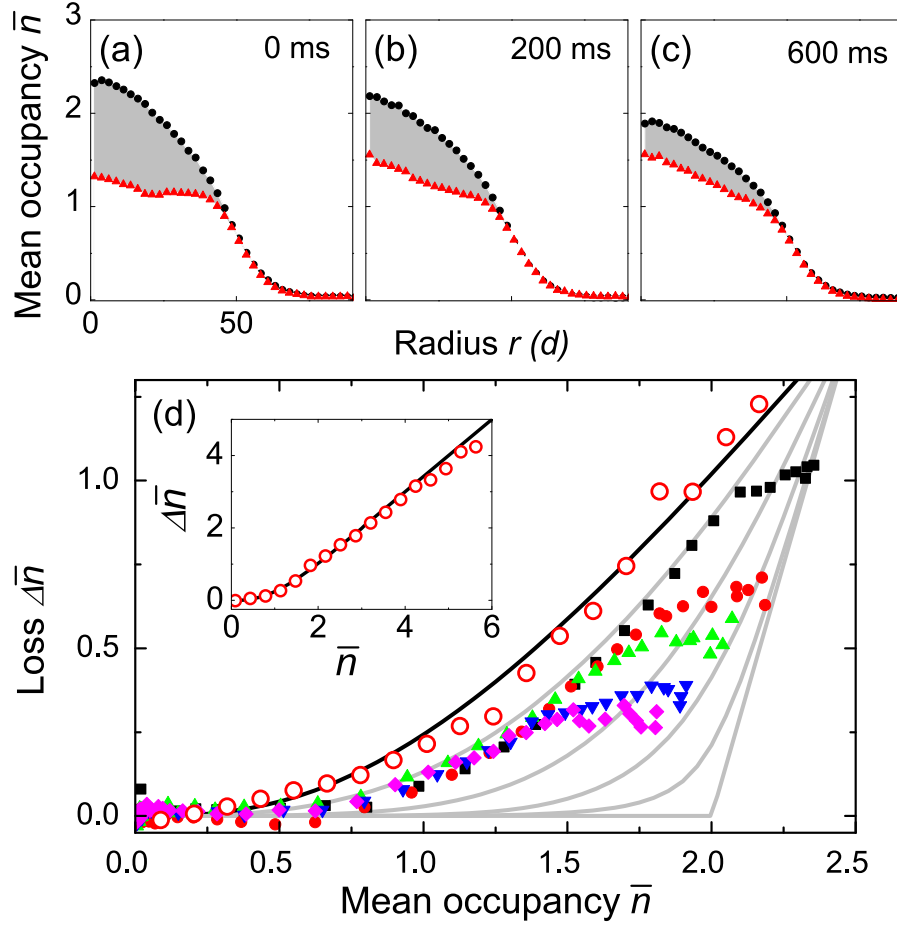
Figure 6.3: Evolution of the on-site statistics in a Mott insulator. ($N = 1.6 \times 10^4$, $\tau_c = 300$ ms, $V_f = 13$ E_R). Upper figures show the density profiles of the samples held in the final depth $V_f = 13$ E_R for $\tau_{hold} =$ (a) 0 ms, (b) 200 ms, (c) 600 ms and then imaged with (triangles) and without (circles) the recombination pulse. Shaded areas mark the loss fractions. (d) shows the loss $\Delta \bar{n}$ versus mean occupancy $\bar{n}$ measured after different hold times (filled symbols): 0 ms (squares), 200 ms (circles), 400 ms (upward triangles), 600 ms (downward triangles) and 800 ms (diamonds). Gray lines are the loss derived from an insulator model, see text, assuming $k_B T/U = 1$ (higher curve), 0.5, 0.3, 0.2 and 0 (lower curve). The black line, derived from the Poisson distribution, is in good agreement with an ideal gas measurement (open circles). The inset shows an extended view.

$\bar{n} > 2$, where the occupancy $n \geq 3$ is unavoidable.

Surprisingly, our loss measurements do not follow the model with a uniform temperature for up to 800 ms hold time. Using $U = k_B \times 26$ nK and describing the deviation from a constant temperature contour by an effective local temperature $T_{\text{eff}}(r)$, we find the center of the cloud has a lower $T_{\text{eff}} \sim 6$ nK, while for the wing $T_{\text{eff}} \sim 20$ nK even after 800 ms of hold time. This persistent temperature variation across the sample suggests that the heat flow is insufficient to establish a global thermal equilibrium even after 800 ms hold time. This may be aggravated by a large heat capacity of the atoms in the wing.

6.5   Conclusion

Both the slow mass and heat flows observed in this work raise the issue of describing quantum gases in optical lattices using a thermodynamic model. We suspect that the slow dynamics is partially due to our large sample size of $(100 \text{ sites})^2$ and the dimensionality of our system, and partially associated with the critical behavior of the system. Across the SF-MI transition, the sample enters the quantum critical regime, where long equilibration times are expected [148, 152]. Other interesting mechanisms include the long lifetime of the excited doublon [145], which could slow down statistical redistribution of occupancies while supporting mass transport. Moreover, the slow recombination loss preferentially removes atoms at the center of the sample, creating $\sim 20\%$ observed reduction in the mean occupancy during 800 ms of hold time, which could lead to a radial temperature gradient assuming sufficient local rethermalization.

In summary, we show that the *in situ* density profiles of atoms in a 2D optical lattice provide a viable tool for investigating dynamic processes induced by chemical potential and temperature imbalance. In both cases, we find equilibration times much longer than the microscopic tunneling time scale. Further investigation into these processes and the relevance of our observation to the quantum dynamics in the critical regime will be reported in the future.

CHAPTER 7

OBSERVATION OF SCALE INVARIANCE AND UNIVERSALITY IN TWO-DIMENSIONAL BOSE GASES

The collective behavior of a many-body system near a continuous phase transition is insensitive to the details of its microscopic physics[50]. Characteristic features near the phase transition are that the thermodynamic observables follow generalized scaling laws[50]. The Berezinskii-Kosterlitz-Thouless (BKT) phase transition[16, 17] in two-dimensional (2D) Bose gases presents a particularly interesting case because the marginal dimensionality and intrinsic scaling symmetry[153] result in a broad fluctuation regime which manifests itself in an extended range of universal scaling behavior. Studies on BKT transition in cold atoms have stimulated great interest in recent years[18, 154, 19, 20, 155, 156], clear demonstration of a critical behavior near the phase transition, however, has remained an elusive goal. Here we report the observation of a scale-invariant, universal behavior of 2D gases through in-situ density and density fluctuation measurements at different temperatures and interaction strengths. The extracted thermodynamic functions confirm a wide universal region near the BKT phase transition, provide a sensitive test to the universality prediction by classical-field theory [103, 107] and quantum Monte Carlo (MC) calculations[108], and point toward growing density-density correlations in the fluctuation region. Our assay raises new perspectives to explore further universal phenomena in the realm of classical and quantum critical physics.

This is a published work by C.-L. Hung, X. Zhang, N. Gemelke, and C. Chin in *Nature* **470**, 239 (2011).

7.1 Introduction

In 2D Bose gases, critical behavior develops in the BKT transition regime, where an ordered phase with finite-ranged coherence competes with thermal fluctuations and induces a continuous phase transition from normal gas to superfluid with quasi-long range order[17]. In this fluctuation region, a universal and scale-invariant description for the system is expected through the power-law scaling of thermodynamic quantities with respect to the coupling strength and a characteristic length scale[107, 100], e.g., thermal de Broglie wavelength (Fig. 7.1a). For weakly interacting gases at finite temperatures, in particular, the scale invariance prevails over the normal, fluctuation, and superfluid regions because of the density-independent coupling constant[96] and the symmetry of underlying Hamiltonian[153].

In this chapter, we experimentally verify the scale invariance and universality of interacting 2D Bose gases, and identify BKT critical points. We test scale invariance of *in situ* density and density fluctuations of ^{133}Cs 2D gases at various temperatures. We study the universality near the BKT transition by tuning the atomic scattering length using a magnetic Feshbach resonance[6] and observing a universal scaling behavior of the equation of state and the quasi-condensate density. Finally, by comparing the local density fluctuations and the compressibility derived from the density profiles, we provide strong evidence of a growing density-density correlation in the fluctuation regime.

7.2 Experiment

We begin the experiment by loading a nearly pure ^{133}Cs Bose condensate of $N = 2 \times 10^4$ atoms into a single pancake-like optical potential with strong confinement in the vertical (z-) direction and weak radial confinement in the horizontal (r-) direction[149, 157]. The trapping potential, $V(r, z) = m\omega_r^2 r^2/2 + m\omega_z^2 z^2/2$, has mean harmonic trapping frequencies $\omega_r = 2\pi \times 10$ Hz and $\omega_z = 2\pi \times 1900$ Hz. Here, r denotes the radial distance to the trap center and m is the cesium
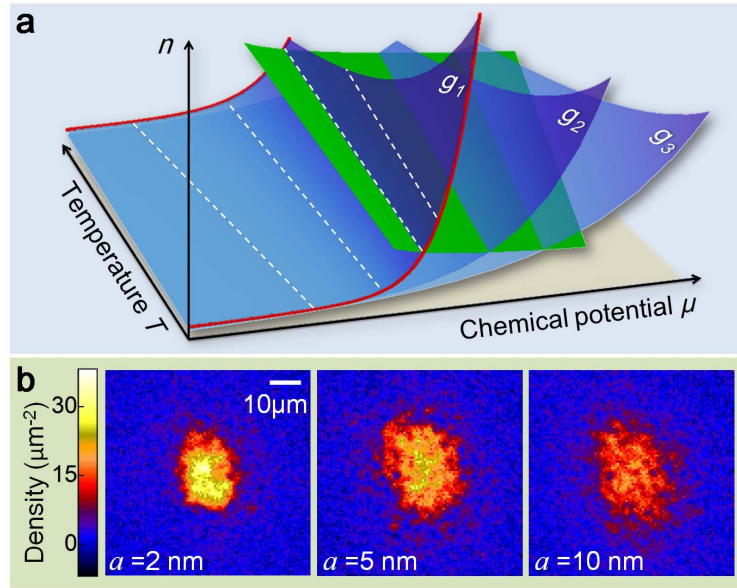
Figure 7.1: Illustration of scale invariance and universality in 2D quantum gases. (a) Scale invariance links any thermodynamic observable at different μ and T via a simple power-law scaling. In a 2D Bose gas with coupling constant $g \ll 1$, atomic density n measured at different temperatures (red lines) can be scaled through constant μ/T and n/T contours (dashed lines). Near the BKT phase transition boundary (green plane), systems with different $g = g_1, g_2...$ (blue planes) scale universally. (b) *In situ* density measurements of trapped 2D gases provide crucial information to test the hypotheses of scale invariance and universality. Sample images at different scattering lengths a are obtained from single shot.

atomic mass. In this trap, we reach temperatures as low as $T = 15$ nK and moderate peak chemical potential $\mu_0 < k_B T$. The ratio $\hbar\omega_z/\mu_0 > \hbar\omega_z/k_B T \sim 6$ indicates that the sample is deeply in the 2D regime with $< 1\%$ population in the vertical excited states. Here, $\hbar = h/2\pi$, h is the Planck constant, and k_B is the Boltzmann constant. The 2D coupling constant is evaluated according to $g = \sqrt{8\pi}a/l_z$ [96], where a is the atomic scattering length and $l_z = 200$ nm is the vertical harmonic oscillator length. We control the scattering length a in the range of $2 \sim 10$ nm$\ll l_z$, resulting in weak coupling strengths $g = 0.05 \sim 0.26$. Here, the density-dependent correction to g[96, 158] is expected to be small and negligible ($< 2\%$).

We obtain *in situ* density distributions of 2D gases by performing absorption imaging perpendicular to the horizontal plane with a commercial microscope objective and a CCD camera[157] (see Fig. 7.1b for sample images). About 50 images are collected for each experiment condition, and the average density n and the density variance δn^2 are evaluated pixel-wise (see Section 7.7). We obtain the radial density $n(r)$ and variance $\delta n^2(r)$ profiles (Fig. 7.2 insets) by accounting for the cloud anisotropy and performing azimuthal averaging[149].

We obtain the equation of state $n(\mu, T)$ from the averaged density profile by assigning a local chemical potential $\mu(r) = \mu_0 - V(r, 0)$ to each point according to local density approximation. Both T and μ_0 can be determined from the low density wing where the sample is assumed normal and the density profile can be fit to a mean-field formula $n(\mu, T) = -\lambda_{dB}^{-2} \ln[1 - \exp(\mu/k_B T - gn\lambda_{dB}^2/\pi)]$[155], where $\lambda_{dB} = h/\sqrt{2\pi m k_B T}$ is the thermal de Broglie wavelength.

7.3 Observation of scale invariance

We confirm the scale invariance of a 2D gas by first introducing the dimensionless, scaled form of density $\tilde{n} = n\lambda_{dB}^2$ (phase space density), fluctuation $\delta\tilde{n}^2 = \delta n^2 \lambda_{dB}^4$, and chemical potential
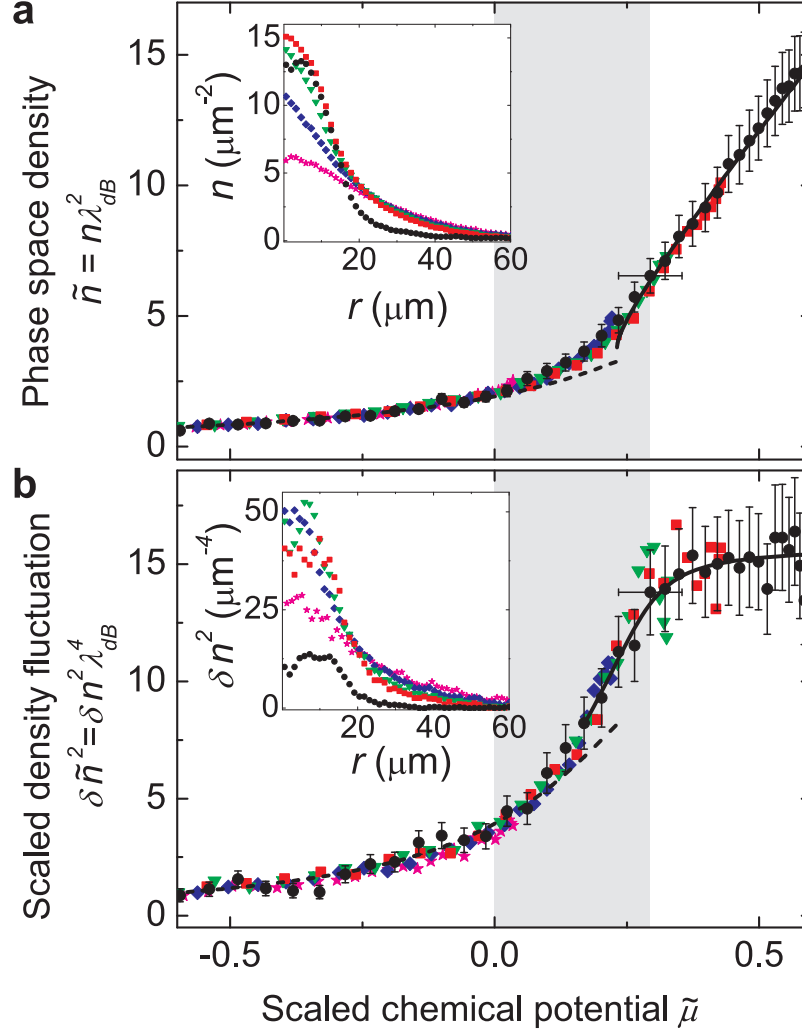
Figure 7.2: Scale invariance of density and its fluctuation. (a) Scaled density (phase space density) $\tilde{n} = n\lambda_{dB}^2$ as a function of the scaled chemical potential $\tilde{\mu} = \mu/k_B T$ measured at five different temperatures: $T = 21$ nK (black circles), 37 nK (red squares), 42 nK (green triangles), 49 nK (blue diamonds), and 60 nK (magenta stars), and coupling strength $g = 0.26$. Mean-field expectations for normal gas (dashed line) and superfluid (solid line) are shown for comparison. Inset shows the radial density profiles before scaling. (b) Scaled fluctuation $\delta\tilde{n}^2 = \delta n^2 \lambda_{dB}^4$ at different temperatures. Dashed line is the mean-field calculation based on the fluctuation-dissipation theorem[20]. Solid line is an empirical fit to the crossover feature from which the critical chemical potential $\tilde{\mu}_c$ is determined. Inset shows the radial fluctuation profiles before scaling. The shaded area marks the fluctuation region $0 < \tilde{\mu} < \tilde{\mu}_c$. Error bars show standard deviation of the measurement.

$\tilde{\mu} = \mu/k_B T$, and showing that the equation of state and the fluctuation satisfy the following forms:

$$\tilde{n} = F(\tilde{\mu}) \tag{7.1}$$

$$\delta\tilde{n}^2 = G(\tilde{\mu}), \tag{7.2}$$

where F and G are generic functions. This suggests both energy and length scales are set solely by the thermal energy and the de Broglie wavelength, respectively. An example at $g = 0.26$ ($a = 10$ nm) is shown in Fig. 7.2. Here we show that while the original density and fluctuation profiles are temperature dependent (see Fig. 7.2 insets), all profiles collapse to a single curve in the scaled units. At negative chemical potential $\tilde{\mu} < 0$, the system is normal and can be described by a mean-field model (dashed lines). In the range of $0 < \tilde{\mu} < 0.3$, the system enters the fluctuation regime and deviation from the mean-field calculation becomes evident. Crossing from normal gas to this regime, however, we do not observe sharp transition feature in the equation of state. At even higher $\tilde{\mu} > 0.3$, the system becomes a superfluid and the density closely follows a mean-field prediction[107] $\tilde{n} = 2\pi\tilde{\mu}/g + \ln(2\tilde{n}g/\pi - 2\tilde{\mu})$. We notice that the mean-field theory in the superfluid limit also cannot accurately describe the system in the fluctuation regime. Transition into the BKT superfluid phase is most easily seen in the scaled fluctuation $\delta\tilde{n}^2$, which crosses over to a nearly constant value due to the suppression of fluctuation in the superfluid regime[159]. In the density profile $\tilde{n}$, a corresponding transition feature can be found when one computes the derivative $\partial\tilde{n}/\partial\tilde{\mu}$, i.e., the scaled compressibility $\tilde{\kappa}$, as suggested by the fluctuation-dissipation theorem discussed in later paragraphs and Fig. 7.4. Finally, our measurement suggests that the validity of scale invariance extends to all thermal, fluctuation and superfluid regimes, a special feature for weakly-interacting 2D gases[153] which guided the analysis of a recent experiment[109].

7.3.1   Determination of the BKT critical points

We associate the crossover feature in the density fluctuations $\delta\tilde{n}^2$ and the scaled compressibility $\tilde{\kappa}$ with the BKT transition[159, 160]. To estimate the location of the transition point, we apply an empirical fit to this feature and determine the critical chemical potential $\tilde{\mu}_c$ and the critical phase space density $\tilde{n}_c$ (see Section 7.7). Results at different g in the range of 0.05 to 0.26 are shown in Fig. 7.3c-d and compared to the theoretical prediction of $\tilde{n}_c = \ln(\xi/g)$ and $\tilde{\mu}_c = (g/\pi)\ln(\xi_\mu/g)$[102], where $\xi = 380$ and $\xi_\mu = 13.2$ are determined from a classical-field MC calculation[103]. Our results show good agreement with the theory, apart from a potential systematic error from the choice of the fit function, which can account for a down shift of 10% in the fit values of $\tilde{\mu}_c$ and $\tilde{n}_c$.

7.4   Observation of universality

Further comparison between profiles at different interaction strengths allows us to test the universality of 2D Bose gases. Sufficiently close to the BKT critical point with $|\tilde{\mu} - \tilde{\mu}_c| < g$, one expects the phase space density shows a universal behavior[107],

$$\tilde{n} - \tilde{n}_c = H(\frac{\tilde{\mu} - \tilde{\mu}_c}{g}), \tag{7.3}$$

where H is a generic function. Here, density and chemical potential are offset from the critical values $\tilde{n}_c$ and $\tilde{\mu}_c$, which remove the non-universal dependence on the microscopic details of the interaction[100, 107].

To test the universality hypothesis, we rescale $\tilde{\mu}$ to $\tilde{\mu}/g$ and look for critical values $\tilde{n}_c$ and $\tilde{\mu}_c$ such that the equations of state at all values of g display a universal curve in the phase transition regime (see Section 7.7). Indeed, we find that all rescaled profiles can collapse to a single curve in the fluctuation region $-1 < (\tilde{\mu} - \tilde{\mu}_c)/g < 0$ and remain overlapped in an extended range of

$|\tilde{\mu} - \tilde{\mu}_c|/g \leq 2$ (see Fig. 7.3a), which contrasts the very different equations of state $\tilde{n}(\tilde{\mu})$ at various g shown in the inset of Fig. 7.3a. Our result closely follows the classical-field prediction[107] and quantum MC calculations[108] assuming strictly 2D mean-field contribution, and the fitting parameters: critical density $\tilde{n}_c$ and chemical potential $\tilde{\mu}_c$ show proper dependence on g and are in fair agreement with the theory prediction[103] (see Fig. 7.3c-d). We emphasize that critical values determined from the density fluctuations (see Fig. 7.3c-d) match well with those determined from the universal behavior, indicating that universality is a powerful tool to determine the critical point from a continuous and smooth density profile. Similar agreement with the theory on the critical densities has also been reported based on different experiment techniques[154, 20, 156].

Further universal features near the phase transition can be revealed in the growth of the quasi-condensate (QC) density $n_q = \sqrt{n^2 - \delta n^2}$ across the phase transition[103, 107, 161]. QC is a measure of the non-thermal population in a degenerate Bose gas. A finite QC density does not necessarily imply superfluidity, but can be responsible for a non-Gaussian distribution observed in the momentum space[20]. QC is predicted to be universal near the critical point following[107]

$$\tilde{n}_q = Q(\frac{\tilde{\mu} - \tilde{\mu}_c}{g}), \tag{7.4}$$

where Q is a generic function and $\tilde{n}_q = n_q \lambda_{dB}^2$.

We employ both of our density and fluctuation measurements to evaluate $\tilde{n}_q$ at various g. Adopting $\tilde{\mu}_c$ determined from the universal behavior of the density profile, we immediately find that all measurements collapse to a single curve in the range of $|\tilde{\mu} - \tilde{\mu}_c|/g \leq 2$ with apparent growth of QC density entering the fluctuation region (Fig. 7.3b). The generic function Q we determined is in good agreement with the classical-field[107] and quantum MC[108] calculations with no fitting parameters. Both our density and fluctuation measurements show universal behaviors throughout the fluctuation region where a mean-field description fails and confirm universality in a 2D Bose gas near the BKT phase transition[107, 108].
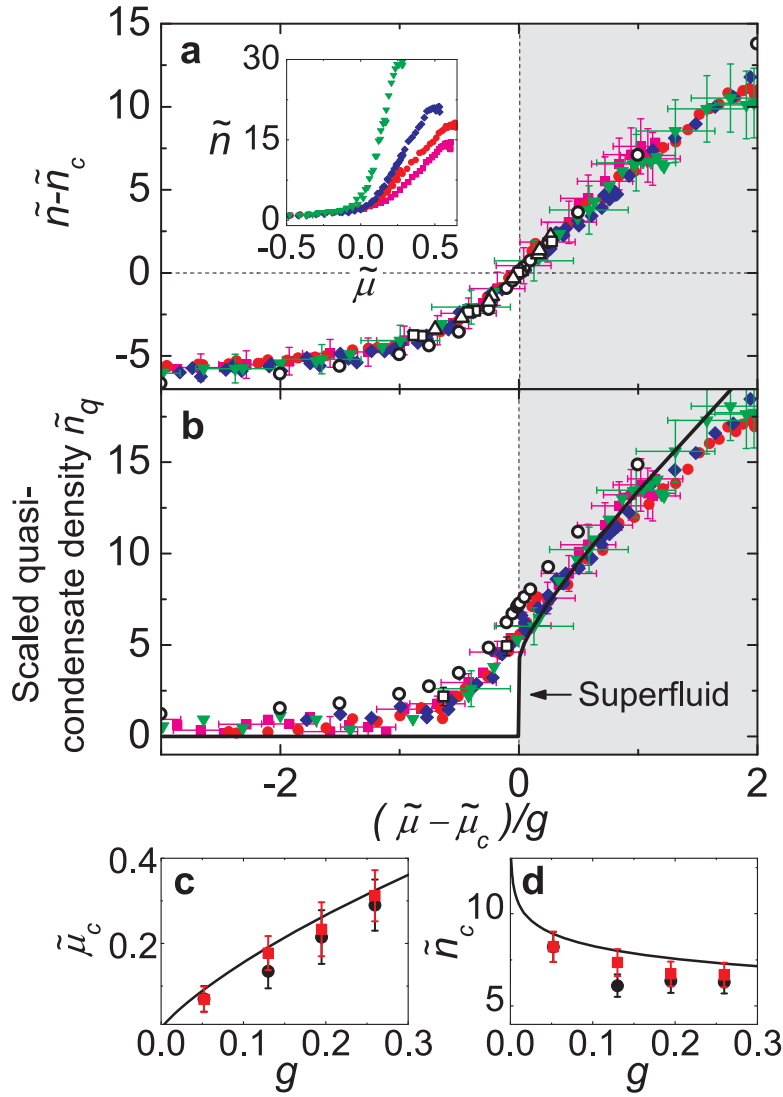
Figure 7.3: Universal behavior near the BKT critical point. (a) Rescaled density profiles $\tilde{n} - \tilde{n}_c$ measured at various coupling strengths, $g = 0.05$ (green triangles), 0.13 (blue diamonds), 0.19 (red circles), and 0.26 (magenta squares). Inset shows the original equations of state $\tilde{n}(\tilde{\mu})$. (b) scaled quasi-condensate density $\tilde{n}_q = \sqrt{\tilde{n}^2 - \delta\tilde{n}^2}$ at different interaction strengths. In both plots, MC calculations from Ref. [107] (open circles) and Ref. [108] ((a)open squares for $g = 0.07$ and open triangles for $g = 0.14$; (b) open squares) are plotted for comparison. The shaded area marks the superfluid regime and the solid line in (b) shows the superfluid phase space density calculation[12]. (c-d) critical values $\tilde{\mu}_c$ and $\tilde{n}_c$ determined from the following methods: universal scaling as shown in (a) (see Section 7.7, red squares), density fluctuation crossover (see text, black circles), and MC calculation from Ref. [103] (solid line). Experiment values coincide at $g = 0.05$ identically, as a result of our analysis (see Section 7.7). Error bars show the standard deviation of the measurement.

7.5 Observation of growing density-density correlations in the critical fluctuation region

The generic functions we described in the previous paragraphs offer new avenues to investigate the critical behavior of the 2D gas. Following the framework of scale invariance, we compare the dimensionless compressibility $\tilde{\kappa} = \partial\tilde{n}/\partial\tilde{\mu} = F'(\tilde{\mu})$ and the fluctuation $\delta\tilde{n}^2 = G(\tilde{\mu})$ extracted from the measurements at $g = 0.05$ and 0.26 (see Fig. 7.4). In the normal gas regime at low phase space density $(G(\tilde{\mu}), F'(\tilde{\mu}) < 3)$, a simple equality $G = F'$ is observed. This result is consistent with the fluctuation-dissipation theorem (FDT) for a classical grand canonical ensemble[162], which gives $k_B T \frac{\partial N}{\partial\mu} = \delta N^2$, where N is the particle number in a detection cell. In the fluctuation and the superfluid regimes at higher phase space density, our measurement shows that density fluctuations drop below the compressibility $G < F'$.

Natural explanations for the observed deviation include non-vanishing dynamic density susceptibility at low temperature[163] and the emergence of correlations in the fluctuation region[164]. While the former scenario is outside the scope of this article, we show that the correlation alone can explain our observation. Including correlation, the compressibility conforms to[165, 164]

$$\tilde{\kappa}(\mathbf{r}) = \lambda_{dB}^{-2} \int \langle \delta\tilde{n}(\mathbf{r})\delta\tilde{n}(\mathbf{r}+\mathbf{r}')\rangle d^2 r' \tag{7.5}$$

$$= \delta\tilde{n}^2(\mathbf{r})(1+z), \tag{7.6}$$

where $\langle...\rangle$ denotes ensemble average and $z = \frac{1+n(\mathbf{r})\int[g^{(2)}(\mathbf{r},\mathbf{r}+\mathbf{r}')-1]d^2 r'}{1+n(\mathbf{r})\int_v [g^{(2)}(\mathbf{r},\mathbf{r}+\mathbf{r}')-1]d^2 r'} - 1$ is the relative strength of correlation to local fluctuation $\delta\tilde{n}^2$ [164]. Here $g^{(2)}$ is the normalized second-order correlation function[94] and v denotes the effective area of the resolution limited spot. When the sample is uncorrelated, we have $z = 0$; non-zero z suggests finite correlations in the sample. In the fluctuation region shown in Fig. 7.4, observing a lower fluctuation than would be indicated
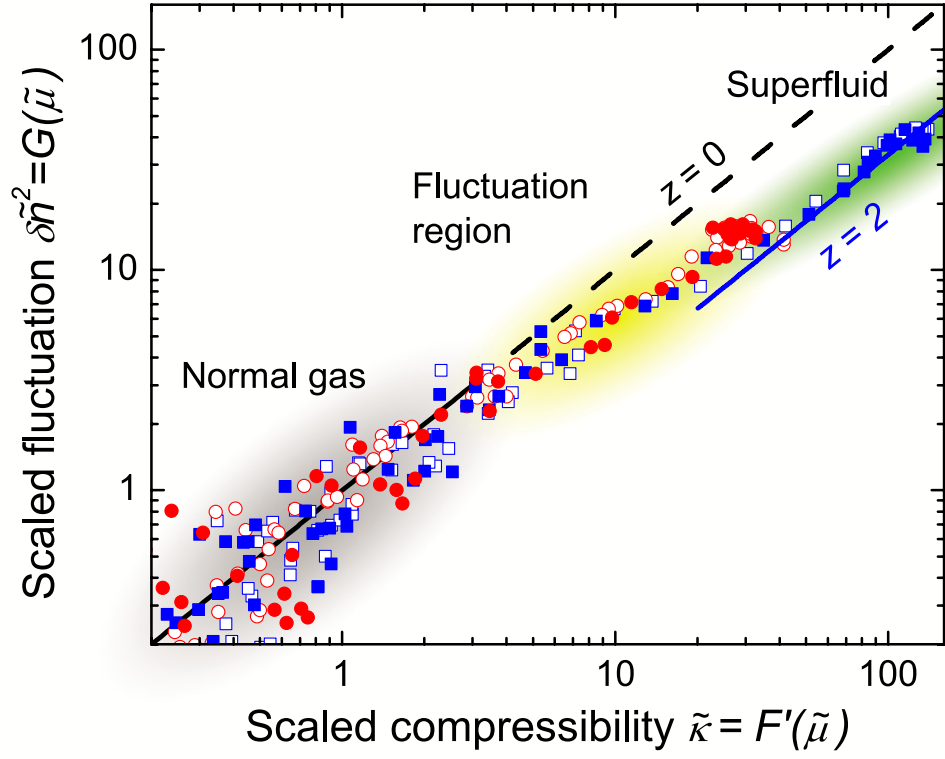
Figure 7.4: Fluctuation versus compressibility. Scaled compressibility $\tilde{\kappa} = F'(\tilde{\mu})$ and scaled density fluctuation $\delta\tilde{n}^2 = G(\tilde{\mu})$ are derived from measurements at two interaction strengths, $g = 0.05$ (squares) and $g = 0.26$ (circles), each containing two different temperatures between 20 and 40 nK (solid and open symbols, respectively). Diagonal line shows the expectation of $G = F'$ in the normal gas region. Solid line shows suppressed fluctuation $G = F'/(1 + z)$ with $z = 2$.

by the compressibility, with z approaching 2, suggests that the correlation length approaches or even exceeds our imaging cell dimension $\sqrt{v} \sim 2~\mu$m. This observation is in agreement with the expected growth of correlation when the system enters the fluctuation region. Similar length scales were also observed in the first-order coherence near the BKT phase transition using an interferometric method[20] and near the superfluid phase transition in three dimensions[117].

7.6   Conclusion

In summary, based on *in situ* density measurements at different chemical potential, temperature, and scattering length, we have explored and confirmed the global scale invariance of a weakly-interacting 2D gas, as well as the universal behavior near the critical point. Our results provide detailed description of critical thermodynamics near the BKT transition and offer new prospects to investigate other critical phenomena near classical or quantum phase transitions. In particular, we present experimental evidence of the growing correlations in the fluctuation region through the application of the fluctuation-dissipation theorem. Further investigations into the correlations will provide new insights into the rich critical phenomena near the transition point, for instance, critical opalescence and critical slowing.

7.7   Methods Summary

Preparation and detection of cesium 2D Bose gases are similar to those described in Ref. [157] . We adjust the temperature of the sample by applying magnetic field pulses near a Feshbach resonance to excite the atoms. We then tune the scattering length to a designated value, followed by 800 ms wait time to ensure full thermalization of the sample.

Absorption imaging is performed *in situ* using a strong resonant laser beam, saturating the sample to reduce the optical thickness. Atom-photon resonant cross-section and atomic density are independently calibrated. Averaged atom number N_i and number fluctuation δN_i^2 at i-th CCD

pixel are evaluated pixel-wise based on images taken under identical experiment conditions. The photon shot-noise, weakly depending on the sample's optical thickness, is calibrated and removed from the measured number variance. We correct the effect of finite imaging resolution on the remaining number variance using calibration from dilute thermal gas measurements. The density fluctuation δn_i^2 is obtained from the recovered atom number variance using $\delta n_i^2 \lambda_{dB}^2 = \delta N_i^2 / A$, which replaces the dependence on the CCD pixel area A by a proper area scale λ_{dB}^2.

7.7.1 Calibration of the atomic surface density and the atom number fluctuation.

The atomic surface density n of the 2D gas is evaluated with similar schemes discussed in Ref. [128], where the resonant cross-section σ_0 is independently calibrated using a thin 3D Bose condensate with similar optical thickness and the known atom number-to-Thomas-Fermi radius conversion. The resulting value can be compared to that determined from the atom shot-noise amplitude in dilute 2D thermal gases, where the noise is evaluated using binned CCD pixels to remove finite resolution effects. For dilute thermal gases, we expect $\delta N^2 = N$, where N is the mean atom number; we compare the fluctuation amplitude to the mean and extract the value of σ_0. Two results agree to within 10% and the residual non-linearity in the density calibration is negligible.

We evaluate the atom number variance δN^2 pixel-wise based on images taken under identical experiment conditions. The photon shot-noise contribution δN_p^2, which weakly depends on the sample's optical thickness $n\sigma_0$, is calibrated and removed from the atom number fluctuation using $\delta N_p^2 = (\delta N_0^2/2)[1 + \frac{(1+\gamma e^{-n\sigma_0})^2}{(1+\gamma)^2} e^{n\sigma_0}]$, where δN_0^2 is the photon shot-noise without atoms and γ is the ratio of the imaging beam intensity to the saturation intensity. Both δN_0^2 and γ are experimentally calibrated. We then correct for the effect of finite resolution on the number fluctuation[149] by comparing the atom number variance in a dilute thermal cloud to its mean atom number, using $\delta N^2 = N$, and applying this calibration to all fluctuations measured at lower temperatures and

higher densities.

7.7.2 *Density-density correlation in the fluctuation measurement.*

In the fluctuation measurement, we determine δn^2 from the pixel-wise atom number variance using the formula $\delta n^2 \lambda_{dB}^2 = \delta N^2 / A$, which replaces the dependence on the pixel area A by a natural area scale λ_{dB}^2. This definition, however, does not fully eliminate the dependence on the imaging resolution spot size $v \sim (2~\mu\text{m})^2$. In particular, when the density-density correlation length ξ approaches or exceeds the resolution, the measured fluctuation can depend on the fixed length scale $\sqrt{v}$, which can complicate the scaling behavior. However, we do not see clear deviation of scale invariance and universality within our measurement uncertainties (Fig. 7.2b and 3b). We attribute this to the small variation of the non-scale invariant contribution within our limited range of sample temperature. Further analysis on the correlations and fluctuations is in progress and the result will be published elsewhere.

7.7.3 *Determination of the BKT critical values from the fluctuation data.*

We use a hyperbolic function $y(\tilde{\mu}) = s(\tilde{\mu} - \tilde{\mu}_c) - \sqrt{s^2(\tilde{\mu} - \tilde{\mu}_c)^2 + w^2}$ to empirically fit the crossover feature of the density fluctuation near the transition region, assuming $\delta\tilde{n}^2(\tilde{\mu}) = De^{y(\tilde{\mu})}$, where the critical chemical potential $\tilde{\mu}_c$, the fluctuation in the superfluid regime D, the slope of the exponential rise s, and the width of the transition region w are fitting parameters. The critical phase space density is then determined from the density profile as $\tilde{n}_c = \tilde{n}(\tilde{\mu}_c)$. Other choices of fit functions give similar results, contributing only small systematics from the choice of different models.

7.7.4 Obtaining the universal function $H(x)$.

We use the density profiles in the inset of Fig. 7.3a to look for critical values $\tilde{n}_c$ and $\tilde{\mu}_c$ such that the equations of state at all values of g collapse to a single universal curve $H(x) = \tilde{n}(\tilde{\mu}) - \tilde{n}_c$, where $x = (\tilde{\mu} - \tilde{\mu}_c)/g$ is the rescaled chemical potential. To do this, we take the profile measured at $g = 0.05 \equiv g_r$ as the reference, evaluate $H_r(x) = \tilde{n}(g_r x + \tilde{\mu}_{c,r}) - \tilde{n}_{c,r}$ using the critical values $\tilde{n}_{c,r}$ and $\tilde{\mu}_{c,r}$ determined from the fluctuation crossover feature, and smoothly interpolate the data to make a continuous reference curve $H_r(x)$ in the range of $|x| \leq 1$. Using this model, we perform minimum chi-square fit to the profiles measured at all other values of g according to $\tilde{n}(\tilde{\mu}) = \tilde{n}_c + H_r(\frac{\tilde{\mu} - \tilde{\mu}_c}{g})$, with only $\tilde{n}_c$ and $\tilde{\mu}_c$ as free parameters. This procedure successfully collapses all density profiles (see Fig. 7.3a), and is independent of any theoretical model. The resulting critical values $\tilde{n}_c$ and $\tilde{\mu}_c$ are plotted in Fig. 7.3c-d.

CHAPTER 8

EXTRACTING DENSITY-DENSITY CORRELATIONS FROM IN SITU IMAGES OF ATOMIC QUANTUM GASES

In this chapter, we present a complete recipe to extract the density-density correlations and the static structure factor of a two-dimensional (2D) atomic quantum gas from *in situ* imaging. Using images of non-interacting thermal gases, we characterize and remove the systematic contributions of imaging aberrations to the measured density-density correlations of atomic samples. We determine the static structure factor and report results on weakly interacting 2D Bose gases, as well as strongly interacting gases in a 2D optical lattice. In the strongly interacting regime, we observe a strong suppression of the static structure factor at long wavelengths.

The is a published work by C.-L. Hung, X. Zhang, L.-C. Ha, S.-K. Tung, N. Gemelke, and C. Chin in *New J. Phys.* **13**, 075019 (2011) in a focus issue on *Quantum simulation*.

8.1 Introduction

Fluctuations and correlations result from the transient dynamics of a many-body system deviating away from its equilibrium state. Generally, fluctuations are stronger at higher temperatures and when the system is more susceptible to the external forces (as governed by the fluctuation-dissipation theorem, see [162, 34]). Local fluctuations and their correlations can thus be a powerful tool to probe thermodynamics, and to identify phase transition of a many-body system due to the sudden change of the susceptibility to the thermodynamic forces.

Measurement of fluctuations and correlations on degenerate atomic gases can reveal much information about their quantum nature [166]. Experiment examples include the quantum statistics of the atoms [167, 131, 168, 169, 170], pairing correlations [171] and quantum phases in reduced dimensions [172, 173]. In these experiments, images of the sample are taken after the time-of-flight

expansion in free space, from which the momentum-space correlations are extracted.

In situ imaging provides a new and powerful tool to examine the density fluctuations in real space [137, 149, 174, 175, 176, 121, 33, 177, 178], offering a complimentary description of the quantum state. This new tool has been used to resolve spatially separated thermodynamic phases in inhomogeneous samples. From *in situ* measurements, both Mott insulator density plateaus and a reduction of local density fluctuations were observed [149, 121, 33, 157]. Furthermore, a universal scaling behavior was observed in the density fluctuations of 2D Bose gases [179].

Precise measurements of spatial correlations, however, present significant technical challenges. In *in situ* imaging, one typically divides the density images into small unit cells or pixels and then evaluates the statistical correlation of the signals in the cells. If both the dimension of the cell and the imaging resolution are much smaller than the correlation length of the sample, the interpretation of the result is straightforward. In practice, because the correlation length of quantum gases is typically on the order of 1 μm, comparable to the optical wavelength that limits the image resolution, interpreting experimental data is often more difficult. Finite image resolution, due to either diffraction, aberrations or both, contributes to systematic errors and uncertainties in the fluctuation and correlation measurements.

In this paper, we present a general method to determine density-density correlations and static structure factors of quantum gases by carefully investigating and removing systematics due to imaging imperfections. In Section 2, we review the static structure factor and its relation to the real space density fluctuations. In Section 3, we describe how the density fluctuation power spectrum of a non-interacting thermal gas can be used to calibrate systematics in an imperfect imaging system, and show that the measurement can be explained by aberration theory. In Section 4, we present measurements of density fluctuations in weakly interacting 2D Bose gases and strongly interacting gases in a 2D optical lattice, and extract their static structure factors from the density-density correlations.

157

8.2 The density-density correlation function and the static structure factor

We start by considering a 2D, homogeneous sample at a mean density $\bar{n}$. The density-density correlation depends on the separation $\mathbf{r}_1 - \mathbf{r}_2$ between two points, and the static correlation function $\nu(\mathbf{r})$ is defined as [180]

$$
\begin{aligned}
\nu(\mathbf{r}_1 - \mathbf{r}_2) &= \bar{n}^{-1} \langle \delta n(\mathbf{r}_1) \delta n(\mathbf{r}_2) \rangle \\
&= \delta(\mathbf{r}_1 - \mathbf{r}_2) + \bar{n}^{-1} \langle \hat{\Psi}^\dagger(\mathbf{r}_1) \hat{\Psi}^\dagger(\mathbf{r}_2) \hat{\Psi}(\mathbf{r}_1) \hat{\Psi}(\mathbf{r}_2) \rangle - \bar{n}
\end{aligned}
\tag{8.1}
$$

where $\langle ... \rangle$ denotes the ensemble average, and $\delta n(\mathbf{r}) = n(\mathbf{r}) - \bar{n}$ is the local density fluctuation around its mean value $\bar{n}$. The Dirac delta function $\delta(\mathbf{r}_1 - \mathbf{r}_2)$ represents the autocorrelation of individual atoms, and $\langle \hat{\Psi}^\dagger(\mathbf{r}_1) \hat{\Psi}^\dagger(\mathbf{r}_2) \hat{\Psi}(\mathbf{r}_1) \hat{\Psi}(\mathbf{r}_2) \rangle = G^{(2)}(\mathbf{r}_1 - \mathbf{r}_2)$ is the second-order correlation function [94]. When the sample is completely uncorrelated, only atomic shot noise is present and $\nu(\mathbf{r}_1 - \mathbf{r}_2) = \delta(\mathbf{r}_1 - \mathbf{r}_2)$. At sufficiently high phase space density, when the inter-particle separation becomes comparable to the thermal de Broglie wavelength λ_{dB} or the healing length, density-density correlation becomes non-zero near this characteristic correlation length scale and $\nu(\mathbf{r})$ deviates from the simple shot noise behavior.

The static structure factor is the Fourier transform of the static correlation function [180, 35]

$$
S(\mathbf{k}) = \int \nu(\mathbf{r}) e^{-i\mathbf{k}\cdot\mathbf{r}} d\mathbf{r},
\tag{8.2}
$$

where $\mathbf{k}$ is the spatial frequency wave vector. We can rewrite the static structure factor in terms of the density fluctuation in the reciprocal space as [35]

$$
S(\mathbf{k}) = \frac{\langle \delta n(\mathbf{k}) \delta n(-\mathbf{k}) \rangle}{N} = \frac{\langle |\delta n(\mathbf{k})|^2 \rangle}{N},
\tag{8.3}
$$

where $\delta n(\mathbf{k}) = \int \delta n(\mathbf{r}) e^{-i\mathbf{k}\cdot\mathbf{r}} d\mathbf{r}$, and N is the total particle number. Here, $\delta n(-\mathbf{k}) = \delta n^*(\mathbf{k})$

since the density fluctuation $\delta n(\mathbf{r})$ is real. The static structure factor is therefore equal to the density fluctuation power spectrum, normalized to the total particle number N. A non-correlated gas possesses a structureless, flat spectrum $S(\mathbf{k}) = 1$ while a correlated gas shows a non-trivial $S(\mathbf{k})$ for k near or smaller than inverse of the correlation length ξ^{-1}.

The static structure factor reveals essential information on the collective and the statistical behavior of thermodynamic phases [34, 35, 36, 37]. It has been shown that, through the *generalized fluctuation-dissipation theorem* [163], the static structure factor of a Bose condensate is directly related to the elementary excitation energy $\epsilon(\mathbf{k})$ as [35, 181]

$$S(\mathbf{k}) = \frac{\hbar^2 k^2}{2m\epsilon(\mathbf{k})} \coth \frac{\epsilon(\mathbf{k})}{2k_B T},\qquad(8.4)$$

where m is the atomic mass, T is the temperature, $\hbar$ is the Planck constant h divided by 2π, and k_B is the Boltzmann constant. See references [35, 36, 37] on the static structure factor of a general system with complex dynamic density response in the frequency domain.

Previous experimental determinations of the static structure factor in the zero-temperature limit, based on two-photon Bragg spectroscopy, have been reported for weakly interacting Bose gases [182, 183] and strongly interacting Fermi gases [184]. Here, we show that $S(\mathbf{k})$ at finite temperatures can be directly determined from *in situ* density fluctuation and correlation measurements.

Experimental determination of $S(\mathbf{k})$ from density fluctuations is complicated by artificial length scales introduced by the measurement, including, for example, finite image resolution and size of the pixels in the charge-coupled device (CCD). Figure 8.1 shows a comparison between the measurement length scales (the resolution limited spot size and CCD pixel size), the correlation length ξ, and the thermal de Broglie wavelength λ_{dB}. Ideally, a density measurement should count the atom number inside a detection cell (pixel) with sufficiently high image resolution, and the dimension of the cell should be small compared to the atomic correlation length. In our experiment, the image resolution is determined by the imaging beam wavelength $\lambda = 852$ nm, the numerical aper-
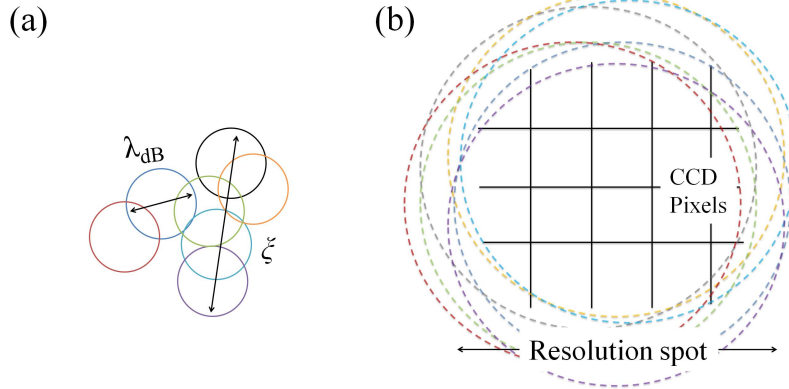
Figure 8.1: A comparison between physical length scales and measurement length scales. In (a), each atom is represented by a color circle with its diameter equal to the thermal de Broglie wavelength, λ_{dB}. ξ is the correlation length. An ideal measurement detects atom with perfect resolution. (b) shows the experimental condition where the image resolution is larger than the other length scales. Here, the image of an atom forms a resolution limited spot (dashed circles), and is large compared to the correlated area ξ^2 and the CCD pixel area. The grid lines represent the CCD pixel array.

ture N.A. $= 0.28$, and the aberrations of the imaging system. The image of a single atom on the CCD chip would form an Airy-disk like pattern with a radius comparable to or larger than λ_{dB} or ξ. The imaging magnification was chosen such that the CCD pixel size $\sqrt{A} = 0.66\ \mu$m in the object plane is small compared to the diffraction limited spot radius $\sim 1.8\ \mu$m. The atom number N_j recorded on the j-th CCD pixel is related to the atom number density $\int d\mathbf{r} n(\mathbf{r}) \mathcal{P}(\mathbf{r}_j - \mathbf{r})$, assuming the point spread function $\mathcal{P}(\mathbf{r})$ is approximately flat over the length scale of a single pixel,

$$n_{exp}(\mathbf{r}_j) \equiv \frac{N_j}{A} \approx \int d\mathbf{r} n(\mathbf{r}) \mathcal{P}(\mathbf{r}_j - \mathbf{r}), \tag{8.5}$$

where $\mathbf{r}_j$ is the center position of the j-th pixel in the object plane, $n(\mathbf{r})$ is the atom number density distribution, and the integration runs over the entire $x - y$ coordinate space. The atom

number fluctuation measured at the j-th pixel is related to the density-density correlation as

$$\langle \delta N_j^2 \rangle \approx A^2 \int d\mathbf{r} \int d\mathbf{r}' \langle \delta n(\mathbf{r}) \delta n(\mathbf{r}') \rangle \mathcal{P}(\mathbf{r}_j - \mathbf{r}) \mathcal{P}(\mathbf{r}_j - \mathbf{r}'), \qquad (8.6)$$

where $\delta N_j = N_j - \langle N_j \rangle$ is the atom number fluctuation around its mean value $\langle N_j \rangle$.

In the Fourier space, Eq. (8.5) can be written as

$$\delta n_{exp}(\mathbf{k}_l) \approx \delta n(\mathbf{k}_l) \mathcal{P}(\mathbf{k}_l), \qquad (8.7)$$

where $\delta n_{exp}(\mathbf{k}_l) \equiv \sum_j \delta N_j e^{-i\mathbf{k}_l \cdot \mathbf{r}_j}$ is the discrete Fourier transform of δN_j, approximating the continuous Fourier transform. Here, $\mathbf{k}_l = \frac{2\pi}{L}(l_x, l_y)$, L is the linear size of the image, l_x and l_y are integer indices in $\mathbf{k}$-space. From Eq. (8.3) and (8.7), the power spectrum of the density fluctuation is related to the static structure factor as

$$\langle |\delta n_{exp}(\mathbf{k}_l)|^2 \rangle \approx N S(\mathbf{k}_l) \mathcal{M}^2(\mathbf{k}_l), \qquad (8.8)$$

where the modulation transfer function $\mathcal{M}(\mathbf{k}) = |\mathcal{P}(\mathbf{k})|$ accounts for the imaging system's sensitivity at a given spatial frequency $\mathbf{k}$, and is determined by the point spread function. Also, from Eq. (8.6), the pixel-wise atom number fluctuation is related to the weighted static structure factor integrated over the $\mathbf{k}$-space,

$$\langle \delta N_j^2 \rangle \approx \frac{\langle N_j \rangle A}{4\pi^2} \int d\mathbf{k} S(\mathbf{k}) \mathcal{M}^2(\mathbf{k}). \qquad (8.9)$$

Generalization of the above calculations to arbitrary image resolution and detection cell size is straightforward. In addition to convolving with the point spread function, the measured atom number density must also be convolved with the detection cell geometry. Equation (8.5) can therefore be written as $N_j/A = \int d\mathbf{k} n(\mathbf{k}) \mathcal{P}(\mathbf{k}) \mathcal{H}(\mathbf{k}) e^{i\mathbf{k} \cdot \mathbf{r}_j}$, where $\mathcal{H}(\mathbf{k}) = \int_A e^{i\mathbf{k} \cdot \mathbf{r}} d\mathbf{r}/A$ and the integration

goes over the area A of the detection cell. This suggests simply replacing $\mathcal{M}^2(\mathbf{k})$ by $\mathcal{M}^2(\mathbf{k})\mathcal{H}^2(\mathbf{k})$ to generalize Eq. (8.8) and (8.9). Finally, in all cases, the discrete Fourier transform defined in Eq. (8.7) should well approximate the continuous Fourier transform for spatial frequencies smaller than the sampling frequency $1/\sqrt{A}$.

We view the factor $\mathcal{M}^2(\mathbf{k})\mathcal{H}^2(\mathbf{k})$ as the general imaging response function, describing how the imaging apparatus responds to density fluctuations occurring at various spatial frequencies. To extract the static structure factor from *in situ* density correlation measurements, one therefore needs to characterize the imaging response function at all spatial frequencies to high precision. Since our pixel-size is much smaller than the diffraction and aberration limited spot size, we will from here forward assume $\mathcal{H}^2(\mathbf{k}) = 1$; $\mathcal{H}^2(\mathbf{k})$ decays around $k \sim 4/\sqrt{A} = 6~\mu\text{m}^{-1}$ ($1/e$ radius), which is much larger than $k = 2\pi\text{N.A.}/\lambda = 2.1~\mu\text{m}^{-1}$, where $\mathcal{M}^2(\mathbf{k})$ terminates.

8.3   Measuring the imaging response function $\mathcal{M}^2(\mathbf{k})$

In this section, we show how to use density fluctuations of thermal atomic gases to determine the imaging response function $\mathcal{M}^2(\mathbf{k})$. Other approaches based on imaging individual atoms can be found, for example, in Refs. [185, 186].

8.3.1   Experiment

Measuring density fluctuations in low density thermal gases provides an easy way to precisely determine the imaging response function. An ideal thermal gas at low phase-space density has an almost constant static structure factor up to $k = \lambda_{dB}^{-1}$ [94] which, in our case, is larger than the sampling frequency $1/\sqrt{A}$. Therefore, the density fluctuation power spectrum derived from an ideal thermal gas reveals the square of the modulation transfer function, as indicated by Eq. (8.8).

We prepare a 2D thermal gas by first loading a three-dimensional ^{133}Cs Bose-Einstein condensate with 2×10^4 atoms into a 2D pancake-like optical potential with trap frequencies $\omega_z =$
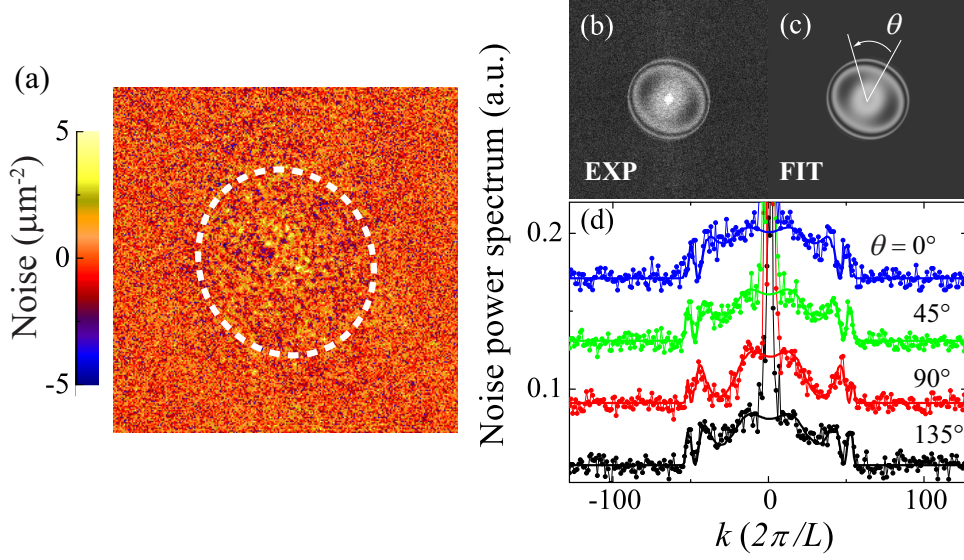
Figure 8.2: Determination of the imaging response function $\mathcal{M}^2(\mathbf{k})$ from *in situ* images of 2D thermal gases. (a) Image noise of a 2D thermal gas, obtained by subtracting the averaged density image from a single-shot image. The dashed ellipse encircles the location of thermal atoms. (b) Noise power spectrum evaluated from 60 images, using discrete Fourier transform defined following Eq. (8.7). Zero spatial frequency is shifted to the image center. (c) Fit to the image noise power spectrum using imaging response function defined in Eq. (8.12) and aberration parameters defined in Eqs. (8.10) and (8.11). (d) Sample line-cuts of experiment (circles) and fit (solid lines), with cutting angle θ indicated in the graph. The profiles are plotted with offset for clarity. Image size: $L^2 = 256 \times 256$ pixels.

$2\pi \times 2000$ Hz (vertical) and $\omega_r = 2\pi \times 10$ Hz (horizontal) [157, 179]. We then heat the sample by applying magnetic field pulses near a Feshbach resonance. After sufficient thermalization time, we ramp the magnetic field to 17 G where the scattering length is nearly zero. The resulting thermal gas is non-interacting at a temperature $T = 90$ nK and its density distribution is then recorded through *in situ* absorption imaging [179].

We evaluate the density fluctuation power spectrum $\mathcal{M}^2_{exp}(\mathbf{k}_l) = \langle |\delta n_{exp}(\mathbf{k}_l)|^2 \rangle$ using 60 thermal gas images (size: 256×256 pixels). Figure 8.2(a) shows a sample of the noise recorded in the images. Outside the cloud (whose boundary roughly follows the dashed line), the noise is dominated by the optical shot noise, and is therefore uncorrelated and independent of spatial frequency. In the presence of thermal atoms, we observe excess noise due to fluctuations in the thermal atom density. The noise power spectrum is shown as an image in Fig. 8.2(b), with line-cuts shown in Fig. 8.2(d). We note that the power spectrum acquires a flat offset extending to the highest spatial frequency, due to the photon shot noise in the imaging beam. Above the offset, the contribution from atomic density fluctuations is non-uniform and has a hard edge corresponding to the finite range of the imaging response function. Close to the edge, ripples in the noise power spectrum appears because of aberrations of the imaging optics, discussed in later paragraphs. Finally, the bright peak at the center corresponds to the large scale density variation due to the finite extent of the trapped atoms, and is masked out in our following analysis.

To fully understand the imaging response function with imaging imperfections, we compare our result with calculations based on Fraunhofer diffraction and aberration theory [187] as described in the following paragraphs.

8.3.2   Point spread function in absorption imaging

We consider a single atom illuminated by an imaging beam, the latter is assumed to be a plane wave with a constant phase across both the object and the image planes. The atom, driven by

the imaging electric field, scatters a spherical wave (dark field) which interferes destructively with the incident plane wave [27]. The dark field is clipped by the limiting aperture of the imaging optics and is distorted by the imaging aberrations. An exit pupil function p is used to describe the aberrated dark field at the exit of the imaging optics [187], and its Fourier transform $p(\mathbf{k})$ with $\mathbf{k} \propto \mathbf{R}$ describes the dark field distribution on the CCD chip, where $\mathbf{R}$ is the position in the image plane. The image of a single atom is then an absorptive feature formed by the interference between the dark field and the incident plane wave in the image plane.

We extend this to absorption imaging of many atoms with density $n(\mathbf{r}) = \sum_i \delta(\mathbf{r} - \mathbf{r}_i)$, where $\mathbf{r}_i$ is the location of the i-th atom in the object plane. The total scattered field in the image plane is[1] $\Delta E = \sum_i \epsilon p(\mathbf{k} - \mathbf{k}_i)$, with each atom contributing a dark field amplitude ϵ, and $\mathbf{k}$ relates to the position $\mathbf{r}$ in the object plane through $\mathbf{k} = \mathbf{r}/ad$, where a is the radius of the limiting aperture and $d = \lambda/(2\pi \text{N.A.})$. The dark field $\epsilon \propto e^{i\delta_s} E_0$ is proportional to the incident field E_0, and carries with a phase shift δ_s associated with the laser beam detuning from atomic resonance. For a thin sample illuminated by an incident beam with intensity I_0, the beam transmission is $t^2 = |E_0 + \Delta E|^2/|E_0|^2 \approx 1 + 2\Re[\Delta E/E_0]$ and the atomic density $n_{exp} \propto -\ln(t^2) + (1 - t^2)I_0/I_{sat}$ [128, 179] leads to $n_{exp} \propto -2(1 + I_0/I_{sat})\Re[\Delta E/E_0] \propto \sum_i \Re[e^{i\delta_s} p(\mathbf{k} - \mathbf{k}_i)]$. Here, $\Re[.]$ refers to the real part and I_{sat} is the saturation intensity for the imaging transition. Comparing the above expression to Eq. (8.5), we derive the point spread function as $\mathcal{P}(\mathbf{r}) \propto \Re[e^{i\delta_s} p(\mathbf{k})]|_{\mathbf{k}=\mathbf{r}/ad}$, in contrast to the form $|p(\mathbf{k})|^2$ in the case of fluorescence or incoherent imaging.

When the dark field passes through aberrated optics, neither the amplitude nor the phase at the exit pupil is uniform, but is distorted by imperfections of the imaging system. To account for attenuation and phase distortion, We can modify the exit pupil function as

$$p(r_p, \theta_p) = U(r_p/a, \theta_p)e^{i\Theta(r_p/a, \theta_p)}, \tag{8.10}$$

---

1. We consider the density n of the 2D gas in a range that the photon scattering cross section remains density-independent [109].

where r_p and θ_p are polar coordinates on the exit pupil, $U(\rho, \theta)$ is the transmittance function, and $\Theta(\rho, \theta)$ is the wavefront aberration function. We assume U to be azimuthally symmetric and model it as $U(\rho) = H(1 - \rho)e^{-\rho^2/\tau^2}$, where $H(x)$ is the Heaviside step function setting a sharp cutoff when r_p reaches the radius a of the limiting aperture. The factor $e^{-\rho^2/\tau^2}$, with $1/e$ radius $r_p = a\tau$, is used to model the weaker transmittance at large incident angle due to, e.g., finite acceptance angle of optical coatings. For the commercial objective used in the experiment, we need only to include a few terms in the wavefront aberration function

$$\Theta(\rho, \theta) \approx S_0\rho^4 + \alpha\rho^2 \cos(2\theta - 2\phi) + \beta\rho^2, \tag{8.11}$$

where the parameters used to quantify the aberrations are: S_0 for spherical aberration, α for astigmatism (with ϕ the azimuthal angle of the misaligned optical axis), and β for defocusing due to atoms not in or leaving the focal plane during the imaging.

Using the exit pupil function in Eq. (8.10), we can evaluate the point spread function via $\mathcal{P}(\mathbf{r}) \propto \Re[e^{i\delta_s}p(\mathbf{k})]|_{\mathbf{k}=\mathbf{r}/ad}$ with proper normalization. We can also calculate the modulation transfer function $\mathcal{M}(\mathbf{k}) = |\mathcal{P}(\mathbf{k})|$. In fact, determination of any one of $p(\mathbf{r}_p)$, $\mathcal{P}(\mathbf{r})$, or $\mathcal{M}(\mathbf{k})$ leads to a complete characterization of the imaging system including its imperfections.

8.3.3 Modeling the imaging response function

We fit the exit pupil function p in the form of Eq. (8.10), using a discrete Fourier transform, by comparing

$$\mathcal{M}^2_{fit} = |\mathcal{FT}(\Re[e^{i\delta_s}\mathcal{FT}(p)])|^2 \tag{8.12}$$

to the thermal gas noise power spectrum $\mathcal{M}^2_{exp}$ shown in Fig. 8.2(b). Here, $\mathcal{FT}(.)$ denotes the discrete Fourier transform. Figure 8.2(c) shows the best fit to the measurement, which captures most of the relevant features in the experiment data. Sample line-cuts with uniform angular spacing

are shown in Fig. 8.2(d). This experimental method can in principle be applied to general coherent imaging systems, provided the signal-to-noise ratio of the power spectrum image is sufficiently good to resolve all features contributed by the aberrations. Moreover, one can obtain analytic expressions for the point spread function and the modulation transfer function once the exit pupil function is known (see Section 8.5).

Having determined the imaging response function, one can remove systematic contributions from imaging imperfections to the static structure factor as extracted from the power spectrum of atomic density fluctuations, see Eq.(8.8).

8.4 Measuring density-density correlations and static structure factors of interacting 2D Bose gases

We measure the density-density correlations of interacting 2D Bose gases based on the method presented in the previous sections. This study is partially motivated by a finding in our earlier work that the local density fluctuation of a 2D Bose gas is suppressed when it enters the Berezinskii-Kosterlitz-Thouless (BKT) fluctuation and the superfluid regions [179]. We attributed this phenomenon to the emergence of long density-density correlation length exceeding the size of the imaging cell and the resolution. This results in a smaller pixel-wise fluctuation $\delta N^2/A$ than the simple product of the thermal energy $k_B T$ and the compressibility κ, as is expected from the classical fluctuation-dissipation theorem (FDT) [162]. Below, we present a careful analysis of the density-density correlations of interacting 2D Bose gases and discuss the role of correlations in the FDT.

To extract local properties from a trapped sample, we limit our analysis to a small central area of the sample where the density is nearly flat. In addition, the area is chosen to be large enough to offer sufficient resolution in the Fourier space. We choose the patch size to be $32{\times}32$ pixels. Figure 8.3 shows a typical image and the density fluctuations inside the patch.
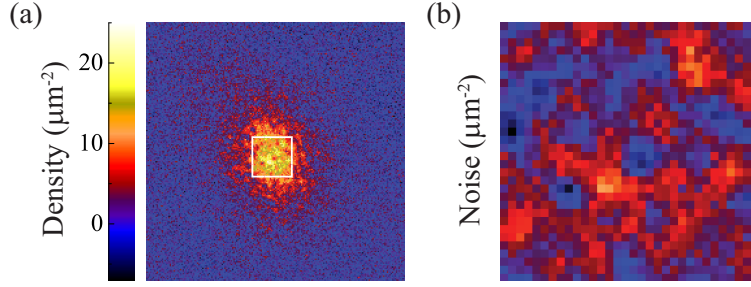
Figure 8.3: Illustration of the patch selected for the static structure factor analysis. (a) shows a typical cloud image of 200×200 pixels. The selected patch is located at the center of the cloud, bounded by a box with an area of 32×32 pixels. (b) shows the density fluctuations inside the patch.

To ensure that we obtain an accurate static structure factor using the small patch, we perform a measurement on a non-interacting 2D thermal gas at a phase space density $n\lambda_{dB}^2 = 0.5$ and compare the measured static structure factor to the theory prediction [94]. We first calculate the imaging response function $\mathcal{M}^2(\mathbf{k})$ for a patch size of 32×32 pixels and divide the thermal gas noise power spectrum by $\mathcal{M}^2(\mathbf{k})$. The resulting spectrum should represent the static structure factor of an ideal 2D thermal gas. In Fig. 8.4, we plot the azimuthally averaged static structure factor with data points uniformly spaced in k, up to the resolution limited spatial frequency $k = 2\pi \mathrm{N.A.}/\lambda$. The measured static structure factor is flat and agrees with the expected value of $S(k) \approx 1.3$ for $k < \lambda_{dB}^{-1} = 2\ \mu\mathrm{m}^{-1}$[2].

Applying the same analysis to *interacting* 2D Bose gases, we observe very different strengths and length scales for the density fluctuations. In Fig. 8.4(a-c), we present the single-shot image noise of samples prepared under three different conditions: weakly interacting gases at the temper-

---

2. Following the calculation in Ref. [94], we find the static correlation function of an ideal 2D thermal gas is $\nu(r) = \delta(r) + |g_1(z, e^{-\pi r^2/\lambda_{dB}^2})|^2/g_1(z,1)\lambda_{dB}^2$, where $z = e^{\mu/k_B T}$ is the local fugacity and $g_\gamma(x,y) = \sum_{k=1}^{\infty} x^k y^{1/k}/k^\gamma$ is the generalized Bose function. Fourier transforming $\nu(r)$ to obtain the static structure factor $S(k)$, we find $S(k) \approx 1.3$ remains flat for $k\lambda_{dB} < 1$.

ature $T = 40$ nK (below the BKT critical point), with dimensionless interaction strength[1] $g = 0.05$ and 0.26 (phase space density $n\lambda_{dB}^2 = 9$ and 7); and a strongly interacting 2D gas at the temperature $T = 8$ nK, prepared in a 2D optical lattice at a mean site occupancy number of 2.6, and a depth of 7 E_R, where $E_R = h \times 1.3$ kHz is the recoil energy. Due to the tight confinement, the sample in the optical lattice has a high effective interaction strength[1] $g_{\mathrm{eff}} = 1.0$ [38]. Details on the preparation of the 2D gases in the bulk and in an optical lattice can be found in Refs. [179] and [38], respectively.

The difference in the density fluctuations shown in Fig. 8.4(a-c) can be characterized in their static structure factors shown in Fig. 8.4(d). We observe positive correlations above the shot noise level $S(k) = 1$ in the two weakly interacting samples. The one at $g = 0.05$ shows stronger density correlations at small k than does the sample at $g = 0.26$. The enhanced density correlations $S(k) > 1$ at low momenta are expected since the thermally induced phonon excitations can populate states with length scale $1/k$ longer than the healing length $\xi = 1/\sqrt{ng}$. For gases with stronger interactions, excitations cost more energy and the excited states are less populated. At smaller g, the correlation length is longer and, therefore, the static structure factor decays at a smaller k.

The most intriguing observation is the negative correlations $S(k) < 1$ in the strongly interacting gas with $g_{\mathrm{eff}} = 1.0$. We observe a below-shot-noise spectrum at low momentum k, showing that long wave-length excitations are strongly suppressed due to a stronger interaction energy $n\hbar^2 g_{\mathrm{eff}}/m = k_B \times 34$ nK compared to the thermal energy $k_B \times 8$ nK. As the momentum k increases, the excitation populations gradually return to the shot noise level. Our observation is consistent with the prediction in Ref. [181] that when the thermal energy drops below the interaction energy, global density fluctuations in a superfluid are suppressed.

Finally, we discuss the contribution of finite density-density correlations in the FDT. Including

---

1. The dimensionless interaction strength of a weakly interacting 2D Bose gas is $g = \sqrt{8\pi}a_s/l_z$, where a_s is the atomic scattering length and $l_z = \sqrt{\hbar/m\omega_z}$ is the vertical harmonic oscillator length. For a 2D gas in a 2D optical lattice, the effective interaction strength is $g_{\mathrm{eff}} = mUl^2/\hbar^2$ [38], where U is the on-site interaction and l is the lattice constant.
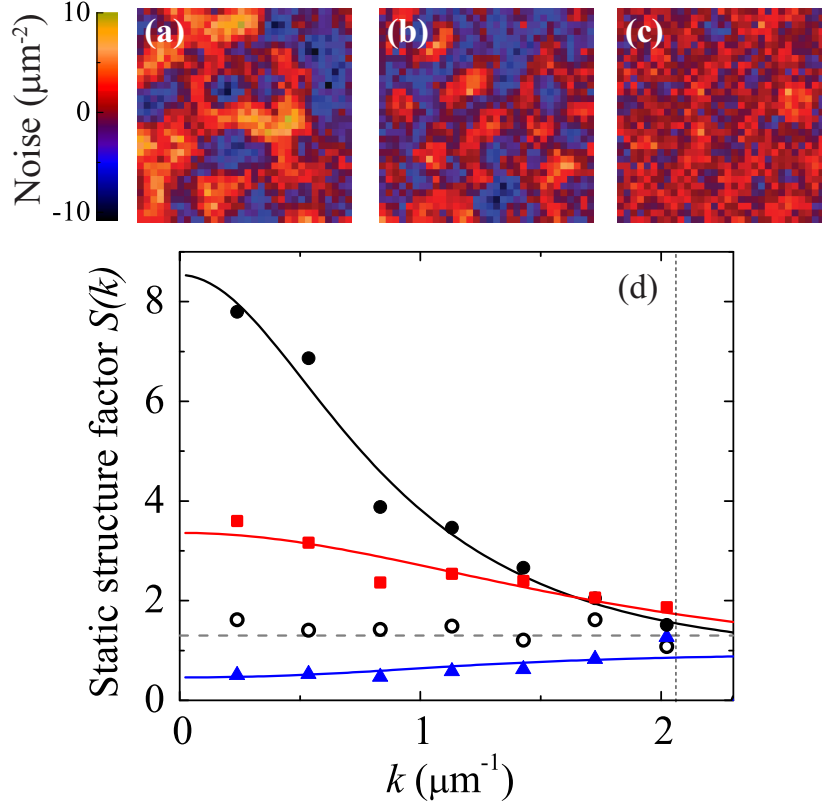
Figure 8.4: Density fluctuations and the static structure factors of 2D Bose gases. (a) and (b) Image noise of weakly interacting 2D Bose gases in the superfluid phase at dimensionless interaction strength $g = 0.05$ and 0.26. (c) Image noise of a strongly interacting 2D Bose gas at $g_{\text{eff}} = 1.0$ prepared in a 2D optical lattice at a depth of 7 E_R. (d) shows the static structure factors extracted from the noise power spectra of interacting 2D gases as shown in (a) (black circles), (b) (red squares), and (c) (blue triangles). The static structure factor of an ideal thermal gas at phase space density $n\lambda_{dB}^2 = 0.5$ (open circles) and the expected value of $S(k) \approx 1.3$ (gray dashed line) are plotted for comparison. Solid lines are the guides to the eye. Vertical dashed line indicates the resolution limited spatial frequency $k = 2\pi\text{N.A.}/\lambda = 2.1$ μm^{-1}.

correlations, we can write the FDT as $k_B T \kappa(\mathbf{r}) = \int \langle \delta n(\mathbf{r}) \delta n(\mathbf{r}') \rangle d\mathbf{r}' = n(\mathbf{r}) S(0)$ [181]. We compare the measured static structure factor, extrapolated to zero-k, to the value of $k_B T \kappa / n$, where $\kappa = \partial n / \partial \mu$ is the experimentally determined compressibility [179], and indeed find that $n S(0)$ equals to $k_B T \kappa$ to within our experimental uncertainties of $10 \sim 20\%$ for all three interacting samples. This agreement shows that the measured correlations and thus the static structure factor can be linked to the thermodynamic quantities via the FDT. Our ability to determine $S(0)$ and κ from *in situ* images also suggests a new scheme to determine temperature of the sample from local observables as $k_B T = n S(0) / \kappa$.

8.5 Full analysis of the point spread function and the modulation transfer function

8.5.1 Point spread function

Here, we describe our approach to characterize imaging imperfections using extended Nijboer-Zernike diffraction theory [188]. To obtain the point spread function from the exit pupil function $p(r_p, \theta_p)$, it is convenient to first decompose the exit pupil function using a complete set of orthogonal functions on the unit disk in the polar coordinates

$$p(r_p, \theta_p) = \sum_{n=0}^{\infty} \sum_{m=-n}^{n} \beta_n^m Z_n^m(\frac{r_p}{a}, \theta_p), \tag{8.13}$$

where $Z_n^m(\rho, \theta) = R_n^{|m|}(\rho) e^{im\theta}$ is a Zernike polynomial, the radial function

$$R_n^m(\rho) = \sum_{k=0}^{(n-m)/2} \frac{(-1)^k (n-k)!}{k![(n+m)/2 - k]![(n-m)/2 - k]!} \rho^{n-2k} \tag{8.14}$$

terminates at $\rho = 1$, and $R_n^m = 0$ when $n - m$ is odd. The expansion coefficient β_n^m is given by

$$\beta_n^m = \frac{n+1}{\pi a^2} \int_0^a \int_0^{2\pi} p(r_p, \theta_p) Z_n^{-m}(r_p/a, \theta_p) r_p dr_p d\theta_p. \tag{8.15}$$

If we then apply the expansion Eq. (8.13) to the Fourier transform of the exit pupil function $p(k, \theta) = \int_0^a \int_0^{2\pi} p(r_p, \theta_p) e^{-ikr_p \cos(\theta - \theta_p)} r_p dr_p d\theta_p$ and carry out the integration using the Zernike-Bessel relation $\int_0^1 R_n^m(\rho) J_m(\xi\rho)\rho d\rho = (-1)^{(n-m)/2} J_{n+1}(\xi)/\xi$, we arrive at the following formula

$$p(k, \theta) = 2\pi a^2 \sum_{n=0}^{\infty} \sum_{m=-n}^{n} i^n \beta_n^m e^{im(\theta+\pi)} \frac{J_{n+1}(ka)}{ka}, \tag{8.16}$$

where $J_n(z)$ is the n-th order Bessel function of the first kind. The point spread function $\mathcal{P}(r, \theta)$ is the real part of $e^{i\delta_s} p(k, \theta)|_{k=r/ad}$ with proper normalization

$$\mathcal{P}(r, \theta) = \frac{1}{\mathcal{N}} \sum_{n=0}^{\infty} \sum_{m=-n}^{n} \Re[i^n \beta_n^m e^{im(\theta+\pi)+i\delta_s}] \frac{J_{n+1}(r/d)}{r/d}, \tag{8.17}$$

where $\mathcal{N} = 2\pi d^2 \Re[e^{i\delta_s} p(\mathbf{r}_p)]|_{\mathbf{r}_p=0} = 2\pi d^2 \cos\delta_s$ is the normalizing factor such that $\int \mathcal{P}(\mathbf{r})d^2r = 1$. For a non-aberrated system, only β_0^0 is non-zero and the above equation reduces to the form $J_1(z)/z$, as expected.

Using the above equations, we can derive the point spread function from the fitted exit pupil function shown in Fig. 8.5(a). We calculate the expansion coefficients β_n^m and evaluate the corresponding point spread function, see Fig. 8.5(b-c).

8.5.2   *Modulation transfer function*

It is straightforward to evaluate the modulation transfer function $\mathcal{M}(\mathbf{k}) = |\mathcal{P}(\mathbf{k})|$ and the imaging response function $\mathcal{M}^2(\mathbf{k}) = |\mathcal{P}(\mathbf{k})|^2$ directly from the exit pupil function $p(r_p, \theta_p)$. Since the

172
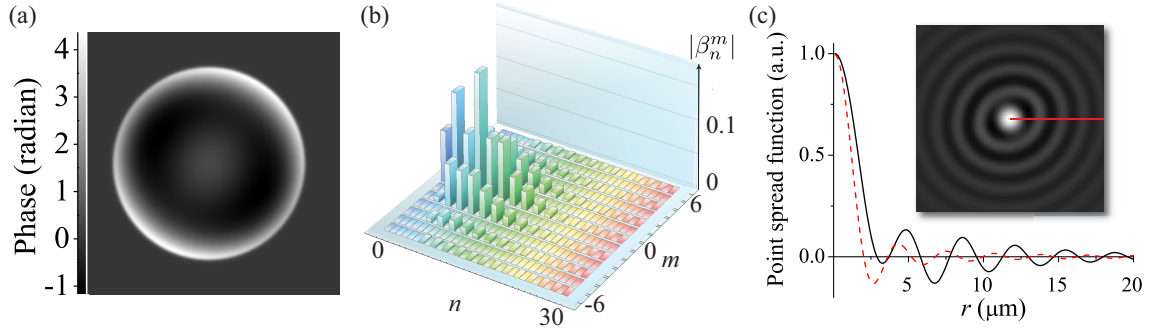
Figure 8.5: Analysis of the imaging aberrations and the point spread function. (a) shows the wave-front aberration (the phase of the exit pupil function) determined from the fit to the experiment. (b) shows the expansion coefficients $|\beta_n^m|$ determined from Eq. (8.15), using the exit pupil function in (a). (c) shows a line-cut of the derived point spread function (solid line). The unaberrated point spread function is plotted for comparison (dashed line). Inset shows the 2D distribution of the aberrated point spread function and red line indicates the direction of the line-cut. Image size is $(33 \ \mu\text{m})^2$.

point spread function can be written as $\mathcal{P}(\mathbf{r}) = [e^{i\delta_s}p(\mathbf{k}) + e^{-i\delta_s}p^*(\mathbf{k})]/4\pi a^2 \mathcal{N}|_{\mathbf{k}=\mathbf{r}/ad}$, its Fourier transform is

$$\mathcal{P}(\mathbf{k}) \quad = \quad \frac{\pi d^2}{\mathcal{N}}[e^{i\delta_s}p(r_p, \theta + \pi) + e^{-i\delta_s}p^*(r_p, \theta)]|_{r_p = kad}, \tag{8.18}$$

where $k = |\mathbf{k}|$ is the spatial frequency and θ is the polar angle of $\mathbf{k}$ in the image plane. From Eq. (8.18), the imaging response function is $\mathcal{M}^2(\mathbf{k}) \propto |p(kad, \theta + \pi) + e^{-2i\delta_s}p^*(kad, \theta)|^2$. This result shows that the phase shift δ_s is important since $\mathcal{M}^2(\mathbf{k})$ depends on the interference between $p(kad, \theta + \pi)$ and $p^*(kad, \theta)$. The transmittance U, defined in the exit pupil function Eq. (8.10), accounts for the radial envelope in $\mathcal{M}^2(\mathbf{k})$, leading to the sharp edge at $k = d^{-1} = 2\pi \text{N.A.}/\lambda$. Either the continuous function Eq. (8.18) or the discrete Fourier model Eq. (8.12) can be used to calculate the imaging response function.

8.6 Conclusion

In this chapter, we demonstrated the extraction of density-density correlations and static structure factors from *in situ* images of 2D Bose gases. Careful analysis and modeling of the imaging response function allow us to fully eliminate the systematic effect of imaging imperfections on our measurements of density-density correlations. For thermal gases, our measurement of the static structure factor agrees well with theory. For interacting 2D gases below the BKT critical temperature, intriguingly, we observe positive density-density correlations in weakly interacting samples ($g \ll 1$) and negative correlations in the strong interaction regime ($g_{\text{eff}} = 1.0$). For all interacting gases, our static structure factor measurements agree with the prediction of the FDT as $S(0) = k_B T \kappa / n$. Extension of our 2D measurement can further test the prediction of anomalous density fluctuations in a condensate [180, 189, 190, 191] and strong correlations in the quantum critical region [116, 192]. Finally, our analysis can be applied to perform precise local thermometry [165] and can potentially be used to extract the local excitation energy spectrum through the application of the generalized fluctuation-dissipation theorem [35, 163].

CHAPTER 9

OUTLOOK

We discuss some prospects of studying quantum critical dynamics using cold atoms in optical lattices. Prominent dynamic phenomena include quantum critical transport of mass and entropy, and dynamics of defect generation across the quantum critical point as described by the Kibble-Zurek mechanism [193, 148].

This chapter contains a proposal and an experiment by X. Zhang, C.-L. Hung, S.-K. Tung, N. Gemelke, and C. Chin published in part of *New J. Phys.* **13**, 045011 (2011) in a focus issue on *Strongly correlated quantum fluids: From ultracold quantum gases to QCD plasmas.*

9.1   Quantum critical transport

Mass and heat transport across the quantum critical regime provide important tests for quantum critical theory [49]. Sufficiently close to the critical point, one expects that transport coefficients obey universal scaling relations independent of microscopic physics [49, 194]. In two dimensions, in particular, we expect that the static mass transport exhibits a universal behavior, in analogous to the prediction on the electrical conductivity [195, 196], and the static mass conductivity at the critical point is given by

$$\sigma = \frac{m}{\hbar}\Phi_\sigma, \tag{9.1}$$

which only depends on the fundamental constants $m/\hbar$ and a dimensionless, universal number Φ_σ determined from the universality class of the underlying phase transition. Here $\hbar$ is the reduced Planck constant, and m is the atomic mass. Analytic predictions on the transport coefficients in the quantum critical regime were recently reported on the basis of the anti-de Sitter/conformal field theory duality [196, 197]. Measurements of transport coefficients in general can be of fundamental interest in quantum field theory [196]; the relation between mass and thermal conductivities is in

close analogy to the Wiedemann-Franz relation between charge and thermal transport coefficients in electronic systems, which is shown to break down near the quantum critical point in a recent experiment [198].

Mass and heat transport are induced by generalized forces such as chemical potential gradient and temperature gradient. A natural approach to study dynamics of atoms in optical lattices is to first create non-equilibrium density distributions in the sample and then measure the subsequent evolution of density profiles.

Non-equilibrium density distributions can be induced in various ways. For example, one can create a controlled perturbation in the local chemical potential and induce transport by dynamically changing the envelope trapping potential in an equilibrated system or changing the on-site interaction U near a Feshbach resonance [6]. On the other hand, applying lattice ramps slow compared to local microscopic time scales can still violate global adiabaticity and induce macroscopic mass and heat flow [157]. This is aggravated by the pronounced difference in the equilibrium density and entropy profiles between superfluid and Mott insulator phases, as shown in Fig. 9.1. In a non-equilibrated system, we expect quantum critical dynamics to take place near integer site occupation numbers.

While measuring the evolution of the density profile is straightforward using our *in situ* imaging technique [149, 157], heat or entropy measurement in the quantum critical regime remains a challenging task. Nevertheless, the entropy profile is readily measurable deeply in the Mott-insulating regime by counting occupancy statistics using single-site resolved florescence imaging in combination with on-site number filtering [33, 121], or can be extracted from counting average site occupancies before and after on-site number filtering processes [157]. Since the local equilibration time scale (on the order of $\hbar/U$ [121]) is sufficiently decoupled from the global dynamics [199], a locally isentropic projection from the quantum critical regime deeply into the MI regime can be achieved and the local entropy profile measured.

From the density and entropy profile measurements, we can determine their current densities

through the application of a generic continuity equation $\frac{\partial \rho}{\partial \tau} + \nabla \cdot \vec{J}_\rho = \Gamma_\rho$. Here $\rho(\vec{x}, \tau)$ represents experimentally measured mass or entropy density, $\vec{J}_\rho$ is the corresponding current density, and Γ_ρ is a source term which characterizes, for example, particle loss ($\Gamma_\rho < 0$) or entropy generation ($\Gamma_\rho > 0$).

Mass conductivity σ and thermal conductivity κ can be determined by relating the mass and entropy current densities, $\vec{J}_n$ and $\vec{J}_s$, as functions of position $\vec{x}$ and time τ, to the generalized forces: the local chemical potential gradient $\vec{\nabla}\mu$, the potential energy gradient $\vec{\nabla}V$, and the temperature gradient $\vec{\nabla}T$. They obey the following transport equations [200]

$$\vec{J}_n(\vec{x}, \tau) = -\sigma\vec{\nabla}[\mu(\vec{x}, \tau) + V(\vec{x}, \tau)] - \frac{mL_{nq}}{k_B}\vec{\nabla}T(\vec{x}, \tau) \tag{9.2}$$

$$\vec{J}_s(\vec{x}, \tau) = -\frac{L_{qn}}{k_B}\vec{\nabla}[\mu(\vec{x}, \tau) + V(\vec{x}, \tau)] - \frac{\kappa}{T}\vec{\nabla}T(\vec{x}, \tau). \tag{9.3}$$

Here L_{nq} and L_{qn} are phenomenological coefficients similar to the Seebeck and Peltier coefficients in the thermoelectric effect and can be related via the Onsager reciprocity relation [201].

Finally, to obtain precise information of spatially resolved chemical potential gradient and temperature gradient, we resort to the equilibrium properties of the sample which can be determined from measurements of the equilibrium density and density fluctuation. The complementary knowledge of the equation of state $n(\mu, T)$ and its fluctuation $\delta n^2(\mu, T)$ in equilibrium can be inverted to obtain $\mu(n, \delta n^2)$ and $T(n, \delta n^2)$. We propose that, in a sample driven out of equilibrium globally but remaining locally equilibrated, local density and fluctuation measurements can still be used to extract its local chemical potential and temperature. This assumption can be further examined by comparing local compressibility to density fluctuation and extracting local temperature through the application of the fluctuation-dissipation theorem [165].
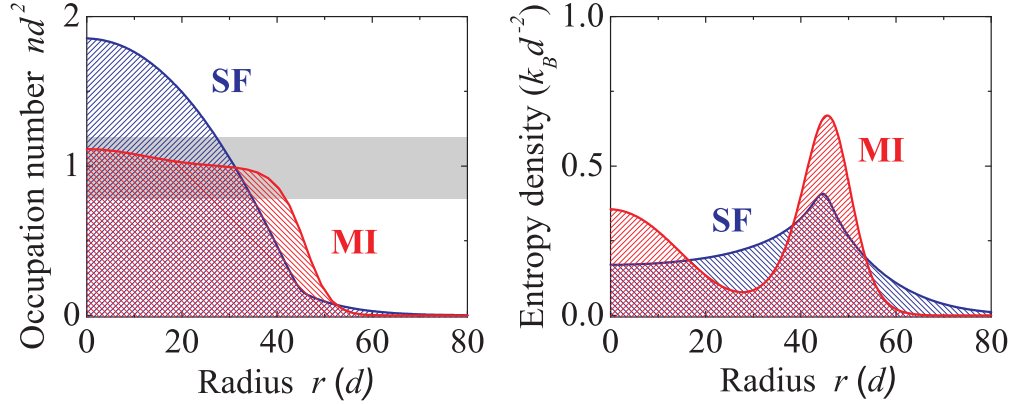
Figure 9.1: Sketch of density and entropy profiles of a trapped, finite-temperature gas in the tunneling-dominated regime where the center of the cloud is a superfluid (SF), and in the interaction-dominated regime where the cloud shows a Mott-insulating domain (MI) with unit occupation number. The calculation is done with the same particle number and total entropy for the two regimes. The gray shaded area marks an extended region near unit site occupation number ($nd^2 = 1$) where quantum critical transport can take place when global adiabaticity breaks down during the lattice loading process. $d = 532$ nm is the lattice constant.

9.1.1 Experiment - Dynamics of mass flow

Our recent experiment studied global mass transport and statistical evolution in a 2D sample across the SF-MI phase boundary [157]. We discovered slow equilibration dynamics with time scales more than 100 times longer than the microscopic time scales for the on-site interaction and tunneling energy. This suggests that transport can limit the global equilibration process inside a sample traversing a quantum critical point.

In Fig. 9.2 (a-c), we plot the evolution of density profiles of a 2D gas containing $N = 2 \times 10^4$ atoms after a short 50 ms ramp from zero to a final lattice depth of 10 E_R. At this lattice depth, $U/t = 11$ is below the critical point $U/t = 17$ for the Mott insulator state with unit occupation number [202]. We record density profiles after holding the sample at the final lattice depth for various hold times τ. With an equilibration time scale around 180 ms, the cloud gently expands and the peak density slowly decreases due to the increase of repulsive atomic interaction during the lattice ramp. This equilibration time scale can depend on the sample size and the local properties
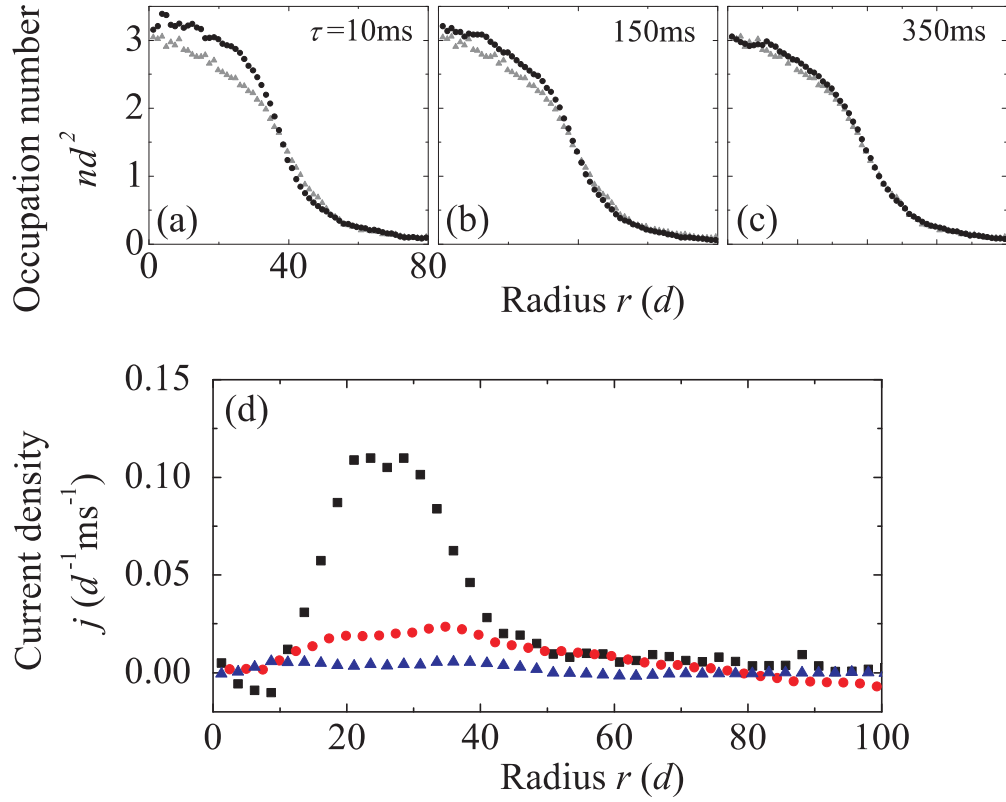
Figure 9.2: Evolution of the density profile and the atom number current density after a short 50 ms lattice ramp from zero depth to a final depth of 10 E_R ($U/t = 11$). Upper figure shows the density profile after holding the sample at a constant final depth for hold times $\tau =$(a) 10, (b) 150, and (c) 350 ms (black circles). In each figure (a-c), the near-equilibrated density profile measured at long hold time $\tau = 500$ ms (gray triangles) is plotted for comparison. Each profile is based on an average of 20 to 30 *in situ* images. (d) shows the atom number current density at hold time $\tau = 10$ (black squares), 150 (red circles), and 350 (blue triangles) ms, derived from the density profiles measured near hold times shown in (a-c) using Eq. (9.2).

of the coexisting phases in an inhomogeneous sample.

We further extract the evolution of local mass current density, leading to detailed local transport properties beyond a single equilibration time scale. We compute the mass current density $\vec{J}_n$ by comparing density profiles taken at adjacent hold times ($\Delta\tau = 10 \sim 50$ ms) and applying the continuity equation, $m\frac{\Delta n}{\Delta\tau} + \nabla \cdot \vec{J}_n(r, \tau) = 0$, to evaluate $\vec{J}_n(r, \tau)$. Here, we assume no atom loss in the analyses for short hold times $\tau < 500$ ms. Assuming that mass flow only occurs in the radial direction ($\hat{r}$) due to azimuthal symmetry of the sample, we write the mass current density as $\vec{J}_n(r, \tau) = mj(r, \tau)\hat{r}$. The number current density $j(r, \tau)$ is computed according to

$$j(r, \tau) = -\frac{1}{2\pi r}\frac{N(r, \tau + \Delta\tau) - N(r, \tau)}{\Delta\tau}, \tag{9.4}$$

where $N(r, \tau) = \int_0^r n(r', \tau)2\pi r' \mathrm{d}r'$ is the number of atoms located inside a circle of radius r at hold time τ. Positive j means a current flowing toward larger radius r, and vice versa.

In Fig. 9.2(d), we show $j(r, \tau)$ computed from density profiles measured near hold times shown in Fig. 9.2 (a-c). We observe overall positive mass flow, which is consistent with the picture of an expanding sample inside the optical lattice. The mass current density varies across the sample. Shortly after the lattice ramp at $\tau = 10$ ms, mass transport is most apparent inside a radius $r = 40d$, where the occupation number $nd^2 > 1$ and the atoms respond to the increase of on-site repulsion. The current density peaks around an annular area $20d < r < 30d$ when the occupation number is in the range $2 < nd^2 < 3$; outside this annular area, the current density is suppressed when the occupation number is in the range $nd^2 > 3$ or $nd^2 < 2$. At a larger hold time $\tau = 150$ ms, similar transport continues to take place but with smaller amplitude. At a long hold time $\tau = 350$ ms when the sample is closer to equilibrium, the current density j becomes smaller than our measurement noise.

In this section, we have shown that spatially resolved mass current density is readily measurable using our *in situ* imaging technique. We expect that local transport coefficients can be

extracted using Eq. (9.2), from further measurements of local temperature gradients and chemical potential gradients. Our interest lies in mass transport in the quantum critical regimes near integer occupation numbers, where the static mass conductivity is predicted to be universal (Eq. (9.1)). Measurements of local entropy density are under future investigations, with details outlined in Section 9.1.

9.2 The Kibble-Zurek mechanism (KZM)

Based on general critical scaling arguments, the KZM predicts the formation of topological defects after a system dynamically crosses through a second-order thermodynamic [203, 204] or quantum phase transition [193, 148]. For optical lattice experiments, the KZM applies when the system is quenched from a gapped Mott insulator state to a gapless superfluid phase, and predicts that the density of defects scales with the ramp rate of the coupling strength g [148].

The scaling behavior can reveal critical exponents of the underlying quantum phase transition [148, 205, 206]. When the coupling strength g is adiabatically ramped close to g_c, the many-body gap Δ scales as $\Delta \propto |g - g_c|^{z\nu} = |\lambda(\tau)|^{z\nu}$, where $\lambda(\tau) = g(\tau) - g_c$ characterizes the time dependence of the ramp. The adiabaticity criterion breaks down at a time $\tau = \tau_a$ when the gap Δ becomes small enough and the ramp rate violates $\frac{d\Delta}{d\tau}\frac{\hbar}{\Delta} \leq \Delta$, yielding excitations with a characteristic energy scale $\Delta_a \propto |\lambda'(\tau_a)|^{z\nu/(z\nu+1)}$ or length scale $\xi_a \propto \Delta_a^{-1/z}$. The density of defects n_{ex} should therefore scale universally as [148, 205]

$$n_{ex} \propto \xi_a^{-D} \propto \gamma_a^{D\nu/(z\nu+1)}, \tag{9.5}$$

where $\gamma_a = |\lambda'(\tau_a)|$ is the magnitude of the ramp rate at which adiabaticity fails.

In a two-dimensional superfluid, topological defects are vortices. Observing vortices in an optical lattice using *in situ* imaging is challenging, largely due to the smallness of a typical vortex core

size (< 1 μm) compared to the imaging resolution (≥ 5 μm) available in most experiments. While the latter can be technically improved, increasing the vortex core size by reducing the atomic interaction can also be achieved experimentally either through tuning a magnetic Feshbach resonance [6] or releasing atoms for a short time-of-flight time [207, 208].

Further extensions of the KZM consider finite-temperature and finite-size effects [206]. In general, the scaling of excitations also depends on the pathway of quenching [148, 206, 209], and the system can enter the Landau-Zener regime in nearly defect-free processes [193]. Detailed experiments could reveal the wealth in the dynamics of quantum critical phenomena as well as the intriguing connection between quantum mechanics and thermodynamics in genuine quantum systems [210, 211].

APPENDIX A

LIST OF PUBLICATIONS

1. Accelerating evaporative cooling of atoms into Bose-Einstein condensation in optical traps
   C.-L. Hung, X. Zhang, N. Gemelke, and C. Chin, *Phys. Rev. A* **78**, 011604 (Rapid Commun.) (2008).

2. Exploring universality of few-body physics based on ultracold atoms near Feshbach resonances
   N. Gemelke, C.-L. Hung, X. Zhang, and C. Chin, *Pushing the frontiers of atomic physics, Proceedings of the XXI International Conference on Atomic Physics* p.240 (2008).

3. In situ observation of incompressible Mott-insulating domains in ultracold atomic gases
   N. Gemelke, X. Zhang, C.-L. Hung, and C. Chin, *Nature* **460**, 995 (2009).

4. Slow mass transport and statistical evolution of an atomic gas across the superfluid-Mott insulator transition
   C.-L. Hung, X. Zhang, N. Gemelke, and C. Chin, *Phys. Rev. Lett.* **104**, 160403 (2010).

5. Observation of scale invariance and universality in two-dimensional Bose gases
   C.-L. Hung, X. Zhang, N. Gemelke, and C. Chin, *Nature* **470**, 239 (2011).

6. Exploring quantum criticality based on ultracold atoms in optical lattices
   X. Zhang, C.-L. Hung, S.-K. Tung, N. Gemelke, and C. Chin, *New J. Phys.* **13**, 045011, Focus issue on *Strongly correlated quantum fluids: From ultracold quantum gases to QCD plasmas* (2011).

7. Extracting density-density correlations from in situ images of atomic quantum gases
   C.-L. Hung, X. Zhang, L.-C. Ha, S.-K. Tung, N. Gemelke, and C. Chin, *New J. Phys.* **13**, 075019, Focus issue on *Quantum simulation* (2011).

APPENDIX B

UNIT CONVERSION

Tracking units of measurement is often a tedious process in calculating physical quantities involving multiple physical constants, units, and variables. Similar to the units of electron volt often used in high energy physics, all units of measurement in our experiment can be converted into Hz by setting the Plank constant $h = 1$, the Boltzmann constant $k_B = 1$, the Bohr magneton $\mu_B = 1$, and the cesium mass $m = 1$ Hz. I used this set of *cesium units*, listed in Tables B.1 and B.2, to conveniently calculate all physical quantities in my thesis work. Conversion from and to SI units can be done using Table B.2.

Name of constant	symbol	*cesium units*
Planck constant	h	1
Boltzmann constant	k_B	1
Bohr magneton	μ_B	1
Cesium-133 atomic mass	m	1 Hz

Table B.1: *Cesium units.*

Name of constant	symbol	*cesium units*
Lattice constant	$d = 532$ nm	0.009709/Hz
Recoil energy	E_R	1326 Hz
Nano Kelvin	nK	20.84 Hz
Gauss	G	1.400 MHz

Table B.2: Useful constants in *cesium units*.

APPENDIX C

MATHEMATICA CODES FOR BAND STRUCTURE CALCULATION

```
V = 5; (*lattice depth in Er*)
s = -V / 4; (*-V/4Er*)
ν[q_, n_] := q + Sign[q] (-1)^n * (n + Mod[n, 2]);
(*characteristic exponent*)
BandE[q_, n_, s_] := MathieuCharacteristicA[ν[q, n], s] - 2 s;
(*E^n_q as a function of qd/π where d=λ/2 is the lattice constand*)
Plot[{BandE[q, 0, s], BandE[q, 1, s], BandE[q, 2, s],
  BandE[q, 3, s], BandE[q, 4, s]}, {q, -0.999, 0.999},
 AxesOrigin → {-1, -0.1}, PlotRange → {-0.1, 30}]
 (*Plot the band structure as a funtion of in the unit of Er*)
```
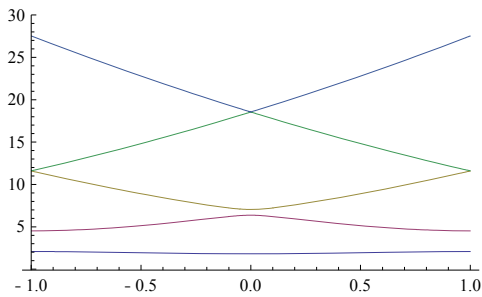


```
(*Bloch wave*)
BlochRe[q_, n_, x_, s_] :=
  MathieuC[MathieuCharacteristicA[ν[q, n], s], s, x];
BlochIm[q_, n_, x_, s_] := If[q ≠ 0,
   Sign[q] MathieuS[MathieuCharacteristicA[ν[q, n], s], s, x],
   MathieuS[MathieuCharacteristicA[ν[q, n], s], s, x]];
 (*Real and imaginary parts of Bloh wave as functions of x/dπ*)
Plot[{BlochRe[0., 0, π * x, s]^2 + BlochIm[0., 0, π * x, s]^2,
  BlochRe[0.0000001, 1, π * x, s]^2 + BlochIm[0.0000001, 1, π * x, s]^2},
 {x, -1, 1}](*plot the probability density*)
```
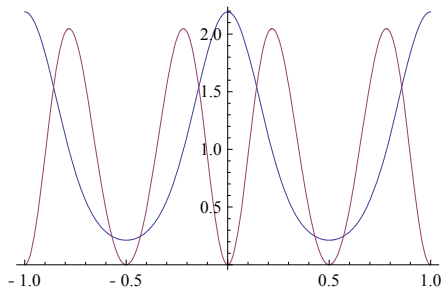
```
(*We only calculate Wannier wave function in the ground band*)
L = 1 / Sqrt[4];(*Normalizing factor, making the integration
   Total[Table[Wannier[1,x,0]^2,{x,-∞,∞,dx}]]*dx = 1*)
d = 1;(*lattice constant*)
Wannier[Vlat_, x_, xi_] :=
 2 * L * NIntegrate[Cos[q * xi] MathieuC[MathieuCharacteristicA[
        q, -Vlat / 4], -Vlat / 4, π * x / d] + Sin[q * xi]
     MathieuS[MathieuCharacteristicA[q, -Vlat / 4], -Vlat / 4, π * x / d],
   {q, 0, 0.999999999}, AccuracyGoal → 9]
(*Wannier wave function W(kx)*)
Plot[Wannier[V, x, 0], {x, -1.5 * d, 1.5 * d}]
(*wannier is real and symetric around xi since BlochIm[q,x]=
 -BlcohIm[-q,x]*)
```
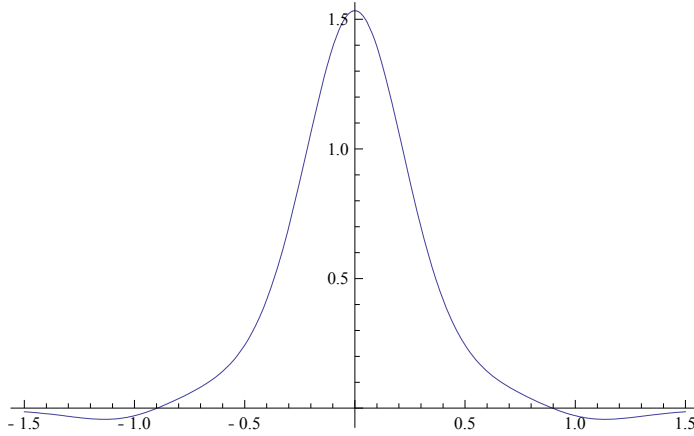


```
(*Calculate on-site interaction U and tunneling t*)
dx = 0.1;(*sufficient for integration, good to 50ppm*)
infty = 6 d;
Ud2ovg[VLat_] :=
 (Total[Table[Wannier[VLat, x, 0]^4, {x, -infty, infty, dx}]] * dx)^2
(*On-site interaction Ud^2/g as a function of lattice depth*)
t1[Vlat_] := N[(MathieuCharacteristicA[0.9999, -Vlat / 4] -
     MathieuCharacteristicA[0, -Vlat / 4]) / 4]
(*nearest site tunneling in the unit of Er, E(q) = -2∑ t_n Cos(nqd),
E(π/d)-E(0)=4 (t_1 + t_3 + ....)*)
Ud2ovg[V]
t1[V]
```

BIBLIOGRAPHY

[1] Steven Chu. Cold atoms and quantum control. *Nature*, 416(6877):206–210, 2002.

[2] M. H. Anderson, J. R. Ensher, M. R. Matthews, C. E. Wieman, and E. A. Cornell. Observation of Bose-Einstein condensation in a dilute atomic vapor. *Science*, 269(5221):198–201, 1995.

[3] K. B. Davis, M. O. Mewes, M. R. Andrews, N. J. van Druten, D. S. Durfee, D. M. Kurn, and W. Ketterle. Bose-Einstein condensation in a gas of sodium atoms. *Phys. Rev. Lett.*, 75(22):3969–3973, 1995.

[4] C. C. Bradley, C. A. Sackett, and R. G. Hulet. Bose-Einstein condensation of lithium: Observation of limited condensate number. *Phys. Rev. Lett.*, 78(6):985–989, 1997.

[5] C. Pethick and H. Smith. *Bose-Einstein condensation in dilute gases*. Cambridge University Press, 2002.

[6] C. Chin, R. Grimm, P. Julienne, and E. Tiesinga. Feshbach resonances in ultracold gases. *Rev. Mod. Phys.*, 82(2):1225–1286, 2010.

[7] Richard P. Feynman. Simulating Physics with Computers. *Int. J. Theor. Phys.*, 21(6):467–488, 1982.

[8] M. Greiner, O. Mandel, T. Esslinger, T. W. Hänsch, and I. Bloch. Quantum phase transition from a superfluid to a Mott insulator in a gas of ultracold atoms. *Nature*, 415(6867):39–44, 2002.

[9] M. P. A. Fisher, P. B. Weichman, G. Grinstein, and D. S. Fisher. Boson localization and the superfluid-insulator transition. *Phys. Rev. B*, 40(1):546–570, 1989.

[10] D. Jaksch, C. Bruder, J. I. Cirac, C. W. Gardiner, and P. Zoller. Cold bosonic atoms in optical lattices. *Phys. Rev. Lett.*, 81(15):3108–3111, 1998.

[11] Thilo Stöferle, Henning Moritz, Christian Schori, Michael Köhl, and Tilman Esslinger. Transition from a strongly interacting 1D superfluid to a Mott insulator. *Phys. Rev. Lett.*, 92(13):130403, Mar 2004.

[12] M. Köhl, H. Moritz, T. Stöferle, C. Schori, and T. Esslinger. Superfluid to Mott insulator transition in one, two, and three dimensions. *Journal of Low Temperature Physics*, 138(3):635–644, 2005.

[13] I. B. Spielman, W. D. Phillips, and J. V. Porto. Mott-insulator transition in a two-dimensional atomic Bose gas. *Phys. Rev. Lett.*, 98(8):080404, Feb 2007.

[14] I. Bloch, J. Dalibard, and W. Zwerger. Many-body physics with ultracold gases. *Rev. Mod. Phys.*, 80(3):885–964, 2008.

[15] Sabine Stock, Zoran Hadzibabic, Baptiste Battelier, Marc Cheneau, and Jean Dalibard. Observation of phase defects in quasi-two-dimensional Bose-Einstein condensates. *Phys. Rev. Lett.*, 95(19):190403, Nov 2005.

[16] V. L. Berezinskii. Destruction of long-range order in one-dimensional and two-dimensional systems possessing a continuous symmetry group xii. quantum systems. *Sov. Phys. JETP*, 34:610–616, 1972.

[17] J. M. Kosterlitz and D. J. Thouless. Ordering, metastability and phase transitions in two-dimensional systems. *Journal of Physics C: Solid State Physics*, 6(7):1181–1203, 1973.

[18] Z. Hadzibabic, P. Krüger, M. Cheneau, B. Battelier, and J. Dalibard. Berezinskii-Kosterlitz-Thouless crossover in a trapped atomic gas. *Nature*, 441(7097):1118–1121, 2006.

[19] V. Schweikhard, S. Tung, and E. A. Cornell. Vortex proliferation in the Berezinskii-Kosterlitz-Thouless regime on a two-dimensional lattice of Bose-Einstein condensates. *Phys. Rev. Lett.*, 99(3):030401, 2007.

[20] P. Cladé, C. Ryu, A. Ramanathan, K. Helmerson, and W. D. Phillips. Observation of a 2D Bose gas: From thermal to quasicondensate to superfluid. *Phys. Rev. Lett.*, 102(17):170401, 2009.

[21] Lewi Tonks. The complete equation of state of one, two and three-dimensional gases of hard elastic spheres. *Phys. Rev.*, 50(10):955–963, Nov 1936.

[22] M Girardeau. Relationship Between Systems of Impenetrable Bosons and Fermions in One Dimension. *Journal of Mathematical Physics*, 1(6):516–523, 1960.

[23] Belén Paredes, Artur Widera, Valentin Murg, Olaf Mandel, Simon Fölling, Ignacio Cirac, Gora V. Shlyapnikov, Theodor W. Hänsch, and Immanuel Bloch. Tonks-Girardeau gas of ultracold atoms in an optical lattice. *Nature*, 429(6989):277–281, 2004.

[24] Toshiya Kinoshita, Trevor Wenger, and David S. Weiss. Observation of a one-dimensional Tonks-Girardeau gas. *Science*, 305(5687):1125–1128, 2004.

[25] Toshiya Kinoshita, Trevor Wenger, and David S. Weiss. Local pair correlations in one-dimensional Bose gases. *Phys. Rev. Lett.*, 95(19):190406, Nov 2005.

[26] Elmar Haller, Russell Hart, Manfred J. Mark, Johann G. Danzl, Lukas Reichsollner, Mattias Gustavsson, Marcello Dalmonte, Guido Pupillo, and Hanns-Christoph Nägerl. Pinning quantum phase transition for a Luttinger liquid of strongly interacting bosons. *Nature*, 466(7306):597–600, 2010.

[27] W. Ketterle, D. S. Durfee, and D. M. Stamper-Kurn. Making, probing and understanding Bose-Einstein condensates. *Proceedings of the International School of Physics "Enrico Fermi"*, Course CXL:p67, 1999.

[28] Simon Fölling, Artur Widera, Torben Müller, Fabrice Gerbier, and Immanuel Bloch. Formation of spatial shell structure in the superfluid to Mott insulator transition. *Phys. Rev. Lett.*, 97(6):060403, 2006.

[29] Tin-Lun Ho and Qi Zhou. Obtaining the phase diagram and thermodynamic quantities of bulk systems from the densities of trapped gases. *Nature Physics*, 6(2):131–134, 10.

[30] S. Nascimbène, N. Navon, K. J. Jiang, F. Chevy, and C. Salomon. Exploring the thermodynamics of a universal Fermi gas. *Nature*, 463(7284):1057–1060, 2010.

[31] N. Navon, S. Nascimbène, F. Chevy, and C. Salomon. The equation of state of a low-temperature Fermi gas with tunable interactions. *Science*, 328(5979):729–732, 2010.

[32] Waseem S. Bakr, Jonathon I. Gillen, Amy Peng, Simon Folling, and Markus Greiner. A quantum gas microscope for detecting single atoms in a hubbard-regime optical lattice. *Nature*, 462(7269):74–77, 2009.

[33] Jacob F. Sherson, Christof Weitenberg, Manuel Endres, Marc Cheneau, Immanuel Bloch, and Stefan Kuhr. Single-atom-resolved fluorescence imaging of an atomic Mott insulator. *Nature*, 467(7311):68–72, 2010.

[34] D. Forster. *Hydrodynamic fluctuations, broken symmetry, and correlation functions*. Advanced Books Classics. Perseus Books, 1995.

[35] L. Pitaevskii and S. Stringari. *Bose-Einstein condensation*. Oxford : Oxford University Press, 2003.

[36] D. Pines and P. Nozières. *The Theory of Quantum Liquids*, volume I. New York : W A Benjamin, 1966.

[37] P. Nozières and D. Pines. *The Theory of Quantum Liquids*, volume II. Reading, MA : Addison-Wesley, 1990.

[38] Xibo Zhang, Chen-Lung Hung, Shih-Kuang Tung, Nathan Gemelke, and Cheng Chin. Exploring quantum criticality based on ultracold atoms in optical lattices. *New Journal of Physics*, 13(4):045011, 2011.

[39] Cheng Chin, Vladan Vuletić, Andrew J. Kerman, Steven Chu, Eite Tiesinga, Paul J. Leo, and Carl J. Williams. Precision Feshbach spectroscopy of ultracold Cs_2. *Phys. Rev. A*, 70(3):032701, Sep 2004.

[40] Tino Weber, Jens Herbig, Michael Mark, Hanns-Christoph Nagerl, and Rudolf Grimm. Bose-Einstein condensation of cesium. *Science*, 299(5604):232–235, 2003.

[41] Jens Herbig, Tobias Kraemer, Michael Mark, Tino Weber, Cheng Chin, Hanns-Christoph Nägerl, and Rudolf Grimm. Preparation of a pure molecular quantum gas. *Science*, 301(5639):1510–1513, 2003.

[42] M. Mark, F. Ferlaino, S. Knoop, J. G. Danzl, T. Kraemer, C. Chin, H.-C. Nägerl, and R. Grimm. Spectroscopy of ultracold trapped cesium Feshbach molecules. *Phys. Rev. A*, 76(4):042514, Oct 2007.

[43] Johann G. Danzl, Elmar Haller, Mattias Gustavsson, Manfred J. Mark, Russell Hart, Nadia Bouloufa, Olivier Dulieu, Helmut Ritsch, and Hanns-Christoph Nägerl. Quantum gas of deeply bound ground state molecules. *Science*, 321(5892):1062–1066, 2008.

[44] T. Kraemer, M. Mark, P. Waldburger, J. G. Danzl, C. Chin, B. Engeser, A. D. Lange, K. Pilch, A. Jaakkola, H.-C. Näerl, and R. Grimm. Evidence for Efimov quantum states in an ultracold gas of caesium atoms. *Nature*, 440(7082):315–318, 2006.

[45] F. Ferlaino, S. Knoop, M. Berninger, W. Harm, J. P. D'Incao, H.-C. Nägerl, and R. Grimm. Evidence for universal four-body states tied to an efimov trimer. *Phys. Rev. Lett.*, 102(14):140401, Apr 2009.

[46] J. von Stecher, J. P. D'Incao, and Chris H. Greene. Signatures of universal four-body phenomena and their relation to the efimov effect. *Nature Physics*, 5(6):417–421, 2009.

[47] Kenneth G. Wilson. The renormalization group: Critical phenomena and the kondo problem. *Rev. Mod. Phys.*, 47(4):773–840, Oct 1975.

[48] P. C. Hohenberg and B. I. Halperin. Theory of dynamic critical phenomena. *Rev. Mod. Phys.*, 49(3):435–479, Jul 1977.

[49] Sachdev S. *Quantum Phase Transitions*. Cambridge: Cambridge University Press, 1999.

[50] H. E. Stanley. Scaling, universality, and renormalization: Three pillars of modern critical phenomena. *Rev. Mod. Phys.*, 71:S358–S366, 1999.

[51] John A. Hertz. Quantum critical phenomena. *Phys. Rev. B*, 14(3):1165–1184, Aug 1976.

[52] T. Senthil, Leon Balents, Subir Sachdev, Ashvin Vishwanath, and Matthew P. A. Fisher. Quantum criticality beyond the landau-ginzburg-wilson paradigm. *Phys. Rev. B*, 70:144407, 2004.

[53] Hilbert v. Löhneysen, Achim Rosch, Matthias Vojta, and Peter Wölfle. Fermi-liquid instabilities at magnetic quantum phase transitions. *Rev. Mod. Phys.*, 79(3):1015–1075, Aug 2007.

[54] Philipp Gegenwart, Qimiao Si, and Frank Steglich. Quantum criticality in heavy-Fermion metals. *Nature Physics*, 4(3):186–197, 2008.

[55] J. L. Tallon and J. W. Loram. The doping dependence of T* - what is the real high-tc phase diagram? *Physica C: Superconductivity*, 349(1-2):53–68, 2001.

[56] D. van der Marel, H. J. A. Molegraaf, J. Zaanen, Z. Nussinov, F. Carbone, A. Damascelli, H. Eisaki, M. Greven, P. H. Kes, and M. Li. Quantum critical behaviour in a high-Tc superconductor. *Nature*, 425(6955):271–274, 2003.

[57] Cheng Chin, Vladan Vuletić, Andrew J. Kerman, and Steven Chu. High resolution Feshbach spectroscopy of cesium. *Phys. Rev. Lett.*, 85(13):2717–2720, Sep 2000.

[58] A. D. Lange, K. Pilch, A. Prantner, F. Ferlaino, B. Engeser, H.-C. Nägerl, R. Grimm, and C. Chin. Determination of atomic scattering lengths from measurements of molecular binding energies near Feshbach resonances. *Phys. Rev. A*, 79(1):013622, Jan 2009.

[59] Paul J. Leo, Carl J. Williams, and Paul S. Julienne. Collision properties of ultracold $cs133$ atoms. *Phys. Rev. Lett.*, 85(13):272–2724, 2000.

[60] Keith Burnett, Paul S. Julienne, Paul D. Lett, Eite Tiesinga, and Carl J. Williams. Quantum encounters of the cold kind. *Nature*, 416(6877):225–232, 2002.

[61] M. Gustavsson, E. Haller, M. J. Mark, J. G. Danzl, G. Rojas-Kopeinig, and H.-C. Nägerl. Control of interaction-induced dephasing of Bloch oscillations. *Phys. Rev. Lett.*, 100(8):080404, Feb 2008.

[62] P. O. Fedichev, M. W. Reynolds, and G. V. Shlyapnikov. Three-body recombination of ultracold atoms to a weakly bound s level. *Phys. Rev. Lett.*, 77(14):2921–2924, Sep 1996.

[63] Esben Nielsen and J. H. Macek. Low-energy recombination of identical bosons by three-body collisions. *Phys. Rev. Lett.*, 83(8):1566–1569, Aug 1999.

[64] B. D. Esry, Chris H. Greene, and James P. Burke. Recombination of three atoms in the ultracold limit. *Phys. Rev. Lett.*, 83(9):1751–1754, Aug 1999.

[65] P. F. Bedaque, Eric Braaten, and H.-W. Hammer. Three-body recombination in Bose gases with large scattering length. *Phys. Rev. Lett.*, 85(5):908–911, Jul 2000.

[66] Tino Weber, Jens Herbig, Michael Mark, Hanns-Christoph Nägerl, and Rudolf Grimm. Three-body recombination at large scattering lengths in an ultracold atomic gas. *Phys. Rev. Lett.*, 91(12):123201, Sep 2003.

[67] V. Efimov. Energy levels arising from resonant two-body forces in a three-body system. *Phys. Lett. B.*, 33:563–564, 1970.

[68] V. Efimov. Weakly-bound states of three resonantly-interacting particles. *Sov. J. Nucl. Phys.*, 12:589–595, 1971.

[69] C. Wieman and T. W. Hänsch. Doppler-free laser polarization spectroscopy. *Phys. Rev. Lett.*, 36(20):1170–1173, May 1976.

[70] Pearman,C. P., Adams, C. S., Cox, S. G., Griffin, P. F., Smith, D. A., and Hughe, I. G. Polarization spectroscopy of a closed atomic transition: applications to laser frequency lockin. *J. Phys. B: At. Mol. Opt. Phys.*, 35:5141–5151, 2002.

[71] Daniel A. Steck. Cesium d line data. *http://steck.us/alkalidata*, 2008. revision 2.0.1, 2 May.

[72] Mark, M., Kraemer, T., Herbig, J., Chin, C., Nägerl, H.-C., and Grimm, R. Efficient creation of molecules from a cesium Bose-Einstein condensate. *Europhys. Lett.*, 69(5):706–712, 2005.

[73] E. L. Raab, M. Prentiss, Alex Cable, Steven Chu, and D. E. Pritchard. Trapping of neutral sodium atoms with radiation pressure. *Phys. Rev. Lett.*, 59(23):2631–2634, 1987.

[74] J. Dalibard and C. Cohen-Tannoudji. Laser cooling below the Doppler limit by polarization gradients: simple theoretical models. *J. Opt. Soc. Am. B*, 6(11):2023–2045, 1989.

[75] H. J. Metcalf and P. van der Straten. *Laser Cooling and Trapping*. Springer, New York, 1999.

[76] Andrew J. Kerman, Vladan Vuletić, Cheng Chin, and Steven Chu. Beyond optical molasses: 3D Raman sideband cooling of atomic cesium to high phase-space density. *Phys. Rev. Lett.*, 84(3):439–442, 2000.

[77] Andrew J. Kerman. *Raman Sideband Cooling and Cold Atomic Collisions in Optical Lattices*. PhD thesis, Stanford University, 2002.

[78] Marshall T. DePue, Colin McCormick, S. Lukman Winoto, Steven Oliver, and David S. Weiss. Unity occupation of sites in a 3D optical lattice. *Phys. Rev. Lett.*, 82(11):2262–2265, Mar 1999.

[79] M. D. Barrett, J. A. Sauer, and M. S. Chapman. All-optical formation of an atomic Bose-Einstein condensate. *Phys. Rev. Lett.*, 87(1):010404, 2001.

[80] S. R. Granade, M. E. Gehm, K. M. O'Hara, and J. E. Thomas. All-optical production of a degenerate Fermi gas. *Phys. Rev. Lett.*, 88(12):120405, Mar 2002.

[81] Cindy A. Regal, Christopher Ticknor, John L. Bohn, and Deborah S. Jin. Creation of ultracold molecules from a Fermi gas of atoms. *Nature*, 424(6944):47–50, 2003. 10.1038/nature01738.

[82] Yosuke Takasu, Kenichi Maki, Kaduki Komori, Tetsushi Takano, Kazuhito Honda, Mitsutaka Kumakura, Tsutomu Yabuzaki, and Yoshiro Takahashi. Spin-singlet Bose-Einstein condensation of two-electron atoms. *Phys. Rev. Lett.*, 91(4):040404, 2003.

[83] L Luo, B Clancy, J Joseph, J Kinast, A Turlapov, and J E Thomas. Evaporative cooling of unitary Fermi gas mixtures in optical traps. *New Journal of Physics*, 8(9):213, 2006.

[84] Toshiya Kinoshita, Trevor Wenger, and David S. Weiss. All-optical Bose-Einstein condensation using a compressible crossed dipole trap. *Phys. Rev. A*, 71(1):011602, 2005.

[85] T. Kraemer, J. Herbig, M. Mark, T. Weber, C. Chin, H. C. Nägerl, and R. Grimm. Optimized production of a cesium Bose-Einstein condensate. *Applied Physics B: Lasers and Optics*, 79(8):1013–1019, 2004.

[86] W. Ketterle and N. J. Van Druten. Evaporative cooling of trapped atoms. *Advances in Atomic, Molecular, and Optical Physics*, 37:181–236, 1996.

[87] Andrew J. Kerman, Vladan Vuletić, Cheng Chin, and Steven Chu. Beyond optical molasses: 3D raman sideband cooling of atomic cesium to high phase-space density. *Phys. Rev. Lett.*, 84(3):439, 2000.

[88] T. Kraemer, M. Mark, P. Waldburger, J. G. Danzl, C. Chin, B. Engeser, A. D. Lange, K. Pilch, A. Jaakkola, H. C. Nägerl, and R. Grimm. Evidence for efimov quantum states in an ultracold gas of caesium atoms. *Nature*, 440(7082):315–318, 2006.

[89] Cheng Chin, Vladan Vuletić, Andrew J. Kerman, Steven Chu, Eite Tiesinga, Paul J. Leo, and Carl J. Williams. Precision Feshbach spectroscopy of ultracold cs2. *Phys. Rev. A*, 70(3):032701, 2004.

[90] O. J. Luiten, M. W. Reynolds, and J. T. M. Walraven. Kinetic theory of the evaporative cooling of a trapped gas. *Phys. Rev. A*, 53(1):381, 1996.

[91] K. M. O'Hara, M. E. Gehm, S. R. Granade, and J. E. Thomas. Scaling laws for evaporative cooling in time-dependent optical traps. *Phys. Rev. A*, 64(5):051403, 2001.

[92] E. L. Surkov, J. T. M. Walraven, and G. V. Shlyapnikov. Collisionless motion and evaporative cooling of atoms in magnetic traps. *Phys. Rev. A*, 53(5):3403, 1996.

[93] P. W. H. Pinkse, A. Mosk, M. Weidemler, M. W. Reynolds, T. W. Hijmans, and J. T. M. Walraven. One-dimensional evaporative cooling of magnetically trapped atomic hydrogen. *Phys. Rev. A*, 57(6):4747, 1998.

[94] M. Naraschewski and R. J. Glauber. Spatial coherence and density correlations of trapped Bose gases. *Phys. Rev. A*, 59(6):4595–4607, 1999.

[95] K. Hung. *Statistical Mechanics*. Wiley, 1987.

[96] D. S. Petrov, M. Holzmann, and G. V. Shlyapnikov. Bose-Einstein condensation in quasi-2D trapped gases. *Phys. Rev. Lett.*, 84(12):2551–2555, 2000.

[97] D. S. Petrov and G. V. Shlyapnikov. Interatomic collisions in a tightly confined Bose gas. *Phys. Rev. A*, 64(1):012706, 2001.

[98] Vanderlei Bagnato and Daniel Kleppner. Bose-Einstein condensation in low-dimensional traps. *Phys. Rev. A*, 44(11):7439–7441, Dec 1991.

[99] P. C. Hohenberg. Existence of long-range order in one and two dimensions. *Phys. Rev.*, 158(2):383–386, Jun 1967.

[100] M. Holzmann, G. Baym, J. P. Blaizot, and F. Laloë. Superfluid transition of homogeneous and trapped two-dimensional Bose gases. *Proceedings of the National Academy of Sciences of the United States of America*, 104(5):1476–1481, 2007.

[101] David R. Nelson and J. M. Kosterlitz. Universal jump in the superfluid density of two-dimensional superfluids. *Phys. Rev. Lett.*, 39(19):1201–1205, Nov 1977.

[102] V.N. Popov and J. Niederle. *Functional Integrals in Quantum Field Theory and Statistical Physics*. D. Reidel Publishing Company, 1983.

[103] N. Prokof'ev, O. Ruebenacker, and B. Svistunov. Critical point of a weakly interacting two-dimensional Bose gas. *Phys. Rev. Lett.*, 87(27 I):270402, 2001.

[104] Gordon Baym, Jean-Paul Blaizot, Markus Holzmann, Franck Laloë, and Dominique Vautherin. The transition temperature of the dilute interacting Bose gas. *Phys. Rev. Lett.*, 83(9):1703–1706, Aug 1999.

[105] Peter Arnold and Guy Moore. Bec transition temperature of a dilute homogeneous imperfect Bose gas. *Phys. Rev. Lett.*, 87(12):120401, Aug 2001.

[106] Subir Sachdev and Eugene Demler. Competing orders in thermally fluctuating superconductors in two dimensions. *Phys. Rev. B*, 69(14):144504, 2004.

[107] N. Prokof'ev and B. Svistunov. Two-dimensional weakly interacting Bose gas in the fluctuation region. *Phys. Rev. A*, 66(4):43608, 2002.

[108] M. Holzmann, M. Chevallier, and W. Krauth. Universal correlations and coherence in quasi-two-dimensional trapped Bose gases. *Phys. Rev. A*, 81(4):043622, 2010.

[109] S. P. Rath, T. Yefsah, K. J. Günter, M. Cheneau, R. Desbuquois, M. Holzmann, W. Krauth, and J. Dalibard. Equilibrium state of a trapped two-dimensional Bose gas. *Phys. Rev. A*, 82(1):013609, 2010.

[110] N.W. Ashcroft and N.D. Mermin. *Solid state physics*. Holt, Rinehart and Winston, 1976.

[111] M. Abramowitz and I.A. Stegun. *Handbook of mathematical functions with formulas, graphs, and mathematical tables*. Number v. 55, no. 1972 in Applied mathematics series. U.S. Govt. Print. Off., 1964.

[112] Ana Maria Rey. *Ultracold bosonic atoms in optical lattices*. PhD thesis, University of Maryland at College Park, 2004.

[113] J. K. Freericks and H. Monien. Strong-coupling expansions for the pure and disordered Bose-Hubbard model. *Phys. Rev. B*, 53(5):2691–2700, 1996.

[114] N. Elstner and H. Monien. Dynamics and thermodynamics of the Bose-Hubbard model. *Phys. Rev. B*, 59(19):12184–12187, 1999.

[115] Barbara Capogrosso-Sansone, Şebnem Güneş Söyler, Nikolay Prokof'ev, and Boris Svistunov. Monte Carlo study of the two-dimensional Bose-Hubbard model. *Phys. Rev. A*, 77(1):015602, 2008.

[116] Subir Sachdev. Universal relaxational dynamics near two-dimensional quantum critical points. *Phys. Rev. B*, 59(21):14054–14073, Jun 1999.

[117] T. Donner, S. Ritter, T. Bourdel, A. Öttl, M. Köhl, and T. Esslinger. Critical behavior of a trapped interacting Bose gas. *Science*, 315(5818):1556–1558, 2007.

[118] Massimo Campostrini, Martin Hasenbusch, Andrea Pelissetto, Paolo Rossi, and Ettore Vicari. Critical behavior of the three-dimensional xy universality class. *Phys. Rev. B*, 63(21):214503, 2001.

[119] Marcos Rigol, George G. Batrouni, Valery G. Rousseau, and Richard T. Scalettar. State diagrams for harmonically trapped bosons in optical lattices. *Phys. Rev. A*, 79(5):053605, 2009.

[120] Gretchen K. Campbell, Jongchul Mun, Micah Boyd, Patrick Medley, Aaron E. Leanhardt, Luis G. Marcassa, David E. Pritchard, and Wolfgang Ketterle. Imaging the Mott insulator shells by using atomic clock shifts. *Science*, 313(5787):649–652, 2006.

[121] W. S. Bakr, A. Peng, M. E. Tai, R. Ma, J. Simon, J. I. Gillen, S. Föling, L. Pollet, and M. Greiner. Probing the superfluidtoMott insulator transition at the single-atom level. *Science*, 329(5991):547–550, 2010.

[122] K. Jiménez-García, R. L. Compton, Y.-J. Lin, W. D. Phillips, J. V. Porto, and I. B. Spielman. Phases of a two-dimensional Bose gas in an optical lattice. *Phys. Rev. Lett.*, 105(11):110401, 2010.

[123] F. Gerbier. Boson Mott insulators at finite temperatures. *Phys. Rev. Lett.*, 99(12):120405, 2007.

[124] T. L. Ho and Q. Zhou. Intrinsic heating and cooling in adiabatic processes for bosons in optical lattices. *Phys. Rev. Lett.*, 99(12):120404, 2007.

[125] Tin-Lun Ho and Qi Zhou. Squeezing out the entropy of Fermions in optical lattices. *Proceedings of the National Academy of Sciences*, 106(17):6916–6920, 2009.

[126] Vladan Vuletić, Andrew J. Kerman, Cheng Chin, and Steven Chu. Observation of low-field Feshbach resonances in collisions of cesium atoms. *Phys. Rev. Lett.*, 82(7):1406–1409, Feb 1999.

[127] J Hecker Denschlag, J E Simsarian, H Häffner, C McKenzie, A Browaeys, D Cho, K Helmerson, S L Rolston, and W D Phillips. A Bose-Einstein condensate in an optical lattice. *Journal of Physics B: Atomic, Molecular and Optical Physics*, 35(14):3095, 2002.

[128] G. Reinaudi, T. Lahaye, Z. Wang, and D. Guéry-Odelin. Strong saturation absorption imaging of dense clouds of ultracold atoms. *Optics Letters*, 32(21):3143–3145, 2007.

[129] T. Yefsah, R. Desbuquois, L. Chomaz, K. J. Günter, and J. Dalibard. Exploring the thermodynamics of a two-dimensional Bose gas. *arXiv:1106.0188v1*, 2011.

[130] I. B. Spielman, W. D. Phillips, and J. V. Porto. Condensate fraction in a 2D Bose gas measured across the Mott-insulator transition. *Phys. Rev. Lett.*, 100(12):120402, 2008.

[131] Simon Fölling, Fabrice Gerbier, Artur Widera, Olaf Mandel, atjana Gericke, and Immanuel Bloch. Spatial quantum noise interferometry in expanding ultracold atom clouds. *Nature*, 434(7032):481–484, 2005.

[132] Fabrice Gerbier, Simon Fölling, Artur Widera, Olaf Mandel, and Immanuel Bloch. Probing number squeezing of ultracold atoms across the superfluid-Mott insulator transition. *Phys. Rev. Lett.*, 96(9):090401, Mar 2006.

[133] M. I. Kaganov and A. V. Chubukov. Interacting magnons. *Uspekhi Fizicheskikh Nauk.*, 153:537–578, 1987.

[134] B. Capogrosso-Sansone, N. V. Prokof'ev, and B. V. Svistunov. Phase diagram and thermodynamics of the three-dimensional Bose-Hubbard model. *Phys. Rev. B*, 75(13):134302, Apr 2007.

[135] C. L. Hung, X. Zhang, N. Gemelke, and C. Chin. Accelerating evaporative cooling of atoms into Bose-Einstein condensation in optical traps. *Phys. Rev. A*, 78:011604, 2008.

[136] G. G. Batrouni, V. Rousseau, R. T. Scalettar, M. Rigol, A. Muramatsu, P. J. H. Denteneer, and M. Troyer. Mott domains of bosons confined on optical lattices. *Phys. Rev. Lett.*, 89(11):117203, Aug 2002.

[137] J. Esteve, J.-B. Trebbia, T. Schumm, A. Aspect, C. I. Westbrook, and I. Bouchoule. Observations of density fluctuations in an elongated Bose gas: Ideal gas and quasicondensate regimes. *Phys. Rev. Lett.*, 96(13):130403, Apr 2006.

[138] M. Lewenstein, A. Sanpera, V. Ahufinger, B. Damski, A. Sen, and U. Sen. Ultracold atomic gases in optical lattices: Mimicking condensed matter physics and beyond. *Advances in Physics*, 56(2):243–379, 2007.

[139] S. Trotzky, L. Pollet, F. Gerbier, U. Schnorrberger, I. Bloch, N. V. Prokof/'ev, B. Svistunov, and M. Troyer. Suppression of the critical temperature for superfluidity near the Mott transition. *Nature Physics*, 6(12):998–1004, 2010.

[140] R. Jördens, N. Strohmaier, K. Gnter, H. Moritz, and T. Esslinger. A Mott insulator of Fermionic atoms in an optical lattice. *Nature*, 455(7210):204–207, 2008.

[141] U. Schneider, L. Hackermller, S. Will, Th Best, I. Bloch, T. A. Costi, R. W. Helmes, D. Rasch, and A. Rosch. Metallic and insulating phases of repulsively interacting Fermions in a 3D optical lattice. *Science*, 322(5907):1520–1525, 2008.

[142] J. Hubbard. Electron correlations in narrow energy bands. *Proceedings of the Royal Society of London. Series A. Mathematical and Physical Sciences*, 276(1365):238–257, 1963.

[143] T. Kinoshita, T. Wenger, and D. S. Weiss. A quantum newton's cradle. *Nature*, 440(7086):900–903, 2006.

[144] K. Winkler, G. Thalhammer, F. Lang, R. Grimm, J. Hecker Denschlag, A. J. Daley, A. Kantian, H. P. Bchler, and P. Zoller. Repulsively bound atom pairs in an optical lattice. *Nature*, 441(7095):853–856, 2006.

[145] Niels Strohmaier, Daniel Greif, Robert Jördens, Leticia Tarruell, Henning Moritz, Tilman Esslinger, Rajdeep Sensarma, David Pekker, Ehud Altman, and Eugene Demler. Observation of elastic doublon decay in the Fermi-Hubbard model. *Phys. Rev. Lett.*, 104(8):080401, Feb 2010.

[146] E. Altman, A. Polkovnikov, E. Demler, B. I. Halperin, and M. D. Lukin. Superfluid-insulator transition in a moving system of interacting bosons. *Phys. Rev. Lett.*, 95(2):020402, 2005.

[147] J. Mun, P. Medley, G. K. Campbell, L. G. Marcassa, D. E. Pritchard, and W. Ketterle. Phase diagram for a Bose-Einstein condensate moving in an optical lattice. *Phys. Rev. Lett.*, 99(15):150604, 2007.

[148] F. M. Cucchietti, B. Damski, J. Dziarmaga, and W. H. Zurek. Dynamics of the Bose-Hubbard model: Transition from a Mott insulator to a superfluid. *Phys. Rev. A*, 75(2):023603, 2007.

[149] N. Gemelke, X. Zhang, C. L. Hung, and C. Chin. In situ observation of incompressible Mott-insulating domains in ultracold atomic gases. *Nature*, 460(7258):995–998, 2009.

[150] S. R. Clark and D. Jaksch. Dynamics of the superfluids to Mott-insulator transition in one dimension. *Phys. Rev. A*, 70(4):043612, 2004.

[151] T. Gericke, F. Gerbier, A. Widera, S. Fölling, O. Mandel, and I. Bloch. Adiabatic loading of a Bose-Einstein condensate in a 3D optical lattice. *Journal of Modern Optics*, 54(5):735–743, 2007.

[152] J. Zakrzewski and D. Delande. Breakdown of adiabaticity when loading ultracold atoms in optical lattices. *Phys. Rev. A*, 80:013602, 2009.

[153] L. P. Pitaevskii and A. Rosch. Breathing modes and hidden symmetry of trapped atoms in two dimensions. *Phys. Rev. A*, 55(2):R853–R856, 1997.

[154] P. Krüger, Z. Hadzibabic, and J. Dalibard. Critical point of an interacting two-dimensional atomic Bose gas. *Phys. Rev. Lett.*, 99(4):040402, 2007.

[155] Z. Hadzibabic, P. Krger, M. Cheneau, S. P. Rath, and J. Dalibard. The trapped two-dimensional Bose gas: From Bose-Einstein condensation to berezinskii-Kosterlitz-Thouless physics. *New Journal of Physics*, 10:045006, 2008.

[156] S. Tung, G. Lamporesi, D. Lobser, L. Xia, and E. A. Cornell. Observation of the presuperfluid regime in a two-dimensional Bose gas. *Phys. Rev. Lett.*, 105(23):230408, 2010.

[157] C. L. Hung, X. Zhang, N. Gemelke, and C. Chin. Slow mass transport and statistical evolution of an atomic gas across the superfluid-Mott-insulator transition. *Phys. Rev. Lett.*, 104(16):160403, 2010.

[158] C. Mora and Y. Castin. Ground state energy of the two-dimensional weakly interacting Bose gas: First correction beyond Bogoliubov theory. *Phys. Rev. Lett.*, 102(18):180404, 2009.

[159] T. P. Simula, M. J. Davis, and P. B. Blakie. Superfluidity of an interacting trapped quasi-two-dimensional Bose gas. *Phys. Rev. A*, 77(2):023618, 2008.

[160] M. Holzmann and W. Krauth. Kosterlitz-Thouless transition of the quasi-two-dimensional trapped Bose gas. *Phys. Rev. Lett.*, 100(19):190402, 2008.

[161] R. N. Bisset, M. J. Davis, T. P. Simula, and P. B. Blakie. Quasicondensation and coherence in the quasi-two-dimensional trapped Bose gas. *Phys. Rev. A*, 79(3):033626, 2009.

[162] Kerson Huang. *Statistical mechanics*. New York : Wiley, 2nd ed. edition, 1987.

[163] R. Kubo. The fluctuation-dissipation theorem. *Reports on Progress in Physics*, 29(1):255–284, 1966.

[164] M. Toda, R. Kubo, and N. Saitō. *Statistical physics I: equilibrium statistical mechanics*. Springer series in solid-state sciences. Springer, 1995.

[165] Qi Zhou and Tin-Lun Ho. Universal thermometry for quantum simulation. *Phys. Rev. Lett.*, 106(22):225301, May 2011.

[166] Ehud Altman, Eugene Demler, and Mikhail D. Lukin. Probing many-body states of ultracold atoms via noise correlations. *Phys. Rev. A*, 70(1):013603, Jul 2004.

[167] M. Schellekens, R. Hoppeler, A. Perrin, J. Viana Gomes, D. Boiron, A. Aspect, and C. I. Westbrook. Hanbury brown twiss effect for ultracold quantum gases. *Science*, 310(5748):648–651, 2005.

[168] T. Rom, Th Best, D. van Oosten, U. Schneider, S. Fölling, B. Paredes, and I. Bloch. Free Fermion antibunching in a degenerate atomic Fermi gas released from an optical lattice. *Nature*, 444(7120):733–736, 2006.

[169] T. Jeltes, J. M. McNamara, W. Hogervorst, W. Vassen, V. Krachmalnicoff, M. Schellekens, A. Perrin, H. Chang, D. Boiron, A. Aspect, and C. I. Westbrook. Comparison of the hanbury brown-twiss effect for bosons and Fermions. *Nature*, 445(7126):402–405, 2007.

[170] Christian Sanner, Edward J. Su, Aviv Keshet, Ralf Gommers, Yong-il Shin, Wujie Huang, and Wolfgang Ketterle. Suppression of density fluctuations in a quantum degenerate Fermi gas. *Phys. Rev. Lett.*, 105(4):040402, Jul 2010.

[171] M. Greiner, C. A. Regal, J. T. Stewart, and D. S. Jin. Probing pair-correlated Fermionic atoms through correlations in atom shot noise. *Phys. Rev. Lett.*, 94(11):110401, Mar 2005.

[172] S. Hofferberth, I. Lesanovsky, T. Schumm, A. Imambekov, V. Gritsev, E. Demler, and J. Schmiedmayer. Probing quantum and thermal noise in an interacting many-body system. *Nature Physics*, 4(6):489–495, 2008.

[173] S. Manz, R. Bücker, T. Betz, Ch. Koller, S. Hofferberth, I. E. Mazets, A. Imambekov, E. Demler, A. Perrin, J. Schmiedmayer, and T. Schumm. Two-point density correlations of quasicondensates in free expansion. *Phys. Rev. A*, 81(3):031610, Mar 2010.

[174] Amir Itah, Hagar Veksler, Oren Lahav, Alex Blumkin, Coral Moreno, Carmit Gordon, and Jeff Steinhauer. Direct observation of a sub-poissonian number distribution of atoms in an optical lattice. *Phys. Rev. Lett.*, 104(11):113001, Mar 2010.

[175] Torben Müller, Bruno Zimmermann, Jakob Meineke, Jean-Philippe Brantut, Tilman Esslinger, and Henning Moritz. Local observation of antibunching in a trapped Fermi gas. *Phys. Rev. Lett.*, 105(4):040401, Jul 2010.

[176] J. Armijo, T. Jacqmin, K. V. Kheruntsyan, and I. Bouchoule. Probing three-body correlations in a quantum gas using the measurement of the third moment of density fluctuations. *Phys. Rev. Lett.*, 105(23):230402, Nov 2010.

[177] Christian Sanner, Edward J. Su, Aviv Keshet, Wujie Huang, Jonathon Gillen, Ralf Gommers, and Wolfgang Ketterle. Speckle imaging of spin fluctuations in a strongly interacting Fermi gas. *Phys. Rev. Lett.*, 106(1):010402, Jan 2011.

[178] Thibaut Jacqmin, Julien Armijo, Tarik Berrada, Karen V. Kheruntsyan, and Isabelle Bouchoule. Sub-poissonian fluctuations in a 1D Bose gas: From the quantum quasicondensate to the strongly interacting regime. *Phys. Rev. Lett.*, 106(23):230405, Jun 2011.

[179] Chen-Lung Hung, Xibo Zhang, Nathan Gemelke, and Cheng Chin. Observation of scale invariance and universality in two-dimensional Bose gases. *Nature*, 470(7333):236–239, 2011.

[180] S. Giorgini, L. P. Pitaevskii, and S. Stringari. Anomalous fluctuations of the condensate in interacting Bose gases. *Phys. Rev. Lett.*, 80(23):5040–5043, Jun 1998.

[181] Pitaevskii L P Klawunn M, Recati A and Stringari S. Local atom number fluctuations in quantum gases at finite temperature. *arXiv:1102.3805v1*, 2011.

[182] D. M. Stamper-Kurn, A. P. Chikkatur, A. Görlitz, S. Inouye, S. Gupta, D. E. Pritchard, and W. Ketterle. Excitation of phonons in a Bose-Einstein condensate by light scattering. *Phys. Rev. Lett.*, 83(15):2876–2879, Oct 1999.

[183] J. Steinhauer, R. Ozeri, N. Katz, and N. Davidson. Excitation spectrum of a Bose-Einstein condensate. *Phys. Rev. Lett.*, 88(12):120407, Mar 2002.

[184] E. D. Kuhnle, H. Hu, X.-J. Liu, P. Dyke, M. Mark, P. D. Drummond, P. Hannaford, and C. J. Vale. Universal behavior of pair correlations in a strongly interacting Fermi gas. *Phys. Rev. Lett.*, 105(7):070402, Aug 2010.

[185] R Bücker, A Perrin, S Manz, T Betz, Ch Koller, T Plisson, J Rottmann, T Schumm, and J Schmiedmayer. Single-particle-sensitive imaging of freely propagating ultracold atoms. *New Journal of Physics*, 11(10):103039, 2009.

[186] M. Karski, L. Förster, J. M. Choi, W. Alt, A. Widera, and D. Meschede. Nearest-neighbor detection of atoms in a 1D optical lattice by fluorescence imaging. *Phys. Rev. Lett.*, 102(5):053001, Feb 2009.

[187] Goodman J W. *Introduction to Fourier Optics*. Greenwood Village: Roberts & Co, 2005.

[188] Augustus J. E. M. Janssen. Extended Nijboer-Zernike approach for the computation of optical point-spread functions. *J. Opt. Soc. Am. A*, 19(5):849–857, May 2002.

[189] G. E. Astrakharchik, R. Combescot, and L. P. Pitaevskii. Fluctuations of the number of particles within a given volume in cold quantum gases. *Phys. Rev. A*, 76(6):063616, Dec 2007.

[190] F. Meier and W. Zwerger. Anomalous condensate fluctuations in strongly interacting super-fluids. *Phys. Rev. A*, 60(6):5133–5135, Dec 1999.

[191] W. Zwerger. Anomalous fluctuations in phases with a broken continuous symmetry. *Phys. Rev. Lett.*, 92(2):027203, Jan 2004.

[192] Subir Sachdev and Emily R. Dunkel. Quantum critical dynamics of the two-dimensional Bose gas. *Phys. Rev. B*, 73(8):085116, Feb 2006.

[193] Wojciech H. Zurek, Uwe Dorner, and Peter Zoller. Dynamics of a quantum phase transition. *Phys. Rev. Lett.*, 95(10):105701, Sep 2005.

[194] Subir Sachdev and Oleg A. Starykh. Thermally fluctuating superconductors in two dimensions. *Nature*, 405(6784):322–325, 2000.

[195] Min-Chul Cha, Matthew P. A. Fisher, S. M. Girvin, Mats Wallin, and A. Peter Young. Universal conductivity of two-dimensional films at the superconductor-insulator transition. *Phys. Rev. B*, 44(13):6883–6902, Oct 1991.

[196] Subir Sachdev and Markus Müller. Quantum criticality and black holes. *Journal of Physics: Condensed Matter*, 21(16):164216, 2009.

[197] Ofer Aharony, Steven S. Gubser, Juan Maldacena, Hirosi Ooguri, and Yaron Oz. Large N field theories, string theory and gravity. *Physics Reports*, 323(3-4):183 – 386, 2000.

[198] Makariy A. Tanatar, Johnpierre Paglione, Cedomir Petrovic, and Louis Taillefer. Anisotropic violation of the Wiedemann-Franz law at a quantum critical point. *Science*, 316(5829):1320–1322, 2007.

[199] Stefan S. Natu, Kaden R. A. Hazzard, and Erich J. Mueller. Local versus global equilibration near the bosonic Mott-insulator-superfluid transition. *Phys. Rev. Lett.*, 106(12):125301, Mar 2011.

[200] J. Rammer. *Quantum Transport Theory*. Frontiers in Physics. Massachusetts: Perseus books, 1998.

[201] Jr Walter T. Grandy. *Entropy and the Time Evolution of Macroscopic Systems*. Oxford University Press, Oxford, 2008.

[202] Barbara Capogrosso-Sansone, Şebnem Güneş Söyler, Nikolay Prokof'ev, and Boris Svistunov. Monte Carlo study of the two-dimensional Bose-Hubbard model. *Phys. Rev. A*, 77(1):015602, Jan 2008.

[203] T W B Kibble. Topology of cosmic domains and strings. *Journal of Physics A: Mathematical and General*, 9(8):1387, 1976.

[204] W. H. Zurek. Cosmological experiments in superfluid helium? *Nature*, 317(6037):505–508, 1985.

[205] Anatoli Polkovnikov. Universal adiabatic dynamics in the vicinity of a quantum critical point. *Phys. Rev. B*, 72(16):161201, Oct 2005.

[206] C. De Grandi, V. Gritsev, and A. Polkovnikov. Quench dynamics near a quantum critical point. *Phys. Rev. B*, 81(1):012303, Jan 2010.

[207] J. R. Abo-Shaeer, C. Raman, J. M. Vogels, and W. Ketterle. Observation of vortex lattices in Bose-Einstein condensates. *Science*, 292(5516):476–479, 2001.

[208] I. Coddington, P. C. Haljan, P. Engels, V. Schweikhard, S. Tung, and E. A. Cornell. Experimental studies of equilibrium vortex properties in a Bose-condensed gas. *Phys. Rev. A*, 70(6):063607, Dec 2004.

[209] Ralf Schützhold, Michael Uhlmann, Yan Xu, and Uwe R. Fischer. Sweeping from the superfluid to the Mott phase in the Bose-Hubbard model. *Phys. Rev. Lett.*, 97(20):200601, Nov 2006.

[210] Anatoli Polkovnikov and Vladimir Gritsev. Breakdown of the adiabatic limit in low-dimensional gapless systems. *Nature Physics*, 4(6):477–481, 2008.

[211] Marcos Rigol, Vanja Dunjko, and Maxim Olshanii. Thermalization and its mechanism for generic isolated quantum systems. *Nature*, 452(7189):854–858, 2008.